



Dissertation

Nonstoichiometry in SrTiO_3 and its relevance for tunable conductivity and photovoltage

ausgeführt zum Zwecke der Erlangung des akademischen Grades eines Doktors der technischen Wissenschaften (Dr. techn.), eingereicht an der TU Wien, Fakultät für Technische Chemie, von

DI Maximilian Morgenbesser

Mat.Nr.: 1026641

Burggasse 35/7, 1070 Wien

unter der Leitung von

Univ.Prof. Dipl.-Phys. Dr.rer.nat. Jürgen Fleig

Institut für Chemische Technologien und Analytik

Wien, August 2021

Diese Arbeit wurde vom FWF im Rahmen des Projekts W1243-N16
sowie vom Forschungs- und Innovationsprogramm der europäischen Union
im Rahmen von Horizon 2020 im Projekt No. 824072 unterstützt.

Eidesstattliche Erklärung

Ich erkläre an Eides statt, dass die vorliegende Arbeit nach den anerkannten Grundsätzen für wissenschaftliche Abhandlungen von mir selbstständig erstellt wurde. Alle verwendeten Hilfsmittel, insbesondere die zugrunde gelegte Literatur, sind in dieser Arbeit genannt und aufgelistet. Die aus den Quellen wörtlich entnommenen Stellen, sind als solche kenntlich gemacht.

Das Thema dieser Arbeit wurde von mir bisher weder im In- noch Ausland einer Beurteilerin/einem Beurteiler zur Begutachtung in irgendeiner Form als Prüfungsarbeit vorgelegt. Diese Arbeit stimmt mit der von den Begutachterinnen/Begutachtern beurteilten Arbeit überein.

Ich nehme zur Kenntnis, dass die vorgelegte Arbeit mit geeigneten und dem derzeitigen Stand der Technik entsprechenden Mitteln (Plagiat-Erkennungssoftware) elektronisch-technisch überprüft wird. Dies stellt einerseits sicher, dass bei der Erstellung der vorgelegten Arbeit die hohen Qualitätsvorgaben im Rahmen der geltenden Regeln zur Sicherung guter wissenschaftlicher Praxis „Code of Conduct“ an der TU Wien eingehalten wurden. Zum anderen werden durch einen Abgleich mit anderen studentischen Abschlussarbeiten Verletzungen meines persönlichen Urheberrechts vermieden.

Stadt und Datum

Unterschrift

Abstract

One of the most investigated materials in solid state ionics is SrTiO₃, a perovskite-type oxide. Among others, it finds interest in the field of resistive switching for memristive applications as well as in photoionics, i.e photo-induced ionic effects. What makes this material particularly interesting is that its defect structure in the bulk is well investigated and defect models are available for doped and undoped SrTiO₃. In thin films, however, these bulk models often fail to explain or predict the electrochemical properties, and different explanations are discussed in literature, e.g. stress/strain, space charge zones or nonstoichiometry, particularly cation vacancies due to a Sr/Ti ratio deviating from unity. Moreover, in SrTiO₃ under illumination changes of the oxygen vacancies may play an essential role (photoionics).

In this thesis, the various effects of both types of vacancies (i.e. cation vacancies and oxygen vacancies) in SrTiO₃ are investigated in regard to electrical conductivity and photovoltages. Different characterization techniques are employed, ranging from characterization via electrochemical impedance spectroscopy (EIS) to elemental analysis (inductively coupled plasma optical emission spectroscopy, ICP-OES; Rutherford backscattering spectroscopy, RBS), lab-scale X-ray diffraction methods and even synchrotron based methods (X-ray standing wave, XSW; X-ray absorption spectroscopy, XAS; positron annihilation lifetime spectroscopy, PALS). The aim of this thesis is to provide a concise picture of the relationship between electrical properties and vacancies in SrTiO₃ thin films.

First, the electrical conductivity of Fe doped SrTiO₃ thin films is characterized by means of impedance spectroscopy. Surprisingly, at about 350 °C – 700 °C, electronically pseudo-intrinsic conductivity is measured for these thin films despite 2 % Fe doping. Furthermore, a Sr deficiency is found. An experimental route towards bulk-like conductivity is developed by adding excess Sr to the target for the pulsed laser deposition (PLD), and indeed a tremendous increase in conductivity results up to bulk-like values. PALS measurements also reveal a change of the predominant point defect from Sr vacancies to clusters of titanium vacancies and oxygen vacancies. In the next step, the very nature of the pseudo-intrinsic conductivity found in doped SrTiO₃ thin films is investigated. Here, different doping concentrations and dopants (Fe, Al, Ni) are used, revealing appearance of electronically intrinsic conductivity for a vast number of samples. Synchrotron based experiments indicate a change in Fe site occupation for slightly Fe doped SrTiO₃ (XSW), which is accompanied by a change in Fe oxidation state or electronic surrounding (XAS).

Moreover, Sr vacancies are found in nominally undoped and slightly Fe doped thin films using positron annihilation lifetime spectroscopy. Based on these and other observations, a model is deduced for explaining the pseudo-intrinsic behavior. This model postulates Sr vacancies as mid gap states, pinning the electrical conductivity to the intrinsic value. Moreover, polycrystalline SrTiO₃ pellets with different cation nonstoichiometry were investigated in regard to their conductivity. An increase in conductivity is observed for Sr deficient SrTiO₃ pellets in contrast to thin films and discussion in terms of Schottky disorder.

Finally, SrTiO₃ single crystal based heterojunctions are investigated as high temperature photovoltaic cells. Time resolved voltage measurements reveal a time dependency of the photovoltage, which is attributed to oxygen vacancy related processes. Moreover, a long-lasting increase of the current (and power) was found in such a cell under UV illumination. This “self-enhancing” effect is explained by stoichiometry polarization due to the photovoltage being applied to the bulk SrTiO₃, again highlighting how essential oxygen vacancies are for understanding electrochemical properties and processes in SrTiO₃. The findings are then compared to thin film photovoltaic cells. Again, a vastly different behavior is found for single crystals and thin films and the changes in photovoltage can be attributed to the special defect situation in thin film due to Sr vacancy induced gap states.

Kurzfassung

Eines der am besten erforschten Materialien im Bereich der Festkörperionik ist Strontiumtitanat, SrTiO_3 , ein Oxid in Perowskitstruktur, welches unter anderem für umschaltbare Widerstände, für Speicheranwendungen und im Bereich von lichtinduzierten ionische Effekten in Oxiden von Interesse ist. Vorteilhaft ist hierbei auch, dass die Defektstruktur von SrTiO_3 sehr gut erforscht und verstanden ist und Modelle hinsichtlich der relevanten Defektkonzentrationen für dotiertes und undotiertes Strontiumtitanat vorhanden sind. In Dünnschichten hingegen scheitern diese Modelle oft daran, experimentell beobachtete Eigenschaften zu erklären. In der Literatur werden hier unterschiedliche Faktoren diskutiert, die hinter dem abweichenden Verhalten stecken, etwa Spannungen, Raumladungen und Nichtstöchiometrie, besonders Kationennichtstöchiometrie. Darüber hinaus spielen Sauerstoffleerstellen im Bereich der Photoionik von SrTiO_3 eine essentielle Rolle.

In dieser Arbeit werden die unterschiedlichen Effekte beider Arten von Leerstellen (Kationenleerstellen und Sauerstoffleerstellen) untersucht, insbesondere im Hinblick auf elektrische Leitfähigkeiten und Photospannungen. Unterschiedliche Charakterisierungsmethoden werden angewandt, etwa elektrochemische Impedanzspektroskopie, optische Emissionsspektroskopie sowie unterschiedliche Röntgentechniken im Labormaßstab sowie bei Synchrotronanlagen (Röntgenabsorption, stehende Röntgenwelle, Positronen-Annihilations-Lebensdauer-Spektroskopie). Dabei ist das Ziel dieser Arbeit, ein möglichst präzises Bild vom Wechselspiel aus elektrochemischen Eigenschaften und Leerstellen in SrTiO_3 zu vermitteln.

Zuerst werden Fe dotierte SrTiO_3 Dünnschichten mit Impedanzspektroskopie im Hinblick auf deren elektrische Leitfähigkeit untersucht. Überraschenderweise entspricht die bei 350 °C bis 700°C gefundene Leitfähigkeit dem elektronisch intrinsischen Wert, obwohl die Dünnschichten mit 2 % Fe dotiert sind. Weiters wird eine Sr Verarmung in den Schichten gefunden. Eine experimentelle Route zur Leitfähigkeitserhöhung wird erarbeitet, indem ein Sr Überschuss im Ausgangsmaterial für die gepulste Laserdeposition zugegeben wird. Eine deutliche Leitfähigkeitserhöhung bis hin zu den erwarteten Leitfähigkeitswerten von makroskopischen Proben kann dadurch erreicht werden. Messungen mit Positronen-Annihilations-Lebensdauer-Spektroskopie zeigen einen Wechsel des dominanten Punktdefekts von Sr Leerstellen hin zu Komplexen aus einer Titanleerstelle und einer Sauerstoffleerstelle. Im Folgenden wird die Natur dieser elektronisch pseudo-intrinsischen Leitfähigkeit in SrTiO_3 Dünnschichten genauer untersucht. Hierbei werden unterschiedliche

Dotierelemente und Dotierkonzentrationen verwendet, wobei bei allen untersuchten Proben pseudo-intrinsische Leitfähigkeit gefunden wird. Synchrotronbasierte Experimente zeigen einen Wechsel der Platzbesetzung des Fe vom B-Platz hin zum A-Platz, der mit einem dementsprechenden Wechsel der Oxidationsstufe beziehungsweise elektronischen Umgebung verbunden ist. In den untersuchten Filmen liegen laut Positronen-Annihilations-Lebensdauer-Spektroskopie Sr Leerstellen als vorherrschender Punktdefekt vor. Basierend auf diesen und anderen Beobachtungen wird ein Modell entwickelt, um das pseudo-intrinsische Leitfähigkeitsverhalten zu erklären. Das Modell postuliert Sr Leerstellen als Zustände genau in der Mitte der Bandlücke, welche die Leitfähigkeit am pseudo-intrinsischen Wert fixieren. In diesem Zusammenhang werden auch polykristalline SrTiO₃ Presslinge mit unterschiedlicher Kationennichtstöchiometrie im Hinblick auf ihre Leitfähigkeit untersucht. Im Gegensatz zu Dünnschichten wird bei Presslingen eine Leitfähigkeitserhöhung beobachtet für Proben mit Sr Verarmung. Dies wird im Zusammenhang mit der Schottky Fehlordnung diskutiert.

Schließlich werden auf SrTiO₃-Einkristallen basierende Heteroübergänge als Hochtemperaturphotovoltaikzellen untersucht. Zeitaufgelöste Spannungsmessungen zeigen eine Zeitabhängigkeit der Photospannung, welche Prozessen mit Sauerstoffleerstellen zugeschrieben werden. Darüber hinaus ergibt sich ein lang andauernder Anstieg des Stroms (und damit auch der Leistung) unter UV Licht. Dieser „Selbstverbesserungseffekt“ kann durch Stöchiometriepolarisation aufgrund der Photospannung, die am SrTiO₃ Einkristall abfällt, erklärt werden. Auch dies zeigt die Wichtigkeit von Sauerstoffleerstellen für das Verständnis von elektrochemischen Eigenschaften und Vorgängen in SrTiO₃. Diese Ergebnisse werden anschließend mit Dünnschichten verglichen. Wieder ergibt sich ein deutlich verschiedenes Verhalten für Einkristalle und Dünnschichten und die Änderungen der Photospannung werden der speziellen Defektstruktur in Dünnschichten, insbesondere der von Sr Leerstellen induzierten Zustände, zugeschrieben.

Danksagung

An dieser Stelle möchte ich mich bei den zahlreichenden Mitwirkenden und Ermöglichenden dieser Arbeit bedanken:

- Zu allererst bei meinen Betreuer Prof. Jürgen Fleig für seine Ideen, Diskussionen und Erklärungen, für seine ansteckende Freude an der Festkörperionik und für die Förderung, etwa im Rahmen von Konferenzbesuche oder durch Synchrotronmessungen.
- Bei Markus für die schier endlose Geduld bei Erklärungen zu meinen Fragen, auch wenn es columbogleich die gefühlt siebzehnte „noch eine Frage“ am selben Vormittag war.
- Bei Steffi, Christopher, Niklas sowie den beiden Alexen (S. und V.) für die wertvollen Beiträge zu meiner Arbeit, angefangen von XRD Messungen, chemischen Analysen, Leitfähigkeitsmessungen, Synchrotronmessungen und Modellrechnungen.
- Bei Federico für die sehr schöne Zusammenarbeit und die hilfreichen Vorschläge beim Paperschreiben.
- Bei meinen Bürokollegen Stefan und Christine für die angenehme Atmosphäre und die lustigen Plaudereien.
- ~~Beim Lavalampenclub mit den Gründungsmitgliedern~~ ES GIBT KEINEN LAVALAMPENCLUB. EINFACH WEITERLESEN.
- Bei der gesamten Arbeitsgruppe für die vielen gemeinsamen Mittagessen (oder im Fall von Harald für das eine gemeinsame Mittagessen), für wissenschaftliche Diskussionen und einfach auch für den Zusammenhalt und die Zusammenarbeit miteinander.
- Bei Freunden und Verwandten, bei all denen, die mir in den letzten Jahren Rückhalt gegeben haben und Verständnis entgegengebracht haben.
- Ganz speziell bei Thomas, Stefan, Michi, Bernhard und Benni für unsere Diskussionen, DSA-Spieleabende und das Hochhalten der Memekultur.
- Bei meiner Katze Flauschhilda, weil sie ein glorreicher Halunke ist.
- Bei meiner Freundin Vroni für den Rückhalt, die Unterstützung und, dass du immer da warst für mich.
- Bei meinen Eltern, Kurt und Helga, für die vielgestaltige Unterstützung in allen Lebenslagen. Danke für alles!

DANKESCHÖN!

Table of content

Chapter 1: Introduction	11
1.1 Motivation	11
1.2 State of the art.....	11
Chapter 2: Cation non-stoichiometry in Fe:SrTiO ₃ thin films and its effect on the electrical conductivity.....	15
2.1 Introduction	15
2.2 Experimental.....	17
2.3 Results and Discussion	21
2.3.1 Pseudo-intrinsic conductivity of films from stoichiometric targets.....	21
2.3.2 Structural, chemical and defect analysis of pseudo-intrinsic SrTiO ₃ films	23
2.3.3 SrTiO ₃ film tuning by controlling the deposition conditions (stoichiometric targets) ..	29
2.3.4 SrTiO ₃ film tuning using different target compositions	30
2.4 Conclusions	35
2.5 Supplementary Information.....	36
2.5.1 ICP-OES measurements.....	36
2.5.2 Three arguments supporting the use of a transmission line based fitting model of impedance spectra obtained for thin films deposited from stoichiometric targets	38
2.5.3 Comparison with data from literature on films from 0.4 % Fe doped targets	39
2.5.4 XRD of Sr overstoichiometric targets.....	41
2.5.5 XRD of thin films deposited from overstoichiometric targets.....	42
2.5.6 Discussion of the capacitances found for the thin films deposited from Sr overstoichiometric targets	42
Chapter 3: Unravelling the origin of ultra-low conductivity in doped SrTiO ₃ thin films: Sr vacancies as the key driver for Fermi level pinning.....	44
3.1 Introduction	44
3.2 Experimental.....	46
3.2.1 Sample preparation	46
3.2.2 Impedance spectroscopy	48
3.2.3 Elemental analysis	48
3.2.4 X-ray diffraction	49
3.2.5 Positron annihilation lifetime spectroscopy	50
3.2.6 X-ray standing wave measurements	50
3.2.7 X-ray absorption spectroscopy.....	51

3.3 Results	52
3.3.1 Conductivity measurements	52
3.3.2 Elemental analysis	55
3.3.3 X-ray diffraction	57
3.3.4 Positron annihilation lifetime spectroscopy	59
3.3.5 X-ray standing wave	60
3.3.6 X-ray absorption spectroscopy.....	63
3.4. Discussion.....	64
3.4.1. Basic Model	64
3.4.2. Specific states relevant in our SrTiO ₃ films.....	66
3.4.3. Model calculations for testing the consistency	70
3.4.4. Chemical Analogue.....	73
3.5 Conclusion	75
3.6 Supplementary Information:.....	75
3.6.1 Conductivity measurements for donor doped SrTiO ₃	75
3.6.2 Reciprocal mapping of the (103) reflection	76
3.6.3 ICP-OES measurements.....	77
3.6.4 XAS measurements for total electron yield	80
3.6.5 XAS simulation.....	81
Chapter 4: Cation nonstoichiometry in polycrystalline SrTiO ₃ bulk: A different situation than in thin films?.....	83
4.1 Introduction	83
4.2 Experimental.....	84
4.2.1 Pellet preparation	84
4.2.2 Single crystal preparation.....	84
4.2.3 Electrochemical impedance spectroscopy	84
4.3 Results and Discussion	85
4.3.1 Electrochemical characterization of polycrystals	85
4.3.2 Comparison with single crystals	88
4.3.3 Comparison with thin films	89
4.4 Conclusions	91
Chapter 5: Interaction between SrTiO ₃ and (ultraviolet) light: Photovoltage.....	92
5.1 Low temperature effects	94
5.2 High temperature effects	100
Chapter 6: SrTiO ₃ based high temperature solid oxide solar cells: Photovoltages, photocurrents and mechanistic insight	102

6.1 Introduction	102
6.2. Experimental.....	103
6.2.1 Sample preparation and characterization	103
6.2.2 Photo-voltage and photo-current measurements.....	105
6.2.3 Spectroscopic ellipsometry measurements	106
6.2.4 Electrochemical impedance spectroscopy measurements.....	107
6.3 Results and Discussion	108
6.3.1 Photo-voltages.....	108
6.3.2 Photocurrent under UV	113
6.3.3 Electrochemical impedance spectroscopy	116
6.3.4 Interpretation of the OCV measurements	119
6.4. Conclusion	122
Chapter 7: Completing the circle: Application of thin films in SrTiO ₃ based solar cells	123
7.1 Introduction	123
7.2 Experimental.....	123
7.2.1 Preparation of pellets	123
7.2.2 Preparation of thin films	124
7.2.3 Voltage measurements	124
7.3 Results	125
7.3.1 Polycrystalline solar cells	125
7.3.2 Towards thin film cells: Introduction of additional SrTiO ₃ layers in single crystal based solar cells	126
7.3.3 Thin film based solar cells	128
7.3.4 Micro-electrode measurements	129
7.3.5 A new hope: Using an ohmic contact	131
7.4 Discussion.....	132
7.5 Conclusions	134
Chapter 8: Summary.....	136
Chapter 9: References	139

Chapter 1: Introduction

1.1 Motivation

In the last couple of years, the discussion of the menacing climate change [1-4] has brought the need for green and environmentally friendly sources of energy closer to a worldwide audience and the relevance of e.g. photovoltaics or hydrogen fuel is generally accepted [5-8]. The interdisciplinary field of solid state ionics might be a key driver for future energy technologies including solid oxide fuel cells (SOFCs) [9, 10], solid oxide electrolyzer cells (SOEC) [11, 12] and high temperature photovoltaic (PV) or photoelectrochemical cells (PEC) [13]. Also other new technologies with vast potential emerge such as solid state memory devices [14-16] or the internet of things (IoT) [17, 18], for which decentralized small-scale power supply is essential [19]. In all these applications, defects (e.g. oxygen vacancies) play an essential role for the general functionality. Here, SrTiO₃ often serves as a model material for understanding defect chemistry and defect interaction, but is also in the focus of research due to its outstanding properties, especially in the field of resistive switching for memristive devices [20-23], photocatalysis [24, 25] and various energy applications [26-28]. In several fields, miniaturization is key for possible applications due to size limitations and potential power output increase (i.e. less resistance due to smaller dimension), e.g. for powering sensors used in the internet of things. Thus, understanding defects in SrTiO₃ – especially in SrTiO₃ thin films – is an interesting topic. While the defect model for bulk SrTiO₃ is well-investigated [29, 30], thin films often deviate from the expected bulk behavior, e.g. exceeding the expected (thermodynamic) level of Sr vacancies [31] or exhibiting electronically intrinsic conductivity despite doping [32]. Therefore, this work aims at a better understanding of the role of vacancies (both oxygen vacancies and cation vacancies) involved in a) photoelectrochemical processes relevant for high temperature photoelectrochemical cells and b) the special defect situation in SrTiO₃ thin films.

1.2 State of the art

Strontium titanate (SrTiO₃) is among the most investigated materials in the field of electroceramics

and solid state ionics [33]. The material's defect chemistry has been studied intensely, with defect models being available for undoped and donor as well as acceptor doped SrTiO₃ [29, 30]. Due to its controlled and well-defined defect chemistry, it is frequently employed as a model material in the field of electroceramics, e.g. for large band-gap materials or perovskite-type titanates such as BaTiO₃ or (Pb,Zr)TiO₃. SrTiO₃ is a mixed ionic and electronic conductor [33] and its conductivity can be tailored by the introduction of dopants [34]. Donor doping, e.g. Nb⁵⁺ at the Ti⁴⁺ site is compensated by either the introduction of cation vacancies or electrons, yielding n-type SrTiO₃ in the latter case. Acceptor doping, e.g. by substituting a Ti⁴⁺ ion with an Fe³⁺ ion, is charge-compensated by oxygen vacancies or electron holes, leading to p-type SrTiO₃ in the case of hole compensation. The respective defect reactions are

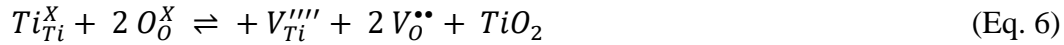
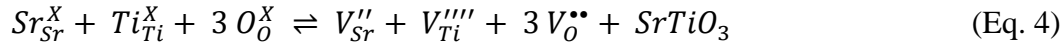


denoting to an donor or acceptor, respectively. Furthermore, the oxygen nonstoichiometry is also affected by oxygen release or uptake, depending on the oxygen partial pressure:



Alternatively, Eq. 3 can be written with electron holes instead of electrons (see Eq. 12). Here, the role of nonstoichiometry is easily accessible via ionic conductivity. Different studies on ionic conductivity in SrTiO₃ for grains [37,38], grain boundaries [37-39] and dislocations [35, 36] are available. Oxygen vacancies also play a fundamental role in understanding the electrochemical behavior and properties of SrTiO₃, e.g. for oxygen incorporation [40, 41], resistive switching in memristive devices [20, 23], photoelectrochemical processes [13, 42], coloration under UV light [41] and stoichiometry polarization [43].

Furthermore, cation vacancies are also present in SrTiO₃. Due to the densely packed perovskite structure, interstitial sites (e.g. introduced via Frenkel disorder) are not expected in SrTiO₃ [44]. However, Schottky disorder is commonly reported in SrTiO₃ and becomes relevant especially at high temperatures [34, 44]. Three different Schottky reactions are possible in SrTiO₃, with Eq. 4 describing the Schottky reaction, while Eq. 5 and 6 correspond to the Schottky-like partial reactions for SrO and TiO₂.



Note that the partial Schottky-like defect reactions in Eq. 5 and 6 do not conserve the stoichiometry in the perovskite phase but lead to the formation of secondary phases (TiO₂, SrO). Here, the most relevant reaction is the SrO partial Schottky reaction, with the total Schottky reaction being energetically only slightly unfavorable than the SrO partial Schottky reaction [34]. However, it is not reported that the TiO₂ related partial Schottky reaction plays a major role in the material's defect chemistry [34]. In addition, cation vacancies can also be introduced during sample preparation, thus often exceeding the expected thermodynamic equilibrium concentrations due to the Schottky disorder, especially in thin films [31].

In this study, the role of both types of vacancies, namely oxygen vacancies and Sr vacancies, is investigated. The influence of Sr vacancies is investigated in differently doped SrTiO₃ thin films prepared by pulsed laser deposition. In literature, SrTiO₃ thin films have been characterized with different methods, including X-ray diffraction [45-47] and positron annihilation lifetime spectroscopy [48-50]. However, the thin film characterization and optimization is often decoupled from considering the respective thin film properties. In chapter 2, we use an opposite approach: Starting with the surprisingly low conductivity found in slightly Fe doped SrTiO₃ thin films [32], different ways of obtaining bulk-like properties are investigated, such as a variation of the parameters used in pulsed laser deposition and the composition of the target materials. Structural and compositional information is obtained via X-ray diffraction (XRD) or reciprocal space mapping (RSM) and inductively coupled plasma optical emission spectroscopy (ICP-OES), respectively, and differences between the individual films are discussed in regard to their electrical conductivity.

In chapter 3, the origin of the ultra-low conductivity is further investigated using nominally undoped as well as differently doped SrTiO₃ thin films. In addition to lab-scale RSM and ICP-OES, synchrotron based experiments (X-ray standing wave, XSW; X-ray absorption spectroscopy, XAS; positron lifetime annihilation spectroscopy, PALS) were performed in order to investigate the defect structure of the thin films. A comprehensive model is deduced from the data obtained from the thin film characterization, which can explain the very unexpected electrochemical behavior of these thin films. For the sake of comparison, cation nonstoichiometry in bulk SrTiO₃

is investigated in chapter 4. Here, due to high temperatures used in sintering, thermodynamic equilibrium vacancy concentrations become relevant and fundamentally change the outcome of the experiment. The differences between nonstoichiometry effects in thin films and bulk SrTiO₃ are discussed and can be explained using the model derived in chapter 3.

Photoionics (or optoionics) is a rather new field in solid state ionics [51, 52] and finds fascinating applications, e.g. in organic metal halide perovskite-type materials [53] and in high temperature solid oxide photoelectrochemical cells [13]. This thesis deals with SrTiO₃ based solar cells and the role of oxygen vacancies in such devices. In chapter 5, a literature overview over SrTiO₃ based photovoltaic cells is provided, ranging from the low temperature devices, mostly operating without ionic contribution, to high temperature applications, allowing ionic transport and, thus, photo-induced ionic processes. Notable examples of high temperature photovoltaic cells are reported for SrTiO₃/La_{0.9}Sr_{0.1}CrO₃ interfaces yielding high photovoltages [42] and the phenomenological explanation of ionic contribution to the photovoltage observed for SrTiO₃ single crystals [13].

In chapter 6, open circuit voltage measurements are employed to investigate the photovoltage of different SrTiO₃ based heterojunctions. The time dependency of the photovoltage is linked to the oxygen vacancy transport in such photovoltaic cells. In short circuit measurements, a long-lasting current increase is visible, which we term “self-enhancing-effect”. The origin of this behavior is attributed to stoichiometry polarization occurring in short-circuit conditions. Further mechanistic information, especially regarding the space charge resistance, is gained by electrochemical impedance spectroscopy. Finally, the UV behavior of SrTiO₃ thin film cells is investigated in chapter 7. Severe differences between thin films and bulk properties become apparent. These are attributed to the defect induced change in Fermi level of the thin films.

Chapter 2: Cation non-stoichiometry in Fe:SrTiO₃ thin films and its effect on the electrical conductivity

The results presented in this chapter were also submitted as a scientific paper to Nanoscale Advances.

2.1 Introduction

SrTiO₃ (STO) single crystals and thin films are currently a cornerstone for the study of multiple phenomena such as resistive switching in memristive devices [22, 23, 54, 55], photoconductivity [56], increased oxygen incorporation under UV light [40, 41], photovoltages in bulk SrTiO₃ [13, 42], and interfacial conductivity, especially with LaAlO₃ [57, 58]. However, SrTiO₃ thin films are not fully understood yet and show great variability in properties depending on the fabrication conditions. For instance, thin films prepared by pulsed laser deposition (PLD) showed that the film structure and composition depends on the deposition parameters, particularly on the laser fluence [47, 48, 59, 60] and on the oxygen partial pressure [47]. The combination of different effects such as scattering of elements in the plasma plume and incongruent ablation may cause substantial cation non-stoichiometries leading to either Ti-rich thin films at higher fluences (due to preferential ablation of Ti species) or, opposite, Sr-rich thin films at low fluences (due to enhanced scattering of Ti) [60]. Stoichiometric thin films are reported when using a laser fluence of 1.1 J/cm² [60]. Overall, the existing literature clearly indicates that the preparation of truly stoichiometric films by pulsed laser deposition is far from trivial.

Despite the numerous studies performed so far, there is still only a limited understanding of the structure-composition-property relations in SrTiO₃ thin films. For example, it remains unclear how the crystal structure, the defect structure and the electrical properties of SrTiO₃ thin films are correlated and how much those properties differ from the values found for single crystals. Particularly, charge transport properties might be very sensitive to changes in the point defect chemistry (e.g. due to cation non-stoichiometry) and thus pulsed laser deposited thin films may behave electrically very different compared to bulk samples. For example, a correlation between conductivity and lattice constant was found for Nb:SrTiO₃ thin films [61, 62]. Other studies on

nominally 0.4 mol% Fe doped SrTiO₃ thin films (100 to 413 nm thickness) showed conductivities with values being orders of magnitude lower than those of the corresponding targets [32, 63]. Interestingly, these conductivities were very close to those expected for hypothetical ultrapure electronically intrinsic SrTiO₃. Similarly, conductivities of Nb-donor doped SrTiO₃ thin films have been varied by orders of magnitude simply by modifying the laser fluence in PLD deposited layers, which was correlated with different lattice expansion and, thus, cation non-stoichiometries [64]. Also the properties of conducting SrTiO₃/LaAlO₃ heterointerfaces have been proved to be strongly affected by small variations of the LaAlO₃ composition [65, 66].

Owing to this sensitivity of properties to the exact composition and/or structure of the thin films, it is mandatory to have sensitive tools for quantitatively evaluating the quality of PLD films and to control the deposition parameters for a proper tuning of the layers. A common tool for evaluating the film quality is the analysis of out-of-plane lattice constants in high resolution X-ray diffraction (HR-XRD) measurements [47, 67-69]. In these measurements, additional reflections (indicating different out-of-plane lattice parameters of epitaxially grown films) can be interpreted in terms of the presence of cation vacancies [45, 47, 70], revealing the existence of severe cation non-stoichiometries, i.e. Sr or Ti vacancies. Regarding the control of the layers, a common approach for the optimization of the film composition or film structure is the modification of deposition parameters (laser fluence, oxygen partial pressure, etc.) such that deviations of lattice constants vanish.

In this work, we study Fe-doped SrTiO₃ films deposited using different parameters and target stoichiometries to elucidate their effect on the resulting layers (cation stoichiometry, structure and conductivity). The cation non-stoichiometry in 2 % Fe doped SrTiO₃ thin films is studied using HR-XRD, ICP-OES (inductively coupled plasma optical emission spectroscopy), positron annihilation lifetime spectroscopy (PALS) and by measuring across plane conductivities by means of electrochemical impedance spectroscopy (EIS). Film properties are modified by varying the PLD deposition parameters (laser fluences ranging from 0.55 J/cm² to 1.375 J/cm²) and by using non-stoichiometric targets (ranging from 3 % to 11 % Sr excess). The latter approach turns out to be highly efficient when aiming at stoichiometric Fe:SrTiO₃ films with conductivities close to those of macroscopic bulk Fe:SrTiO₃. The sensitivity of the different tools for quantitative evaluation of the cation non-stoichiometry is compared.

2.2 Experimental

Thin film preparation: Fe-doped SrTiO₃ (Fe:STO) thin films were prepared on different substrates by pulsed laser deposition (PLD). The laser source was a 248 nm KrF excimer laser (COMPex Pro 201F, Coherent, The Netherlands) with a pulse duration of 25 ns. The system was operated at two different pulse frequencies, 5 and 1 Hz, respectively. Laser fluences ranging from 0.55 J/cm² to 1.375 J/cm² were achieved by using nominal laser energies between 200 and 500 mJ. In the following, unless specified differently, a combination of 5 Hz and 1.1 J/cm² is used (see Ref. [60]). In all cases, substrate temperature and oxygen partial pressure were 650°C and 0.15 mbar, respectively, with a substrate to target distance of 55 mm. Not surprisingly the film thickness changes with changing laser fluence, laser frequency or target composition. In this study, deposition times were adapted such that all resulting films were of similar thickness for the impedance measurements, i.e. in the thickness range of about 150 to 350 nm for electrochemical measurements. Film thicknesses were measured by means of profilometry. Polycrystalline Fe doped SrTiO₃ with 2 % Fe per SrTiO₃ unit cell was used as target material for most films, see below. Deposition parameters are summarized in Tab. 1.

Table 1: Pulsed laser deposition (PLD) parameters used for the preparation of the Fe-doped SrTiO₃ thin films. Temperature and substrate material are the same for all samples, only frequency and – most importantly – laser fluence were varied. As a substrate, Nb:SrTiO₃ (0.5 wt% Nb) was used for electrochemical characterization and positron lifetime annihilation spectroscopy, MgO and STO were used for XRD and RSM, respectively, and MgO was used as a substrate for chemical analysis.

Parameter set	I		II	III	IV	V	VI	VII	VIII	IX	X
fluence [J/cm ²]	0.55	0.74	0.825	1.1	1.375	1.1	1.1	1.1	1.1	1.1	1.1
frequency [Hz]	5	5	5	5	5	1	1	5	5	5	5
pressure [mbar O ₂]	0.15	0.15	0.15	0.15	0.15	0.15	0.15	0.15	0.15	0.15	0.15
temperature [°C]	650	650	650	650	650	650	650	650	650	650	650
target	Stoichiometric polycrystal (PC)					Single crystal (SC)	PC	3 % Sr excess PC	5 % Sr excess PC	7 % Sr excess PC	11 % Sr excess PC

Polycrystalline targets: The polycrystalline targets were prepared by a mixed oxide route, starting with SrCO_3 , TiO_2 and Fe_2O_3 (Sigma Aldrich, Germany). Stoichiometric as well as nonstoichiometric (3, 5, 7, and 11 % Sr excess compared to the sum of Fe and Ti) amounts of the solids were accurately weighed, thoroughly mixed in an agate mortar and calcined at 1000 °C for 2 h under ambient conditions. For a stoichiometric cation composition (i.e. for a Sr amount corresponding to the amount of Ti + Fe), this preparation step already led to phase pure SrTiO_3 powders. Afterwards the powders were crushed, cold isostatic pressed and sintered at 1200 °C for 5 h in air, resulting in targets used for PLD. The nonstoichiometric powders were calcined under the same conditions, but showed several different phases after the 1000 °C calcination. Nonetheless, the powders were crushed, pressed and sintered at 1200 °C for 5 h. (X-ray characterization still showed different additional phases) and at 1400 °C for 4.5 h, yielding a target material that consisted of SrTiO_3 with some $\text{Sr}_3\text{Ti}_2\text{O}_7$ as an additional phase, see Results.

Substrate material: Fe: SrTiO_3 thin films for conductivity measurements were grown on Nb-doped SrTiO_3 (Nb:STO) single crystals (0.5 wt% Nb content, CrysTec GmbH, Germany). Owing to the high conductivity of Nb: SrTiO_3 , this substrate acts as an electrode and allows across plane conductivity measurements of the thin films. Moreover, slightly doped Nb: SrTiO_3 has the advantage of a very similar lattice parameter compared to undoped or slightly Fe-doped SrTiO_3 [54, 64, 71], which favours an epitaxial growth of the layer. Films grown on Nb: SrTiO_3 were also used for the reciprocal space mapping (RSM) measurements. Fe: SrTiO_3 thin films grown on MgO (CrysTec GmbH, Germany), on the other hand, were used for additional grazing incident X-ray measurements and for the chemical analysis by ICP-OES. The MgO substrate leads to polycrystalline thin films, allowing a clear identification of the SrTiO_3 phase in XRD. Moreover, the chemical analysis of the films can be performed in a standard manner, i.e. by dissolving the layer without quantification problems due to some substrate dissolution.

Chemical characterization of the SrTiO_3 films: The information on the elemental composition became accessible by dissolving the films and subsequent analysis by means of solution based ICP-OES (iCAP 6500, Thermo Fisher Scientific, USA). The SrTiO_3 films on MgO were dissolved in 3 % v/v HNO_3 and 0.3 % v/v HF for 30 min at 25 °C. Quantification was done via external calibration with liquid standard solutions. For a more detailed description, see section 2.5.1.

Structural characterization: Different types of X-ray measurements were used to get information on the phase purity of the target (measurement in Bragg-Brentano geometry, BB), phase purity of the thin films (measurement in grazing incidence geometry, GID) and on the lattice mismatch of

SrTiO₃ layers compared to the substrate (reciprocal space mapping, RSM). For the phase identification of SrTiO₃ targets, a PANalytical XPert Pro (MPD) powder diffractometer was used. A 2θ angle range of 15 to 90° was scanned, allowing a clear identification of SrTiO₃. GID thin film measurements and reciprocal space mapping (RSM) were done on an Empyrean multipurpose diffractometer (PANalytical, Netherlands). The diffractometer was equipped with a Cu-anode operating at 45 kV and 40 mA providing a wavelength of λ=1.5406 Å (Cu K Alpha 1) and λ=1.5444 Å (Cu K Alpha 2). A hybrid monochromator (2xGe(220)) with a ½ divergence slit and a 2 mm mask was located within the incident beam path. On the detector side, a PIXcel 3D detector in scanning mode with an anti-scatter slit of 7.5 mm was used. For the grating incidence measurements, again a range between 15 and 90° was mapped. Reciprocal space maps were conducted for the (002) reflex (2θ = 46.4752°) and the (113) reflex (2θ = 81.7327°). The scan range around these two reflexes was 1° 2θ with a step size of ω of 0.0015° and a continuous scan of 2θ, resulting in a measuring time of around 12 h.

Positron annihilation lifetime spectroscopy: Variable energy positron annihilation lifetime spectroscopy (VEPALS) measurements were conducted on Fe:SrTiO₃ samples at the Mono-energetic Positron Source (MePS) beamline at HZDR, Germany [72]. A digital lifetime CrBr₃ scintillator detector [51 mm diameter (2”) and 25.4 mm length (1”) coupled to a Hamamatsu R13089-100 PMT was utilized. The detector was a μ-metal shielded and housed inside a solid Au casing. For the data acquisition a homemade software was employed, executed from a multi-channel digitizer (SPDevices ADQ14DC-2X) with 14 bit vertical resolution and 2GS/s horizontal resolution. The time resolution of about 0.210 ns was achieved. The resolution function required for spectra analysis uses two Gaussian functions with distinct shifts and intensities, which depend on the positron implantation energy, E_p . All spectra contained at least $1 \cdot 10^7$ counts. Typical lifetime spectrum $N(t)$ is described by $N(t) = \sum (I_i / \tau_i) \exp(-t/\tau_i)$, where τ_i and I_i are the positron lifetime and intensity of the i -th component, respectively ($\sum I_i = 1$). All the spectra were deconvoluted using the non-linearly least-squared based package PALSfit fitting software [73] into two discrete lifetime components, which directly evidence localized annihilation at 2 different defect types (sizes; τ_1 and τ_2). The corresponding relative intensities reflect to a large extent the concentration of each defect type (size) as long as the size of compared defects is in the similar range. In general, positron lifetime is directly proportional to defects size, i.e., the larger is the open volume, the lower is the probability and longer it takes for positrons to be annihilated with electrons [74, 75]. The positron lifetime and its intensity have been probed as a function of positron implantation energy E_p , which

is proportional to the positron implantation depth.

Electrical characterization: The electrical characterization was performed by means of electrochemical impedance spectroscopy (EIS) on Fe:SrTiO₃ films deposited on conducting Nb:SrTiO₃. A sketch of the set-up is given in Fig. 1. Pt top layers were sputtered using a high voltage magnetron coating device (BAL-TEC MED 020, Germany) and microelectrodes with diameters in the range of 100-300 μm were prepared by lift-off photolithography. Pt/Ir needles were used to contact the microelectrodes for impedance measurements.

Electrical measurements were then performed in a homogeneously heated furnace [76] within a temperature range of 250 °C to 720 °C (though meaningful conductivities could be deduced for some films only in a limited temperature range). Impedance spectra were obtained for frequencies from 0.9 MHz to 1 Hz with a resolution of 10 point per frequency decade, measured by an Alpha-A High Resolution Analyzer (Novocontrol, Germany). To ensure the probing in a linear regime, an AC rms amplitude of 20 mV was applied.

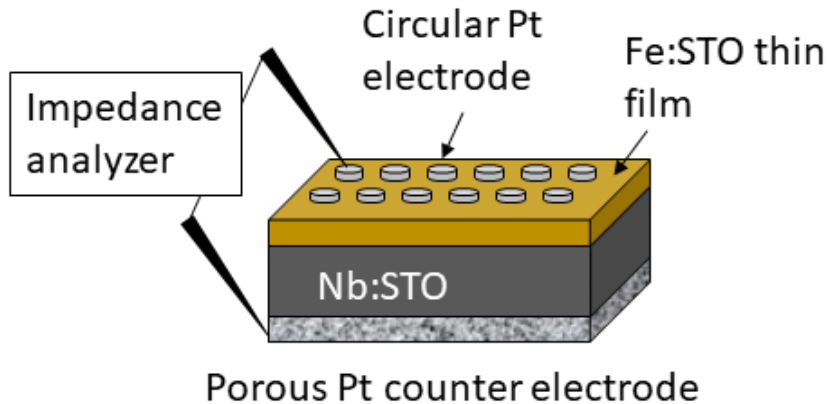


Fig 1: Sketch of the sample consisting on the Nb:SrTiO₃ (Nb:STO) substrate, the Fe:SrTiO₃ (Fe:STO) thin film and a porous Pt counter electrode as well as circular Pt microelectrodes on top.

2.3 Results and Discussion

2.3.1 Pseudo-intrinsic conductivity of films from stoichiometric targets

Fig. 2 shows a typical spectrum for SrTiO₃ thin films prepared from 2 % Fe doped stoichiometric targets. In addition to the somewhat distorted main arc, a well-separated much smaller arc appears at high frequencies. The permittivities deduced from the capacitance of the high frequency arc are very close to the expected SrTiO₃ film bulk capacitances while the capacitance of the main arc is substantially larger (see also below). Typically, two separated arcs may either result from two serial processes, e.g. bulk transport and space charges at interfaces [77] or from two parallel processes such as electron and ion conduction in a mixed conducting material, provided one of the two processes (paths) is blocked at the electrodes [78]. SrTiO₃ is known to be a mixed conductor [33] and our set-up leads to a blocking of ions at one or both electrodes. Thus, use of a parallel path model is realistic here. More specifically, we employed the transmission line impedance model suggested in literature for such materials [79-81]. This model consists of an electronic rail (R_{eon}) and an ionic rail (R_{ion}), which are connected via the chemical capacitance (C_{chem}), and a displacement rail (C_{geom}). The ionic rail is blocked by an interfacial capacitance (C_{int}), as sketched in Fig. 2.b. (In order to avoid over-parameterization, the same C_{int} is used for both electrodes.) This model excellently fits the measurement data of our 2 % Fe-doped SrTiO₃ films (see Fig. 2.a). Three arguments considering the DC resistance as well as the resulting capacitances shown in Fig. 2.d support the validity of the model and the corresponding data interpretation. Those are discussed in section 2.5.2.

An Arrhenius-type diagram of the resulting DC conductivity (i.e. electronic conductivity) of the thin films is shown in Fig. 2.c. For comparison purposes, the electronic bulk conductivity of the corresponding 2 % target material is also shown in Fig. 2.c. (the polycrystalline target leads to a bulk and a grain boundary arc in the complex impedance plane and only the bulk arc is considered here). As clearly visible in Fig. 2.c., values of the 2 % Fe-doped SrTiO₃ thin film are three to five orders of magnitude lower than the expected ones (depending on temperature). Moreover, in accordance with literature data on 0.4 % Fe doped films [32], the electronic conductivity of the 2 % Fe films and its temperature dependence fit very well to that of intrinsic SrTiO₃, calculated for the materials parameters from literature [29], i.e. a band gap E_g of 3.3 eV – $6.0 \cdot 10^{-4}$ eV*T, a hole mobility of $8.9 \cdot 10^5$ (T/K)^{-2.36} cm²*V⁻¹*s⁻¹, an electron mobility of $4.5 \cdot 10^5$ (T/K)^{-2.2} cm²*V⁻¹*s⁻¹

and $K_0 = 7.67 \cdot 10^{42} \text{ cm}^{-6}$. Here, “intrinsic” means identical hole and electron concentrations (c_e, c_h) as for a pure semiconductor without any further defect, i.e. $c_e = c_h = \sqrt{K_0 e^{-E_g/kT}}$ (k = Boltzmann constant, T = temperature). Please note that electron and hole concentrations at 400 °C are thus in the range of $3 \cdot 10^{10} / \text{cm}^3$ and in a usual situation this requires purity levels of semiconductors in the 0.01 ppb range. An exact mechanistic explanation of this pseudo-intrinsic behaviour of Fe:SrTiO₃ thin films, seemingly independent of the dopant concentration in the range between 0.4 to 2 % Fe doping, is beyond the scope of this paper, but the following XRD and chemical analysis gives important empirical information on possible reasons.

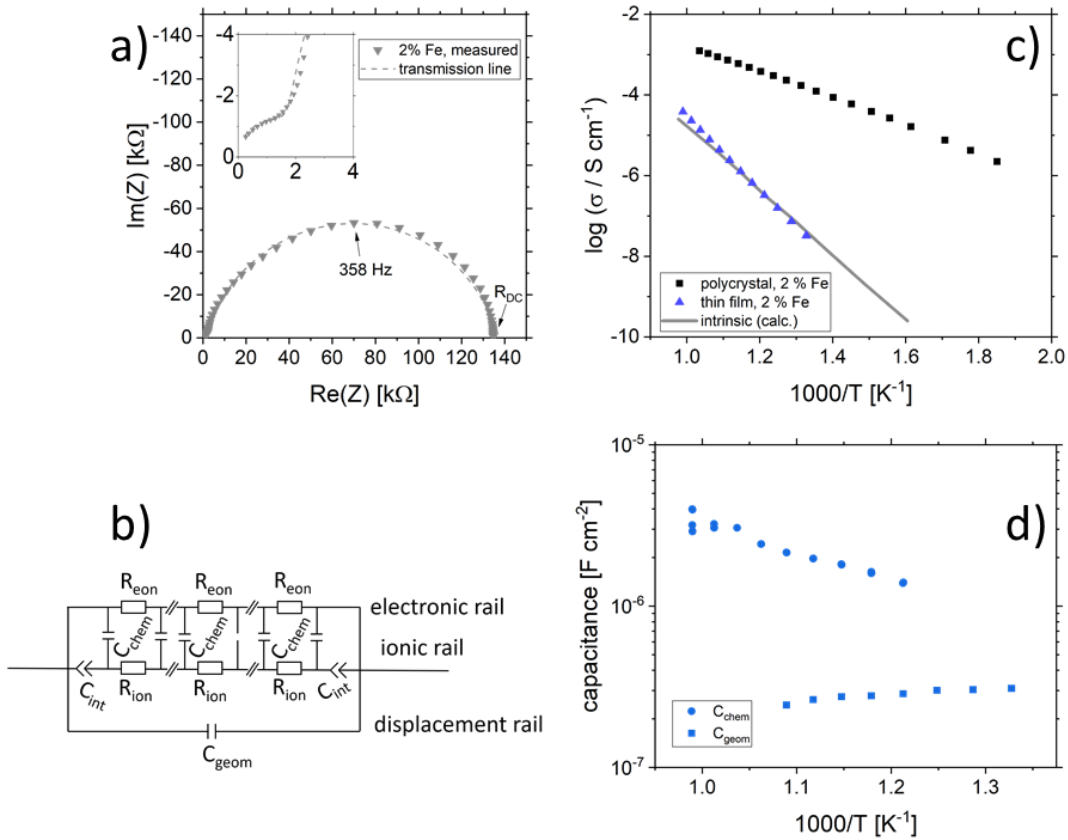


Fig 2: (a) Impedance spectrum of an Fe:SrTiO₃ thin film deposited at 1.1 J/cm² from a stoichiometric polycrystal with 2 % Fe measured at 551 °C. Fitting was done with the transmission line model of a mixed conductor (b), consisting of an electronic rail, a blocked ionic rail and the displacement rail. The conductivity calculated from the DC resistance (= electronic resistance R_{eon}) is plotted in an Arrhenius diagram in (c) and compared with the bulk conductivity of a polycrystalline pellet (2 % Fe) as well as the calculated electronically intrinsic ($c_e = c_h$) conductivity[29]. Temperature dependent geometrical and chemical capacitance values for the 2 % Fe doped film (370 nm thick) are shown in (d).

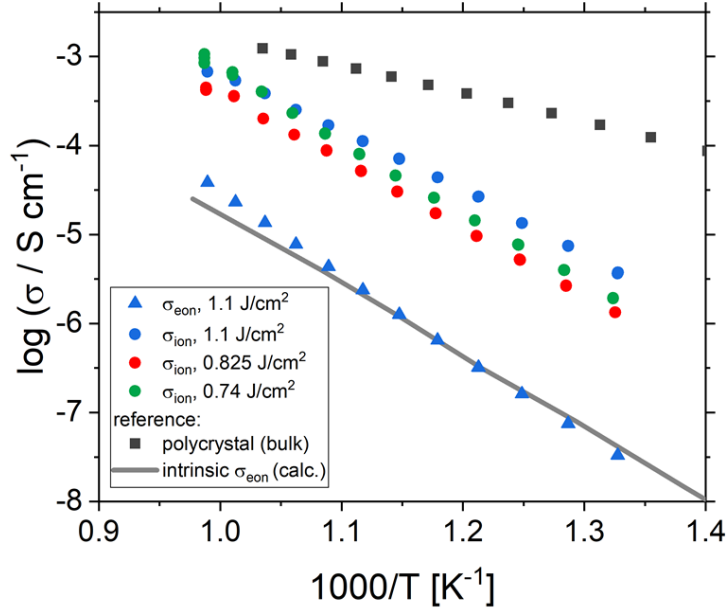


Fig. 3: Electronic and ionic conductivities of SrTiO₃ thin films deposited at 1.1 J/cm² from 2 % Fe doped stoichiometric polycrystals. Both are deduced from the transmission line fits. For comparison, ionic conductivities are also shown for other laser fluences. The intrinsic conductivity σ_{eon} was calculated using Ref. [29].

Ionic conductivities of the same films are plotted in Fig. 3 showing one to two orders of magnitude larger values than the pseudo-intrinsic electronic conductivity. Fig. 3 further displays variations of the ionic conductivities for films prepared with other fluences, see below. Different ionic defects are most probably also the reason behind differences in spectra shapes found between our 2 % doped films and 0.4 % Fe doped films [32, 63]. The yet not interpreted distortion of the spectra for 0.4 % Fe thin films in Refs. [32, 63] thus probably comes from the mixed conduction. This is detailed in section. 2.5.3.

2.3.2 Structural, chemical and defect analysis of pseudo-intrinsic SrTiO₃ films

In the following, results from the structural, chemical and defect analysis of these pseudo-intrinsic SrTiO₃ films are shown. First, we consider the XRD data of the films. Fig. 4 displays results from reciprocal space mapping (RSM) measurements on a thin film deposited with a repetition rate of 5 Hz and a fluence of 1.1 J/cm². This high-resolution X-ray diffraction method can resolve deviations

in the microstructure between the thin film and the substrate material [82]. The diffraction vector $Q_{\langle 002 \rangle}$ normal to the surface is indicated. The detector streak (DS) as well as the monochromator streak (MS) can be attributed to the measurement set-up. The streak normal to the q_{\parallel} axis is the so-called crystal truncation rod (CTR), which is a diffraction phenomenon originating from the fact that the sample has finite dimensions.

The measurement around the symmetric (002) reflex (Fig. 4.a) reveals a small deviation of the layer reflex in comparison to the substrate reflex. The substrate can be identified by the reflex position, which gives a lattice constant of 3.906 Å, in very good agreement with literature data for undoped SrTiO₃ [71, 83, 84]. Moreover, the substrate reflex shows the highest count intensity. The thin film reflex (smaller count intensity) is slightly below the substrate reflex, indicating an expansion Δc of the out-of-plane lattice constant c .

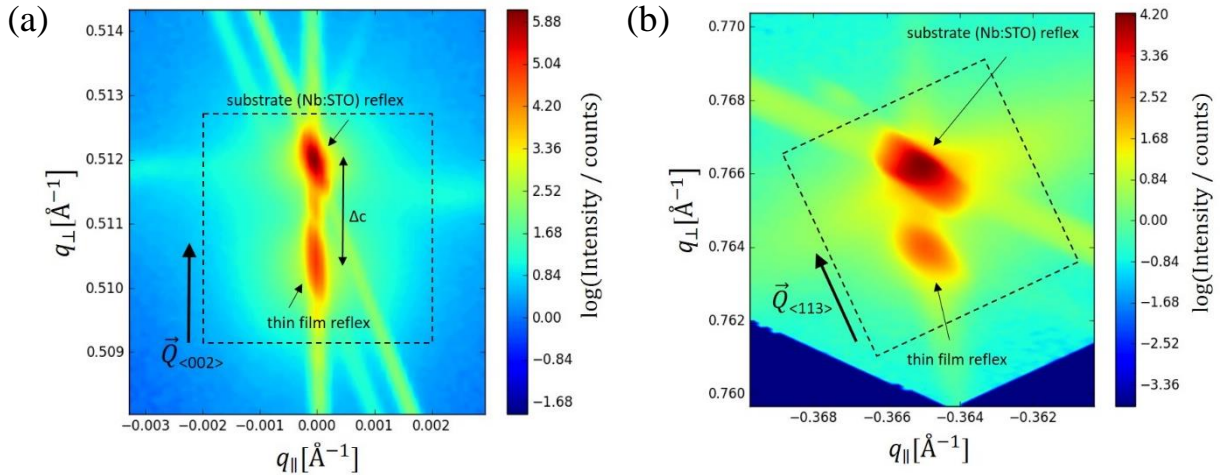


Fig. 4: Reciprocal space mapping measurements for Fe:SrTiO₃ standard thin films deposited from 2 % Fe doped stoichiometric targets on Nb:SrTiO₃ substrate material (PLD parameters [laser fluence, frequency, temperature, pressure, time]: 1.1 J/cm², 5 Hz, 650 °C, 0.15 mbar and 20'). The out-of-plane measurement in close proximity of the (002) reflex is shown in (a). Arrows point at the substrate reflex as well as the thin film reflex. The differences indication a lattice expansion Δc are shown. The same sample was also measured around the (113) reflex (in-plane measurement). The resulting reciprocal space map is shown in (b). For clarification, arrows and dotted boxes indicate the direction of the diffraction vectors $Q_{\langle 002 \rangle}$ and $Q_{\langle 113 \rangle}$, respectively.

A relocation of the measuring spot on the asymmetric (113) reflex gives the reciprocal space map shown in Fig. 4.b. Again, an arrow indicates the diffraction vector $Q_{\langle 113 \rangle}$. The measurement was performed using a grating incident angle giving negative values for q_{\parallel} . The lattice expansion of

the thin film normal to the layer|substrate interface is confirmed by this measurement. In case of the asymmetric measurement, additional information on the in-plane lattice constant can be extracted. For the sample in Fig. 4.b, the lattice parameter of the thin film parallel to the surface is perfectly matching the substrate, i.e. the layer reflex is located at the position $r = 0$. This indicates that the layer undergoes a pseudomorphic growth on top of the single crystalline SrTiO_3 substrate. Hence, we find a film growth with in-plane lattice constants as for the substrate, but significantly different out of plane lattice constants of substrate and film. This phenomenon is well-known in literature [48, 59, 85] and is commonly attributed to the existence of cation vacancies, i.e. to films with a $\text{Sr}/(\text{Ti}+\text{Fe})$ ratio differing from one [45, 46, 86, 87]. For example, Wicklein et al. report that a broad range of different target materials lead to thin films showing either a reduced Sr-content, meaning that Sr vacancies are present, or Ti vacancies in the thin films [60]. Furthermore, adding Fe to the target material can cause a very different ablation. The ablation behaviour changes due to an increased thermal conductance of the target [88, 89], which then causes an increased heat penetration depth and a different dissipation of introduced laser energy [89]. This leads to less material being ablated when Fe is present in the target material. Further mechanistic reasons for this non-stoichiometric deposition are discussed in Refs. [88-90]. In accordance with all the known literature we thus conclude that also our films exhibit a cation non-stoichiometry.

Table 2: Composition of $\text{Fe}:\text{SrTiO}_3$ thin films prepared from stoichiometric targets by different deposition parameters and measured by ICP-OES. A pronounced Sr deficiency was found for all samples prepared from stoichiometric targets with 2 % Fe and from the single crystal (SC) with 0.16 % Fe.

	<i>Sr</i>	<i>Ti</i>	<i>Fe</i>	<i>Sr/(Ti+Fe)</i>
PC, 2 % Fe, 0.55 J/cm ² , 5 Hz	0.94	1.01	0.051	0.88
PC, 2 % Fe, 0.825 J/cm ² , 5 Hz	0.94	1.04	0.023	0.88
PC, 2 % Fe, 1.1 J/cm ² , 5 Hz	0.94	1.02	0.035	0.90
PC, 2 % Fe, 1.375 J/cm ² , 5 Hz	0.95	1.03	0.027	0.90
PC, 2 % Fe, 1.1 J/cm ² , 1 Hz	0.94	1.02	0.014	0.89
SC, 1.1 J/cm ² , 1 Hz	0.96	1.03	0.008	0.92

The estimated cation non-stoichiometry of the film was quantified by chemical analysis of the films. The quantitative data of the ICP-OES analysis of a standard film on MgO is shown in Tab. 2 and Fig. 6. The film shows a drastically reduced Sr content. Assuming that Fe occupies the B-site, we find an A/B site ratio in the film of 0.90 and thus a Sr deficiency in the range of 10 %. Here, the error is well below 1 % for main

components (Sr, Ti) and in the range of 5 % for the Fe dopant, e.g. 0.02 ± 0.001 .

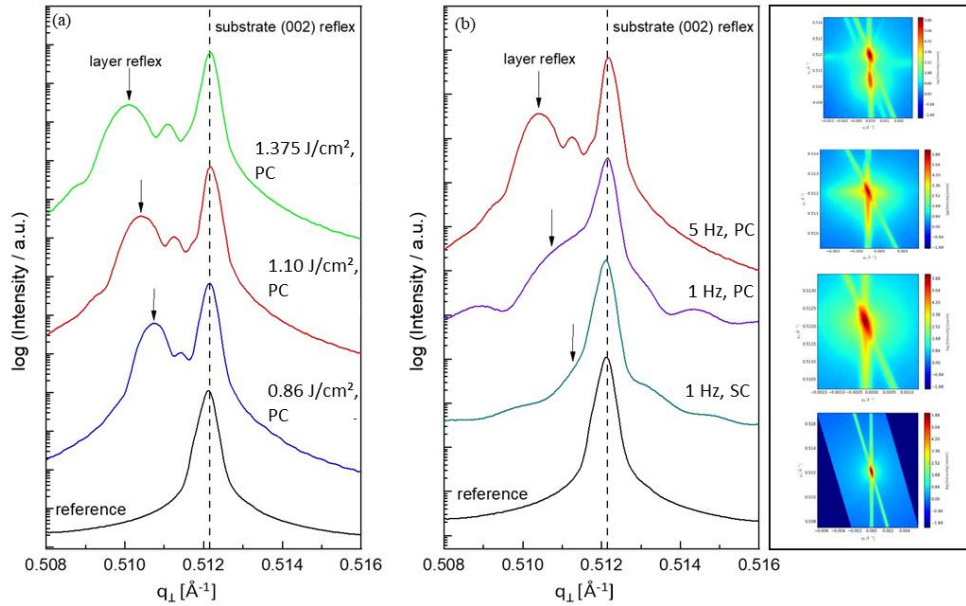


Fig. 5: ω - 2θ scans for various thin film samples. In (a), a comparison of SrTiO₃ films (2 % Fe doped stoichiometric targets) prepared with different laser fluences is shown (all other deposition parameters are held constant). The HR-XRD measurements were conducted around the (002) reflex. A black line indicates that the substrate reflex is in the same position for every sample. As reference the pure Nb:SrTiO₃ substrate was measured. Arrows indicate the substrate reflex and illustrate the shift of these reflexes for changing deposition parameters. In (b), the laser fluence was kept constant at 1.1 J/cm². Varying laser frequency (1 and 5 Hz) as well as target material (polycrystalline, 2 % Fe doped, stoichiometric and single crystalline targets) result in thin films with a distinctly decreased lattice expansion. (Shifting of the layer reflex towards the substrate reflex.) The four RSM images belong to the four curves in b).

In addition, positron annihilation lifetime spectroscopy (PALS) was performed and the implantation energy dependent positron lifetime τ_1 is shown in Fig. 7. The positron lifetimes for lower energies probe the thin film and reveal Sr vacancies as predominant cation based point defect species for the thin film deposited from a stoichiometric target. Positron lifetime τ_1 basically overlaps with the calculated literature value of 281 ps for Sr vacancies [59]. At the same time, the relative intensity I_1 is close to 100 % indicating that Sr vacancies are the most abundant defect type, a typical scenario of large defect concentrations. For larger implantation energies, we see the transition to bulk properties. For films with 5% Sr excess, the film related positron lifetime decreases close to a literature value of $\tau_1 = 225$ ps indicating the emergence of a new smaller dominant defect type, arguably a complex of Ti vacancies and oxygen vacancies [48, 91]. (Please note that a Sr vacancy is a larger and stronger positron trap). Concomitantly a drop in I_1 intensity

reflects a larger chance for positrons to diffuse, as a consequence of a lower number of vacancy traps, and to annihilate with surface states.

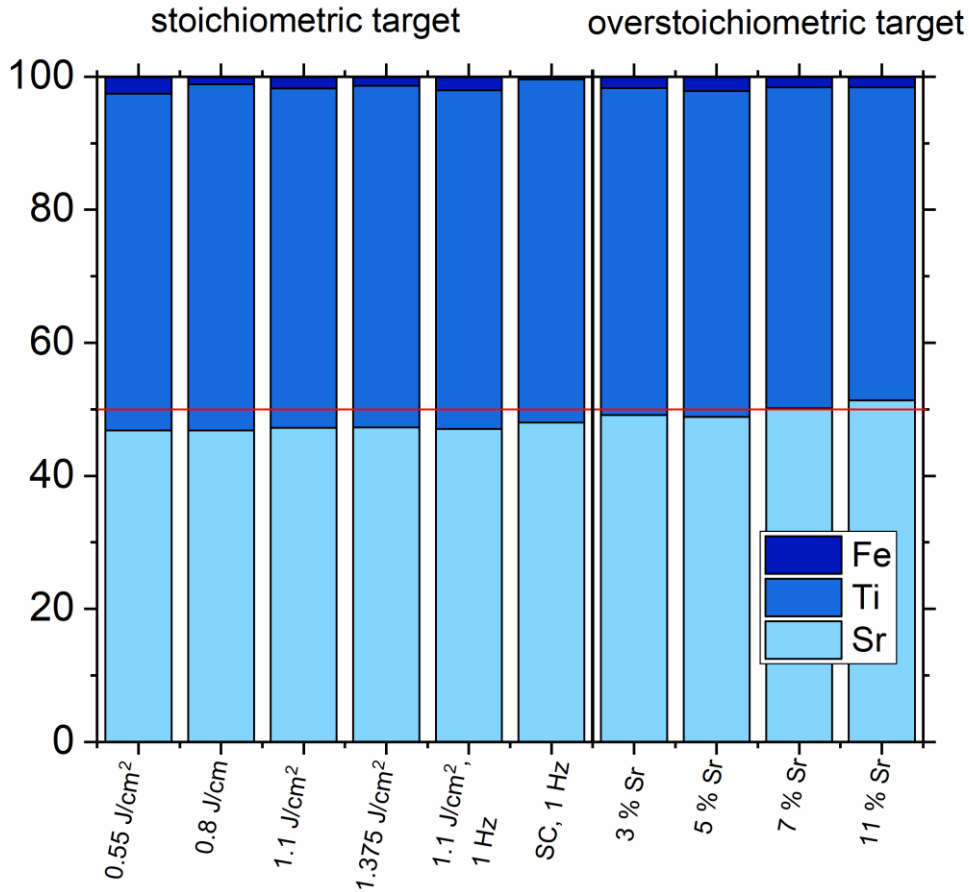


Fig. 6: Composition of different SrTiO₃ thin films on MgO measured by ICP-OES highlighting differences in the Sr content for different deposition parameters (targets without Sr excess: 2 % Fe in PC, 0.16 % Fe in SC) and for different Sr excess in the target. A stoichiometric thin film is only obtained by using a target with a 7 % Sr overstoichiometry. At 11 % Sr excess, a slight Sr excess is present in the thin film. In all other cases, a Sr deficiency can be seen. Fe is counted as B site ion in all cases.

Accordingly, the cation vacancies detected by RSM can be attributed to the A-site. In literature, Sr deficiencies in this range and similar out of plane deviations of lattice parameters were reported [45, 46, 86, 87]. Interestingly, also the Fe content detected in the films was consistently too high, indicating that the PLD process led to an enrichment in Fe, at least in the centre part of the plasma plume used to deposit the films. Measurements showed that indeed an inhomogeneous cation composition is expected in the PLD plasma used for SrTiO₃ deposition and thus deviation of cation compositions compared to the target are not surprising [60, 85]. Similar non-stoichiometries introduced by the PLD process are reported in literature for other materials as well [92-102].

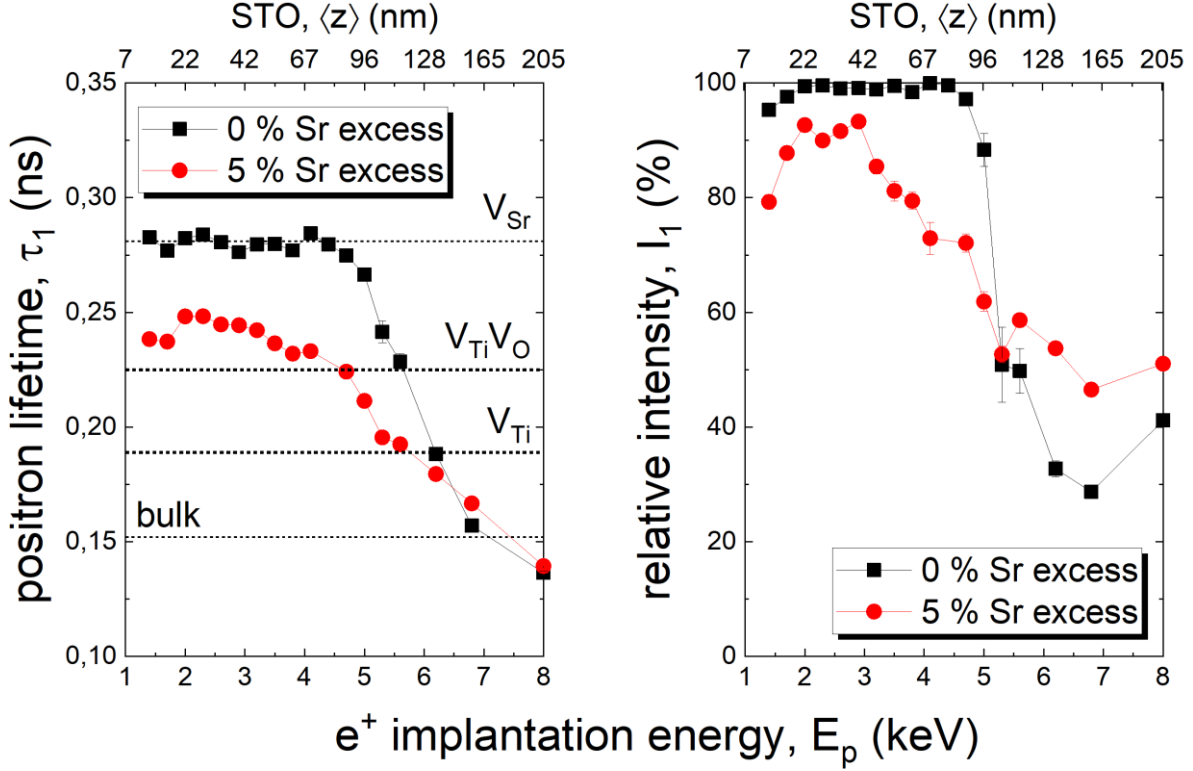


Fig. 7: Positron annihilation lifetime spectroscopy measurements on $Fe:SrTiO_3$ thin films deposited from 2 % Fe doped targets with different cation stoichiometry on $Nb:SrTiO_3$ substrates (5 Hz, 1.1 J/cm²). The thin film deposited from a stoichiometric target (labeled 0 % Sr excess) clearly shows a positron lifetime which fits excellently to Sr vacancies. For larger implantation energies, transition to bulk values is seen. For films prepared from targets with 5 % Sr excess, $V_{Ti}V_O$ clusters are found as the predominant defect type present in the respective thin film, highlighting a severe transition in defect chemistry induced by the introduction of Sr excess to the PLD targets.

We consider it as most plausible that such a severe A/B site non-stoichiometry in the $SrTiO_3$ film is the origin of the pseudo-intrinsic film conductivity. We think that interplay of the Fe dopant (Fe acceptor states), a deep electron trap (possibly site defects [103], e.g. Ti on the A-site [104-106] acting as a donor) as well as a mid-gap state (Sr-vacancies [30]) causes a pinning of the Fermi level close to the centre of the band gap. Different gap states have also been reported for nominally undoped $SrTiO_3$ thin films [107]. However, a detailed mechanistic discussion of this phenomenon needs further investigation and is beyond the scope of this paper.

All together, the complementary tools used here (conductivity measurements, RSM, chemical analysis by ICP-OES, and PALS) directly or indirectly reveal the strongly non-ideal character of the grown $SrTiO_3$ films (non-ideal in the sense of non-bulk $SrTiO_3$ like). In the following, we

discuss how this non-ideality can be reduced or even eliminated and how sensitive the tools are to monitor cation non-stoichiometry of the film.

2.3.3 SrTiO₃ film tuning by controlling the deposition conditions (stoichiometric targets)

One common strategy for reducing the cation non-stoichiometry is the variation of the deposition parameters in PLD grown layers. It is reported that lowering the laser fluence reduces the Sr vacancy concentration [47, 60, 67]. In this work, a range of laser fluences was employed, from 0.55 J/cm² to 1.375 J/cm² (section 2.3.1. reports on 1.1 J/cm²). Moreover, different laser frequencies were employed (1 and 5 Hz) and also a Fe:SrTiO₃ single crystal was used as the target (though with a lower Fe content of 0.16 % Fe). In Fig. 5, rocking curves for thin films deposited using different laser fluences (0.86 J/cm² to 1.375 J/cm²), repetition rates (1 Hz, 5 Hz) and target materials (polycrystal, single crystal) are shown and reveal that the higher laser fluence indeed enhanced the out of plane lattice mismatch while lower laser fluence lowered the mismatch. However, within the given fluence range and for 5 Hz deposition rate a clear indication of a lattice mismatch remained. Reducing the frequency lead to thinner films and thus less pronounced signals but the lattice mismatch itself remained and therefore also indication of the film non-stoichiometry. The thin film prepared from the 0.16 % doped Fe:SrTiO₃ single crystal showed least indication of a cation non-stoichiometry in RSM curves.

Data from the chemical analysis of the films are summarized in Table 2 and Fig. 6 and reveal that the pronounced Sr deficiency is not much affected by the different preparation conditions. Also the film prepared from the single crystal exhibits a slightly smaller but still severe A-site deficiency. In all samples, again more Fe is found than in the target and on average the Fe content is almost twice the nominal one. The impedance spectra were similar to those of the films in section 2.3.1, but the distortion of the main arc became even more prominent in some cases (see Fig 8.a). The fitting procedure for these impedance spectra was carried out as described in section 2.3.1, i.e. with a transmission line based model, and the electronic conductivity, ionic conductivity, relative permittivity and chemical capacitance were deduced. Again, the DC resistance corresponds to the electronic conductivity. The ionic conductivity (Fig. 3) as well as the chemical capacitance (Fig. 8.d) show some fluence dependency. The moderate deviation in bulk permittivity (from C_{geom}) are

probably due to non-idealities of the fit model. However, the electronic conductivity does not change due to the different deposition parameters (Fig. 8.b). Rather, again pseudo-intrinsic conductivity values were found for the samples investigated (0.74 and 0.825 J/cm²).

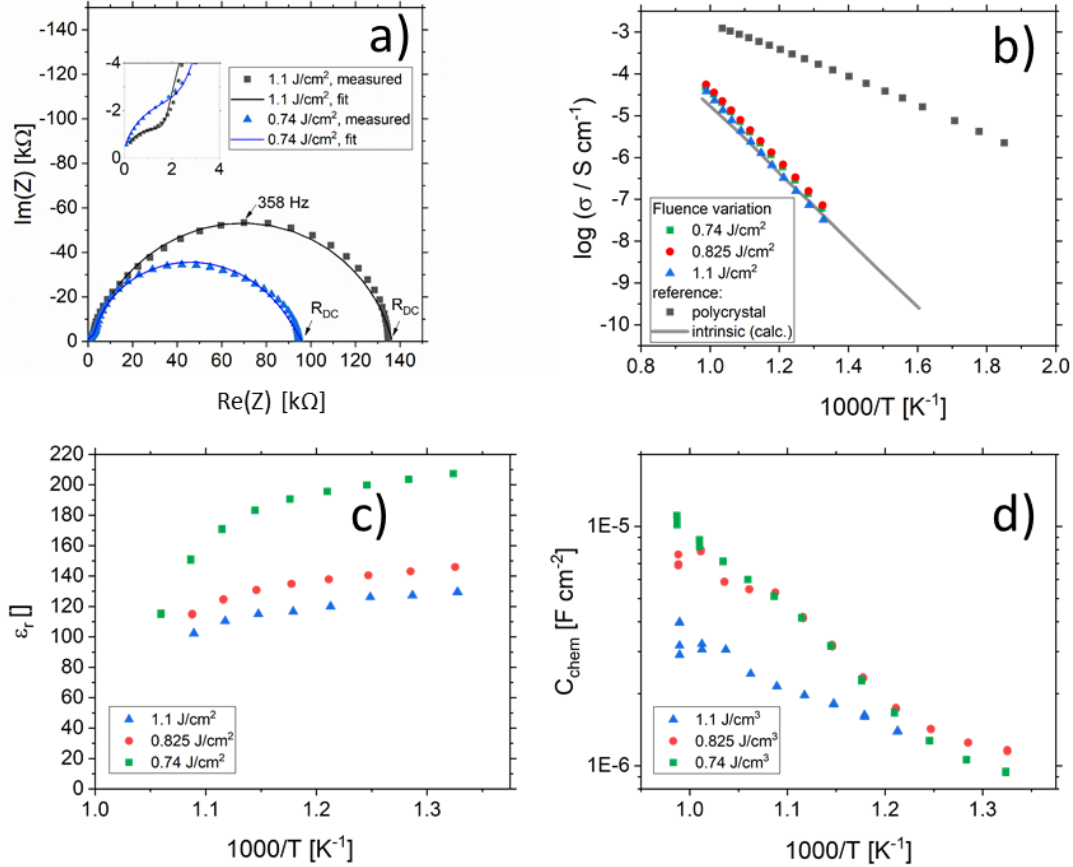


Fig. 8: Impedance spectra of STO thin films deposited from 2 % Fe doped stoichiometric targets using different laser fluences (1.1 J/cm² and 0.74 J/cm²) at 551 °C and 553 °C, respectively, showing a strong distortion for both semicircles (a). The dc (= electronic) conductivities of thin films deposited at different laser fluences are plotted in an Arrhenius plot (b) and are compared to the bulk conductivity of a polycrystal and the electronic intrinsic conductivity calculated using Ref. [29]. Bulk permittivity values and chemical capacitances deduced from the transmission line model are shown in (c) and (d), respectively.

2.3.4 SrTiO₃ film tuning using different target compositions

Based on the knowledge that Sr deficiencies (in the range of several percent) result in films deposited by PLD, we prepared different targets with a Sr surplus of 3 to 11 % (details on the target preparation are given in the experimental part). XRD of these targets clearly revealed the Sr over-

stoichiometry by reflexes from a second phase, namely $\text{Sr}_3\text{Ti}_2\text{O}_7$, and its amount increased with Sr content, see section 2.5.4. The films grown from these targets, however, did not show any indication of a secondary phase, neither in XRD measurements of polycrystalline films on MgO (see section 2.5.5) nor in RSM measurements (see Fig. 9). Rather, their reflections could not be distinguished from the substrate reflections in rocking curves, at least for 3-7 % Sr, see Fig. 9. Only 11 % Sr surplus again caused a shoulder in the RSM curve which is most probably due to Ti vacancies in this case.

Table 3: Composition of differently prepared $\text{Fe}:\text{SrTiO}_3$ thin films, deposited from overstoichiometric targets and measured by ICP-OES. The Sr excess in the target material counterbalances the loss during the PLD process, leading to A:B-ratios closer to unity.

	<i>Sr</i>	<i>Ti</i>	<i>Fe</i>	<i>Sr/(Ti+Fe)</i>
2 % Fe, 0 % Sr, 1.1 J/cm ²	0.94	1.02	0.035	0.90
2 % Fe, 3 % Sr, 1.1 J/cm ²	0.98	0.98	0.034	0.97
2 % Fe, 5 % Sr, 1.1 J/cm ²	0.98	0.98	0.043	0.96
2 % Fe, 7 % Sr, 1.1 J/cm ²	1.00	0.96	0.032	1.01
2 % Fe, 11 % Sr, 1.1 J/cm ²	1.03	0.94	0.032	1.06

On the basis of XRD data, all three films with 3, 5 and 7 % Sr surplus are compatible with stoichiometric compositions. This conclusion, however, was only partly confirmed by the chemical analysis. Tab. 3 and Fig. 6 show the results from ICP-OES measurements. Indeed, the A/B site ratio was much closer to unity for those three films compared to films prepared from the stoichiometric target. However, for 3 and 5 % Sr excess the nominal A/B site ratio is still only 97 or 96 %, respectively (with errors well below ± 1 %). The even slightly lower nominal value for 5 % Sr excess compared to 3 % Sr is within the error bar. Moreover, in these calculations, Fe is always counted as a B site ion, which is not necessarily the case if many A-site vacancies are present. The 7 % Sr film, on the other hand, showed almost exact A/B site stoichiometry in ICP-OES measurements, though still more Fe is present than in the target. For 11 % Sr excess, A/B of 1.06 is measured (see Tab. 3), in accordance with the shoulder in the rocking curve indicating too much Sr (see Fig. 9). Please note, that most of these films have Sr/Ti ratios which can hardly be distinguished by XPS or XRD studies with typical errors in the 5 % range [47, 108, 109].

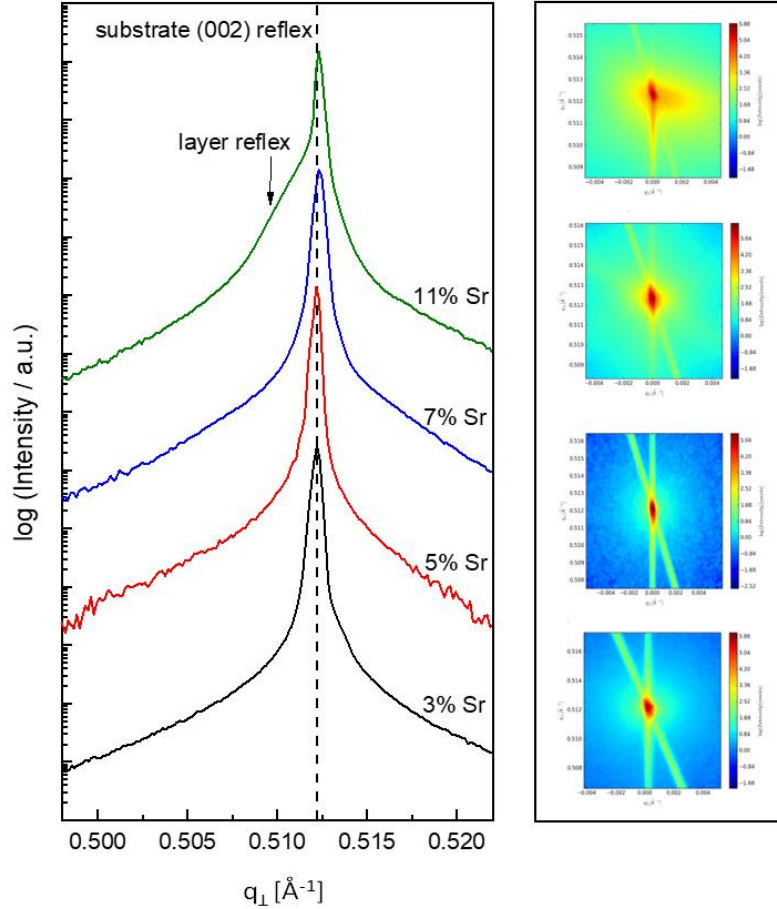


Fig. 9: ω - 2θ scans for various thin film samples deposited from 2 % Fe-doped SrTiO_3 polycrystalline targets with different Sr overstoichiometry. The HR-XRD measurements were conducted around the (002) reflex. The black dashed line indicates that the substrate reflex is in the same position for every sample. Laser fluence was kept constant at 1.1 J/cm^2 . At the right hand side, the corresponding reciprocal space maps are shown as well.

The impedance spectra of these films are very different from those of the pseudo-intrinsic standard films. As an example, we show a spectrum for the 7 % Sr excess case in Fig. 10. At 330°C , it becomes obvious that the spectrum consists of three arcs with dramatically different sizes, a very small high frequency arc or shoulder, a medium sized medium frequency arc and a very large low frequency arc (see Fig. 10.a). However, the total resistance of the large low frequency arc is still much smaller than the main arc measured for the standard films prepared from stoichiometric targets. This is illustrated by comparing spectra of the pseudo-intrinsic standard films with the films from 7 % Sr excess targets measured at 555°C (see Fig. 10.b). At this temperature, only the low and the medium frequency arcs are still visible in the measured frequency range of the 7 % excess film. The entire dc resistance of the 7 % Sr excess film (sum of three arcs) is not much larger than

the high frequency arc of the pseudo-intrinsic film. In general, the high frequency arc of the 7 % Sr excess films is orders of magnitude smaller than that of the standard films. This strongly indicates that also a reinterpretation of the spectra is required for these Sr-excess films.

A fit to three serial R-CPE elements works very well and the interpretation of the spectra is done based on the corresponding capacitances. The capacitance of the high frequency arc (visible in Fig. 10.a) fits well to the geometrical capacitance expected for the entire SrTiO_3 film, i.e. it leads to a very reasonable permittivity in the range of 150 [110]. Hence, this arc is attributed to the total bulk conductivity of the corresponding SrTiO_3 thin films. The other two capacitances are about 10 and 20 times larger than the high frequency capacitance and thus correspond to SrTiO_3 layer regions in the 10 or 20 nm range assuming bulk permittivity. Those are most probably interfacial space charges at the two electrodes, see also 2.5.6. Those come into play since the electronic conductivity is no longer at its lowest possible value (intrinsic). Accordingly, the ionic conductivity plays no longer a role in this interpretation.

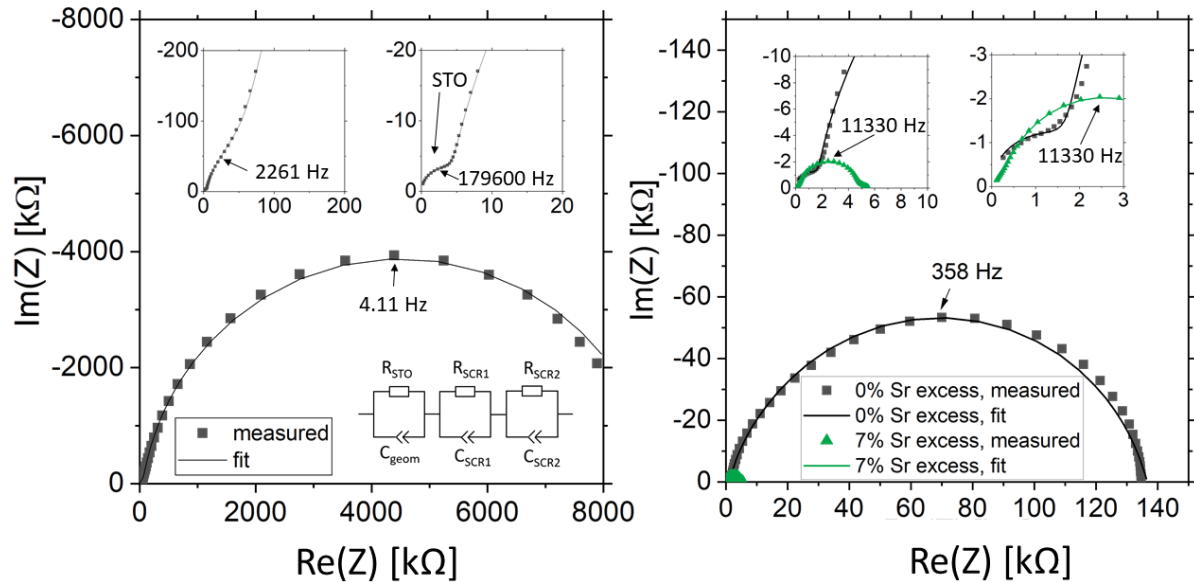


Fig. 10: (a) Impedance spectrum of a thin film deposited from a 2 % Fe doped target with 7 % Sr overstoichiometry measured at 327 °C. The magnification reveals a medium frequency shoulder and an additional small high frequency semicircle. Only the high frequency semicircle (R_{STO}) is attributed to the $\text{Fe}:\text{SrTiO}_3$ bulk according to the geometrical capacitance The medium frequency shoulder and the big low-frequency semicircle are attributed to space charge regions (R_{SCR1} , R_{SCR2}). (b) Impedance spectrum of the same thin film measured at 556 °C and the respective impedance spectrum of a thin film deposited from a stoichiometric target as a reference (measured at 551 °C), highlighting the dramatic change in absolute resistance.

Based on this interpretation, the high frequency arc is used to determine the bulk conductivity of these thin films. For the other Sr excess cases, the spectra have also a high frequency arc with bulk-like capacitance, though partly only one additional interfacial arc is visible. The same type of analysis is thus performed also for the other films. These bulk conductivities of the films prepared from over-stoichiometric targets are shown in Fig. 11. The film prepared from 3 % Sr excess target exhibits bulk conductivities which are higher than the electronic ones of pseudo-intrinsic films (and similar to ionic conductivities of those), but those are still far off the expected electronic bulk conductivity of polycrystalline SrTiO₃. Hence, the improved cation stoichiometry is sufficient to strongly reduce structural deformations (c.f. the rocking curves in Fig. 9), but defect chemical non-idealities are still so large that orders of magnitude lower electronic conductivities are found. This also shows that XRD curves have reduced sensitivity towards off-stoichiometries, i.e. they may indicate severe deviations from the desired cation stoichiometry while absence of rocking curve shoulders cannot be taken as an indication of excellent stoichiometry or defect chemical ideality.

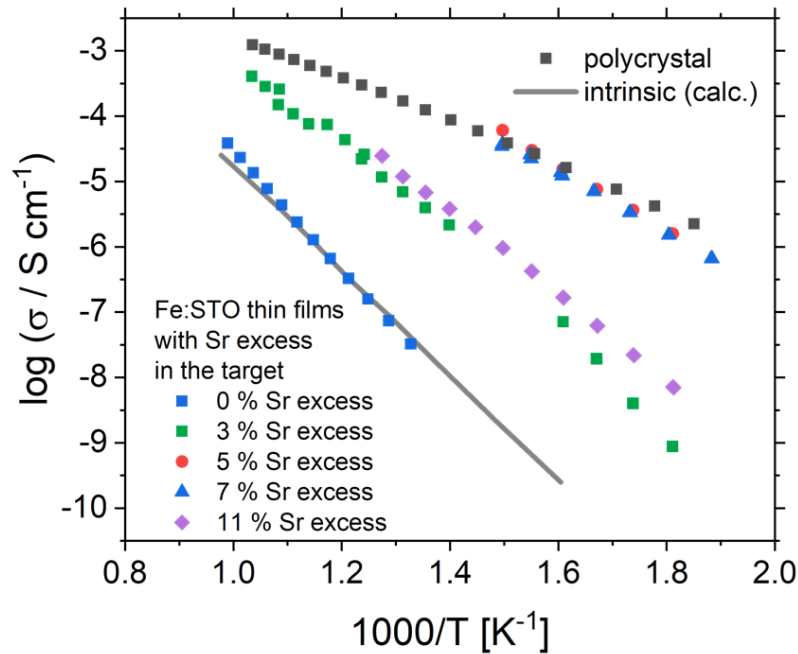


Fig. 11: The total conductivities of Fe:SrTiO₃ thin films deposited from targets with 2 % Fe and different Sr overstoichiometry are plotted in an Arrhenius diagram and compared with the electronic bulk conductivity of a polycrystal as well as the electronic intrinsic conductivity calculated using Ref. [29]. Here, the increase in conductivity of the samples with 5 % and 7 % Sr overstoichiometry up to electronic bulk conductivity of a polycrystal can be seen.

The films prepared from 5 % Sr and 7 % Sr excess, however, show bulk conductivities very close to the expected bulk electronic conductivity of pellets. This agreement supports the interpretation that the total bulk conductivity in the thin film is now largely electronic, as in the bulk sample. Hence, stoichiometry deviations occurring during the deposition process seem to be largely counter-balanced by the Sr excess in the target. In the case of the sample prepared from the 7 % Sr excess, the bulk-like behaviour of the thin film is also in agreement with the excellent stoichiometry revealed by ICP-OES. For the 5 % Sr-excess the agreement between film and bulk pellet is even a bit surprising since the exact stoichiometry is still not hit: A site deficiency is present with a rather large Fe content (4.3 % Fe). However, those deviations (Sr deficiency and Fe excess) might partly counterbalance each other for example by Fe on the A site. Transition metal ions on the A site are, for example reported also for Mn [111]. In any case, the rather ideal conductivity also fits excellent to the PALS experiment, where for 5 % Sr excess no Sr vacancies, but instead associates of titanium vacancies and oxygen vacancies ($V_{Ti}V_O$) are found, compared to the Sr vacancies for the thin film prepared from a stoichiometric target (see Fig. 7). The conductivity of the films with 11 % Sr excess is again rather low, but still larger than that of pseudo-intrinsic $SrTiO_3$ thin films.

All in all, our study reveals the importance of the deposition process in $SrTiO_3$ thin films and the need for a characterization beyond XRD to ensure a proper stoichiometry and, therefore, functionality since a rather small deviations from the main cation stoichiometry strongly affects the conductivity. Here, we propose an efficient way for preparing stoichiometric Fe: $SrTiO_3$ films by using Sr-rich targets (i.e. non phase-pure targets). Since it is known that PLD layers may strongly vary between different systems, the optimal Sr-excess found here might need readjustment in other equipment. Finally, a simple methodology for properly deciding whether a stoichiometric film has been prepared or not seems to be only found in the measurement of the conductivity at elevated temperature, yielding drastically lower conductivities even for rather small deviations from the cation stoichiometry.

2.4 Conclusions

Fe: $SrTiO_3$ thin films prepared from stoichiometric targets show severe Sr deficiencies which are quantified by ICP-OES, revealing about 10 % nominal A-site deficiency, but also enhanced Fe content. Off-stoichiometries are also clearly visible in RSM measurements by additional reflections

due to different out-of-plane lattice constants (compared to single crystalline SrTiO₃). Moreover, PALS measurements show the presence of Sr vacancies. The conductivity of such layers is many orders of magnitude lower than the electronic conductivity of the polycrystalline target material and almost perfectly matches the expected electronic conductivity of ultra-high purity intrinsic SrTiO₃ (with mid-gap fermi level). Variation of PLD deposition conditions affects the out-of-plane lattice constant measured in XRD measurements. However, chemical composition and conductivity of these films are not substantially changed. The use of Sr-rich targets enhances the Sr content in the deposited films and, especially, laser ablation of 7 % Sr-excess targets results in films with the correct A/B cation stoichiometry. Moreover, these stoichiometric films exhibit conductivities almost matching the bulk conductivity of polycrystalline Fe:SrTiO₃. The measurement of the conductivity is thus the most sensitive tool for finding the conditions for which stoichiometric films can be obtained. Opposite, RSM and out-of-plane lattice parameter analysis (often employed as single characterization) only indicates non-idealities for rather pronounced deviations from cation stoichiometry.

2.5 Supplementary Information

2.5.1 ICP-OES measurements

To determine the actual composition of the SrTiO₃ thin films, inductively coupled plasma-optical emission spectroscopy (ICP-OES) was used. Therefore, samples with about 100 nm film thickness were deposited on 5x5 mm² YSZ single crystals. These layers were dissolved in 5 mL of 3 % (v/v) nitric acid (65 mass%, EMSURE®) and 0.3 % (v/v) hydrofluoric acid (40 mass%, Suprapur®). The dissolving agent was prepared by mixing deionised water obtained by Barnstead™ Easypure™ II (18.2 M cm⁻¹), the concentrated acids and 1000 mg kg⁻¹ Eu single element standard (Certipure®, Merck, Germany). The final concentration of Eu was adjusted to 1 mg kg⁻¹ in the diluted acid mixture and was used as an internal standard to correct for possible signal drifts. After 30 min of dissolving time, the obtained sample liquid was transferred into a new polypropylene sample tube to remove the remaining substrate and to stop a possible dissolution process of the substrate. This whole process was conducted under ambient conditions at room temperature and the derived sample solutions were measured without any further dilution.

For signal quantification, single element standards (for details see Table 2) were mixed with the diluted acid mixture (3 vol% HNO₃, 0.3 vol% HF) already containing the internal standard to perform an external calibration. Standard solutions with varying concentration levels from 0.2 to 12.6 mg kg⁻¹ for the main components Sr and Ti and 0.002 to 0.126 mg kg⁻¹ for the Fe dopant were prepared. With the obtained signal intensities, regression lines were derived to calculate the analyte concentration of the unknown samples.

Tab. 4: Optimized ICP-OES parameters used for measurements.

RF power	1200 W
exposure time	10 s
nebulizer gas flow	0.75 L min ⁻¹ argon
type of nebulizer	MiraMist®
sample flow rate	0.7 mL min ⁻¹
pump tubing	Tygon®, 0.64 mm ID (color code: orange-yellow)
cooling gas flow	12 L min ⁻¹ argon
auxiliary gas flow	0.8 L min ⁻¹ argon
viewing height above load-coil	10 mm
Spectral range	Visible
Elements	Emission line [nm]
Sr	421.55*, 346.45, 216.60
Ti	334.45*, 232.45, 338.38
Fe	259.94, 238.20*, 240.49
Eu	381.97*, 412.97

Emission lines marked with * used for evaluation.

Samples and standards were analyzed with an iCAP 6500 ICP-OES spectrometer (ThermoFisher Scientific, Bremen, Germany) equipped with a MiraMist nebulizer and a cyclonic spray chamber (Glass Expansion, Port Melbourne, Australia). Sample-uptake was achieved with the peristaltic pump of the instrument (25 rpm, 0.64 mm ID pump tubing). Background-corrected emission

signals were recorded in the radial viewing mode and processed using Qtegra software (Thermo Scientific, USA). Six replicates with an integration time of 10 s each were measured for samples as well as standard solutions. The optimized ICP-OES parameters and the monitored emission lines are summarized in Table 1. For each element several intense but non interfered emission lines were measured.

Observed signal intensities were normalized using the signal response for the internal standard (Eu), and finally converted into concentration units by means of the external calibration. By using the molar masses of each element, the mole fractions of the cations present in the investigated samples were calculated. Obtained Eu signals were constant over each measurement session (less than 5% relative standard deviation for the whole measurement period, indicating the absence of temporal trends), and no significant difference in Eu-response between samples and calibration standards was observed.

Tab. 5: Single element standards used for signal quantification.

Element	Product information, lot number	Concentration levels
		for calibration [mg kg ⁻¹]
Sr	HC87301854	0.2, 0.4, 0.8, 1.6, 3.2,
Ti	HC99678363	6.4, 12.8
	Certipure®, Merck, Germany	0.002, 0.004, 0.008,
Fe	HC86803426	0.016, 0.032, 0.064, 0.128
Eu	Specpure®, Alfa Aesar, Germany 35753	1.0

2.5.2 Three arguments supporting the use of a transmission line based fitting model of impedance spectra obtained for thin films deposited from stoichiometric targets

We used a transmission line based fitting model with parallel ionic and electronic paths for impedance spectra of thin films deposited from stoichiometric targets. Here, three arguments are given supporting the validity of this approach. The first argument refers to the electronic resistance

R_{eon} . This resistance is essentially the dc resistance and the resulting conductivity σ_{eon} is plotted in Fig. 2.c in the main paper. The conductivity found for the thin film deposited from a target with 2 % Fe doping exhibits an activation energy of 1.57 eV and agrees very well with the intrinsic conductivity of a hypothetical ultrapure SrTiO_3 film. Such an excellent agreement cannot be accidental and can hardly be understood from a simple serial impedance model. The second argument refers to the geometrical capacitance C_{geom} in the fit (which depends mainly on the high frequency arc) – cf. Fig. 2.d in the main paper. The permittivity deduced from this value is rather close to that of SrTiO_3 (ca. 140 – 180 [110], depending on temperature), which supports the appropriateness of the model. The chemical capacitance resulting from the fit gives a third argument and is also shown in Fig. 2.d in the main paper. It comes mainly from the large arc and is about one order of magnitude larger than the geometrical capacitance. Its significant increase with temperature is typical for chemical capacitances, which originate from oxygen stoichiometry changes and thus defect chemical processes in the material upon the application of an alternating voltage. (An even stronger temperature dependence is found for other fluences, see main paper Fig. 8.d). Hence, we conclude that the model is meaningful and the dc resistance is the electronic resistance (due to ion blocking electrodes). The high frequency arc, on the other hand, corresponds to the total conductivity of ions and electrons.

2.5.3 Comparison with data from literature on films from 0.4 % Fe doped targets

The pseudo-intrinsic behaviour of SrTiO_3 thin films was already reported in Ref. [32] for films prepared from 0.4 % Fe doped stoichiometric targets. Interestingly, the rather pronounced high frequency shoulder found in our study on 2 % Fe doped films was not present for the 0.4 % Fe doped films discussed in Ref. [32, 63]. In order to exclude the relevance of artefacts and to further understand the different shape of the spectra, we also prepared 0.4 % Fe doped films here (1.1 J/cm², 5 Hz, investigated with $\text{La}_{0.6}\text{Sr}_{0.4}\text{CoO}_{3-\delta}$ microelectrodes prepared as described in Ref. [112].) All results shown in the earlier studies were excellently reproduced for these 0.4 % Fe: SrTiO_3 films. Fig. 12.a shows a typical EIS spectrum for 0.4 % Fe which consists of one depressed and asymmetric arc with a high frequency intercept, very similar to the earlier study. The conductivity calculated from the low frequency intercept of the main arc (i.e. the dc resistance,

R_{DC}) is shown in the Arrhenius plot of Fig. SI 1.b. The values match very well to those of Ref. [32], i.e. they are again pseudo-intrinsic.

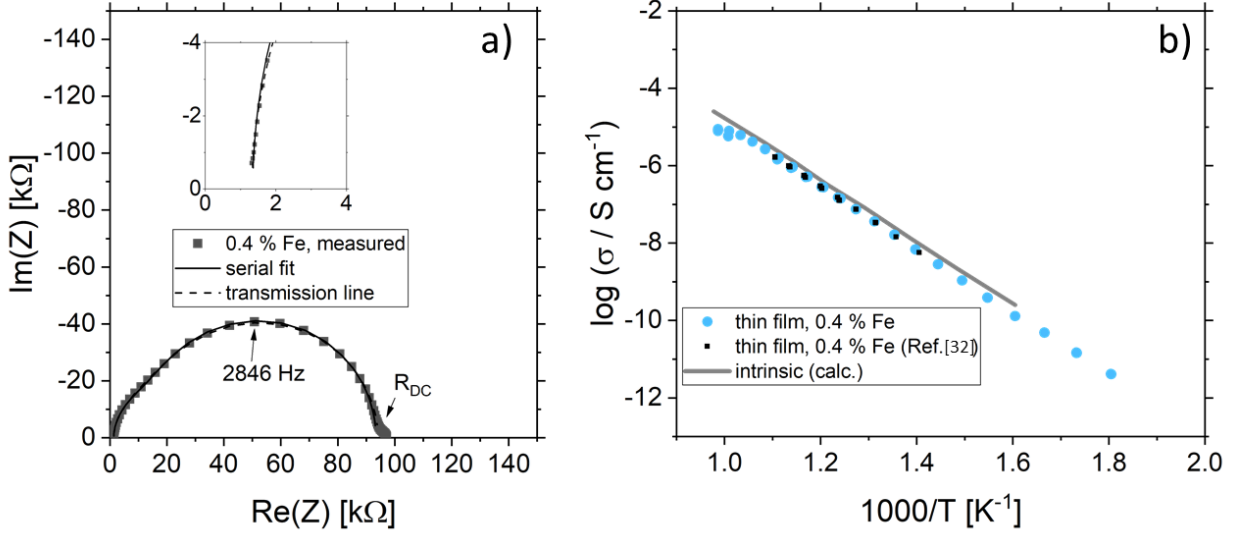


Fig. 12: (a) Impedance spectrum of a $\text{Fe}:\text{SrTiO}_3$ thin film deposited from a stoichiometric target with 0.4 % Fe doping. A distorted arc is visible. Fitting can be done with either using a serial fit or a transmission line base model, see below. The conductivity obtained from the DC resistance (highlighted using an arrow in (a)) is plotted in (b) for different temperatures and compared with the electronic intrinsic conductivity [29] as well as with literature data [32], showing great agreement to both.

The more or less distorted arc with a high frequency intercept found here and in Ref. [32] for 0.4 % Fe doping can be fitted by a serial circuit of a R followed by one or two R-CPE (CPE = constant phase element). The serial R is a contact resistance and is not further considered. For main arcs with little distortion, one R-CPE element is sufficient and the corresponding capacitance then corresponds very well to the expected bulk capacitance of the thin film. However, not surprisingly, also a fit is possible with the transmission line model suggested in the main paper and representing the mixed conducting character of the SrTiO_3 films. Based on this model the small high frequency arc for 2 % Fe doped films indicates a total conductivity which is much higher than the pseudo-intrinsic electronic conductivity due to parallel ion conduction. The absence of the high frequency arc for 0.4 % Fe, on the other hand, thus suggests that either the ionic conductivity is very low and does not strongly enhance the total conductivity, or the corresponding chemical capacitance in the transition line model becomes too small to allow a separation of the arcs, or both.

We think that the appearance of some distortion in Fig. SI 1.a (0.4 % Fe) has essentially the same reason as the much smaller high frequency arc for 2 % Fe, namely an enhanced total conductivity due to ion conduction. However, for 0.4 % Fe doped films the enhancement is only minor since the corresponding ionic conductivity is still in the same range as the pseudo-intrinsic electronic conductivity or even lower. Thus, either only the distortion of the main arc or simply nothing at all indicates existence of some ion conduction in the film, in contrast to the 2 % Fe doped films where the small high frequency arc is caused by the much higher ionic conductivity therein.

2.5.4 XRD of Sr overstoichiometric targets

Fig. 13 shows the X-ray diffraction patterns obtained for pellets prepared with Sr overstoichiometry.

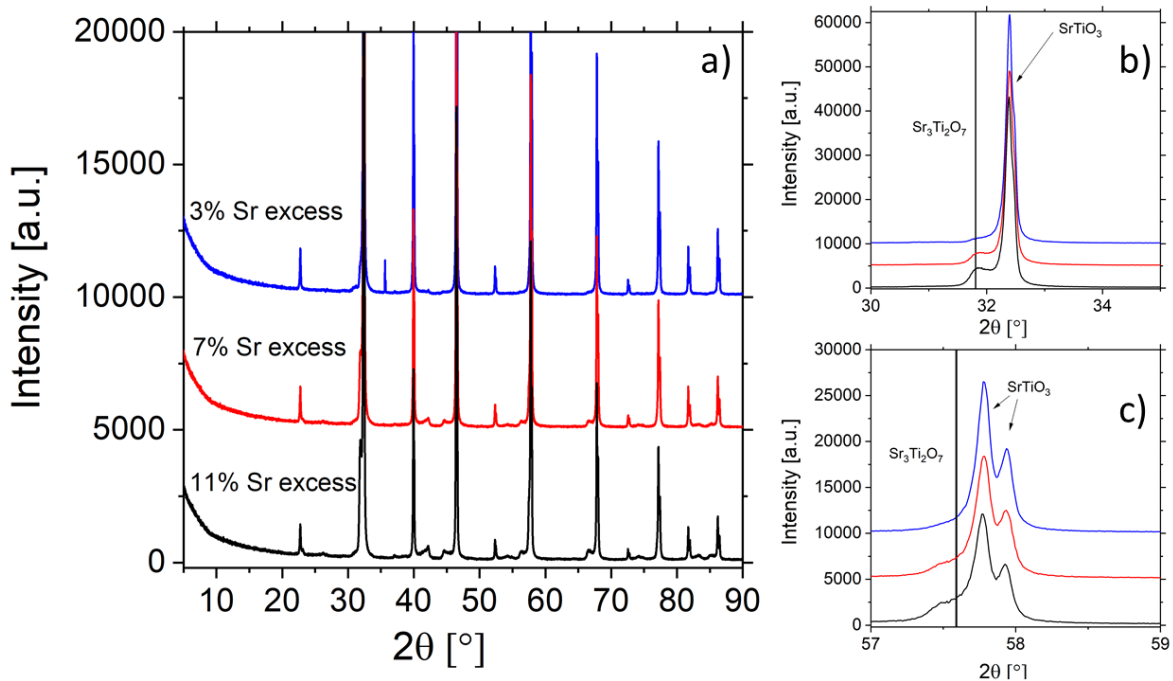


Fig. 13: X-ray diffraction measurements performed for polycrystalline targets of 2 % Fe-doped SrTiO₃ with 3 %, 7 % and 11 % Sr excess (a). The pellets consisted mainly of SrTiO₃ but also showed Sr₃Ti₂O₇ as additional phase. Not surprisingly, the amount of the secondary Sr rich phase directly correlated with the amount of excess Sr in the pellet. This can be seen in (b) and (c) of this figure. The highest Sr excess gives the highest amount of secondary phase after the described temperature treatment.

2.5.5 XRD of thin films deposited from overstoichiometric targets

Fig. 14 shows the X-ray results for thin films deposited from overstoichiometric targets. Surprisingly, the thin films appear to be phase-pure, even though the target pellet were not phase-pure, see Fig. 13.

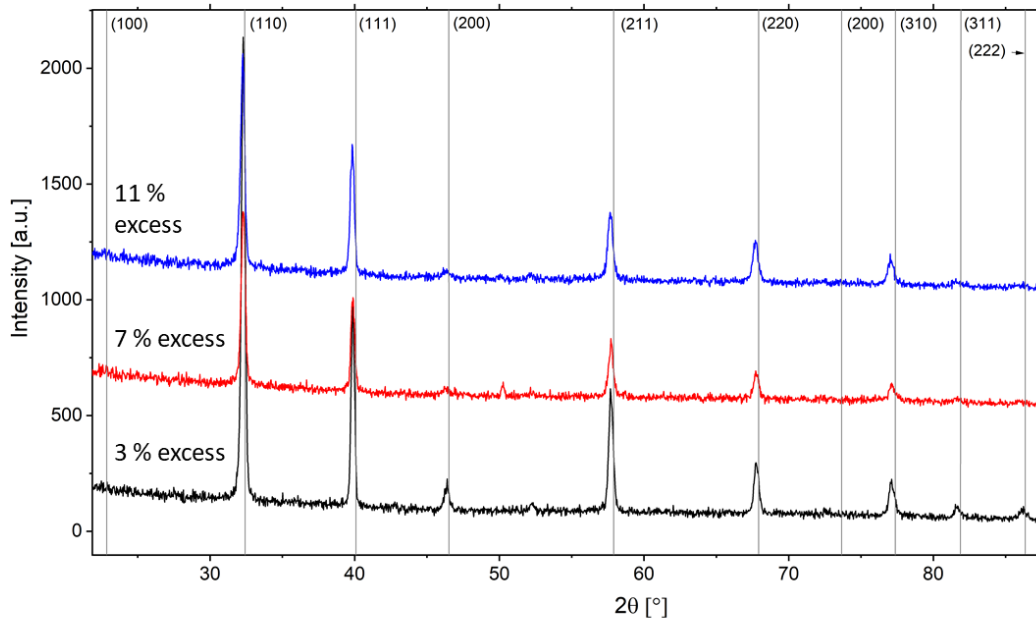


Fig. 14: XRD results for Fe-doped SrTiO₃ thin films on MgO deposited from 2 % Fe doped targets with Sr overstoichiometry of 3 %, 7 %, or 11 %, respectively. The obtained thin films are phase pure according to XRD as only SrTiO₃ reflexes are visible.

2.5.6 Discussion of the capacitances found for the thin films deposited from Sr overstoichiometric targets

As mentioned in the main part, the high frequency arc in the impedance spectra found for thin films deposited from Sr overstoichiometric targets is attributed to the SrTiO₃ bulk due to the match with expected geometrical capacitances. The capacitances of the two other R-CPE circuits fit pretty well to space charge layers; for bulk SrTiO₃ with 2 % Fe, a relative permittivity of 150 and a space charge potential of 600 mV, for example, ca. 6 nm result for one space charge [113]. It is thus reasonable to assume that the corresponding capacitances are due to the space charge layers at the two electrodes, with the Nb:SrTiO₃/Fe:SrTiO₃ junction probably having the smaller capacitance

(due to two similarly thick space charge zones in both SrTiO₃ parts). Hence, the large low frequency arc would be the space charge between SrTiO₃ film and Pt. From the measured peak frequencies, we can estimate the space charge potential and a rather realistic value of ca. 700 mV is found [113]. Accordingly, the dc resistance does no longer reflect the electronic conductivity.

Chapter 3: Unravelling the origin of ultra-low conductivity in doped SrTiO₃ thin films: Sr vacancies as the key driver for Fermi level pinning

The results presented in this chapter were prepared for submission as a scientific paper.

3.1 Introduction

The electrochemical bulk properties of SrTiO₃ (STO), a perovskite-type oxide, have been thoroughly investigated in many studies and different bulk defect models are available for doped and undoped SrTiO₃ [29, 30]. These models are well in line with the corresponding experimentally found conductivities at different temperatures and oxygen partial pressures. Therefore, SrTiO₃ often serves as a model material for other perovskite-type titanates (e.g. BaTiO₃, Pb(Zr,Ti)O₃) [33], since its bulk properties and bulk defect concentrations are so well understood. SrTiO₃ is a mixed conductor [33], enabling tailored conductivity ranging from predominantly electronic (i.e. via electrons or electron holes) to ionic (via oxygen vacancies), depending on temperature and on oxygen partial pressure [29, 113, 114].

Another way of tailoring the conductivity of SrTiO₃ to one's needs is the introduction of dopant elements. Donor doping can be achieved via trivalent ions on the A-site (e.g. La³⁺) or pentavalent ions on the B-site (e.g. Nb⁵⁺). In this case, cation vacancies or electrons compensate the charge. Accordingly, acceptor dopants in SrTiO₃ are monovalent ions on the A-site (e.g. K⁺) or trivalent ions on the B-site (e.g. Fe³⁺). In such a material, the charge is compensated by oxygen vacancies or electron holes. Also, co-doping (e.g. Sr_{1-x}La_xTi_{1-y}Cr_yO₃) is possible and allows to change optical, catalytic and electrochemical properties of SrTiO₃ for different purposes [115, 116]. Furthermore, the existence of trivalent “magic dopants” (e.g. Mn³⁺) is reported in literature [111], acting simultaneously as a donor and as an acceptor, depending on the site occupation, which is in line with a self-compensation mechanism suggested in theoretical studies for trivalent dopants [34]. Also, for other dopant elements including chromium [117], erbium [118], magnesium [119] and rhodium [120, 121], both A- and B-site occupation are discussed in SrTiO₃. In addition, Ti antisite defects are reported for SrTiO₃ thin films [104-106, 122]. Note that the change in site occupation for Ti⁴⁺ from the B-site (Ti_{Ti}^X) to the A-site ($Ti_{Sr}^{\bullet\bullet}$) is accompanied with the introduction of donor states.

Furthermore, vacancies strongly influence the defect model of SrTiO₃ and, thus, change the conductivity. While the direct influence of oxygen vacancies as charge carriers on the conductivity is easily accessible via ionic conductivity, the impact of their cation counterpart (i.e. cation vacancies) is less clear. In many cases, cation vacancies are immobile due to the higher temperatures needed for cation migration [31]. However, they can still affect the activation barrier of other defects (e.g. oxygen vacancies [31, 123, 124]). Furthermore, vacancies also act as dopants, i.e. cation vacancies act as acceptor dopants and oxygen vacancies act as donor dopants [31, 125-128], thereby strongly affecting the respective concentration of charge carriers and properties of SrTiO₃.

For doped materials, the interplay between the deliberate dopant and (usually unintended) doping via cation nonstoichiometry has to be considered – especially in the field of thin films, where cation nonstoichiometry is easily introduced during the deposition process [47, 48, 60, 61, 67, 68, 85, 129-131]. Thin films are becoming more and more interesting, e.g. in the field of resistive switching [20, 21, 32, 54, 55, 132-134] and for various light induced phenomena [13, 40-42, 77, 135] of the emerging field of opto-ionics [51]. SrTiO₃ thin films as well as other perovskite-type thin films are known to show different behavior than their bulk-like single or polycrystalline counterparts [31, 32, 63, 113, 136]. Structural differences (interfaces, strain, stress) [137-139], dominating space charge zones [113, 140] or nonstoichiometry accommodation [31, 48, 59, 141] have been discussed for thin films in literature and could be reasons for their deviating behavior. Even pseudo-intrinsic electronic conductivity was previously reported for Fe doped SrTiO₃ thin films, meaning that a mid-gap Fermi level leads to almost identical and extremely low electron and hole concentrations in differently doped samples [32, 63]. A correlation with Sr stoichiometry was found, obtaining this ultra-low conductivity only for substantial Sr vacancy concentrations [142].

In this study, doped as well as undoped SrTiO₃ thin films were characterized via electrochemical impedance spectroscopy (EIS) and their conductivity was investigated. For a broad range of dopants (Fe, Ni, Al) and dopant concentrations (up to 10 %), pseudo-intrinsic behavior with extremely low conductivities was found. To explain this rather unique thin film property, different additional characterization methods were employed, revealing specific details of elemental composition via inductively-coupled plasma optical emission spectroscopy (ICP-OES) and Rutherford backscattering spectroscopy (RBS), structure via X-ray diffraction (XRD) and X-ray standing wave (XSW), and defect chemistry via X-ray absorption spectroscopy (XAS) and positron annihilation lifetime spectroscopy (PALS). Combining all these pieces of information, a model is

deduced explaining the ultra-low conductivity of many doped and undoped SrTiO₃ films and compared to theoretical calculations. This model suggests that similar phenomena may exist also in many other large band gap multicomponent oxides.

3.2 Experimental

3.2.1 Sample preparation

Different SrTiO₃ powders were prepared via a mixed oxide route, starting with SrCO₃, TiO₂ and depending on the dopant Fe₂O₃, NiO, or Al₂O₃ (Sigma Aldrich, Germany). Stoichiometric amounts of the respective materials were weighed and then mixed for at least 40 min in an agate mortar. Subsequently, the pressed powders were calcined at 1000 °C for 2 h under ambient conditions. After an additional milling step, the powders were pressed using a cold isostatic press and subsequently sintered at 1200 °C for 5 h in air. X-ray diffraction measurements confirmed the phase purity of the obtained pellets, which were then used as targets for pulsed laser deposition (PLD). A summary of all targets used here is given in Tab. 6. Different substrates, namely undoped SrTiO₃ (STO, Crystec GmbH, Germany) Nb doped SrTiO₃ (Nb:STO) single crystals (0.5 wt% Nb content, CrysTec GmbH, Germany) and yttria doped zirconia (YSZ, Crystec GmbH, Germany), were used in this study. For conductivity measurements, Nb doped SrTiO₃ was used as a substrate due to its high conductivity. Thereby, the across-plane conductivity (or resistance) of the different thin films can be measured. In addition, the good agreement in the lattice parameter between undoped or slightly doped SrTiO₃ and the Nb:SrTiO₃ substrate leads to an epitaxial growth of the thin films. For this very reason, undoped SrTiO₃ substrates were used for X-ray diffraction measurements and reciprocal space mapping (RSM). For the chemical analysis, YSZ was used as a substrate. In this case, no epitaxial growth is expected. However, the YSZ substrates do not contain significant impurities from elements relevant for the SrTiO₃ thin films (Sr, Ti, Fe, Ni, Al) and, thus, are highly suitable for elemental analysis.

Tab. 6: Compositional analysis via ICP-OES and RBS/ERDA of different SrTiO₃ thin films deposited from stoichiometric targets. The values here are calculated for two cations per formula unit.

Target material	Thin film composition			Method
	Sr	Ti	dopant	
SrTi _{0.996} Fe _{0.004} O ₃	-	-	-	-
SrTi _{0.99} Fe _{0.01} O ₃	0.950	1.041	0.009	ICP-OES
SrTi _{0.98} Fe _{0.02} O ₃	0.945	1.020	0.035	ICP-OES
SrTi _{0.95} Fe _{0.05} O ₃	0.937	1.015	0.048	RBS (Sr, Ti), ERDA (Fe)
SrTi _{0.9} Fe _{0.1} O ₃	0.960	0.953	0.087	ICP-OES
SrTi _{0.996} Ni _{0.004} O ₃	0.944	1.046	0.010	ICP-OES
SrTi _{0.997} Al _{0.003} O ₃	0.988	1.007	0.005	ICP-OES
SrTiO ₃	0.957	1.043	-	ICP-OES

SrTiO₃ based thin films (undoped, acceptor doped or donor doped) were prepared by pulsed laser deposition (PLD) using a 248 nm KrF excimer laser (COMPex Pro 201F, Coherent, Netherlands) and a pulse duration of 25 ns. For the deposition process, a pulse frequency of 5 Hz, a laser fluence of 1.1 J/cm², a substrate-target distance of 55 mm, an oxygen pressure of 0.15 mbar and a substrate temperature of 650 °C were set. For the sake of comparability, the thin films investigated here were all in the range of 80 nm to 350 nm in thickness [32].

Circular Pt thin film microelectrodes were prepared on the SrTiO₃ thin films. The corresponding Pt thin films were sputtered with a high voltage magnetron coating device (BAL-TEC MED 020, Germany) and subsequently micro-patterned by lift-off photolithography. Only the 0.4 % Fe:SrTiO₃ film has La_{0.6}Sr_{0.4}CoO_{3-δ} microelectrodes prepared as described in Ref. [112] for better comparison with literature. The microelectrodes were contacted with Pr/Ir needles during impedance measurements. A schematic representation of the sample design is given in Fig 15.

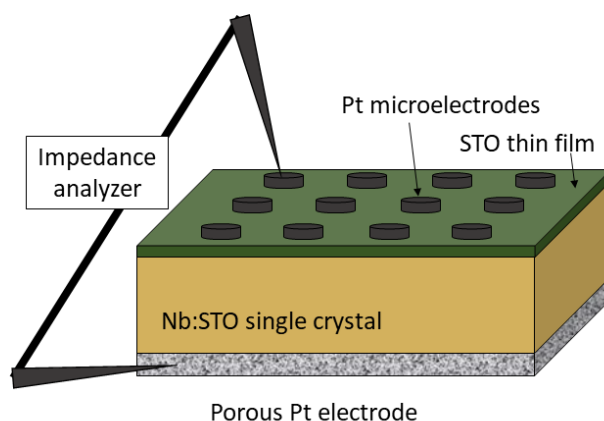


Fig. 15: A sketch of a typical sample for electrochemical characterization is shown. A (doped or nominally undoped) SrTiO_3 (STO) thin film is on a Nb-doped SrTiO_3 (Nb:STO) substrate. For well-defined electrical contact, circular Pt microelectrodes ($300\ \mu\text{m}$ in diameter) are used on top of the SrTiO_3 thin film as well as a porous Pt counterelectrode at the bottom of the Nb: SrTiO_3 single crystal.

3.2.2 Impedance spectroscopy

In order to investigate the conductivity of the thin films, we used electrochemical impedance spectroscopy (EIS) with an Alpha-A High Resolution Analyzer (Novocontrol, Germany). For temperature control, all electrochemical measurements were performed in a homogeneously heated furnace described in Ref. [76] within a temperature range of $380\ ^\circ\text{C}$ to $740\ ^\circ\text{C}$. The impedance was probed in a frequency range from $0.9\ \text{MHz}$ to $1\ \text{Hz}$ with a resolution of 10 points per decade, using an AC rms amplitude of $20\ \text{mV}$.

3.2.3 Elemental analysis

First, the thin films on YSZ were dissolved in $3\ \%$ v/v HNO_3 and $0.3\ \%$ v/v HF for 30 min at $25\ ^\circ\text{C}$ and the obtained solution was subsequently analyzed via solution based ICP-OES (iCAP 6500, Thermo Fisher Scientific, USA). For quantification, liquid standard solutions were used for external calibration. For more details, see section 3.6.3.

For comparison, the Sr/Ti ratio of nominally $5\ \%$ Fe doped SrTiO_3 was investigated using

Rutherford backscattering spectrometry (RBS). Experiments were performed at the ETH Tandatron accelerator using a 2 MeV He beam. Backscattered particles were detected by a silicon PIN diode under 168° and data was analyzed by comparison with RUMP simulations [143]. The Fe/Ti ratio was subsequently investigated using time-of-flight heavy ion elastic recoil detection analysis (ToF-ERDA). 13 MeV ^{127}I was used as primary beam and recoiling sample atoms were analyzed by the combination of a ToF spectrometer with a gas ionization detector [144]. Biparametric data was converted to mass spectra and analyzed using custom software.

3.2.4 X-ray diffraction

In order to investigate the lattice mismatch of deposited SrTiO_3 thin films and the nominally undoped SrTiO_3 substrates, reciprocal space maps of the (002), (103), and (113) reflexes were recorded, since this high-resolution X-ray diffraction method is especially suitable for highlighting differences in the (micro-) structure between the thin film and the substrate [82]. The measurements were conducted on an Empyrean multipurpose diffractometer (Malvern Panalytical Ltd, UK) with a Cu-anode operating at 45 kV and 40 mA, which yields a wavelength of $\lambda=1.5406 \text{ \AA}$ (Cu $K_{\alpha 1}$ radiation) and $\lambda=1.5444 \text{ \AA}$ (Cu $K_{\alpha 2}$ radiation).

A hybrid monochromator ($2\text{xGe}(220)$) with a $1/32$ divergence slit and a 4 mm mask was placed in the incident X-ray beam, while on the detector side we used a GaliPIX 3D detector in the frames based mode. This specific detector adjustment allowed us to measure 6.8672° of 2θ without moving the GaliPIX, the resolution was 0.01434° . The need of only scanning ω with a step size of 0.00716° reduced the required time for data acquisition tremendously. Reciprocal space maps were measured for the (002) ($\omega = 23.2376^\circ$, $2\theta = 46.4752^\circ$), the (103) ($\omega = 20.1378^\circ$, $2\theta = 46.4752^\circ$), and the (113) ($\omega = 15.6000^\circ$, $2\theta = 46.4752^\circ$) reflexes. The (103) and (113) reflexes also depend on the angle ϕ . In order to optimize the obtained signals, ϕ had to be adjusted before each measurement (rotation along the axis perpendicular to the sample's surfaces). In total four different thin films (from nominally undoped, 0.4 % Ni doped, 0.3 % Al doped, and 1 % Fe doped SrTiO_3 targets) deposited on nominally undoped SrTiO_3 single crystals oriented in the (001) direction were measured at ambient conditions.

3.2.5 Positron annihilation lifetime spectroscopy

Variable energy positron annihilation lifetime spectroscopy (VEPALS) measurements were conducted on nominally undoped SrTiO₃ and Fe:SrTiO₃ single crystals as well as thin films at the Mono-energetic Positron Source (MePS) beamline at HZDR, Germany [72]. We used a digital lifetime CrBr₃ scintillator detector [51 mm diameter (2”) and 25.4 mm length (1”) coupled to a Hamamatsu R13089-100 PMT. The detector was μ -metal shielded and housed inside a solid Au casing. For data acquisition, a homemade software was employed, executed from a multi-channel digitizer (SPDevices ADQ14DC-2X) with 14 bit vertical resolution and 2GS/s horizontal resolution. The time resolution of about 0.210 ns was achieved. The resolution function required for spectra analysis uses two Gaussian functions with distinct shifts and intensities, which depend on the positron implantation energy, E_p . All spectra contained at least $1 \cdot 10^7$ counts. Typical lifetime spectrum $N(t)$ is described by $N(t) = \sum (1/\tau_i) I_i \exp(-t/\tau_i)$, where τ_i and I_i are the positron lifetime and intensity of the i -th component, respectively ($\sum I_i = 1$). All the spectra were deconvoluted using the non-linearly least-squared based package PALSfit fitting software [73] into 2 discrete lifetime components, which directly evidence localized annihilation at 2 different defect types (sizes; τ_1 and τ_2). The corresponding relative intensities reflect to a large extent the concentration of each defect type (size) as long as the size of compared defects is in the similar range. In general, positron lifetime is directly proportional to defects size, i.e., the larger is the open volume, the lower is the probability and longer it takes for positrons to be annihilated with electrons [74]. The positron lifetime and its intensity have been probed as a function of positron implantation energy E_p , which is proportional to the positron implantation depth.

3.2.6 X-ray standing wave measurements

The X-ray standing wave (XSW) technique is able to gain real space information with a resolution of pm. Such measurements were conducted at PETRA III P24 beam line located at Deutsches Elektronen-Synchrotron (DESY) in Hamburg, Germany. Thereby, an interference field (X-ray standing wave) was generated by the incoming beam and by Bragg reflected plane X-ray waves of the Fe:SrTiO₃ thin film (deposited on an SrTiO₃ single crystal). Photo-absorption and, thus, fluorescence of the probed atoms strongly depend on the intensity of this interference field. Atoms located at the maxima show enhanced fluorescence whereas atoms at position of destructive

interference show reduced or even no fluorescence at all. By changing ω or the energy of the incident beam, the interference field can be varied, resulting in specific changes in the fluorescence yield of the probed atoms depending on their position (e.g. interstitial, A, and/or B site). Here, the ω dependency of the Fe K-fluorescence yield was measured. To investigate whether Fe is located at a lattice site (A-site and B-site) or at an interstitial site, the (002) reflex was probed. To distinguish between A- and B-site occupancy of Fe, the (001) or (003) reflex can be used. At the (003) reflex, the probed sample volume is smaller, thus minimizing the potential influence of spatial variation of the substrate (e.g. due to substrate imperfections). Therefore, omega scans of the (002) and (003) reflexes were carried out at 220 nm thick Fe doped SrTiO₃ thin films deposited from PLD targets with a stoichiometric composition of Sr_{1.00}Ti_{0.98}Fe_{0.02}O₃ as well as a Sr overstoichiometry of Sr_{1.05}Ti_{0.98}Fe_{0.02}O₃ to compensate Sr loss in the preparation process [142]. For all measurements, we used an incident beam energy of 8.4999 keV, corresponding to a wavelength of 1.4586 Å. Subsequently, the obtained results were compared to simulations for different Fe occupancies (A-site, B-site, mixed, interstitial). All XSW experiments were carried out at ambient conditions.

3.2.7 X-ray absorption spectroscopy

X-ray absorption spectroscopy was performed at the Surfaces/Interfaces: Microscopy (SIM) Beamline using Endstation ES3 at Swiss Light Source (SLS) at Paul Scherrer Institute (PSI), Switzerland. We measured the absorption of linear polarized X-rays in energy ranges of 521.0 - 589.0 eV (O K-edge), 441.0 - 479.0 eV (Ti L_{2,3}-edge), and 691.1 - 749.0 eV (Fe L_{2,3}-edge). At least four spots were probed for each sample. Here, we used a 220 nm thick thin films deposited from a stoichiometric target with 2 % Fe, at first directly after deposition without any further treatment as well as after subsequent annealing for 12 h at 700 °C in air. For these samples, the total electron yield as well as the fluorescence yield were measured, with fluorescence mode being more bulk sensitive [145] while the information depth of total electron yield measurements is in the range of several nm [145, 146] and thus fits rather well to the width of space charge layers [113]. The obtained spectra were normalized to the incident beam intensity using a gold mesh and processed using the Athena program [147]. Interpretation of the XAS spectra is supported by linear

combinations of simulated spectra of Fe in different oxidation state, i.e. Fe^{2+} and Fe^{3+} , in octahedral geometry using TM4XAS [148].

3.3 Results

3.3.1 Conductivity measurements

All films were characterized via electrochemical impedance spectroscopy. Typical impedance spectra for several doping situations are plotted in Fig. 16. The spectra for different thin films differ in the degree of distortion, from rather undistorted (e.g. 0.4 % Ni doped) to a rather pronounced distortion (e.g. 2 % Fe doped). The tiny low-frequency features found in some spectra are not further considered here. We can see in Fig. 2 that the low frequency intercepts of the large arcs (R_{DC}) at approx. 530 °C are rather similar (i.e. in the range of 180 k Ω to 280 k Ω) despite vastly different doping situations, from 0.4 % to 5 % dopant. (Please note that slightly different temperatures and film thicknesses are in play, but still the excellent agreement in the order of magnitude of resistance is surprising.) A detailed discussion of such impedance spectra of SrTiO_3 thin films is given elsewhere [142]. Here, we only summarize the main aspects deduced there: Since SrTiO_3 is an ionic and electronic conducting material, a transmission line model [79-81] with ionic and electronic rails is appropriate for describing the spectra. Since the ionic conduction path is blocked at one or both electrodes, the DC resistance corresponds to the electronic resistance of the film and an electronic conductivity can be calculated from its value. This electronic conductivity seems to be the same for all samples shown in Fig. 16. Depending on the exact ionic conductivity and the chemical capacitance, however, additional features may appear and give rise to the measured distortions. Here, however, we focus on the electronic DC conductivity of the films. The temperature dependent DC conductivity (i.e. electronic conductivity) of the 0.4 % doped film is plotted in Fig. 17.a. Interestingly, this electronic conductivity is several orders of magnitude lower than the expected bulk values from literature in Refs. [32, 149]. Moreover, the film conductivity almost perfectly matches the electronic intrinsic conductivity of SrTiO_3 calculated by assuming a mid-gap Fermi level and thus equal hole and electron concentrations. The calculated pseudo-intrinsic conductivity value is obtained using literature data [29], i.e a band gap E_g of 3.3 eV – 6.0×10^{-4} eV \times T, a hole mobility of 8.9×10^5 (T/K) $^{-2.36}$ cm $^2 \times$ V $^{-1} \times$ s $^{-1}$, an electron mobility

of $4.5 \times 10^5 (\text{T/K})^{-2.2} \text{ cm}^2 \times \text{V}^{-1} \times \text{s}^{-1}$ and $K_0 = 7.67 \times 10^{42} \text{ cm}^{-6}$. This pseudo-intrinsic behavior was also reported in [32, 142], but was not understood so far. There must be a fundamental difference between the acceptor-type bulk conductivity and the pseudo-intrinsic thin film conductivity and this is further investigated and explained in the following.

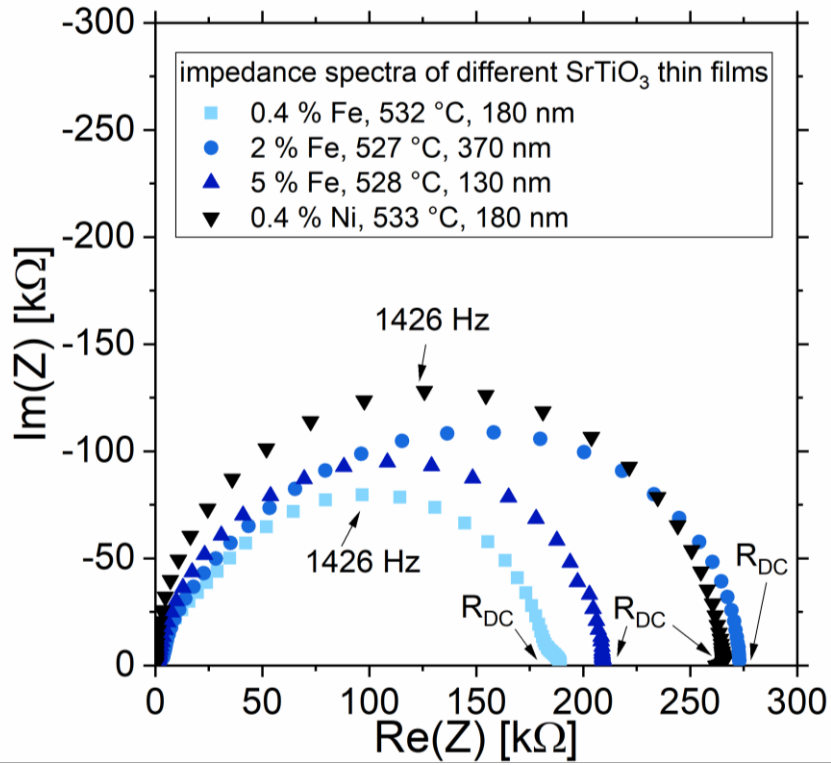


Fig. 16: Electrochemical characterization of different SrTiO_3 thin films deposited from targets with 0.4 %, 2 % and 5 % Fe as well as 0.4 % Ni doping doping at the B-site. The measurement temperatures deviate slightly for the individual samples, but are all in the range of 527 °C to 533 °C. Film thicknesses are in the range of 130 nm to 370 nm. The DC resistance of the main arc (R_{DC}) is indicated for the different impedance spectra with an arrow and is in the range of 180 kΩ to 280 kΩ. Different degrees of distortion can be identified, e.g. nearly undistorted for 0.4 % Ni to heavily distorted for 2 % Fe doping.

Also an increase in doping concentration does not lead to an increase in the DC conductivity for Fe:SrTiO₃ thin films. This is plotted in Fig. 18.a for different Fe doping concentrations (0.4 %, 1 %, 2 %, 5 %, 10 %). Not only does the conductivity remain unchanged for this vast increase in dopant concentration, the DC conductivity also always stays at the calculated pseudo-intrinsic conductivity. For the sake of comparison, we also measured the conductivity of thin films deposited from a target with 30 % Fe (STF73). The conductivities of 30 % Fe-doped SrTiO₃ films are about five orders of magnitude higher at 350 °C (and these thin films can even be used as thin film

electrodes in fuel cells), thus showing that we face a true thin film effect and not an artefact. In a separate paper, we demonstrated that the Sr stoichiometry of the target strongly affects the film properties with 7 % Sr overstoichiometric targets finally leading to much higher conductivities (close to the expected bulk value) [142]. Common defect models fail to predict or explain such a pronounced doping independent conductivity behavior with mid-gap Fermi level pinning. Furthermore, the conductivity of a thin film deposited from a target containing 0.4 % Fe doping is independent of the oxygen partial pressure over an oxygen partial pressure range of five orders of magnitude (see Fig. 17.b), which is also in contrast to Fe doped bulk SrTiO_3 [114]. For further characterization, films from nominally undoped SrTiO_3 as well as Ni doped SrTiO_3 and Al doped SrTiO_3 targets were measured (see Fig. 18.b). The DC conductivity of these thin films again perfectly matches the calculated very low pseudo-intrinsic conductivity (i.e. $c_h = c_e$).

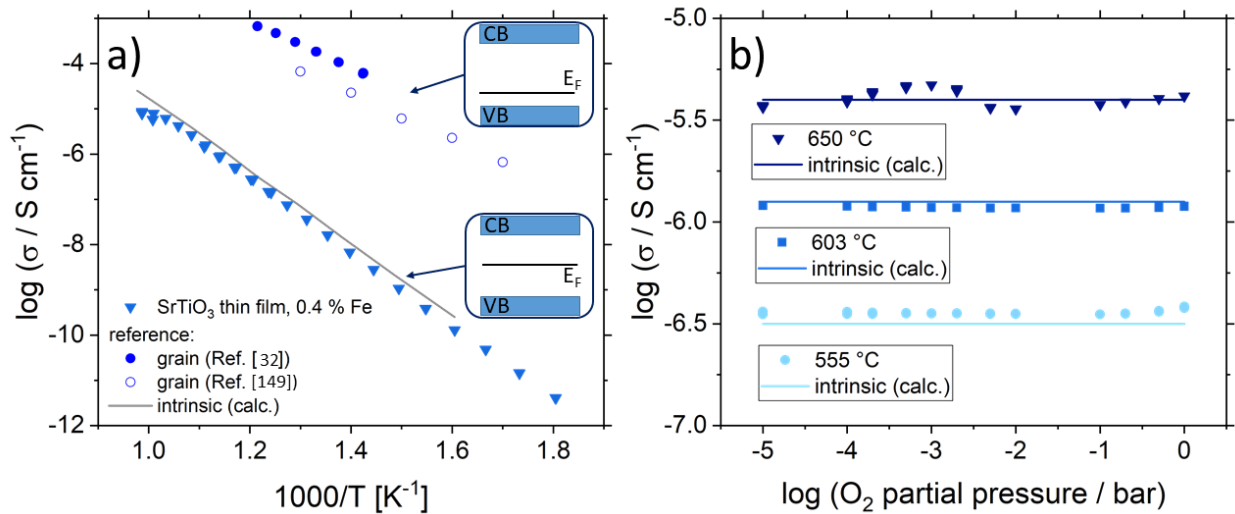


Fig. 17: Electrochemical characterization of Fe doped SrTiO_3 thin films deposited from a target with 0.4 % Fe doping. The DC conductivity obtained from the DC resistance for is plotted in (a) and compared with the expected conductivity values for bulk samples [32, 149] and with the calculated conductivity of pseudo-intrinsic electronic conductivity ($c_h = c_e$) [29]. Surprisingly, the conductivity of the Fe: SrTiO_3 thin film deposited from a target with 0.4 % Fe is orders of magnitude lower than the respective bulk value from literature, but perfectly matches the intrinsic conductivity of SrTiO_3 , despite doping and being measured in air. The corresponding band structures for the respective conductivities are highlighted. Here, intrinsic conductivity corresponds to a mid-gap Fermi level. In (b), the oxygen partial pressure dependence of the conductivity of a Fe doped thin film deposited from a target with 0.4 % Fe is shown for three different temperatures (555 °C, 603 °C and 650 °C). No variation of the conductivity is observed in an oxygen partial pressure range between 10 ppm oxygen to 1 bar oxygen, the conductivity matches the pseudo-intrinsic conductivities of the respective temperature.

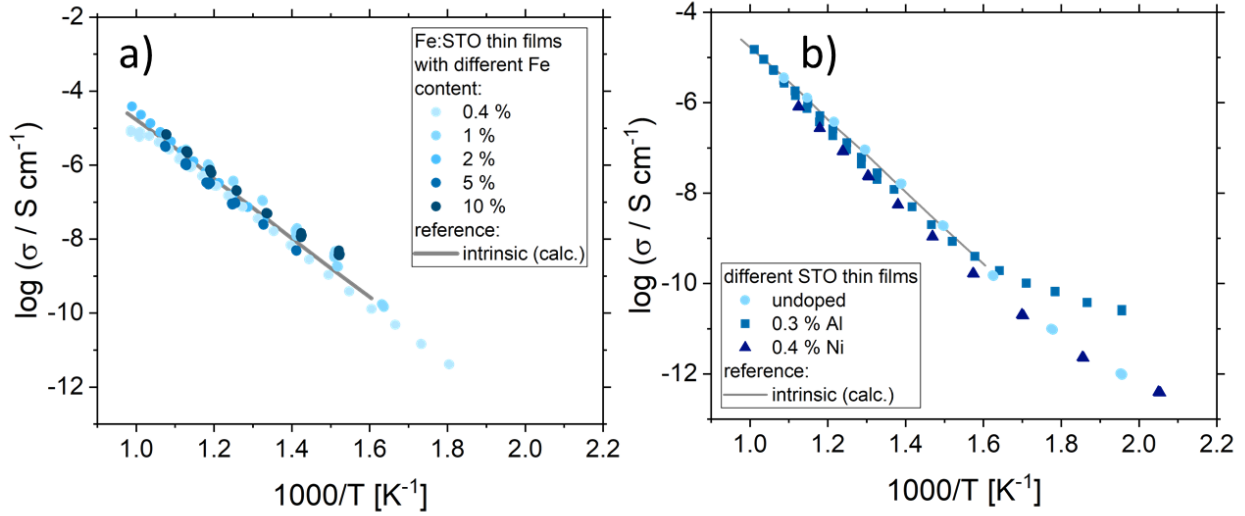


Fig. 18: The DC conductivity of Fe doped SrTiO_3 thin films deposited from targets with different doping concentrations ranging from 0.4 % up to 10 % is plotted in (a) and compared to the electronically intrinsic conductivity ($c_h = c_e$) [29]. Surprisingly, no significant increase in conductivity is observed for increasing dopant concentrations. In contrast, the various DC conductivities are all in perfect agreement with the intrinsic conductivity. Furthermore, the DC conductivity of nominally undoped SrTiO_3 thin films and slightly acceptor doped thin films with different dopings (Ni: SrTiO_3 , Al: SrTiO_3) matches the calculated intrinsic conductivity (b), highlighting the more general nature of this effect.

Thus, for a vast number of different films, doping does not affect the conductivity. Neither the dopant concentration nor the dopant itself (Fe, Ni, Al) changes the pseudo-intrinsic conductivity, highlighting the extremely robust nature of this effect. We thus conclude that we do not face a special feature of Fe doped SrTiO_3 , but an inherent property of many SrTiO_3 thin films deposited via pulsed laser deposition (PLD). Consequently, a phenomenon present in all our SrTiO_3 films should be the source of this effect. A first hint was already reported in a separate paper: When using highly off-stoichiometric targets with 5 – 7 % Sr excess, SrTiO_3 films result with “normal” conductivity behavior (i.e. like doped bulk samples rather than pseudo-intrinsic) [142]. This Sr excess in the target was shown to compensate the Sr vacancies otherwise present in the films. In the following, we describe results from several methods applied to gain further information on atomic reasons behind the pseudo-intrinsic behavior.

3.3.2 Elemental analysis

The results for the chemical analysis are plotted in Fig. 19 and summarized in Tab. 6. Different

SrTiO₃ thin films, ranging from Fe doped or Ni doped to Al doped and nominally undoped, were investigated using inductively coupled plasma optical emission spectroscopy (see Fig. 5.a). A more or less pronounced Sr deficiency, i.e. a deviation of the Sr/(Ti+dopant) ratio from unity, is found for all thin films. Note that the dopant is attributed to the B-site in this consideration. The amount of dopant found in the samples also shows some deviations from the target compositions. Little deviation was measured for a target with 1 % Fe, where 0.9 % Fe resulted in the thin film. Similarly, for a pellet with 10 % Fe at the B-site 8.7 % Fe was found in the respective thin film. In case of the Ni doped SrTiO₃, 1 % Ni was found instead of the target concentration of 0.4 % Ni. The error for these measurements is usually well below 1 % for main components (Sr, Ti), but is in the 5 % range with respect to the given amount for minor components (i.e. dopants), e.g. 0.01 ± 0.0005 . Different processes including preferential scattering and incongruent ablation during pulsed laser deposition might lead to the discrepancy between the nominal and the experimentally found composition of these thin films [67, 68, 88]. Similar differences are also reported for other materials, e.g. LaMnO₃ [92], Ca₃Co₄O₉ [94] and SrMnO₃ [96].

The compositional results were confirmed by Rutherford backscattering spectroscopy (RBS), see Fig. 19.b. Here, a Fe doped SrTiO₃ thin film (with a nominal Fe content of 5 % Fe at the B-site) on a SrTiO₃ substrate was investigated. Using RBS, a clear difference between the thin film and the substrate can be seen. This difference is attributed to a different Sr/Ti ratio of the thin film, compared to the substrate, but also differences in the oxygen stoichiometry might play a role. For the thin film, less Sr than Ti was found, whereas nominally less Ti would be expected. With RBS, the Fe content could not be determined reasonably because of the huge background from the Sr signal. The use of characteristic X-rays (PIXIE) was excluded since the substrate material and the thin film are basically the same material, making it impossible to properly normalize the Fe X-ray yield to another element. Therefore, heavy ion elastic recoil detection analysis (ToF-ERDA) was performed. Here, a Fe/Ti ratio of 0.047 ± 0.005 was obtained, which is in line with the nominally expected value of 0.052, corresponding to a 5 % dopant concentration at the B-site.

Altogether, chemical analysis revealed Sr deficiency in all films. There are different ways for SrTiO₃ to accommodate this Sr deficiency, e.g. via Sr vacancies in the lattice, by formation of Ruddlesden-Popper phases, segregation of Ti rich secondary phases (e.g. TiO₂) or antisite defects (e.g. $Ti_{Sr}^{\bullet\bullet}$ [104-106, 122]). In order to resolve the predominant effect in our films, further film characterization was performed.

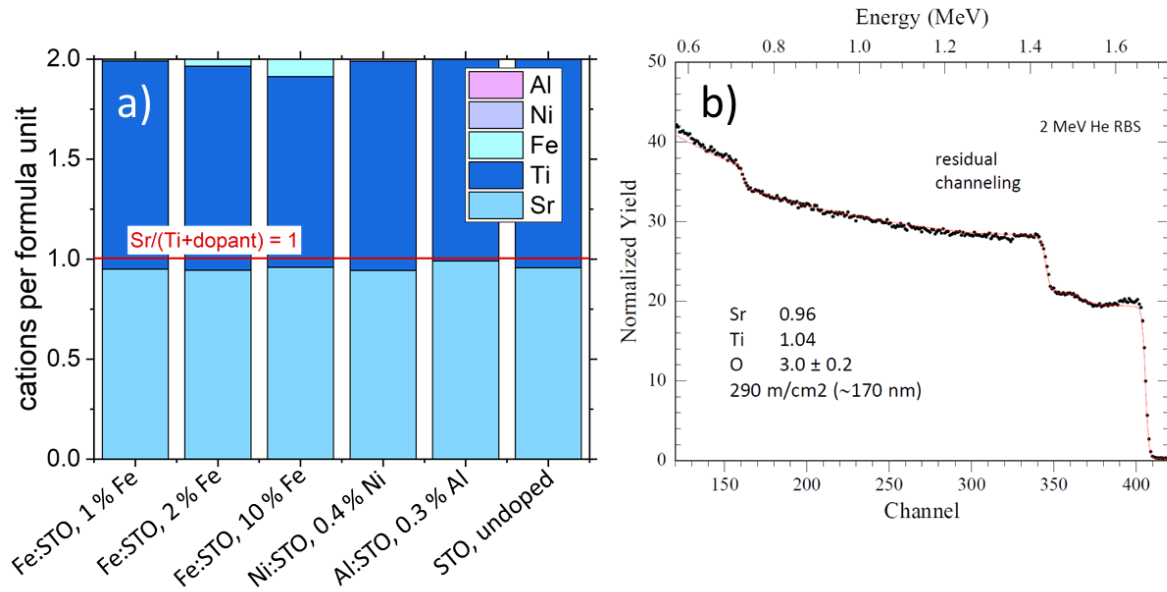


Fig. 19: Elemental analysis of different thin films deposited from stoichiometric targets using pulsed laser deposition (PLD). In (a), the results of inductively coupled plasma optical emission spectroscopy (ICP-OES) are presented for different Fe doped thin films with Fe doping concentrations of the respective targets ranging from 1 % to 10 %, a Ni and an Al doped SrTiO₃ thin film as well as a nominally undoped SrTiO₃. The ideal stoichiometry, corresponding to a Sr/(Ti+dopant) ratio of unity, is highlighted as a red line, revealing Sr deficiency for all thin films analyzed. Note that the dopants are attributed to the B-site here. As a comparison, a thin film with a nominal Fe concentration of 5 % was also analyzed by means of Rutherford backscattering spectroscopy (RBS), shown in (b), and elastic recoil detection analysis. Using RBS, a severe Sr deficiency was found. Both methods are therefore in good agreement, highlighting the Sr deficiency in thin films deposited from stoichiometric targets.

3.3.3 X-ray diffraction

In general, SrTiO₃ exhibits a cubic unit cell and all cell parameter obtained from the RSM measurements were found to be ca. 3.9 Å, which is in line with literature data [71, 83, 84]. However, the reciprocal space maps of the (002) reflexes plotted in Fig. 20 show an elongated c cell parameter compared to the nominally undoped SrTiO₃ substrate for all deposited thin films except for the Al doped layer. As a result, two separated diffraction peaks, one originating from the substrate and one from the thin film, can be seen. Further reflexes, namely the (103) and the (113) reflexes were investigated. In each reciprocal space map of the (103) reflexes (see section 3.6.2), again two reflexes only differing in q_1 can be seen (except in the case of Al: SrTiO₃),

confirming the enlarged c cell parameters found in most of the deposited thin films. A deviation of the in-plane cell parameters of the thin films from the substrate would result either in a shift in q_{\parallel} or in the intensities of the thin film peaks, which we did not observe.

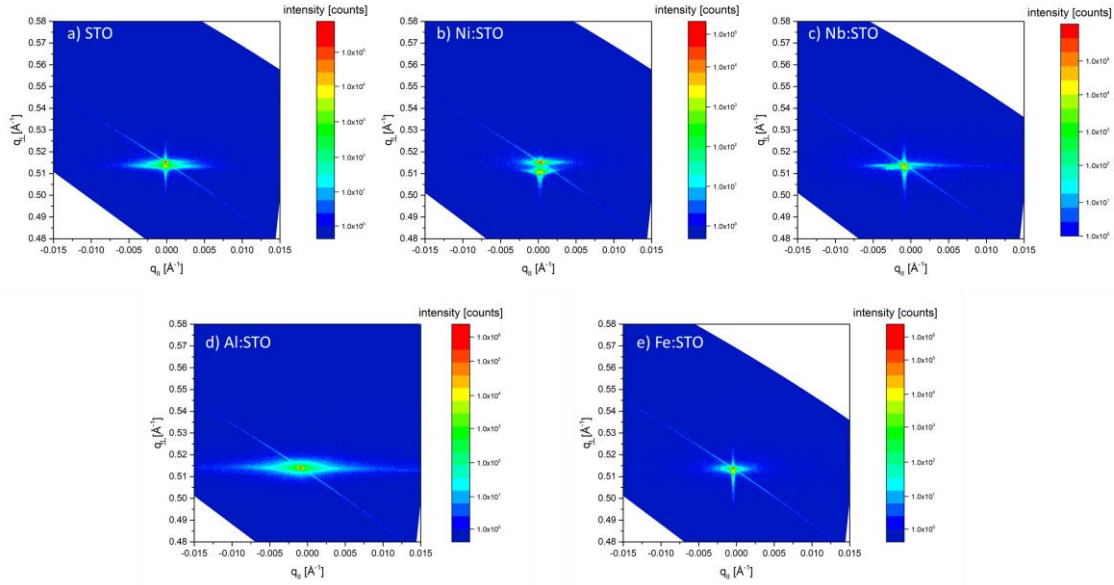


Fig. 20: Structural characterization of different SrTiO_3 thin films on top of nominally undoped SrTiO_3 single crystals oriented in the (001) direction. Thin films were deposited from nominally undoped (a), 0.4 % Ni doped (b), 2 % Nb doped (c), 0.3 % Al doped (d), and 1 % Fe doped (e) SrTiO_3 targets. Here, reciprocal space maps (RSM) for the (002) reflex are shown, revealing a severe deviation in the lattice parameter for the thin films compared to the underlying SrTiO_3 substrates. Except for the Al doped thin film (d) the c cell parameter from each of the prepared thin films is elongated compared to the substrate. As a consequence, in the RSM two separated reflexes can be found. The deviation between the thin film and the substrate can be attributed to cation vacancies. Taking the Sr deficiency found by elemental analysis into account, the cation vacancies are identified as Sr vacancies.

To further clarify this point, additional reciprocal space maps of the (113) reflexes were measured (see Fig. 21), showing shifts only in q_{\perp} direction (except for Al: SrTiO_3 exhibiting no shift at all). (Note that Sr deficiency is also comparatively lower in Al-doped thin films than in the other thin films, thus decreasing the difference in lattice parameter, as also observed in [142] for similar cases.) Thus, no difference in the in-plane cell parameters are found for any thin film compared to the single crystalline substrate. However, an elongation of the c cell parameter reduces the symmetry of the thin films and leads to a tetragonal lattice. The results of the recorded reciprocal space map are in line with literature data on SrTiO_3 thin films [48, 59, 85] and are attributed to the existence of cation vacancies, i.e. to films with a Sr/Ti ratio (or Sr/(Ti+dopant)) deviating from

unity [45, 46, 86]. Thus, we can conclude that at least part of the nominal Sr deficiency found in section 3.3.2 is materialized in the form of Sr vacancies. This is also in agreement with the surprisingly high Sr vacancy concentration reported for SrTiO₃ films in literature [31].

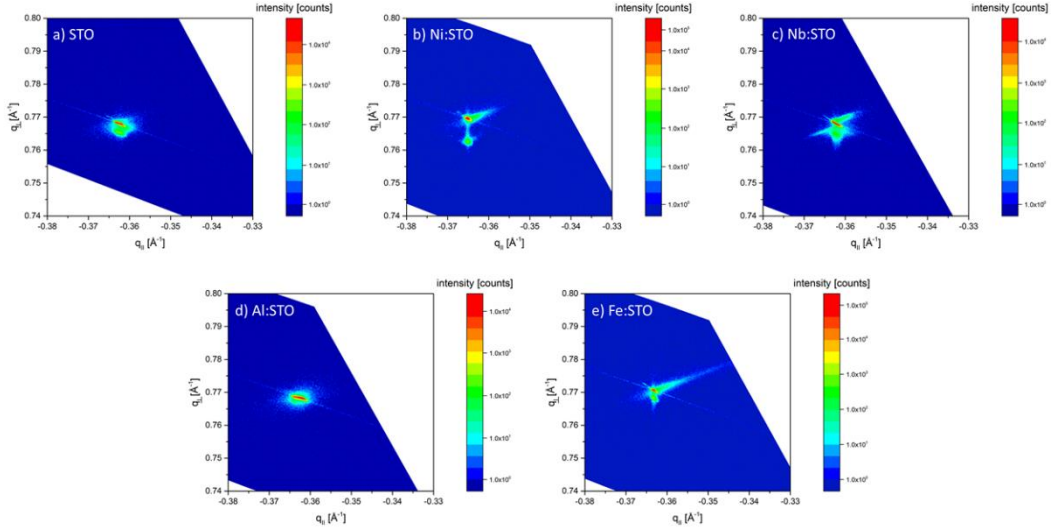


Fig. 21: Reciprocal space maps for the (113) reflex thin films deposited from nominally undoped (a), 0.4 % Ni doped (b), 2 % Nb doped (c), 0.3 % Al doped (d), and 1 % Fe doped (e) SrTiO₃ targets on nominally undoped SrTiO₃ single crystals oriented in (001) direction. A difference between the more intense substrate reflection and the thin film reflex indicates structural differences (found for all investigated samples except for the Al doped thin film). The reflexes for substrate and thin film shown in each map only differ in q_{\perp} , thus thin films and single crystals exhibit the same in-plane (i.e. a and b) cell parameters, with elongation being present only in the out of plane axis (i.e. c cell parameter).

3.3.4 Positron annihilation lifetime spectroscopy

In Fig. 22.a, a nominally undoped SrTiO₃ thin film is characterized and compared with a nominally undoped SrTiO₃ single crystal. The dependence of lifetime on implantation energies for the film on the substrate reflects a depth dependent change of the main ionic defect. Comparing the near surface signal of the film with the signal of the pure bulk sample reveals severe differences. In the thin film, the predominant point defect is the Sr vacancy (lifetime: 281 ps), which is in agreement with the chemical analysis (see section 3.3.2) as well as the RSM data (see section 3.3.3). This is in contrast to single crystals, where the point defect chemistry is dominated by titanium vacancies (lifetime: 189 ps). The same trend can be observed for an Fe doped SrTiO₃ thin film (deposited on

Nb:SrTiO₃ and from a pellet with 2 % Fe), see Fig. 22.b, in which it is compared to an Fe doped single crystal (0.15 % Fe). Again, Sr vacancies are found in the thin film, while titanium vacancies are present in the single crystal. Taking the similar levels of Sr deficiency (obtained from ICP-OES measurements in section 3.3.2) into account, Sr vacancies are probably also present in all the other thin films investigated in this study. However, this does not mean that the entire Sr deficiency leads to A-site vacancies. Rather, B-site ions on the A-site might reduce the A-site vacancy concentration compared to the nominal Sr-deficiency. Ti on the A-site was found or discussed in several studies. Another option is the dopant occupying an A-site, which is considered next.

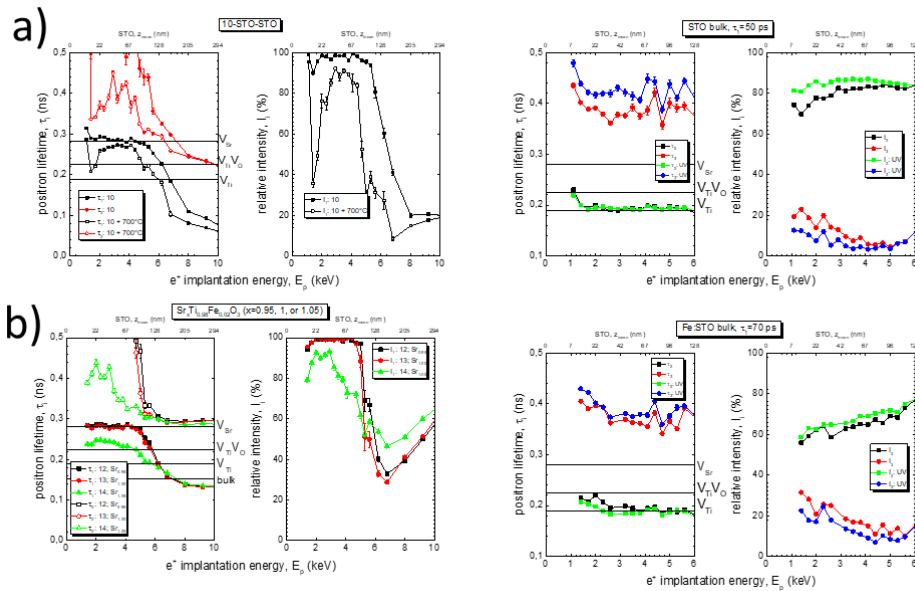


Fig 22: Positron lifetime annihilation spectroscopy (PALS) measurements to reveal the common point defect in thin films and single crystals. In (a), a point defects found in a nominally undoped SrTiO₃ thin film are compared to those of a nominally undoped SrTiO₃ single crystal. In (b), the results for a thin film deposited from a 2 % Fe doped SrTiO₃ target are contrasted with the respective defects found in a Fe doped single crystal with 0.15 % Fe. A significant change in the defects found in thin films and single crystals can be observed for both cases. In thin films, Sr vacancies are the dominant point defect, whereas in single crystals titanium vacancies are present.

3.3.5 X-ray standing wave

X-ray standing wave (XSW) technique was used to determine whether Fe is located at an interstitial, A- or the B-site. In Fig. 23.a, the normalized Fe K-fluorescence of the (002) Bragg reflex is shown in dependency of ω . The fluorescence first has a minimum followed by a maximum,

which indicates that Fe is not present at an interstitial position according to simulations. The sharp peak at 20.16° is caused by the substrate and does not have any impact on our interpretation. This reflection is sensitive towards lattice site and interstitial site. Here, we analyzed a sample deposited from a target with 2 % Fe and 5 % Sr excess, corresponding to a stoichiometric thin film [142] as a reference. As expected, in a bulk-like material, the Fe is located at a lattice site. To differentiate between A- and B-site occupation of the Fe, we performed measurements on the (003) reflection, which is sensitive towards the different lattice sites. The simulation in Fig. 23.b. show the change of the normalized fluorescence yield when the Fe occupancy changes from only B-site ($\xi = 0$) to only A-site ($\xi = 1$), with mixed occupation in between. The ratio of A/B-site occupation of Fe determines the normalized fluorescence yield. A ratio of < 1 leads first to a maximum which is followed by a minimum. If the ratio becomes > 1 a minimum is followed by a maximum, thus, the sequential arrangement swaps. XSW measurements of the (003) reflex in Fig. 23.c thus suggest that in Sr deficient films deposited from stoichiometric targets up to 30 - 40 % of Fe is located at the A-site. On the other hand, in films deposited from a target with 5 % Sr excess (i.e. $\text{Sr}_{1.05}\text{Ti}_{0.98}\text{Fe}_{0.02}\text{O}_3$) in order to compensate Sr-loss in the deposition process [142], Fe is only present on the B-site. The obtained data are in reasonable agreement with our simulations, even though the small amounts of Fe ions in the thin films leads to a substantial scatter of the data. A change in site occupation towards the A-site in SrTiO_3 was also reported for other transition metals, e.g. Mn [111, 150]. Such redistribution of Fe towards the A-site in Sr deficient thin films has a drastic defect chemical impact, since Fe at the B-site is an acceptor, while Fe at the A-site acts as a (probably deep) donor. Thus, a severe change in the dopant type is found for the Fe-doped SrTiO_3 thin films exhibiting pseudo intrinsic conductivity. To further investigate the differences between intrinsic and bulk-like thin films, X-ray absorption spectroscopy was performed.

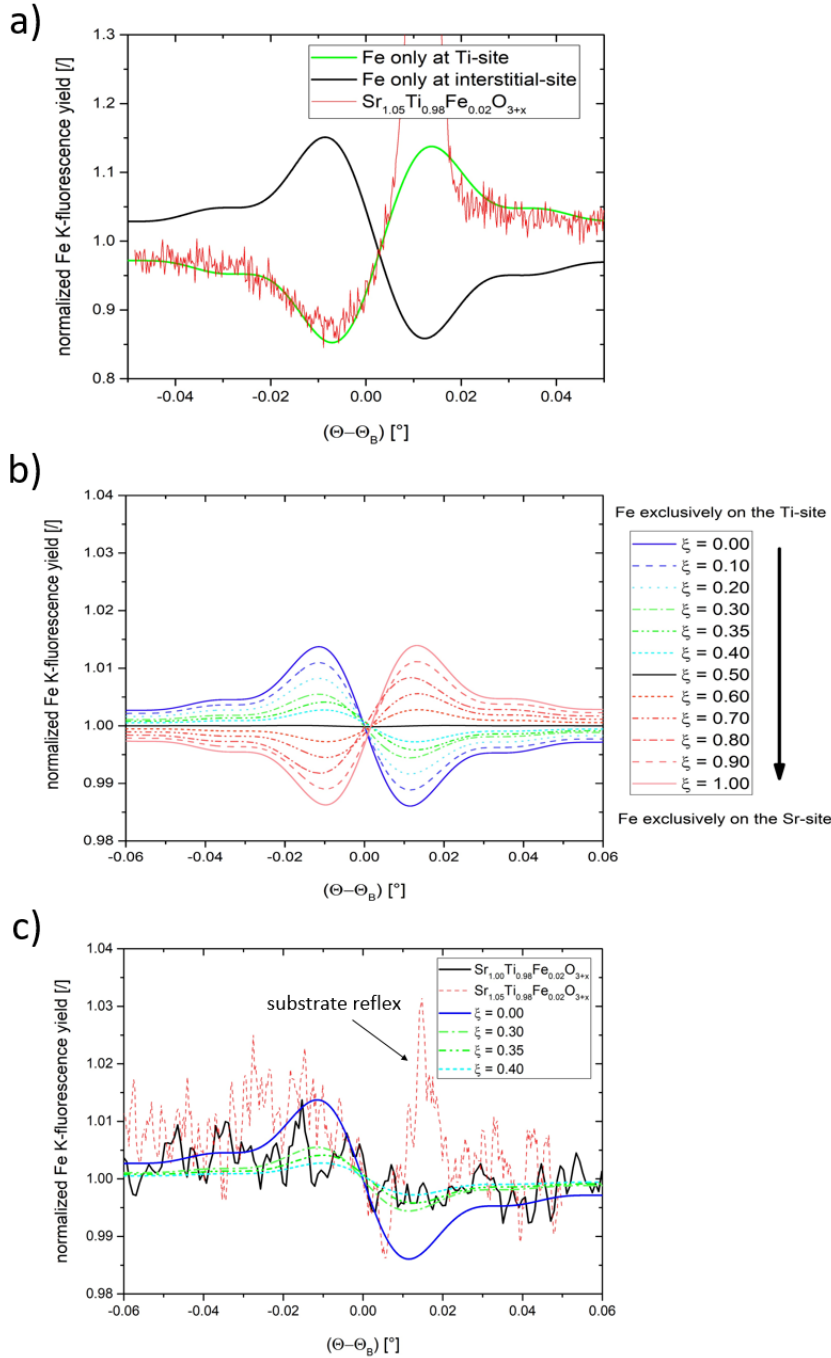


Fig. 23: Using X-ray standing wave measurements (XSW) the position of Fe in Fe doped SrTiO_3 thin films deposited on SrTiO_3 single crystals can be determined. (a) Normalized Fe L-fluorescence yield induced by the interference field of the (002) reflex of the Fe: SrTiO_3 thin film. The measurement indicates that Fe is not present at an interstitial position, but exclusively at the A- and/or B-site. To differentiate between A and B-site occupancy simulations (b) and measurements (c) of the Fe L-fluorescence yield at the (003) reflex are necessary. $\xi = 0$ denotes to only B-site occupation, whereas in the simulation $\xi = 1$ Fe is only present at the A-site. In the XSW measurements of a thin film deposited from a target with no Sr excess ($\text{Sr}_{1.00}\text{Ti}_{0.98}\text{Fe}_{0.02}\text{O}_{3+x}$) and a thin film deposited from a target with 5 % Sr excess ($\text{Sr}_{1.05}\text{Ti}_{0.98}\text{Fe}_{0.02}\text{O}_{3+x}$) differences in the site occupation of Fe can be found. The results suggest that up to 40 % of Fe is present at the A-site in

the film deposited from the $Sr_{1.00}Ti_{0.98}Fe_{0.02}O_3$ target. Sr excess in the target seems to prevent A-site occupancy of Fe. (Please note that the $SrTiO_3$ substrate reflex is visible in the data of the thin film deposited from the target with 5 % Sr excess. The substrate reflection for the thin film deposited from a stoichiometric target occurs at higher angles, i.e. the difference between the lattice parameter of the substrate and the thin film is more pronounced for the film deposited from the stoichiometric target.)

3.3.6 X-ray absorption spectroscopy

Fig. 24.a shows the XAS spectra of the Fe L_{2,3}-edge, Ti L_{2,3}-edge, and O K-edge for Fe:SrTiO₃ thin films deposited from a stoichiometric target with 2 % Fe in the fluorescence mode. In order to gain a deeper understanding of the present Fe oxidation states, simulations and linear combinations were carried out. Since the simulated Fe⁴⁺ spectra did not fit the experimental data (as also reported in literature [140]), only Fe²⁺ and Fe³⁺ were considered in the following (see section 3.6.5). For the simulation, we set the Slater integral reduction to 80 % and reduced core spin orbital coupling by 1.0 % for Fe³⁺ and 1.1 % for Fe²⁺. The valence spin orbital coupling amounted to 3.70 % and 3.25 % for Fe²⁺ and Fe³⁺, respectively. The crystal field parameters were fixed to 10 Dq = 1.5 eV and the charge transfer parameters to Δ = 2 eV. Lorentzian broadening was set to 0.2 eV and Gaussian broadening to 0.3 eV. Based on these parameters, best agreement between experimental data and the calculated spectrum was achieved for 10 % Fe²⁺ and 90 % Fe³⁺. (Note that these values are only rough estimates due to the fact that self-absorption, site occupation, and oxygen vacancies as well as cation vacancies are not considered here, which might also explain the deviation of the simulated spectra from the measured ones at higher energies [140]). When comparing the sample measured directly after the PLD process (0.15 mbar O₂) at 650 °C with the sample with an additional annealing step (200 mbar O₂) at 650 °C, no significant changes can be observed, which means that the bulk ratio of Fe²⁺ to Fe³⁺ is independent of the oxygen partial pressure in the range of 0.15 mbar to 200 mbar. In bulk samples, oxygen incorporation is expected under these conditions, corresponding to an increase in Fe oxidation state. However, this deviation from bulk behavior fits well to the oxygen partial pressure independent conductivity measurements in section 3.3.1 (see Fig. 17.b, please note: here a thin film with 0.4 % Fe was investigated). These results are also addressed in section 3.4.2 with regard to donor states in Fe doped SrTiO₃.

The O K-edge and Ti L_{2,3}-edge spectra (see Fig. 24.b and c, respectively) do not change significantly due to annealing as well and are both in good agreement with literature [151-153].

The peaks in the O K-edge spectra can be assigned to electron transitions from the O(1s) level into O(2p) orbitals hybridized with Ti(3d) orbitals at 532.2 and 534.6 eV, Sr(4d) orbitals at 537.2 and 538.9 eV, and Sr(5p) orbitals at 544.7 eV [151]. The Ti L_{2,3}-edge spectra show as expected two pre peaks [154] and splitting into t_{2g} and e_g levels of the L₃ edge (at 459.0 and 461.3 eV) and the L₂ edge (at 464.4 and 466.8 eV) [153, 154]. The results obtained for total electron yield for Fe L_{2,3} are discussed in section 3.6.4.

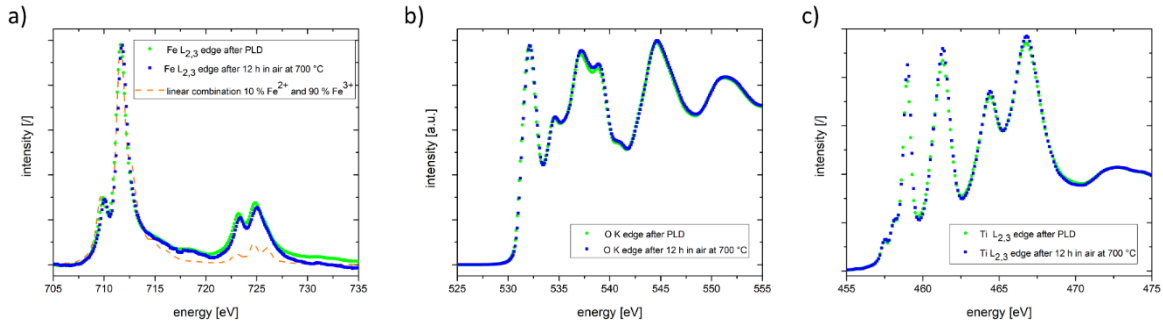


Fig. 24: XAS measurements in fluorescence mode showing the Fe L_{2,3}-edge(a), O K-edge (b), and Ti L_{2,3}-edge of Fe:SrTiO₃ thin films deposited from a stoichiometric target with 2 % Fe directly after the pulsed laser deposition (green dots) and after an additional annealing step at 700 °C in air for 12 h (blue squares). A linear combination of 10 % Fe²⁺ and 90 % Fe³⁺ (orange dashed line) matches the experimental data best.

3.4. Discussion

3.4.1. Basic Model

Based on all these results we can now suggest and discuss a model that explains the pseudo-intrinsic behavior of SrTiO₃ thin films and also the surprising robustness of this effect, occurring for Fe:SrTiO₃ with Fe contents from 0.4 to 10 %, for Ni:SrTiO₃ and Al:SrTiO₃, and even for undoped SrTiO₃. Also p(O₂) variations did not change conductivities between 10⁻⁵ and 1 bar. Essentially, we have to explain why the Fermi level is pinned very close to the mid gap energy in all these cases.

We start the model discussion with the truly intrinsic case with Fermi level mid gap and negligible oxygen vacancy concentration, see Fig. 25.a, where CB denotes the conduction band and VB denotes the valance band. This would require ultrapure SrTiO₃ films with impurity levels in the

sub ppb range since, at 420 °C, for example, $c_h = c_e$ values are as low as 10^{-11} cm^{-3} . Such a purification of the films during deposition completely contradicts the chemical analysis. Adding an acceptor doping shifts the Fermi level towards the valence band (Fig. 25.b). The acceptor dopants used in this study (Fe, Ni, Al) are known to act as deep traps for holes and thus the Fermi-level is below the acceptor level and quite far from mid-gap. (Please note: In this first consideration we neglect that oxygen vacancies are also formed by acceptor doping of SrTiO_3 , this is further discussed below). Adding a donor dopant to the system shifts the Fermi level upwards, but only for a very specific donor concentration the acceptors are exactly counter-balanced and a mid-gap situation is met, Fig. 25.c. This case can also be excluded here due to the robustness of the effect. Combining acceptor-type mid-gap states and the main acceptor doping does also not explain the situation. This would leave the Fermi-level far from mid-gap (Fig. 25.d). However, a very robust mid-gap situation results when combining acceptors, mid-gap acceptors and donors (Fig. 25.e). For a comparatively broad range of concentration ratios, this indeed pins the Fermi level close to mid-gap, see below. A similar three level model was also discussed for semi-insulating GaAs with Cr impurities [155]. Actually, acceptor 1 is even not required; already mid-gap acceptor states and a donor are sufficient to get a Fermi level pinning.

This model has a simple chemical analogy. Ultrapure water exhibits a pH value of 7. Adding a (weak) acid lowers the pH value (corresponding to our acceptor case causing positive holes). When adding NaOH solution the pH raises and for a very specific amount of NaOH the pH of the aqueous solution might be 7 (see Fig. 28). However, the slightest deviation from this specific amount either leads to acidic or alkaline solutions, respectively. When adding another acid with a pK_s value of seven to the first acid (instead of adding NaOH), the pH value becomes even slightly lower than before. However, for a solution with weak acid one (= acceptor doping in our case) and weak acid two (with $pK_s = 7$, corresponding to the acceptor with mid-gap states here), we can “activate” the $pK_s = 7$ buffer system with a proper amount of NaOH. (The proper amount is approximately the amount of acid one plus half the amount of acid two). Accordingly, the pH-value is pinned around $\text{pH} = 7$. This also works without acid one and also with further acids and is a very robust pinning situation.

Accordingly, we have a basic model for explaining the pseudo-intrinsic behavior of SrTiO_3 (or, in our analogy, $\text{pH} = 7$ in water despite adding substantial amounts of acids and bases). The identity of acceptor 1 in our doped SrTiO_3 samples is obvious, it is either Fe, Ni, or Al. In undoped SrTiO_3 we do not have to bother about it since the mid-gap pinning does not require such acceptor dopants,

provided mid gap acceptor states and donors are present. In the following, we discuss what may lead to the two essential states in our pseudo-intrinsic SrTiO₃ thin films, the acceptor-type mid-gap states and the donor states.

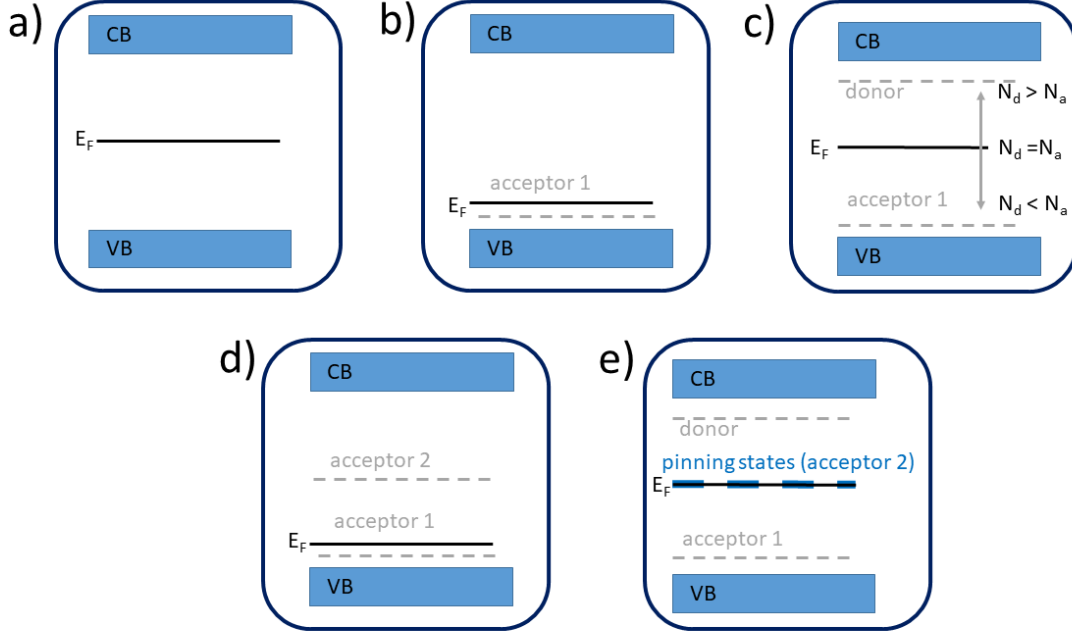


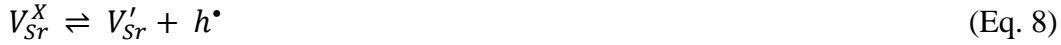
Fig. 25: Band structure of SrTiO₃ for different cases. In (a), the Fermi level is mid gap, corresponding to intrinsic concentrations in a semiconductor. This is the hypothetical case of ultra-pure, defect-free, stoichiometric SrTiO₃. With the introduction of acceptor states (acceptor 1), the Fermi energy is adjusted accordingly (b). With both acceptor and donor dopants present, the Fermi level shifts. For exactly equal amounts of acceptor and donor states, the Fermi level is mid gap (c). When the acceptor/donor ratio differs from unity, the Fermi level moves to the more dominant state. Hence, the Fermi level is not pinned mid-gap in a robust manner. If instead of the donor in (c) a mid-gap acceptor (acceptor 2) is added, the Fermi level is mostly dominated by the acceptor 1 states (d). In (e), both acceptor (acceptor 1), donor and mid-gap states (acceptor 2) are present, allowing robust mid-gap Fermi level pinning.

3.4.2. Specific states relevant in our SrTiO₃ films

First, mid-gap states are considered. Elemental analysis (ICP-OES, RBS), structural analysis (RSM) as well as defect analysis (PALS) point towards Sr (or A-site) vacancies as a common feature present in all doped as well as undoped SrTiO₃ thin films. Such Sr-vacancies act as acceptors in SrTiO₃ and lead to electron holes. (Partial counter-balancing by oxygen vacancies is neglected at this stage, see below). We assume that the energy of the first hole trapping

$$V'_{Sr} \cong V''_{Sr} + h^\bullet \quad (\text{Eq. 7})$$

is mid-gap while the second hole trap



is rather shallow [107]. Interestingly, such a midgap energy of Sr vacancies was already suggested in Ref. [30], even though there it was an assumption without experimental evidence given. The latter reaction thus simply adds further holes to those created by other acceptors dopants such as Fe. The formation of V_{Sr}' by a hole trapping of V_{Sr}'' , however, can pin the Fermi level in the mid gap range. Please note, that the supposed mid-gap energy of the Sr-vacancy is accidental and can be different in other perovskite-type titanates. Hence, such a pseudo-intrinsic behavior might also be peculiar for SrTiO₃, while in other titanates the “buffered” conductivity could be different.

Second, we have to consider possible donor states. As mentioned before, partial occupation of the A-site by typical B-site cations is a realistic option. In literature, a redistribution of Mn to A-sites was experimentally found [111, 150, 156-158] and changes in the site occupation were also suggested for Cr [117], Er [118] and Rh [120, 121]. Moreover, such changes in site occupation are discussed in other perovskite type titanates, e.g. Mg [159], Eu [160, 161] or Y [162] in BaTiO₃, Mn [163] in CaTiO₃ and Al [164] in (Na,Bi)TiO₃. The XSW measurements reported above indicated significant amounts of Fe on the A-site.

A site change of Fe leads to a change of its dopant character, with Fe at the A-site being a donor dopant according to



Owing to the larger ionic radius of Fe²⁺ (*i. e.* Fe_{Sr}^x) compared to Fe³⁺ the corresponding trapping energy of Eq. 3 might be substantial and the corresponding energy level can be expected far below the conduction band. However, as long as the corresponding level is above mid-gap this site change would not only reduce the energetically unfavorable Sr vacancy concentration but would also introduce the supposed donor state to activate the mid-gap Fermi level pinning. The XSW measurements (see Fig. 23) and XAS measurements (see Fig. 24) might give a first clue to the position of the A-site Fe donor states. From the XAS study we can estimate about 10 % Fe²⁺ and 90 % Fe³⁺, after annealing in air. The XSW measurements indicate that about one third of the Fe is at the A-site. Evidently, all of Fe²⁺ is attributed to the A-site, the rest of the Fe at the A-site is thus in the Fe³⁺ state, resulting in a mixture of one third Fe²⁺ and two thirds Fe³⁺ at the A-site. This mixture in oxidation state tells us that the corresponding Fe donor states at the A-site are just slightly above the Fermi level (which must be mid-gap according to conductivity measurements), see Fig. 26. This estimate is certainly prone to some errors and also a very deep Fe_{Sr}^x level beneath

mid-gap is conceivable. However, existence of Fe^{2+} despite mid-gap Fermi level pinning excludes that the Fe_{Sr}^X level is far below mid-gap and possibly this is not the donor states we are looking for in our model. Below we detail the amounts of Fe required on the A-site to explain the pinning.

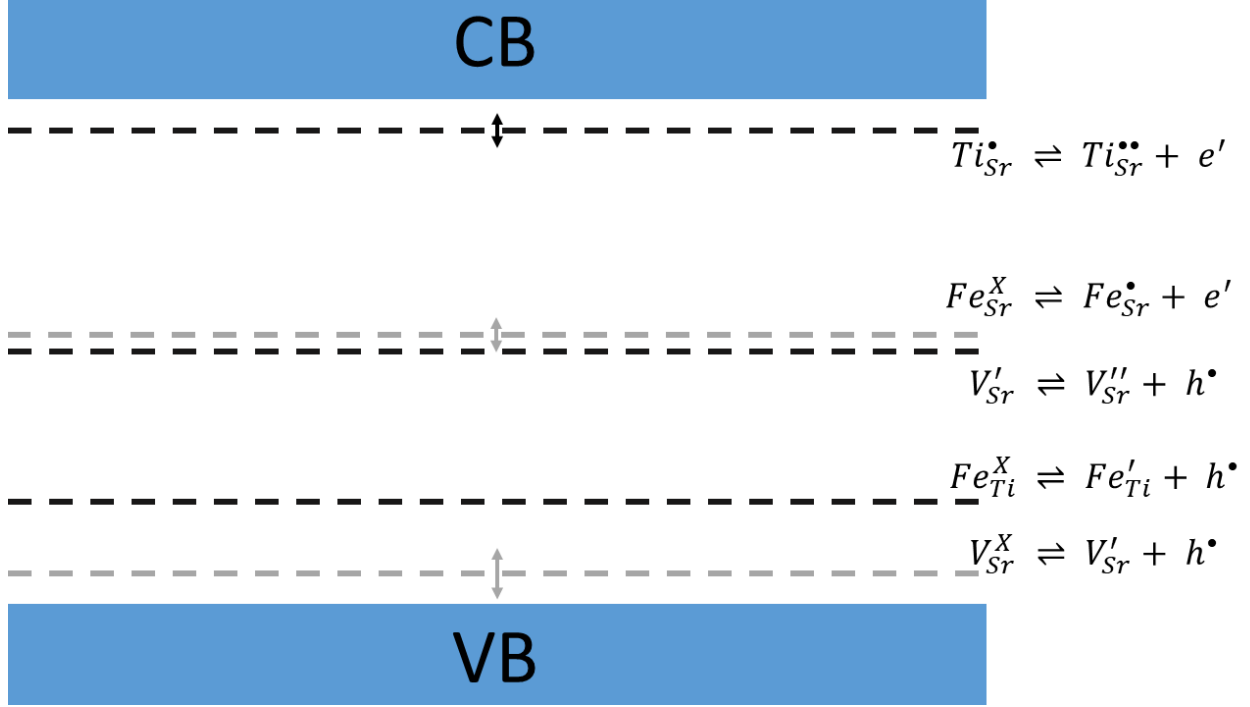


Fig. 26: Suggested band structure of our pseudo-intrinsic $Fe:SrTiO_3$ thin films. Fe at the B-site ($Fe_{Ti}^{\bullet}/Fe_{Ti}^X$) works as an acceptor (black). We suggest V_{Sr}'/V_{Sr}'' states in the middle of the band gap (black). Site changes caused by Sr vacancies lead to donor states. Most important is Ti on the A-site, $Ti_{Sr}^{\bullet\bullet}/Ti_{Sr}^{\bullet}$, corresponding to shallow donor states. The levels corresponding to Fe_{Sr} defects are deep donors, slightly above mid-gap. Sr vacancies also act as acceptor states close to the conduction band (V_{Sr}'/V_{Sr}^X). For the states with an donor, the position of the respective states in the band-gap is only a first estimate; our model does not depend on their exact position (within a certain range).

Similarly, also for other acceptor dopants a site redistribution can lead to the presence of additional electronic states (e.g. Ni on A-sites), which may or may not act as the required donor states [34]. Moreover, also the pseudo-intrinsic behavior of undoped $SrTiO_3$ has to be explained.

Hence we suggest Ti on A-sites as the decisive donor which is present in all our different films. Those were observed experimentally and predicted theoretically [104-106, 122, 165] and can act as a donor according to

$$Ti_{Sr}^{\bullet} \rightleftharpoons Ti_{Sr}^{\bullet\bullet} + e' \quad (\text{Eq. 10})$$

which we suppose to be distinctly above mid-gap, perhaps even close to the conduction band. This

is also sketched in Fig. 26. Accordingly, already the existence of A-site vacancies and Ti ions on A-sites can explain the pseudo-intrinsic behavior. Additional dopants such as Fe then add further states depending on their site, but don not change the essential defect, i.e. the pseudo-intrinsic conductivity. Accordingly, for all nominally acceptor-doped SrTiO₃ thin films as well as for the undoped films we observe Fermi level pinning in the mid gap and thus with ultra-low conductivity. So far we neglected oxygen vacancies, even though it is known that their concentration can be substantial in acceptor-doped materials [166, 167]. Those may serve as donor dopants. However, SrTiO₃ bulk defect chemistry models [29] suggest that for electronically intrinsic thin films (i.e. low c_h), the oxygen vacancy concentration is also very low due to the mass action law

$$K = \frac{[h^*]^2}{[V_O^{**}]\sqrt{pO_2}} \quad (\text{Eq. 11})$$

of the oxygen incorporation reaction



Hence, neglecting free oxygen vacancies in our model seems to be justified. Indeed, ionic conductivities are very low in low Fe-doped SrTiO₃ thin films, but increase for higher doping concentrations [142]. Reasons behind this dopant dependence of the ionic conductivity in otherwise electronically pseudo-intrinsic films are not known yet.

Defect associates may further modify the picture sketched. With Sr vacancy concentrations in the percentage range, defect interaction between negatively charged Sr vacancies and positively charged oxygen vacancies are not only possible, but rather likely [31, 123]. Also dopant vacancy interaction can be expected [168, 169]. Such a defect interaction may increase the total oxygen vacancy concentration compared to that of Eq. 11. However, the general model suggested here for explaining the pseudo-intrinsic behavior (acceptor-type mid-gap species based on Sr-vacancies and additional donor due to B-site cations on A-sites) is not affected by these complications.

Our model explaining pseudo-intrinsic behavior does not need a specific donor (e.g Ti on A-sites) and thus even nominally donor-doped SrTiO₃ thin films with A-site deficiency might exhibit such a behavior. Indeed measurements on such films (deposited from targets with 0.4 % Nb doping) lead to very low conductivities, see section 3.6.1, even though somewhat higher than the pseudo-intrinsic case. Possibly the added donor (Nb) drives the Sr vacancy buffer states to almost complete filling (V_{Sr}^X) and thus the Fermi level begins to leave the pinned mid-gap position.

Moreover, we expect a similar effect to be present also in other thin films of large band gap materials which are prone to some cation nonstoichiometry due to the preparation process, e.g.

PLD. The resulting cation vacancies may trigger some site changes and thus already all states are present that may lead to Fermi level pinning at a position far from what is expected from the deliberate doping. However, in general, this position is not expected to be mid-gap and thus even if a doping insensitive conductivity may be reached this is probably not the pseudo-intrinsic case present here.

This model is also in accordance with the experimental fact that bulk like conductivity can be reached in SrTiO₃ thin films by using PLD targets with a rather pronounced Sr overstoichiometry (of about 7 %) [142]. Such thin films are stoichiometric and show V_{Ti}V_O clusters as predominant point defects while no Sr vacancies being present. Thus, the Fermi energy is defined by the Fe_{Ti} acceptor level and indeed the hole conductivity expected from Fe doped samples is obtained.

3.4.3. Model calculations for testing the consistency

So far, we discussed that in a system consisting of donor states ($Ti_{Sr}^{\bullet\bullet}/Ti_{Sr}^{\bullet}$ in our case) and buffering mid-gap acceptor states (V_{Sr}'/V_{Sr}^X in our case) the Fermi level can be pinned to the intrinsic point (i.e. mid-gap). By the following estimates and calculations, we show that this pinning situation is quite robust with respect to changes in the acceptor/donor ratio.

Before we discuss the consistency of the model in more detail, particularly with respect to calculations pertaining to our Fe:SrTiO₃ films, we briefly consider some general estimations about this buffer system. In order to be effective, the concentration of mid-gap buffer (i.e. Sr vacancies) needs to be higher than those of other dopants with possibly varying ionization, e.g. that of Fe acceptor doping on the B-site. Thus, up to a few percent of Sr vacancies are required, at least in the highly Fe-doped films. Furthermore, the amount of acceptor and donor doping must be in the same concentration range. More specific, an ideal buffer situation is met if all Sr vacancies trap on hole, 50 % Sr vacancies trap a second hole and all other acceptors (here Fe on the B-site) are filled by holes. The ideal singly charged donor concentration thus is 1.5 times the amount of Sr-vacancies plus the amount of Fe-dopant on the B-site. Any deviation from such an ideal 1:1 ratio between acceptor and donor dopant is then balanced by a (slight) shift of the Sr vacancy ionization between V_{Sr}' and V_{Sr}'' and thus the electron and hole concentrations remain close to intrinsic levels (i.e. like in a chemical buffer). Thus, it is not required to have exactly fitting concentrations of donor states (e.g. Ti on A-site) or Sr-vacancies for reaching pseudo-intrinsic conductivity.

Tab. 7: Energy levels of electronic states in Fe:SrTiO₃ at 673 K used for calculating defect concentrations and testing the consistency of our model. Energy levels are given in units of the band gap E_g, relative to the upper valence band edge, and equilibrium constants K_i are given in defects per unit cells (UC). The exact values of the guessed energy levels don not affect the outcome of the calculation as long as they are comparatively close to the band edges

Reaction	Mass action law	Energy level	Equilibrium constant K _i (/UC)	Value obtained from:
$V'_{Sr} \rightleftharpoons V''_{Sr} + h^\bullet$	$K_1 = \frac{[V''_{Sr}] \times [h^\bullet]}{[V'_{Sr}]}$	E _g × 0.5	2.4 × 10 ⁻¹²	this study
$V^x_{Sr} \rightleftharpoons V'_{Sr} + h^\bullet$	$K_2 = \frac{[V'_{Sr}] \times [h^\bullet]}{[V^x_{Sr}]}$	E _g × 0.1	4.7 × 10 ⁻⁰³	guessed
$Fe^\bullet_{Sr} \rightleftharpoons Fe^x_{Sr} + h^\bullet$	$K_3 = \frac{[Fe^x_{Sr}] \times [h^\bullet]}{[Fe^\bullet_{Sr}]}$	E _g × 0.513	1.2 × 10 ⁻¹²	this study
$Ti^\bullet_{Sr} \rightleftharpoons Ti^{\bullet\bullet}_{Sr} + e'$	$K_4 = \frac{[Ti^{\bullet\bullet}_{Sr}] \times [e']}{[Ti^\bullet_{Sr}]}$	E _g × 0.9	4.7 × 10 ⁻³	guessed
$Fe^x_{Ti} \rightleftharpoons Fe'_{Ti} + h^\bullet$	$K_5 = \frac{[Fe'_{Ti}] \times [h^\bullet]}{[Fe^x_{Ti}]}$	E _g × 0.357	1.76 × 10 ⁻⁸	Ref. [29]

In the following, we further quantify this model for exemplary cases in order to show that it explains the robustness of the pseudo-intrinsic behavior of our films with respect to changes of acceptor or donor concentrations and oxygen partial pressure. For our specific Fe-doped thin films yielding “pseudo-intrinsic” conductivity we numerically calculated the defect concentrations as function of oxygen partial pressure and donor doping concentration (from any source, e.g. originating from the change in site occupation of Ti). Assuming chemical equilibrium, the defect chemical reactions listed above (see Eq. 7-10 and Eq. 12) and the hole trapping of Fe on the B-site can be described by mass action laws. The corresponding equilibrium constants are either known from literature [29, 30] or have to be estimated. Specifically, we assume the electronic energy levels and corresponding equilibrium constants listed in Tab. 2. Furthermore, we have to estimate the amount of Sr vacancies as well as Fe and Ti on the A-site. Here, we restrict our considerations to values that are in agreement with both the elemental composition determined by ICP-OES (see Tab. 6) as well as the ratio of A-site Fe suggested by XSW measurements (i.e. approx. one third Fe at A-site, see Fig. 23), both available for the thin films deposited from a target with 2 % Fe, and

having a true composition of $\text{Sr}_{0.945}\text{Ti}_{1.020}\text{Fe}_{0.035}\text{O}_{3-\delta}$ (assuming two cations per formula unit, see Tab. 6). In this case, only one degree of freedom remains, which is the amount of Ti at the A-site. For oxygen partial pressure dependent calculations, we chose an amount that maximizes the buffer effect (cf. Fig. 27.a). However, as we show below in Fig. 27.b, the effect is rather robust with respect to the amount of Ti at the A-site and also holds true for deviating acceptor/donor ratios.

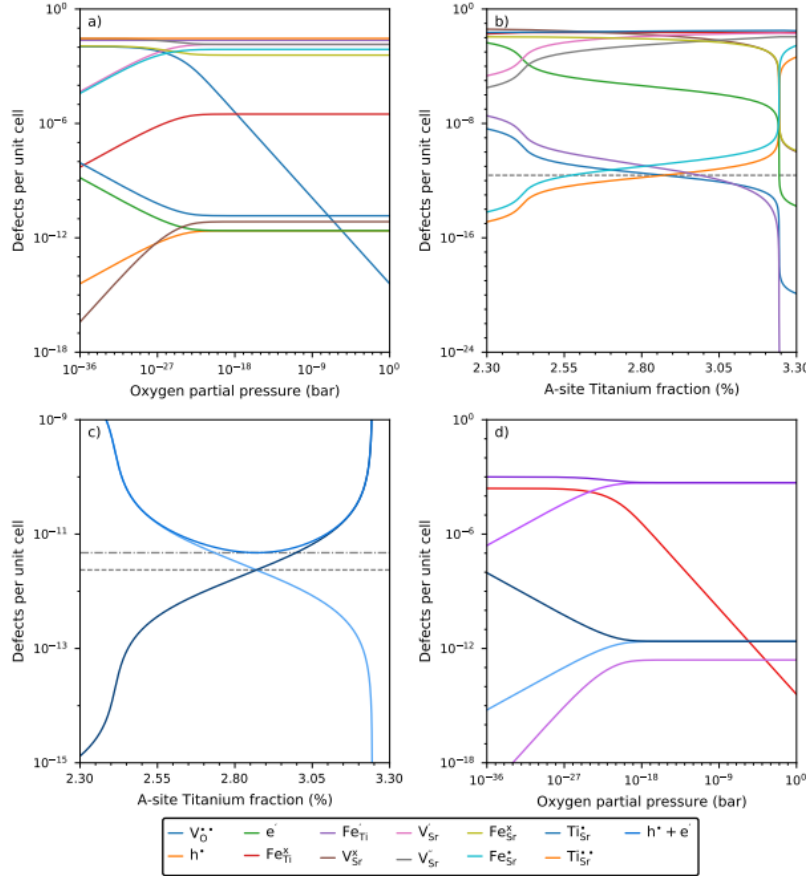


Fig. 27: Defect chemical calculations. (a) A Brouwer diagram for Sr deficient $\text{Fe}:\text{SrTiO}_3$ is shown, including partial A-site occupation by $\text{Fe}^{2+}/\text{Fe}^{3+}$ and $\text{Ti}^{3+}/\text{Ti}^{4+}$, with the site dependent chemical formula $(\text{Sr}_{0.937}\text{Ti}_{1.0287}\text{Fe}_{0.0115})(\text{Ti}_{0.977}\text{Fe}_{0.023})\text{O}_{3-\delta}$. (b) The defect concentrations are plotted as a function of A-site occupation by Ti, constrained to the elemental composition determined by ICP-OES. (c) A magnification of (b) for electrons, holes and total electronic charge carriers. The dashed lines indicate the intrinsic concentrations of electrons/holes and total electronic charge carriers respectively. (d) A Brouwer diagram for Sr deficient (0.1 %) SrTiO_3 with 0.075 % Ti on A-site.

For the calculations in Fig. 27.a, we assume 2.8 % Sr vacancies, as well as 1.15 % Fe and 2.87 % Ti on the A-site, i.e. a formula unit of $(\text{Sr}_{0.937}\text{Ti}_{1.0287}\text{Fe}_{0.0115}\text{V}_{\text{Sr} 0.028})(\text{Ti}_{0.977}\text{Fe}_{0.023})\text{O}_{3-\delta}$, with the

chemical formula in each bracket denoting the composition on A- or B-site, respectively. The resulting Brouwer diagram for this composition at 673 K is shown in Fig. 27.a. Both electron and hole concentration remain at intrinsic levels over a wide oxygen partial pressure range, which is in full agreement with the oxygen partial pressure independent electronic conductivity measured on such Fe doped films (cf. Fig. 17.b).

Figure 27.b shows the defect concentrations at one bar oxygen as a function of the Ti amount on the A-site. Despite appreciable variation of the Ti amount at the A-site (and thus the net amount of donor doping), the concentration of electronic charge carriers stays close to the intrinsic level, see also Fig. 27.c, where also the sum of electrons and holes, i.e. of mobile charge carriers, is shown. Here, we directly see the Sr vacancy buffer in action. Without such a buffer, intrinsic electronic charge carrier concentrations are only obtained if the concentration of donor and acceptor dopants is almost identical. By contrast, with such a buffer, the A-site Ti amount (and thus the net dopant concentration) can be varied between say 2.5 and 3.15 % without much conductivity change.

Lastly, nominally undoped SrTiO_3 is discussed in more detail. Sr vacancies occurring in this material lead to Sr vacancy acceptor states [107] as well as Sr vacancy pinning states, while Ti at the A-site is considered to be the most probable donor doping state. Again, it has to be considered that not the total concentration of acceptor and donor dopants are relevant, but rather their relation. Thus, for very low amounts of acceptor impurities or Sr vacancies already traces of donor dopant might explain the Fermi level pinning. Fig. 27.d shows the Brouwer diagram for undoped SrTiO_3 with 0.1 % Sr vacancies. Again, the electron and hole concentrations are at an intrinsic level over a wide oxygen partial pressure range.

Interestingly, the amount of Ti transferred to the A-site seems to be never so large that almost all Sr-vacancies are filled, otherwise we would get donor doped SrTiO_3 thin films.

3.4.4. Chemical Analogue

Essentially, our model for explaining the pseudo-intrinsic state of SrTiO_3 thin films consists of a donor state (B-site ion on A-site), a mid-gap state which pins the Fermi level to the middle of the gap (Sr-vacancy), and a further acceptor-state from the Sr vacancies. This limits the conductivity to the intrinsic value despite partly very high dopant concentrations.

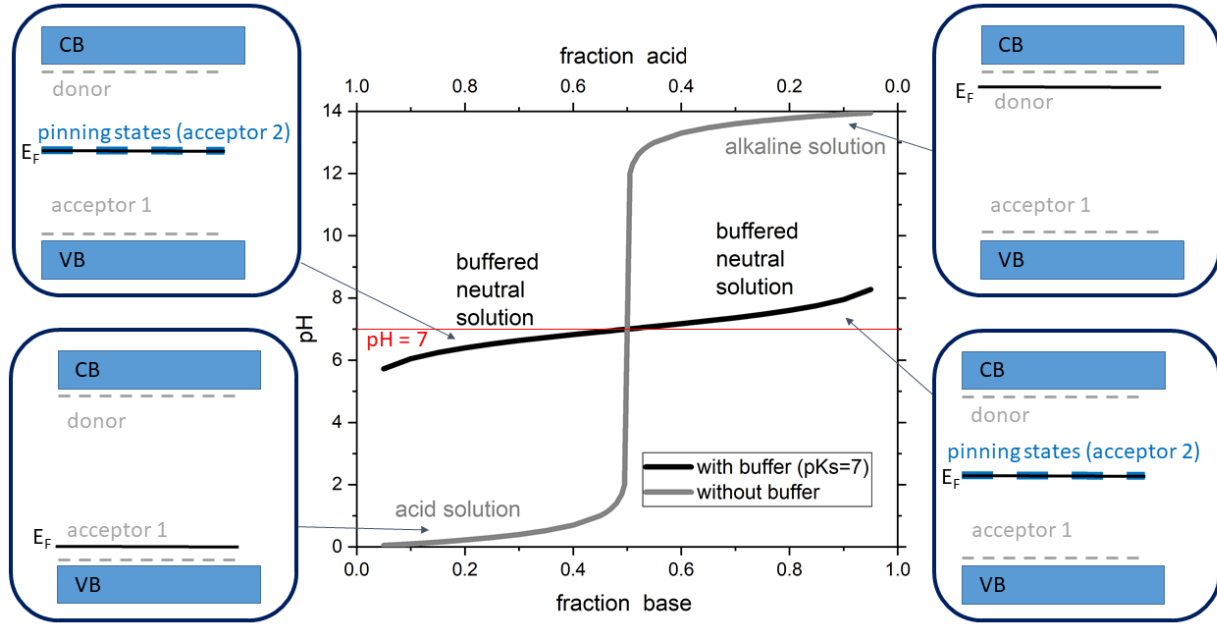


Fig. 28: Chemical analogy of the pinning effect. The pH of a buffered solution ($pK_s = 7$) in black is compared to a mixture of strong acid and base in gray. For the buffered solution, only slight deviation from 7 is observed, while the unbuffered solution ranges from strongly acid to slightly alkaline, exhibiting $pH = 7$ only for exactly the same amount of acid and base. This can be compared to the Fermi level pinning in our $SrTiO_3$. For systems consisting of only a donor and an acceptor, the Fermi level shifts between these two states. Additional mid-gap states, however, can help pin the Fermi level robustly to the middle of the gap.

A chemical analogy for a better understanding of such a system is sulphurous acid (H_2SO_3) with its two dissociation reactions (while omitting the sulfur dioxide formation at low pH values):



The pK_s of 7 corresponds to the “mid gap” state of the pH scale, the chemical reaction in Eq. 7 corresponds to Eq. 13, and Eq. 8 to Eq. 14, respectively. In such a system, four species might occur, H_2SO_3 , HSO_3^- , SO_3^{2-} (corresponding to the respective vacancy related defects V_{Sr}^X , V_{Sr}' and V_{Sr}'') and H^+ (corresponding to the mobile species h^*). When H_2SO_3 is added to water, it dissociates into H^+ and HSO_3^- (and partially further to H^+ and SO_3^{2-}), leading to an acidic solution. This is equivalent to the introduction of a neutral V_{Sr}^X to the crystal, leading to the formation of holes and negatively charged vacancies and thus a p-type material. When a base is added to the solution (e.g. NaOH), the sulfite buffer consisting of the HSO_3^-/SO_3^{2-} system starts to work, buffering the pH around 7 ($c(H^+) = c(OH^-)$) according to the Henderson-Hasselbalch equation in Eq. 15:

$$pH = pK_{S,2} + \log \left(\frac{[SO_3^{2-}]}{[HSO_3^-]} \right) \quad (\text{Eq. 15})$$

In this buffered solution, further addition of H^+ or OH^- shifts the ratio between HSO_3^-/SO_3^{2-} without significantly changing the pH (see Fig. 28). Similarly, the Sr vacancies lead to both acceptor states and mid gap pinning states. Upon introduction of an appropriate amount of donor, the Sr vacancy related “buffer” (V'_{Sr}/V''_{Sr}) is activated, leading to a mid-gap Fermi level pinning, which explains the intrinsic conductivity ($c_h = c_e$) and its robustness with respect to the specific concentrations of the donor and acceptor levels. This donor seems to be Ti on A-sites.

3.5 Conclusion

Intrinsic electronic conductivity ($c_e = c_h$) was found for differently doped (Fe, Ni, Al) $SrTiO_3$ thin films, a broad range of dopant concentrations, and also for nominally undoped $SrTiO_3$ thin films. Conductivities were several orders of magnitude lower than the corresponding bulk values. Thin film characterization revealed a substantial Sr vacancy concentration. Fe: $SrTiO_3$ thin films were further investigated by XAS and XSW, unraveling a redistribution of Fe towards the A-site of the perovskite. Based on these observations we developed a model explaining the very robust pseudo-intrinsic conductivity found in various $SrTiO_3$ thin films. Essential are Sr vacancies as acceptor-type mid-gap states and a donor dopant, which together pin the Fermi level in the middle of the gap. This is analogous to an aqueous system when adding a base to a weak acid of $pK_S = 7$, thus activating the corresponding buffer system and fixing the pH close to 7. Possible donor dopants present in our thin films are discussed and the main source of donors is believed to be B-site ions on A-sites, particularly Ti ions on A-sites. Accordingly, this effect of a dopant-independent conductivity may not only occur under very specific conditions, but could be rather ubiquitous and present in many other materials as well.

3.6 Supplementary Information:

3.6.1 Conductivity measurements for donor doped $SrTiO_3$

In Fig. 29, the conductivities of Nb: $SrTiO_3$ thin films deposited from targets with 0.3 % and 2 %

Nb are plotted. While the conductivities are not pseudo-intrinsic as the acceptor doped counterparts, the conductivities found for these donor doped samples are still far from bulk values. Here, donors outweigh the acceptor states (i.e. only cation vacancies), even exceeding the “buffer capacity” of the Sr vacancy based buffer system. Hence, an increase in conductivity (relative to the intrinsic conductivity found for acceptor doped thin films) is observed.

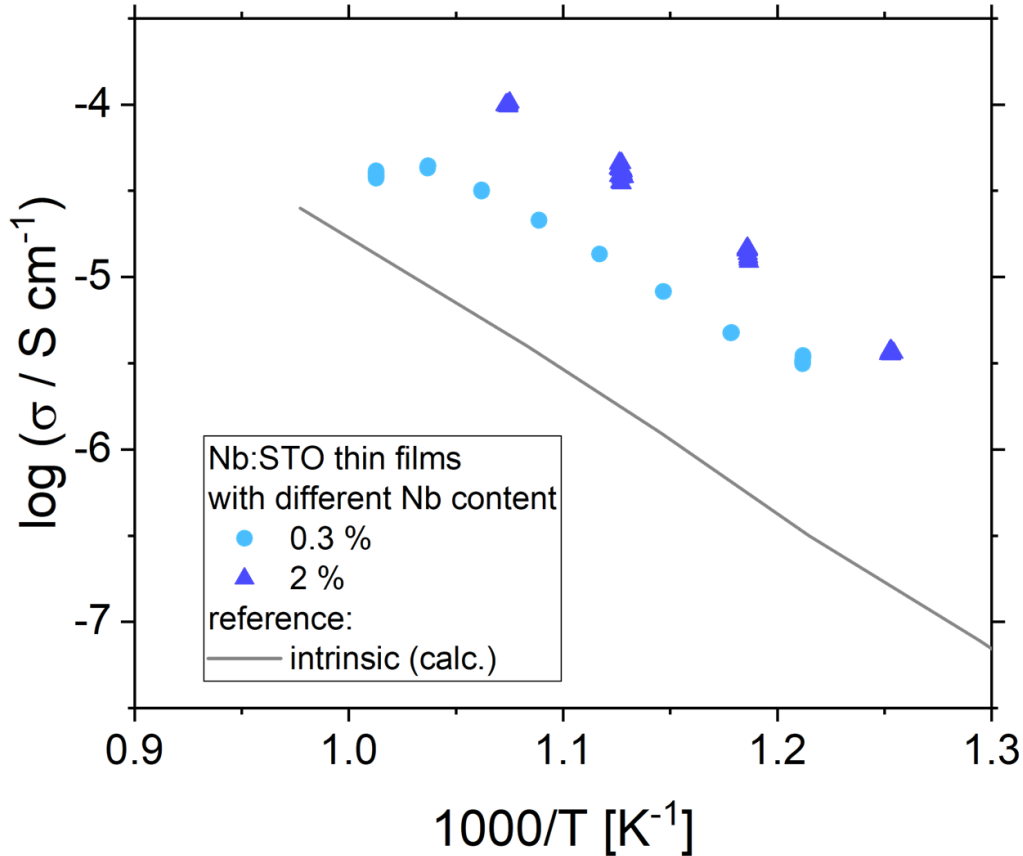


Figure 29: Conductivity measurements for donor doped SrTiO_3 , revealing an ultra-low conductivity close to the intrinsic values.

3.6.2 Reciprocal mapping of the (103) reflection

In all RSM measurements in Fig. 30, either only one for the Al:SrTiO₃ thin film (d) or two reflexes one directly below the other (at the same q_{\parallel} value) ((a),(b),(c),(e)) can be found. In the (103) direction the distance between the two reflexes becomes larger compared to the (002) direction. Thus, they are easier to distinguish. However, the sample Al:SrTiO₃ (d) still exhibits only one

reflex. These results confirm the findings of enlarged c cell parameters in the thin films (except for Al:SrTiO₃) compared to the single crystals.

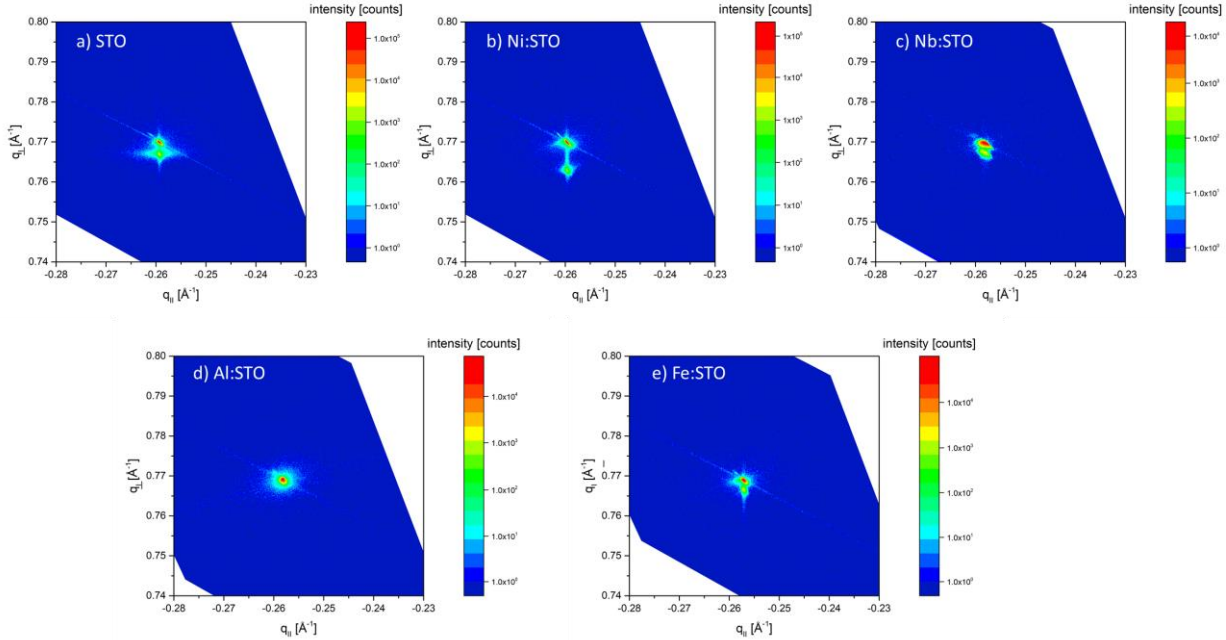


Figure 30: Reciprocal space maps of the (103) reflection for different thin films.

3.6.3 ICP-OES measurements

To determine the actual composition of the SrTiO₃ thin films, inductively coupled plasma-optical emission spectroscopy (ICP-OES) was used. Therefore, samples with about 100 nm film thickness were deposited on 5x5 mm² YSZ single crystals. These layers were dissolved in 5 mL of 3 % (v/v) nitric acid (65 mass%, EMSURE®) and 0.3 % (v/v) hydrofluoric acid (40 mass%, Suprapur®). The dissolving agent was prepared by mixing deionised water obtained by Barnstead™ Easypure™ II (18.2 M cm⁻¹), the concentrated acids and 1000 mg kg⁻¹ Eu single element standard (Certipure®, Merck, Germany). The final concentration of Eu was adjusted to 1 mg kg⁻¹ in the diluted acid mixture and was used as an internal standard to correct for possible signal drifts. After 30 min of dissolving time, the obtained sample liquid was transferred into a new polypropylene sample tube to remove the remaining substrate and to stop a possible dissolution process of the substrate. This whole process was conducted under ambient conditions at room temperature and

the derived sample solutions were measured without any further dilution.

For signal quantification, single element standards (for details see Table 2) were mixed with the diluted acid mixture (3 vol% HNO₃, 0.3 vol% HF) already containing the internal standard to perform an external calibration. Standard solutions with varying concentration levels from 0.2 to 12.6 mg kg⁻¹ for the main components Sr and Ti and 0.002 to 0.126 mg kg⁻¹ for the dopant elements (Fe, Ni, Nb, Al) were prepared. With the obtained signal intensities, regression lines were derived to calculate the analyte concentration of the unknown samples.

Table 8: Optimized ICP-OES parameters used for measurements.

RF power	1200 W
exposure time	10 s
nebulizer gas flow	0.75 L min ⁻¹ argon
type of nebulizer	MiraMist®
sample flow rate	0.7 mL min ⁻¹
pump tubing	Tygon®, 0.64 mm ID (color code: orange-yellow)
cooling gas flow	12 L min ⁻¹ argon
auxiliary gas flow	0.8 L min ⁻¹ argon
viewing height above load-coil	10 mm
Spectral range	Visible
Elements	Emission line [nm]
Sr	421.55*, 346.45, 216.60
Ti	334.45*, 232.45, 338.38
Fe	259.94, 238.20*, 240.49
Ni	341.48*, 221.65, 231.60
Nb	316.34*, 309.42
Al	396.15*, 309.27
Eu	381.97*, 412.97

Emission lines marked with * used for evaluation.

Samples and standards were analyzed with an iCAP 6500 ICP-OES spectrometer (ThermoFisher Scientific, Bremen, Germany) equipped with a MiraMist nebulizer and a cyclonic spray chamber (Glass Expansion, Port Melbourne, Australia). Sample-uptake was achieved with the peristaltic pump of the instrument (25 rpm, 0.64 mm ID pump tubing). Background-corrected emission signals were recorded in the radial viewing mode and processed using Qtegra software (Thermo Scientific, USA). Six replicates with an integration time of 10 s each were measured for samples as well as standard solutions. The optimized ICP-OES parameters and the monitored emission lines are summarized in Table 1. For each element several intense but non interfered emission lines were measured.

Observed signal intensities were normalized using the signal response for the internal standard (Eu), and finally converted into concentration units by means of the external calibration. By using the the molare masses of each element, the mole fractions of the cations present in the investiageted samples were calculated. Obtained Eu signals were constant over each measurement session (less than 5% relative standard deviation for the whole measurement period, indicating the absence of temporal trends), and no significant difference in Eu-response between samples and calibration standards was observed.

Table 9: Single element standards used for signal quantification.

Element	Product information, lot number		Concentration levels for calibration [mg kg⁻¹]
Sr	Certipure®, Merck, Germany	HC87301854	0.2, 0.4, 0.8, 1.6, 3.2, 6.4,
Ti		HC99678363	12.8
Fe		HC86803426	0.002, 0.004, 0.008,
Ni		HC90700236	
Nb		HC398664	0.016, 0.032, 0.064,
Al		HC42545101	0.128
Eu		Specpure®, Alfa Aesar, Germany	35753

3.6.4 XAS measurements for total electron yield

Here, the Fe:SrTiO₃ thin film is investigated by XAS using the total electron yield (see Fig. 31).

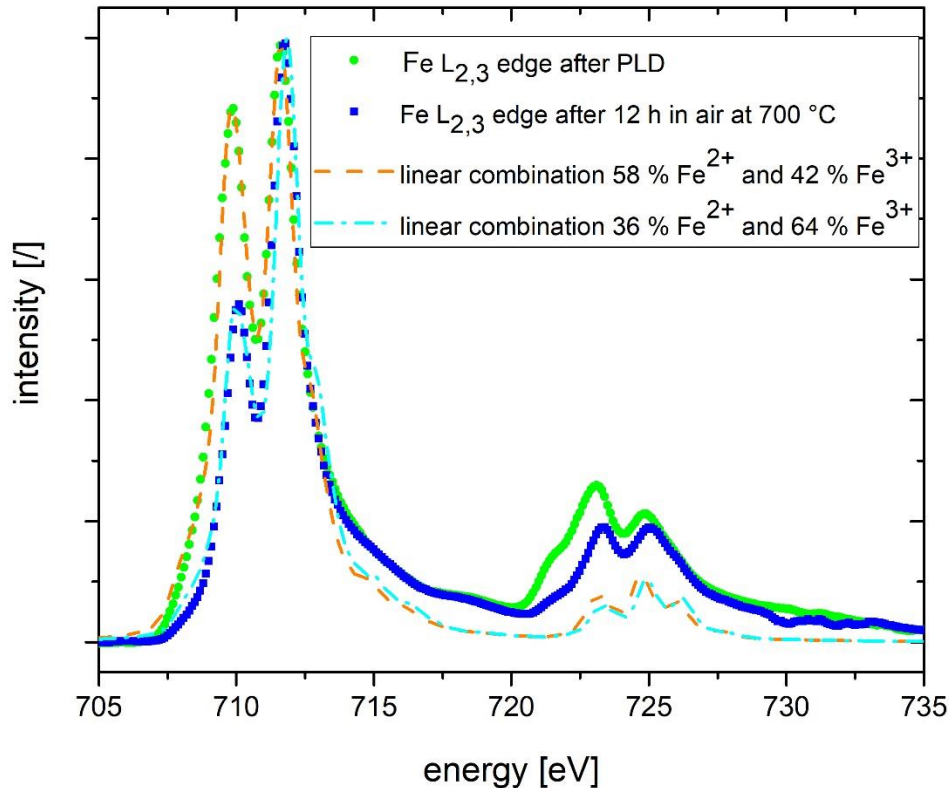


Figure 11: XAS measurements of the Fe L_{2,3}-edge of a Fe:SrTiO₃ thin film directly after the pulsed laser deposition (green dots) and after an additional annealing step at 700 °C in air for 12 h (blue squares). The spectra were recorded in the total electron yield. Near the surface, a significant amount of Fe²⁺ is present. Annealing in air leads to the oxidation of some of the Fe²⁺ to Fe³⁺, increasing the Fe³⁺ to Fe²⁺ ratio. This can be seen in the decrease in the peak at approx. 710 eV (and a shift by 0.2 eV).

At first, we want to focus on the sample measured directly after the PLD process. The peak at approx. 710 eV (attributed to Fe²⁺ states) is strongly increased compared to the spectra measured in the fluorescence yield mode (cf. Fig. 24.a in the main part)). Consequently, we believe that the amount of Fe²⁺ is increased near the surface (measured via total electron yield) compared to the bulk value (obtained via fluorescence yield). Here, it seems that the surface is more reduced than the respective bulk. Furthermore, such changes might be attributed to the space charge region,

which is in the range of a couple of nm, which fits rather well to the information depth of the total electron yield mode. After annealing the Fe:SrTiO₃ thin film for 12 h in air at 700 °C, the X-ray absorption spectra (in total electron yield) is shifted by nearly 0.2 eV and the first peak becomes smaller, which corresponds to a partial oxidation of Fe²⁺ to Fe³⁺. Calculated spectra fit best the experimental data in the lower energy region when 58 % (36 %) of the present Fe is assumed to be Fe²⁺ and 42 % (64 %) Fe³⁺ directly after the thin film deposition (after an additional annealing step respectively). No such change in oxidation state was observed for the bulk measured in fluorescence yield mode (cf. Fig. 24.a of our main contribution).

3.6.5 XAS simulation

In our main contribution, we discuss the shape of XAS spectra for different Fe oxidation states.

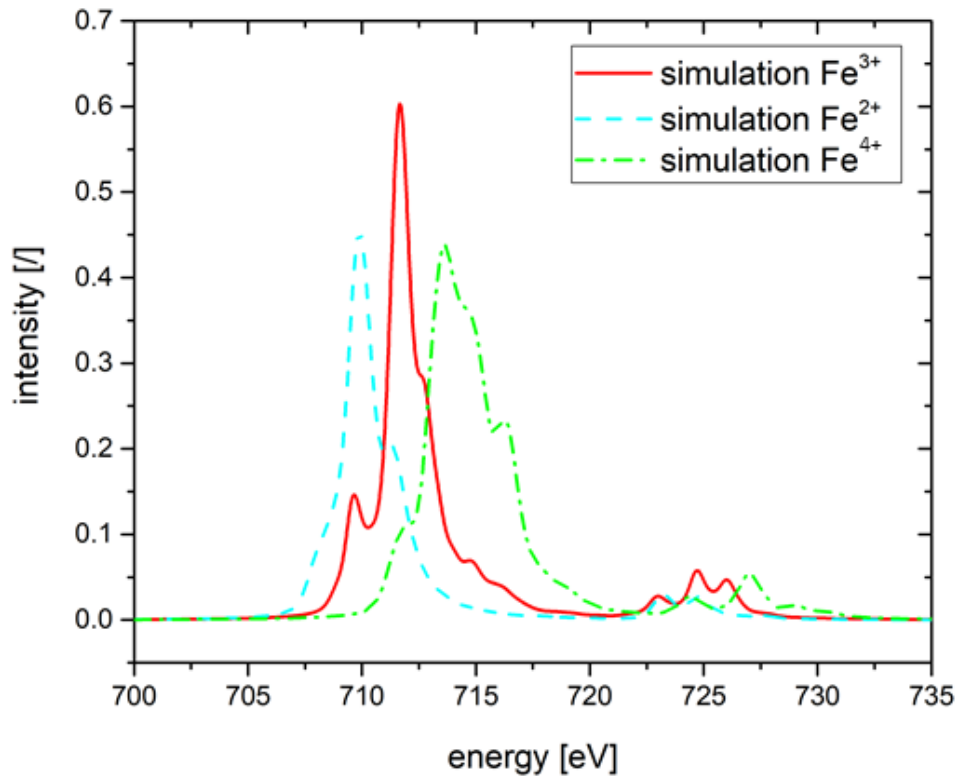


Figure 32: Simulation of Fe³⁺ (red line) and Fe²⁺ (cyan dashed line) as well as Fe⁴⁺ (green dashed line) X-ray absorption spectra at room temperature and in an octahedral symmetry.

In Fig. 32, simulated XAS spectra for the oxidation states of +2, +3 and +4 are shown. By comparison with Fig. 31 or Fig. 24, Fe^{2+} and Fe^{3+} describe the obtained spectra best.

Chapter 4: Cation nonstoichiometry in polycrystalline SrTiO₃ bulk: A different situation than in thin films?

This chapter is based on the diploma thesis written by Niklas Bodenmüller.

4.1 Introduction

SrTiO₃, a perovskite-type oxide, is a material relevant for different possible future applications, such as photoelectrochemical cells [13, 42], gas sensors [170, 171] or memristive devices [20, 21, 32, 54, 133, 134]. Defects are essential for the functionality in all these cases. In SrTiO₃, two different kinds of nonstoichiometry can be present, namely cation (i.e. Sr or Ti) nonstoichiometry or anion (i.e. oxygen) nonstoichiometry. In the densely packed perovskite structure, this nonstoichiometry refers to the formation of the respective vacancies rather than interstitials [34, 44]. Oxygen vacancies are introduced in the material due to partial pressure dependent oxygen release. This process is reversible (at sufficiently high temperatures to ensure proper kinetics), leading to oxygen uptake at higher oxygen partial pressures. Oxygen vacancies play an important role in resistive switching [21], stoichiometry polarization [172], UV induced color change [41] and photoelectrochemical processes [13, 42]. Cation vacancies can be formed due to Schottky disorder [34]. In the case of SrTiO₃, especially the partial Schottky reaction is important leading to the formation of SrO and Sr vacancies and oxygen vacancies [34]. Furthermore, cation deficiency (Sr as well as Ti deficiency) can also be introduced during the sample preparation, e.g. during thin film deposition [31, 48, 59, 60, 85]. Here, the overall cation imbalance is irreversible, leading either to cation vacancies present in the material or to the formation of secondary phases to accommodate the cation nonstoichiometry. The effect of cation vacancies on electrical properties is much less investigated compared to the effects of oxygen vacancies. In this study, we look into two different ways of affecting cation stoichiometry in bulk samples, namely deliberate cation nonstoichiometry introduced during preparation as well as Schottky disorder due to sintering at high temperatures.

4.2 Experimental

4.2.1 Pellet preparation

Nominally undoped or cation vacancy doped SrTiO₃ pellets were prepared with different Sr/Ti ratios using SrCO₃ (99.995 %, sigma Aldrich, USA) and TiO₂ (99.995 %, Alfa Aesar, USA). In comparison to thin films, bulk SrTiO₃ is known to accommodate only a slight cation nonstoichiometry. Thus, Sr/Ti ratios were prepared deviating by 0.5 % from unity. The starting materials were weight in, milled for 40 min by hand in an agate mortar and pressed isostatically for 10 min. Then the pellets were calcined in a corundum crucible at 1150 °C for 3 – 4 h, with an additional 1 h step at 400 °C during heating up. In order to avoid contaminations from the corundum, excess SrTiO₃ powders were placed in the corundum crucible as a sintering bed. The calcined samples were then milled again and pressed isostatically and subsequently sintered at 1500 °C for 12 h. Both oxidizing (air) and reducing (2.5 % H₂ in Ar) atmospheres were used for this sintering step. For better mechanical stability, this last sintering step was repeated. X-ray diffraction (XRD) measurements were carried out to confirm the phase purity of the obtained samples.

4.2.2 Single crystal preparation

SrTiO₃ single crystals in (100) orientation with dimensions of 10 mm x 10 mm and a thickness of 0.5 mm (Crystec, GER) were used in this study. For the sake of comparison with polycrystalline samples, the single crystals were sintered for 12 h in 1500 °C in air. For avoiding possible contaminations during this step (e.g. Al³⁺ from the corundum crucible), the investigated samples were placed on another SrTiO₃ single crystal. This heat treatment was then repeated twice.

4.2.3 Electrochemical impedance spectroscopy

Porous Pt electrodes were brushed on the polycrystalline SrTiO₃ bulk samples to enable good electrical contact. For electrochemical impedance measurements, a symmetrically heated measurement setup was used (see Ref. [76]). The samples were placed between two Pt sheets. The impedance measurements were carried out using a Novocontrol Alpha A High Performance

Frequency Analyzer (Novocontrol Technologies, GER) with a rms amplitude of 100 mV in the 0.9 MHz to 1 Hz frequency range with 10 points per frequency decade.

A general problem when measuring the conductivity of bulk samples is reaching the equilibrium state in order to obtain reproducible and well-defined results. At low temperatures, equilibration takes longer and longer and sometimes does not happen at practicable time scales. Therefore, the samples were equilibrated at 700 °C for at least 12 hours for polycrystals and up to 2 days for the single crystals. Impedance measurements were carried out at 700 °C. Subsequently, the samples were quenched to room temperature, i.e. only small deviation from equilibration at 700 °C should occur. At lower temperatures, the oxygen vacancy concentration should remain frozen in. Therefore, conductivity measurements can be performed without the need for long equilibration times. Impedance measurements were carried out between 200 °C to 400 °C with 25 °C steps.

4.3 Results and Discussion

4.3.1 Electrochemical characterization of polycrystals

A typical impedance spectrum of a polycrystalline SrTiO₃ bulk sample is shown for 280 °C (see Fig. 33.a). A small high-frequency semicircle and a large mid- to low-frequency semicircle can be seen, corresponding to grain and grain boundary, respectively. Two R-CPE (CPE = constant phase element) circuits in serial connection were used for fitting. In contrast, for the pellets sintered in reducing atmosphere only one highly distorted feature was visible at 280 °C (see Fig. 33.b), complicating the fitting process. For the sake of comparison, the same equivalent circuits as in the case for oxidizing sintering conditions were used. Taking the sample geometry into account, the conductivity is obtained from the corresponding resistance. In this work, only the grain conductivity is discussed. For more information on the conductivity of the grain boundary, see Ref. [173].

The temperature dependence of the grain conductivity for samples sintered in oxidizing atmosphere is plotted in Fig. 34.a between 144 °C to 370 °C. The activation energies are in the range of 0.91 to 0.97 eV, which is in line with literature data for undoped or acceptor doped SrTiO₃ [37, 39, 174, 175]. Compared to the nominal Sr/Ti ratio of unity, Sr understoichiometry increases the conductivity, while Sr overstoichiometry hardly changes the conductivity. Note that the nominal

Sr/Ti ratio differs from the “real” defect situation due to Schottky disorder and possible segregation at the grain boundaries, see below. From a defect chemical point of view, a higher influence of the titanium vacancy (V_{Ti}'''') is expected due to its higher charge, but is not found experimentally in this study. Similar findings are also reported in literature [174].

Upon a further sintering step for 24 h at 1500 °C in air, the conductivities increased. This is plotted for the sample with nominally ideal stoichiometry in Fig. 34.b. Interestingly, the differences in the conductivities for samples with different nominal Sr/Ti ratios vanished after this sintering step (see Fig 34.c). This is a good indication that the partial Schottky disorder, which readily occurs at a temperature of 1500 °C, becomes the dominant factor at these sintering temperatures, defining the defect chemistry of the material. Thereby, the partial Schottky reaction leads to a similar defect state in the investigated samples, changing their initial Sr/Ti ratio in the bulk. Activation energies were slightly lower than before, ranging from 0.88 to 0.92 eV.

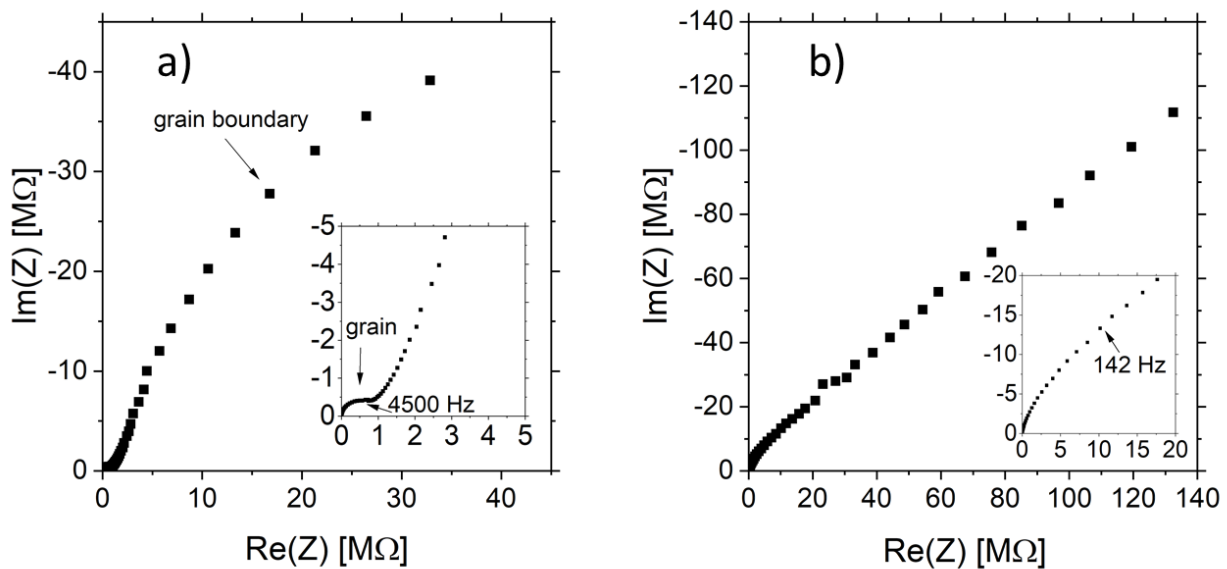


Fig. 33: Impedance spectra of $SrTiO_3$ pellet with a nominal Sr/Ti ratio of 1.000, sintered in air (a) or in 2.5 % H_2 in Ar (b) at 1500 °C. The pellet was equilibrated at 700 °C for 12 h, quenched to room temperature and then measured between 144 °C to 370 °C. The impedance spectrum plotted here were measured at 280 °C (a) and 274 °C (b), respectively. At high frequencies, the grain is visible as a shoulder (see magnification) and the much bigger low-frequency arc corresponds to the grain boundary of the $SrTiO_3$ pellet (a). In (b), the spectra is severely distorted and a separation of grain and grain boundary is challenging.

The Arrhenius plot for the conductivities of samples sintered in reducing atmosphere is shown in Fig. 34.d. A change in activation energy is visible in the range between 246 °C to 296 °C

(depending on the respective nominal Sr/Ti ratio). At higher temperatures, the activation energies are in the range of 0.91 to 1.07 eV. The conductivities of pellets sintered in reducing atmosphere are up to one order of magnitude lower compared with the samples sintered in oxidizing conditions. Again, the partial Schottky reaction discussed for oxidizing conditions might explain the enhanced conductivity observed in samples sintered in oxidizing conditions.

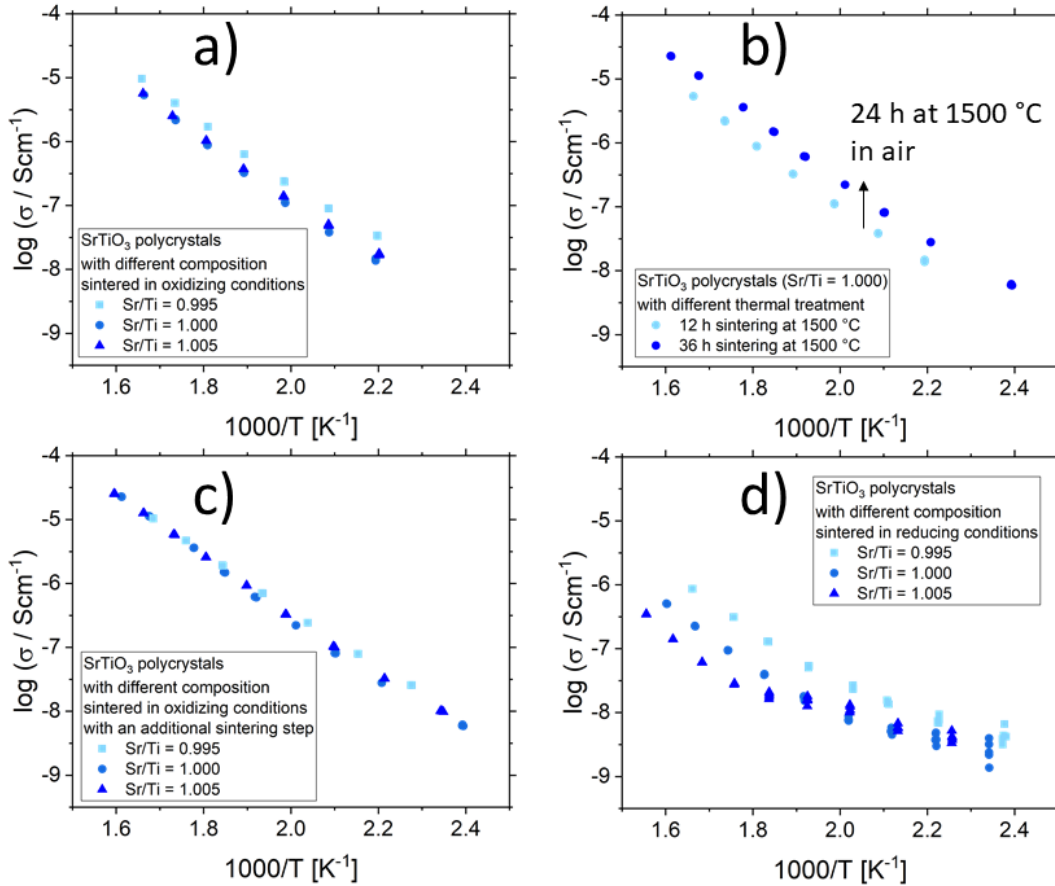


Fig. 34: Grain conductivities of SrTiO₃ polycrystals with different nominal composition, different thermal history and sintered in different atmospheres. In (a), grain conductivities of SrTiO₃ pellets sintered in air show only small differences for nominal cation nonstoichiometry. In (b), the influence of an additional sintering step for 24 h at 1500 °C in air is plotted and an increase in conductivity can be observed. This effect is attributed to the partial Schottky reaction, leading to Sr vacancies in SrTiO₃. In fact, the cation nonstoichiometry imposed via the partial Schottky disorder becomes the dominating factor for the defect chemistry of the material after this second sintering step (c). Here, the small differences in the conductivity from (a) vanish completely and no effect of the nominal composition can be seen. In contrast, sintering in reducing atmospheres does not enhance the partial Schottky reaction and the nominal composition has a stronger influence on the defect state of the material (d). Again, Sr vacancies are beneficial for the conductivity.

4.3.2 Comparison with single crystals

Here, nominally undoped and slightly acceptor doped SrTiO₃ single crystals (with Fe concentrations of 0.008 % and 0.08 %) are investigated in an “as pristine” state (i.e. as delivered by the manufacturer) as well as after one or two sintering steps at 1500 °C for 12 h in air. Due to the formation of cation vacancies occurring in oxidizing conditions, only oxidizing conditions were chosen for comparison here. Starting with nominally undoped SrTiO₃ single crystals, no increase in conductivity was observed for additional sintering steps (see Fig. 35.a). The conductivity of slightly Fe doped single crystals (with 0.016 % and 0.16 % Fe) in Fig. 35.b is higher than the corresponding conductivity of the nominally undoped SrTiO₃ single crystal. Again, no increase in conductivity is found after the high temperature treatment. The reason for this behavior deviating from polycrystals might be the different situation in terms of cation diffusion. In polycrystals, rather short diffusion paths are needed to reach the nearest grain-boundary or surface. Moreover, enhanced cation diffusion along grain boundaries was reported for other perovskite oxides [176]. This might lead to a faster establishing of Schottky disorder in polycrystals of absence of an equilibrium state of Schottky disorder in single crystals.

In Fig. 35.c, the conductivities of the different types of samples are compared. Here, the conductivity of the nominally undoped SrTiO₃ single crystal is well in line with the conductivity of the pellets sintered in reducing atmospheres. However, the conductivity for the polycrystalline samples sintered in air is significantly higher than the conductivity of the nominally undoped single crystal. The conductivities of the polycrystals sintered in air even exceeds the respective values of the slightly Fe doped single crystals. According to the above discussion, oxidizing sintering of polycrystals causes high Sr vacancy concentrations and those act as acceptor dopants here, increasing the conductivity similar to a deliberate acceptor dopant (see Fig. 36.a).

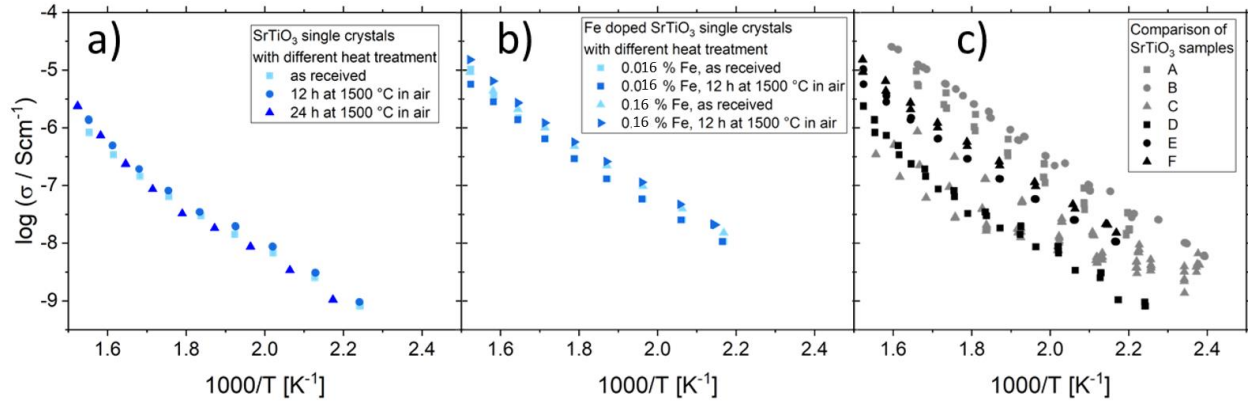


Fig. 35: Conductivity of nominally undoped and slightly Fe doped SrTiO_3 single crystals equilibrated at 700°C and quenched to room temperature. The conductivities measured at a nominally undoped SrTiO_3 single crystal in three different states is shown in (a). No change in conductivity is observed after heat treatments compared to the undefined state (in terms of defect chemistry) of the “as received” sample. Slightly higher conductivities are obtained for samples with 0.016 % and 0.16 % Fe doping (b). Again, no influence of heat treatment can be seen. In (c), the conductivities of different types of samples, e.g. single crystals and polycrystals with different thermal treatment and different sintering atmospheres, are compared (A – SrTiO_3 pellets with different nominal composition sintered in oxidizing atmosphere, B – pellets after an additional 24 h sintering step; C – pellets sintered in reducing atmospheres; D – SrTiO_3 single crystals with different heat treatment; E – 0.016 % Fe doped single crystal with different heat treatment; F – 0.16 % Fe doped single crystal with different heat treatment). Note that the conductivities of the pellets (gray) cover a range of two orders of magnitude and exhibit mostly a higher conductivity than the respective nominally undoped single crystals. Sr vacancy doped SrTiO_3 pellets even have a higher conductivity than slightly Fe doped SrTiO_3 single crystals.

4.3.3 Comparison with thin films

Thin film conductivities investigated in chapter 2 and chapter 3 were measured in another mode, i.e. equilibrium conductivities instead of measuring in a quenched state. Therefore, one cannot directly compare the total conductivity values for the respective temperatures. However, we observed that the impact of Sr vacancies in thin films and bulk is drastically different. As described in chapter 2 and chapter 3, Sr vacancies are considered as the key driver for electronically pseudo-intrinsic conductivity found in SrTiO_3 thin films. Here, Sr vacancies are beneficial for the conductivity of polycrystalline SrTiO_3 .

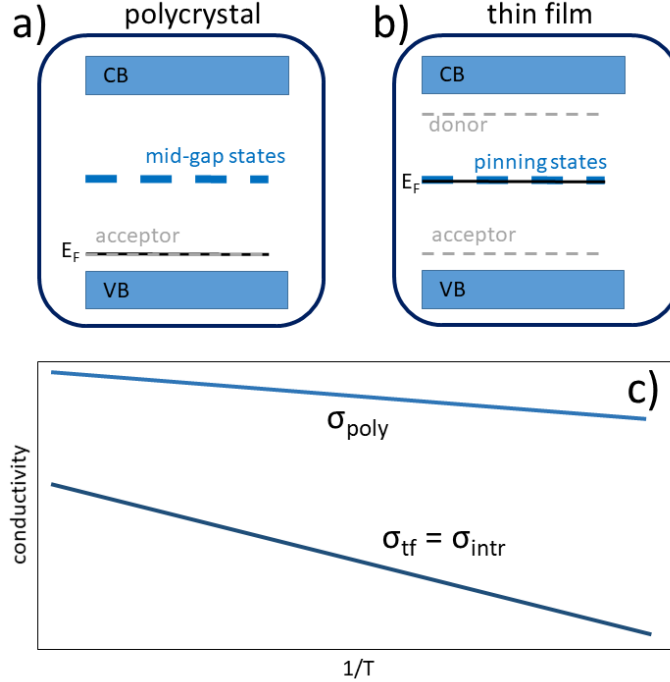


Fig. 36: Band structure of polycrystalline samples (a) and thin films from chapter 2 and chapter 3 (b) and the impact on the conductivity (c). In polycrystals, Sr vacancies lead to mid-gap and acceptor states (a), but without a donor present, no mid-gap Fermi level pinning occurs. Thus, the acceptor states dominate the material's defect chemistry, and a rather high conductivity results for polycrystals (σ_{poly}) in (c). In contrast, thin films also have donors present (e.g. antisite defects such as $Ti_{Sr}^{\bullet\bullet}$). In this case, the Sr vacancy related mid-gap states lead to a Fermi level pinning to the intrinsic state. Therefore, the conductivity of such thin films (σ_{tf}) matches the intrinsic electronic conductivity (σ_{intr}).

To solve this apparent contradiction, the different nonstoichiometry accommodation of thin films and polycrystalline sample has to be addressed: With Sr/Ti ratios of 0.9, thus massively exceeding equilibrium, antisite defects ($Ti_{Sr}^{\bullet\bullet}$) are likely in the thin film (see Fig. 35.b) and are reported for thin films in literature. In contrast, Sr vacancies in polycrystals in this study are most prominently introduced via Schottky disorder at high sintering temperatures and, thus, their concentration corresponds to the equilibrium values. Therefore, at these high temperatures, there is no need for antisite defects as a compensation mechanism. At lower temperatures, their concentration is frozen in. Therefore, the existence of Sr vacancies without antisite defects as compensation is expected in polycrystals, but not in thin films. This argument shows that donors in polycrystals might only come from impurities, but not due to effects in the material itself (as it happens in $SrTiO_3$ thin films with antisite defect donors). Without a donor, the Sr vacancy related mid-gap states cannot act as

a buffer. Therefore, in polycrystalline bulk samples, the Sr vacancy related acceptor states dominate, thus increasing the conductivity, see Fig. 36.c. To come back to the chemical analogy from Chapter 3, this equals the addition of sulphurous acid ($pK_{S,1} = 1.81$, $pK_{S,2} = 7$) to water. Here, an acid solution is the result. The buffer at pH 7 suggested in chapter 3 only becomes relevant, once a base is added.

4.4 Conclusions

Cation nonstoichiometry was introduced in SrTiO_3 polycrystals via both deliberate deviation of the Sr/Ti ratio from unity in the preparation process and Schottky disorder due to sintering at high temperatures. A slight increase in conductivity is found for cation deficient polycrystals. Additional sintering steps increase the conductivity of the polycrystals and level off any differences attributed to the different nominal composition before. At high temperatures, the Schottky disorder becomes the defining factor for the material's defect chemistry, increasing the conductivity. This beneficial effect of Sr vacancies in polycrystals vastly differs from their impact in thin films, in which Sr vacancies are the key driver for intrinsic Fermi level pinning. To address the question from the title of this chapter: Yes, the defect situation in thin films and polycrystals is drastically different. In thin films, donor states are present, which lead to a buffer at Sr vacancy related mid gap states. In polycrystals, no donors are present, thus Sr vacancies act as an acceptor, leading to the increase in conductivity with more Sr vacancies present.

Chapter 5: Interaction between SrTiO₃ and (ultraviolet) light: Photovoltage

This chapter is part of a review article, currently in preparation for submission.

A key interaction of semiconductors with light (above their bandgap) is the generation of electron-hole pairs. Such photo-generated charge carriers in a material can lead to the formation of a photovoltage via different processes/mechanisms.

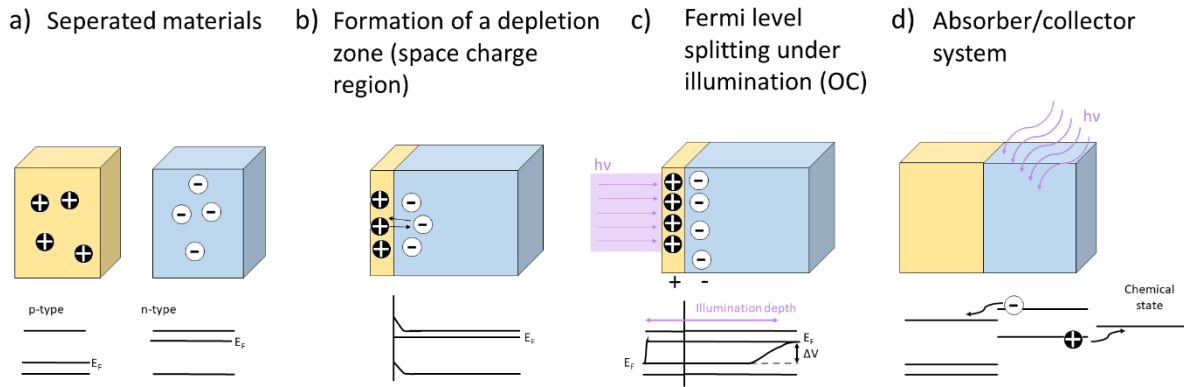


Fig. 37: Schematic representation of the generation of a photovoltage at a heterojunction. A p-type and an n-type material are brought into contact (a), forming a space charge region with a built-in field (b). Under UV illumination and generation of electron/hole pairs, a splitting of the Fermi-level occurs under open circuit conditions (c). Separation of charge carriers may also be achieved in absorber/collector systems consisting of semiconductors and/or chemical systems (d).

Photo-generated electron-hole pairs can also lead to the formation of a photovoltage. In general, a photovoltage can be created whenever charge separation happens due to the characteristics of the present electronic band structures, i.e. when a band offset/band bending is present, e.g. at heterojunctions, p-n junctions or surfaces/interfaces. A well-known example is a p-n junction. Upon equilibration of the Fermi levels, a space charge zone is formed. The built-in field hinders the transfer of the respective majority charge carriers, but not of the minority charge carriers. The lateral extent of the space charge region can be different for the p-type and n-type semiconductor and depends on the dopant concentration. Similarly, a p-i-n junction is formed, when there is an additional intrinsic semiconductor between a p-type and an n-type semiconductor. This leads to the

formation of a wider space charge region via the intrinsic material. If the n-type semiconductor in a p-n junction is exchanged for a metal, a Schottky contact can be obtained. Here, the space charge region only extends into the semiconductor. Another way of creating charge carriers is the use of an absorber, which can also be a semiconductor or even an organic dye. An absorber has excitation levels in a certain wavelength spectrum and absorbing light within this range leads to the generation of free charge carriers (i.e. electrons or holes), which can then subsequently be separated and partially transported into a (second) connected semiconductor. The overall principle for formation of voltages is very similar for these cases and is depicted in Fig. 37. Above-band-gap energy light generates charge carriers, which are then separated according to their charge, thereby creating a photovoltage.

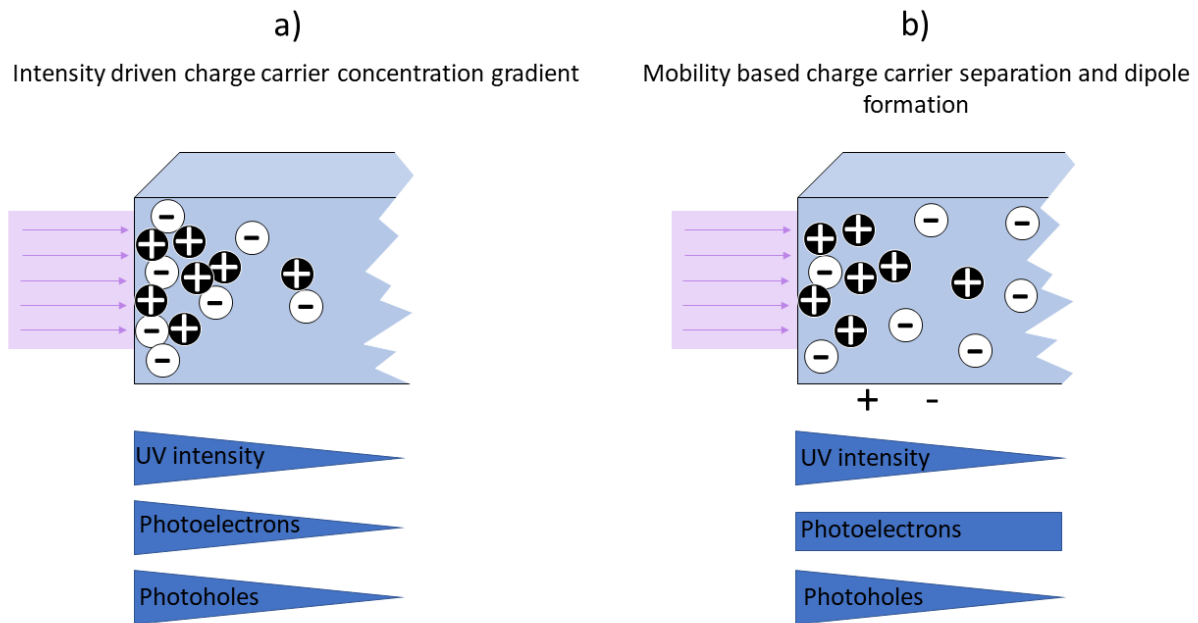


Fig. 38: Schematic representation of the Dember effect showing the intensity driven depth dependence of the generation of photo induced charge carriers (a) resulting in a voltage due to differences in the mobilities of electrons and electron holes (b).

In addition, the Photo-Dember effect can lead to a lateral or vertical photovoltage. According to the Lambert-Beer law, the intensity of light decreases with the depth, leading to a lower generation of photo-induced charge carriers in deeper regions of the semiconductor (see Fig. 38). A gradient of electron/hole concentration within the semiconductor is formed with a higher concentration of electron-hole pairs close to the surface. The Photo-Dember effect is then based on the different mobilities of electrons and holes (both diffusing from their point of generation with their respective

diffusion length) in a semiconductor, leading to a charge separation, given the diffusion lengths are different. Thereby, a dipole and local voltages are created (see Fig. 38).

The photovoltaic effects are important for the surface voltage of SrTiO₃ with regard to photocatalytic reactions [177] and can be used for e.g. solar cells [178] or photodetectors [179, 180]. The photo-response of such systems is usually fast (at moderate and low temperatures) - owing to fast electronic processes - with rise times in the hundred ps range upon illumination with a laser pulse [181]. However, recently high temperature devices with additional slow time dependent processes have been reported with a voltage decay in the range of 10 to 100 s. This behavior has been attributed to ionic effects under UV light [13, 51]. Therefore, we discuss separately the lower temperature regime, in which primarily electron-hole generation and subsequent charge separation are the source of the voltage, and a higher temperature regime, in which a change in oxygen stoichiometry and oxygen transport under illumination have to be considered as well.

5.1 Low temperature effects

Starting with undoped SrTiO₃ (STO) surfaces, the wavelength-dependent absorption of SrTiO₃ single crystals has been reported [181], showing a slight increase from 300 to 385 nm and a sharp drop in absorption at 385 nm. The photovoltage measured between two indium electrodes (remaining in dark at all times) in lateral geometry on these single crystals exhibits ultra-fast photo response at 355 nm, with a rise time of 130 ps and a full width at half maximum time of 230 ps with peak photovoltages upon UV laser irradiation of up to 52 mV [181]. In addition, a dependence of the photovoltage on the tilt angle of miscut SrTiO₃ single crystals is reported [181], showing a maximum in photovoltage at a tilt angle of approx. 20 ° with regard to the (100) direction. Similar results were obtained for Nb doped SrTiO₃ single crystals [182]. The wavelength dependent properties also have been used for UV-sensitive, but visible blind photodetectors with a lateral electrode design on SrTiO₃ single crystals with a reported cut-off wavelength of 390 nm [179]. Regarding the origin of the SrTiO₃ single crystal based photovoltages, a model considering contribution from photoelectronic processes and the Seebeck effect [181] and additionally, a surface-barrier model with $V_o^{\bullet\bullet} - Ti^{3+}$ dipole centers oriented in the field [183] have been suggested.

The photovoltage of SrTiO₃ thin films can be tailored via the oxygen vacancy concentration [184]. By applying an electric field, oxygen vacancies move towards one or the other electrode and affect the measured photovoltage via band bending and, consequently, two reversible photovoltaic states (even with a change in the sign of the photovoltage) have been reported [184]. Also, SrTiO₃ single crystals operated at a 10 V bias could be demonstrated as photodetectors with photovoltages of 2.4 V for one cell and up to 8.1 V for four cells in parallel when irradiated with a 375 nm laser with 10 mW/cm² [185]. However, using fewer cells (e.g. just one cell) results in a faster photoresponse in the range of hundreds of picoseconds [185]. Moreover, SrTiO₃ thin film based photodetectors operated at 10 V show a photovoltage of approximately 0.25 V [180] with a rise time of 330 ps and a full width half maximum of 700 ps when irradiated with a 355 nm laser pulse of 25 ps.

It has also been shown that the photoresponse of SrTiO₃ single crystals depends on the electrode material, showing differences in photocurrent, photovoltage and rise time using Ag, Pt or Ni electrodes [186]. Upon irradiation by a 15 ps laser pulse with a wavelength of 355 nm, photovoltages of approx. 0.8 V, 1.0 V and 1.1 V with rise times of 301.5, 394.4 and 360.9 ps and full width at half-maximum times of 537.2, 966.9 and 576.5 ps for Pt, Ni and Ag, respectively, are reported [186]. A change in photovoltage was also observed for SrTiO₃ single crystals with different metals (Au, Pt) on top, yielding slightly higher photovoltages for Pt in the temperature range from 80 to 300 K due to the difference in work function and, thus, Schottky barrier height [187].

As a further use of the photovoltage generated by undoped SrTiO₃, SrTiO₃ nanoparticles irradiated by white light have been used as a photoelectrode for cathodic protection of different steels in a sodium chloride solution [188].

Furthermore, SrTiO₃ has been frequently employed in heterojunctions (e.g. Schottky or p-n junctions) for the generation of photovoltages. For more information, the reader is referred to the excellent review in Ref. [189]. Here, heterojunctions with different top layers are reported, ranging from organic or metallic coatings to inorganic and oxide top layers. Photovoltages of several 100 mV can be achieved. For instance, Yamaura et al. reported photovoltages of up to 0.7 V in poly(3,4-ethylenedioxythiophene) (PEDOT)/SrTiO₃ junctions [190, 191]. In addition, a multilayer consisting of indium tin oxide (ITO), lead zirconium titanate (PZT), SrTiO₃ and GaAs yields a photovoltage of up to 400 mV in simulated sunlight [192]. The probably best-known SrTiO₃ based interface is the one with LaAlO₃ (LAO), which is well researched and shows interesting effects, such as a 2D electron gas at the interface [57]. A one unit cell thick layer of LaAlO₃ on SrTiO₃ has

been investigated by Liang et al. [193]. A dependence of the photovoltage on the work function of the metal top electrode (Ag, Au, Pt) is found, increasing from 0.2 V for silver to 0.4 V for Pt. When lowering the energy of the light source from 6.7 eV to below the band gap of LaAlO₃, however, the photovoltage decreases from 0.3 V to below 0.1 V for 3.4 eV and solar light. A residual polar field in the ultrathin LaAlO₃ thin film is suggested, which influences the photovoltage [193]. The photovoltage at the LaAlO₃/SrTiO₃ interface is therefore mostly influenced by LaAlO₃.

Beyreuther et al. investigated manganite/SrTiO₃ heterojunctions (for more information on such heterojunctions, please refer to Ref. [194]) using surface photovoltage spectroscopy (SPV), reporting SrTiO₃ related states [195] (i.e. optimization should focus on SrTiO₃), in another work thin film related states were detected as well [196]. Optimization of undoped SrTiO₃ can be achieved via self-doping, i.e. the introduction of oxygen vacancies acting as donor dopant yielding n-type SrTiO₃. Different cells using self-doped n-type SrTiO₃ have been investigated, e.g. SrTiO₃/Si [27, 197], SrTiO₃/GaAs [198] and SrTiO₃/Pt [199]. A p-n junction is formed, consisting of p-type Si and n-type SrTiO₃ (via oxygen vacancies), yielding photovoltages above 100 mV [27, 197]. In the work of Wen et al., a n-type SrTiO₃ thin film is deposited on a p-Si substrate [197]. There, visible light can pass the SrTiO₃ thin film (bandgap 3.2 eV), but leads to the generation of electron-hole pairs in the p-Si. The built-in field leads to charge separation by moving the electrons to the n-type SrTiO₃. In contrast, when using UV light, the photo-induced charge carriers are formed in the SrTiO₃ thin film. Then again, charge separation happens at the interface, leading to a movement of the holes to the p-Si. However, the recombination rate of the photo-induced charge carriers is higher in SrTiO₃ and higher photovoltages were obtained for visible light (632.8 nm) compared to UV light (355 nm) [197]. Jin et al. used SrTiO₃ single crystals with Pt top electrodes and vacuum annealed the SrTiO₃ single crystals at different temperatures [199]. The “as received” sample obtained the highest photovoltage in the study with 1.1 V at 60 K, decreasing down to approx. 200 mV at 300 K. In comparison, samples initially annealed at 650 °C in vacuum exhibit a photovoltage below 100 mV at 60 K. However, between 200 and 250 K the measured photovoltage peaks at approx. 0.5 V. This shows that reducing SrTiO₃ is an effective way of tailoring the temperature dependence of the photoresponse of SrTiO₃-based systems.

Solid solutions and composite materials based on SrTiO₃ powders also showed promising photovoltaic properties. For example, a SrTiO₃/TiO₂ composite has an increased photoresponse compared to both, SrTiO₃ and TiO₂ [200]. This effect is attributed to the band structure of the SrTiO₃/TiO₂ interface enabling an enhanced charge separation and thus leading to a lower

recombination rate of the photo-induced charge carriers [200]. In addition, the photoelectrical properties of SrTiO₃ and BiFeO₃ (BFO) solid solutions are discussed in [201], yielding photovoltages above 1 V. As a notable example, for BiFeO₃ thin films on SrTiO₃, a photovoltage of 25 V has been reported [202]. However, this is a bulk BiFeO₃ effect [202], not an effect due to the interface with SrTiO₃. Furthermore, other oxide materials are suggested as possible top layers for charge separation, e.g. Fe₂O₃ [203], CdS/TiO₂ [204] or BiVO₄ [205].

Owing to its n-type nature, pn-junctions are often investigated based on Nb:SrTiO₃, frequently using p-type (lanthanum) manganites. An overview of the manganite/Nb:SrTiO₃ heterojunctions is shown in Tab. 10, and the results of other top layer materials on Nb:SrTiO₃ is shown in Tab. 11. Photovoltages up to 1 V have been reported, but comparison between values obtained in different studies is difficult due to different excitation wavelengths (ranging from UV to VIS light), light intensities, measurement modes (vertical vs. lateral), and temperatures.

Tab. 10: Parameters for manganite/Nb:SrTiO₃ based heterojunctions

Material on Nb:SrTiO₃	T range (K)	Wavelength [nm]	Energy [mW/mm²]	Voc range [mV]	Voc [V] at RT	Ref.
Doped PrMnO ₃	20 - 300	365, 473, 532	0.003 – 0.7	0.2 – 20	0.005	[28, 206, 207]
Doped LaMnO ₃	17 - 390	210 - 660	0.3 – 15 (if specified)	0.15 – 1000	0.0015 – 1	[26, 206, 208-220]
Alkali doped LaMnO ₃	80 - 300	248, 473	25 – 500	50 – 580	0.3	[221-223]
Other manganites	80-300	365, 460, 660	2.6 (if specified)	2.2 – 345	0.345	[224, 225]

In cells using manganites as a top layer (see Tab. 10), the very importance of the thin film has been reported [26, 214, 221-223], highlighting the effect of the metal/insulator transition on the photovoltage. For instance, a maximum in photovoltage is reported for La_{0.9}Li_{0.1}MnO₃ at 240 K

[223], close to the metal/insulator transition. The importance of magnetic properties is also shown for $\text{La}_{0.7}\text{Ce}_{0.3}\text{MnO}_3$ thin films. Introducing oxygen vacancies weakens the ferromagnetic ordering and a lower photovoltage is observed [216]. In addition, the use of external magnetic fields may affect the photovoltage. Magnetic suppression has been reported in literature [207] for Ca and Sr co-doped praseodymium manganite. Wu et al. further investigated the temperature dependence of Nb:SrTiO₃ based PV cells with hafnium doped lanthanum manganite thin films as a top layer [212]. While magnetoresistance of the thin film could be demonstrated, no dependence of the photovoltage on the magnetic state was found. Higher photovoltages found at lower temperatures are attributed to a thicker depletion region or a higher diffusion voltage of the built-in field at lower temperatures. Naturally, also the thickness of the films on top is affecting the photovoltage on SrTiO₃, e.g. for p-Cu₂O [226] and for $\text{La}_{1-x}\text{Sr}_x\text{MnO}_3$ [209, 218]. For $\text{La}_{1-x}\text{Sr}_x\text{MnO}_3$ an optimum thickness of the length of the depletion zone was found [209, 218]. Thicker thin films enhance recombination, whereas in thinner film the build-in field is weakened. Another way of influencing the photovoltage is via resistive switching, e.g. in Au/Pr_{0.7}Ca_{0.3}MnO₃/Nb:SrTiO₃/Au and Au/La_{0.7}Ca_{0.3}MnO₃/Nb:SrTiO₃/Au [206]. In this regard, a change in photovoltage was observed in Au/Nb:SrTiO₃ systems with different resistive states of the junction, ranging from 0.003 mV at 70 M Ω to 57.6 mV at 900 M Ω [227].

Tab. 11: Parameters for Nb:SrTiO₃ heterojunctions

Material on Nb:SrTiO₃	T range [K]	Wavelength [nm]	Energy [mW/mm²]	Voc range [mV]	Voc [V] at RT	Ref.
YBa ₂ Cu ₃ O ₇	40 – 350	355, solar light	0.5 – 6	0.1 – 1040	0.78 – 1.04	[228-231]
Perovskite oxides	80 – 300	248, 266, 532	2.12 – 14.86 (if specified)	100 – 400	0.1	[232-235]
Other metal oxides	RT	248, 308, solar light	unspecified	3.3 – 565	0.565	[226, 236, 237]

Also, different other oxides have been used as top layers in Nb:SrTiO₃ based photovoltaic cells (see Tab. 11. Here, the YBa₂Cu₃O₇ (YBCO)/Nb:SrTiO₃ heterojunction [228-230] yields overall high photovoltages, e.g. 1.04 V in solar light. A dependence of the photovoltage on the repetition rate of the laser has been reported. For example, a photovoltage of 0.78 V was obtained at 130 K with a repetition rate of 30 Hz and a calculated result of 1.15 V for continuous illumination [230], which is in good agreement with experimental data [229]. Hao et al. investigated the use of different wavelengths, temperatures and intensities on YBa₂Cu₃O₇/Nb:SrTiO₃ interfaces, showing higher photovoltages at low temperatures, high light intensities and lower wavelengths [231]. Indeed, the temperature dependence of the photovoltage shows a kink at 100 - 120 K. This temperature is attributed to the phase transition from cubic to tetragonal SrTiO₃ [231]. In addition, the band gap increases from 3.2 eV at 4.2 K to 3.23 eV near the phase transition and decreases with temperature after the phase transition. In contrast, the superconducting transition of YBa₂Cu₃O₇ at 60 K does not result in any significant feature in the temperature dependent behavior of the photovoltage [231]. Furthermore, the YBa₂Cu₃O₇/Nb:SrTiO₃ interface can also be affected by oxygen annealing. Showing no photovoltaic effect at annealing oxygen pressures of 10⁻⁵ Pa or lower, the photovoltage increases with oxygen annealing pressure up to a maximum of approximately 0.7 V at 10² Pa and after a minimum at 10³ Pa a stable plateau at 0.5 V in the 10⁴ Pa region is reached. The oxygen partial pressure dependence of the photovoltage correlates with the semiconductor-metal transition, changing the interface from a p-n junction to a Schottky junction [228]. Another impact of oxygen annealing (though at low temperatures) was also shown for another metal oxide as a top layer, namely for NdNiO₃ (NNO)/Nb:SrTiO₃ heterojunctions (see Tab. 2). Here, oxygen annealing leads to a dramatic change in the resistance of the NdNiO₃ thin films (thus the short circuit current), while comparable photovoltages in the 0.18 to 0.22 V range were obtained [235]. In addition, the use of an insulating SrTiO₃ layer in between NdNiO₃ and Nb:SrTiO₃, forming a p-i-n junction, doubled the photovoltage to 0.45 V. Similar results have also been shown for the La_{1-x}Sr_xMnO₃/Nb:SrTiO₃ interface when an additional SrTiO₃ or indium tin oxide layer between Nb:SrTiO₃ and La_{1-x}Sr_xMnO₃ was used as an insulator [210].

Regarding the substrate, the impact of different Nb doping concentration on the photovoltage was reported in Ref. [226], showing an increasing photovoltage for higher Nb doping concentrations. This is explained by the stronger built-in field that results for higher donor concentrations in the n-type conductor of a p-n junction [226]. The angular dependence in the photoresponse was observed in miscut Nb:SrTiO₃ single crystals [182] and also for La_{1-x}Ca_xMnO₃ (LCM) layers on top of

miscut Nb:SrTiO₃ single crystals [238]. Additionally, a thickness dependence in the peak photovoltage of miscut Nb:SrTiO₃ single crystals upon illumination with 248 nm laser was found, yielding 180 μm as the optimal thickness. The vertical photovoltage was compared with the lateral photovoltage due to the Dember effect [233, 239] and higher voltages with faster relaxation times were found in the vertical case. In both cases, the transport of photo induced charge carriers is supposed to take place mainly in the Nb:SrTiO₃ substrate.

5.2 High temperature effects

In the temperature regime from nearly 0 to 300 K, usually higher photovoltages were found at very low temperatures [231]. However, surprisingly high photovoltages can be reached when such SrTiO₃ based photovoltaic cells are operated above 600 K [240]. In the work of Walch et al. [13], SrTiO₃ single crystals were investigated between 400 to 500 °C in air using different metal current collectors and also using yttria stabilized zirconia (YSZ) bottom layers. Most importantly, a time dependent behavior upon switching the UV light on or off was found. The time scales here are not in the ps to μs range as they are for the low temperature counterparts, but rather in the couple of minutes range. These slow processes are - in fact – not attributed to electronic processes, but to ionic changes, particularly to a change in oxygen stoichiometry upon illumination via faster oxygen incorporation [40, 41]. This change in oxygen incorporation influences the photovoltaic voltage, as it has been demonstrated in the low temperature counterpart [228]. In Ref. [13], upon switching off the UV light, the photovoltaic voltage goes down to zero almost immediately. However, the changed oxygen stoichiometry persists and – without illumination – is no longer in equilibrium with the gas phase. A Nernst-like (battery-type) voltage results due to the difference in the oxygen potential. The excess oxygen is then slowly released, thereby leading to a slow decrease in this battery type voltage, until the equilibrium with the gas phase is reached. Not surprisingly, a complete electrochemical cell with an oxide ion electrolyte and a counter electrode is needed to measure this battery type voltage. Different metals have been used as a current collector to change the Schottky contact, with Au reaching higher voltages than Pt, in contrast with the results of low temperature measurements [187].

The high temperature photovoltage can be increased dramatically by the use of different top electrodes (at the illuminated side). Brunauer et al. demonstrated that La_{0.8}Sr_{0.2}CrO₃/SrTiO₃

heterojunctions coupled with a solid oxide fuel cell can be operated at temperatures between 400 and 500 °C with photovoltages close to 1.0 V [42]. Such cells can be combined with a solid state electrochemical cell and the photovoltage from the solar cell can be used to pump oxygen through the electrochemical cell. Thus, in principle, this combination could be used for photo-powered water splitting and consequently hydrogen production.

Also, Nb:SrTiO₃ based heterojunctions were operated at high temperatures and the temperature dependence of La_{2/3}Ca_{1/3}MnO₃/Nb:SrTiO₃ heterojunctions was studied in the temperature range from 293 to 723 K [240]. At first, a decrease in the peak photovoltage upon UV laser illumination was observed from 142 mV at 293 K to 48.7 mV at 523 K. When increasing the temperature further, an increase in photovoltage was observed up to 118 mV at 723 K. As the Schottky barrier height is not expected to change with temperature, only the barrier width might change [240]. Indeed, oxygen vacancies in the La_{2/3}Ca_{1/3}MnO₃ thin film are expected to migrate to the interface under positive bias and vice versa. The changes of the oxygen stoichiometry at the interface are supposed to cause the increase in photovoltage at elevated temperatures where oxygen transport is possible. Ni et al. describe two factors affecting the photovoltage [240]: At higher temperatures the recombination of UV induced charge carriers is enhanced, the lifetime of these charge carriers is reduced. The decrease in voltage from 293 to 473 K is attributed to this effect. At higher temperatures, oxygen migration leads to a change in oxygen stoichiometry at the interface and, thus, to a change in band width. At higher temperatures, also tunneling of electrons through the interface barrier is enhanced, which leads to the increase in photovoltage at higher temperatures. The indium tin oxide/Nb:SrTiO₃ junction was studied at 873 K under UV illumination (365 nm) with 261.2 mW/cm² under different oxygen partial pressures [178]. At 1 bar pO₂, a photovoltage of 123 mV was observed, which decreases with lower oxygen partial pressures, e.g. 30 mV at 10⁻⁴ bar. Oxygen partial pressure changes are expected to change the barrier height, thereby influencing the photovoltage [178].

Chapter 6: SrTiO₃ based high temperature solid oxide solar cells: Photovoltages, photocurrents and mechanistic insight

The results presented in this chapter were also submitted as a scientific paper to Solid State Ionics.

6.1 Introduction

Finding clean and sustainable ways of providing energy is a major challenge of the 21st century with global problems such as climate change and air pollution. One promising approach is harvesting and storing abundant energy, such as solar energy. Photovoltaic cells are particularly suitable here, by transferring solar energy directly to electrical energy. While solar cells based on silicon or metal-organic perovskites are very popular and often investigated [241-248], the full oxide counterpart is much less known [249]. Solid oxide based solar cells have been realized using for example metal/Cu₂O Schottky junctions [250-254], Cu₂O/ZnO bilayer heterojunctions [255-257], nanocomposite heterojunctions with nano-structured ZnO or TiO₂ on Cu₂O [258-262], and also BiFeO₃ domain boundaries [202, 263], all operating at room temperature.

Also, many other oxides show interesting properties when irradiated by UV light, such as Nb₂O₅ [264, 265], SnO₂ [266-269], and SrTiO₃ (STO) [135, 270-274]. Among others, it was shown for SrTiO₃ that the uptake of oxygen at elevated temperatures is tremendously enhanced by UV light [40, 41]. Moreover, it is reported that voltages resulting from SrTiO₃ based cells under UV light may consist of a photovoltaic (PV) and an electrochemical contribution (EC), the latter being the result of a change in oxygen stoichiometry in SrTiO₃ due to the enhanced oxygen incorporation under UV irradiation [13]. SrTiO₃ based heterojunctions, e.g. the SrTiO₃/Si interface, generate photovoltages at room temperature with a very fast response [27, 197]. Also, Nb: SrTiO₃ based pn-junctions or Schottky junctions [28, 178, 206, 209-211, 220, 226, 231, 232, 236, 275, 276] have been investigated as photovoltaic devices, mostly operating at room temperature. Recently, it was found that the (La,Sr)CrO₃ (LSCr)/ SrTiO₃ junction can be used to obtain photovoltages up to 1 V at temperatures above 300 °C [42]. Coupling such a high temperature solar cell with a solid oxide electrolyzer cell (SOEC) yields a photoelectrochemical cell (SOPEC) which can pump oxygen and

may ultimately even use UV light to split water, thereby transferring solar energy to electrical energy and further to chemical energy [42].

This type of high temperature SrTiO₃ based solar cells are in the focus of our study. Here, we show why the illuminated surface of such solar cells is crucial and how photovoltages change with different top layer materials. The dopant level of Sr was varied in La_{1-x}Sr_xCrO₃ (LaCrO₃ (LCr), La_{0.9}Sr_{0.1}CrO₃ (LSCr10) and La_{0.8}Sr_{0.2}CrO₃ (LSCr20)) and Cr was replaced by Mn on the B-site of the perovskite, yielding La_{0.8}Sr_{0.2}Cr_{1-y}Mn_yO₃ (LSCrM). Other perovskite type oxides, including La_{0.6}Sr_{0.4}FeO₃ (LSF) and La_{0.6}Sr_{0.4}CoO₃ (LSC) and Pt and Au were tested as metallic top layers. Moreover, we investigated self-enhancement effects under operation and the influence of the SrTiO₃ substrate, with Fe:SrTiO₃ showing slower changes than undoped SrTiO₃. Further mechanistic insight into the processes under UV is gained by impedance spectroscopic measurements.

6.2. Experimental

6.2.1 Sample preparation and characterization

The solar cell consists of a single crystalline substrate, namely (100) oriented undoped SrTiO₃ (10 x 10 x 0.5 mm³, CrysTec GmbH, Ger) or Fe: SrTiO₃ (10 x 10 x 0.5 mm³, 0.016 mol% Fe, Alineason Materials Technology GmbH, Ger) and a thin top layer of another oxide or a metal. All sample types are summarized in Tab. 12. The oxide top layers (e.g. LSCr) were deposited by pulsed laser deposition (PLD) using a Kr/F excimer laser Lambda COMPex Pro 201F with a wavelength 248 nm. The repetition rate was 5 Hz with a nominal energy per pulse of 400 mJ, yielding a laser fluence of 1.1 J/cm². The LSCr and LSCrM thin films were deposited at 700 °C and 0.015 mbar and the deposition time was varied. As a current collector, Pt stripes were deposited by DC magnetron sputtering (BAL-TEC MED 020 Coating System; pressure: 2 x 10⁻² mbar Ar, 100 mA) on top of the oxide thin film. The structuring of the Pt thin film was carried out by lift-off photolithography. At the bottom side of the sample, a porous Pt paste was brushed as a counter electrode. A schematic representation of the sample is given in Fig. 39.a. Metal (Au, Pt) top layers with thicknesses mostly of about 10 nm were sputter deposited in the same way as the current collectors mentioned above. A quartz microbalance was used to determine the deposition rate of Au and Pt.

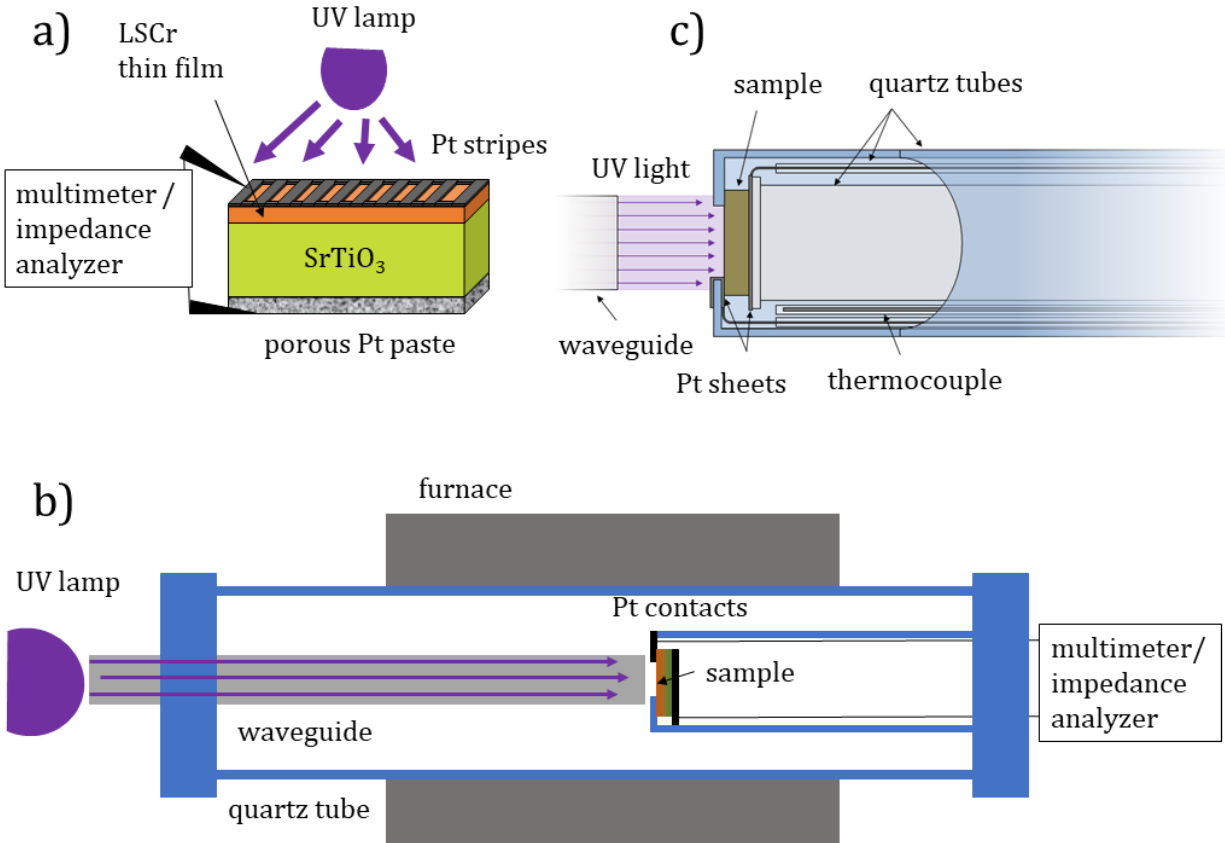


Fig. 39: Typical sample consisting of an SrTiO_3 substrate and an LSCr thin film (a), the measurement setup consisting of a quartz tube in a furnace, a waveguide with a UV lamp and a sample holder with contacts for electrochemical measurements (b), and a detailed view on the sample holder (c).

The oxide thin films on SrTiO_3 were characterized by X-ray diffraction (XRD) and cross-section scanning electron microscope (SEM) imaging. Fig. 40.a displays the diffraction pattern of an LSCr10 film on SrTiO_3 measured with a goniometric scan between the 2-theta angle of 10° and 99° , using $\text{Cu K}\alpha_1$ radiation. Only the (100), (200) and (300) reflexes are visible. In the magnifications of the (100) and (300) reflexes, one can see the sharp reflexes of the SrTiO_3 single crystal (i.e. the substrate) and the broader thin film reflex of the LSCr10 layer. With only the (h00) reflexes being visible, this suggests that the LSCr thin films grow epitaxially on the SrTiO_3 substrates. However, nominally the LSCr10 reflexes are expected at higher angles than the respective (h00) reflexes of SrTiO_3 . The shift towards lower angles is attributed to defects in the thin film, most likely cation vacancies which are frequently found in different complex oxide thin films prepared by pulsed laser deposition [48, 277]. The thickness of the ceramic thin films was determined by profilometry as well as SEM cross sections (see Fig. 40.b). A cross section of the

interface between LSCr10 and SrTiO₃ is shown in Fig 40.b.

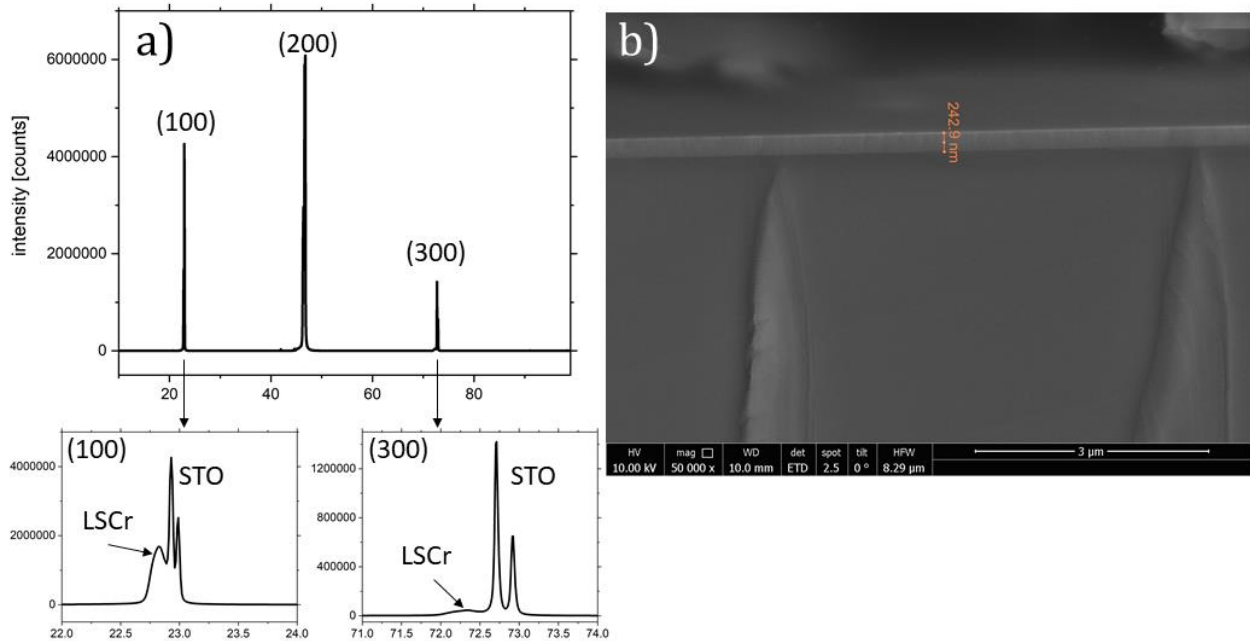


Fig. 40: Thin film characterization. X-ray diffraction pattern of LSCr10 on SrTiO₃, showing very good agreement between the LSCr reflexes and the single crystalline SrTiO₃ reflexes of the substrate, therefore highlighting the epitaxial nature of the LSCr/SrTiO₃ interface (a). SEM image of the interface showing the LSCr10 thin film on top of the SrTiO₃ substrate (b).

6.2.2 Photovoltage and photocurrent measurements

For photovoltage and photocurrent measurements, the sample was placed in a quartz tube inside a furnace. A quartz waveguide (10 mm in diameter) leads the UV light ($\lambda = 365$ nm, $P = 2.9$ W) from the lamp outside the furnace to the sample, as shown in Fig 39.b and c. A Keithley DMM2000 (Keithley Instruments, USA) was used for voltage and current measurements. The resulting voltage was measured mostly in open circuit mode (OCV = open circuit voltage) and the current in short circuit. All measurements were performed at 350 °C in air. The standard procedure for OCV measurements was the following: The voltage was measured for 15 minutes without UV irradiation, followed by 15 min under UV light and then again for 15 min after switching off the light. Thereby, the dark voltage before the experiment, the time dependent evolution of a photovoltage and the persistent [278-280] or decaying photovoltage after illumination can be

observed. Short circuit measurements were done in a similar manner, though partly longer illumination times were used or the current measurement was interrupted for an OCV measurement upon UV. Moreover, time dependent power-voltage and power-current curves were obtained for illuminated cells.

Tab. 12.: Thickness of the ceramic or metallic thin films on SrTiO₃ substrates

Top layer	Substrate	Preparation method	Deposition time [min]	Thickness [nm]
LaCrO ₃ (LCr)	SrTiO ₃ (STO)	PLD	25	180
La _{0.9} Sr _{0.1} CrO ₃ (LSCr10)	SrTiO ₃ (STO)	PLD	5	50
La _{0.9} Sr _{0.1} CrO ₃ (LSCr10)	SrTiO ₃ (STO)	PLD	25	240
La _{0.9} Sr _{0.1} CrO ₃ (LSCr10)	Fe:SrTiO ₃ (Fe:STO)	PLD	25	240
La _{0.8} Sr _{0.2} CrO ₃ (LSCr20)	SrTiO ₃ (STO)	PLD	25	230
La _{0.9} Sr _{0.1} Cr _{0.8} Mn _{0.2} O ₃ (LSCrM)	SrTiO ₃ (STO)	PLD	25	240
La _{0.9} Sr _{0.1} Cr _{0.2} Mn _{0.8} O ₃ (LSCrM)	SrTiO ₃ (STO)	PLD	25	240
La _{0.8} Sr _{0.2} MnO ₃ (LSM)	SrTiO ₃ (STO)	PLD	3	50
La _{0.8} Sr _{0.2} MnO ₃ (LSM)	SrTiO ₃ (STO)	PLD	25	400
Au	SrTiO ₃ (STO)	sputtering	0.16	10
Au	SrTiO ₃ (STO)	sputtering	3.3	200
Pt	SrTiO ₃ (STO)	sputtering	0.26	10

6.2.3 Spectroscopic ellipsometry measurements

Spectroscopic ellipsometry (SE) measurements were carried out in a Horiba iHR320 monochromators UVISEL ellipsometry system, with spectral range 0.6 – 5.0 eV and step size 0.05 eV. The spectra were collected with a light incidence angle of 70° and with the modulator and analyzer set at 0° and 45°, respectively. In order to measure the oxide films, sample replicas of the

materials in Tab. 1. Were prepared, i.e. LaCrO_3 , $\text{La}_{0.8}\text{Sr}_{0.2}\text{CrO}_3$, $\text{La}_{0.9}\text{Sr}_{0.1}\text{Cr}_{0.2}\text{Mn}_{0.8}\text{O}_3$ and $\text{La}_{0.8}\text{Sr}_{0.2}\text{MnO}_3$, on top of an Al_2O_3 (0001) substrate. Modelling of the optical response was carried using DeltaPsi2 software by Horiba. The model followed a geometry in which the material layer is placed on top of a well-defined Al_2O_3 substrate. The thickness of the layers was fixed in agreement with the SEM characterization. A 1 nm material-void (50% each) overlayer was fixed on top of the material layer in order to simulate the contribution of the film roughness. The material was then fitted with a series of 5xTauc-Lorentz (TL) user-defined-formula (udf) dispersion oscillators. The use of TL oscillators has been widely reported to fit the dielectric properties of semiconductor perovskites [281-283]. As a result, one can obtain data on the layers' optical constants.

For analyzing the optical properties of SrTiO_3 , a SrTiO_3 single crystal substrate was kept in the PLD chamber at the deposition conditions of the oxide films (i.e. 25 min of deposition time) before measuring the optical properties. Thus, the measurement is consistent with the nature of the SrTiO_3 present in the photovoltaic device. The model chosen for SrTiO_3 was quite similar to the case of the films, with the roughness overlayer directly placed on top of the substrate material. For properly fitting the SrTiO_3 optical properties, a series of 4xTL oscillators were required. The general expression of light absorption in a solid $I=I_0e^{-\alpha t}$, where I is the transmitted light, I_0 is the incident light, α is the absorption coefficient of the solid and t is the thickness was used to calculate the percentage of adsorbed light at a given wavelength.

6.2.4 Electrochemical impedance spectroscopy measurements

Electrochemical impedance spectroscopy was performed using an Alpha-A High Resolution Dielectric Analyzer (Novocontrol, Germany) in frequency range from 1 MHz to 1 Hz with a resolution of 10 points per decade and an rms amplitude of 20 mV. In special cases, the frequency range was extended down to 31 mHz. Impedance spectra were measured under short circuit conditions (bias 0 V). The obtained impedance data were parameterized by equivalent circuits using ZView3.5 (Scribner, USA).

6.3 Results and Discussion

6.3.1 Photovoltages

Fig. 41 displays the results of a standard OCV experiment on a sample with a 240 nm LSCr10 top layer (15 min dark, 15 under UV, 15 min dark). Upon UV light, an immediate voltage step to almost 730 mV is found, followed by a further increase within about 100 seconds to a nearly constant value of ca. 930 mV. After switching off the UV light, the voltage is reduced but does not immediately jump to zero. Rather, the decay to zero voltage requires several ten seconds or even a few minutes. Generally, the time with a transient change of the voltage was longer after switching off UV compared to switching UV on. The same phenomenon is also found for Fe-doped SrTiO₃ as substrate (Fig. 41), however, the increase of the photovoltage under UV takes even much longer in this case. These time dependencies are most probably caused by changes of the oxygen stoichiometry in SrTiO₃ upon UV light [13, 40, 41] and subsequent relaxation to the equilibrium defect concentrations in dark. This is discussed in more detail below.

Qualitatively, the same features are found for many different oxide top layers. A representative collection of layer variations is shown in Fig. 42. In Fig. 42.a, the Sr dopant concentration of LaCrO₃ was varied between 0 and 20 %. For higher Sr concentration, the total conductivity of the LSCr layer rises [284], but the thin film also changes in color, from a nearly transparent undoped LCr thin films to the light brownish LSCr20. The highest voltage results for undoped LaCrO₃ (LCr) (1008 mV). The cell with LCr top layer also exhibits the slowest voltage relaxation after switching UV off, possibly due to the slow oxygen exchange between LCr and the gas phase, which is required to get the SrTiO₃ back to its equilibrium defect chemical state after UV.

When replacing Cr by Mn while keeping the deposition time constant (i.e. similar layer thickness), we find a decrease of the photovoltage (Fig. 42.b). Fig. 42.c displays effects of the film thickness for LSCr10 and LSM top layers. For LSCr10 thin films, the resulting OCV is very similar for different layer thicknesses, with 930 mV for 240 nm and 990 mV for 50 nm. In case of LSM, however, the thin layer with 50 nm achieved 910 mV while the thicker one with 400 nm only reached 610 mV. Most probably, this is largely due to the much higher UV absorbance of LSM, which makes it much darker than LSCr10 for similar layer thickness. Accordingly, much less light reaches the heterojunction between top layer and SrTiO₃.

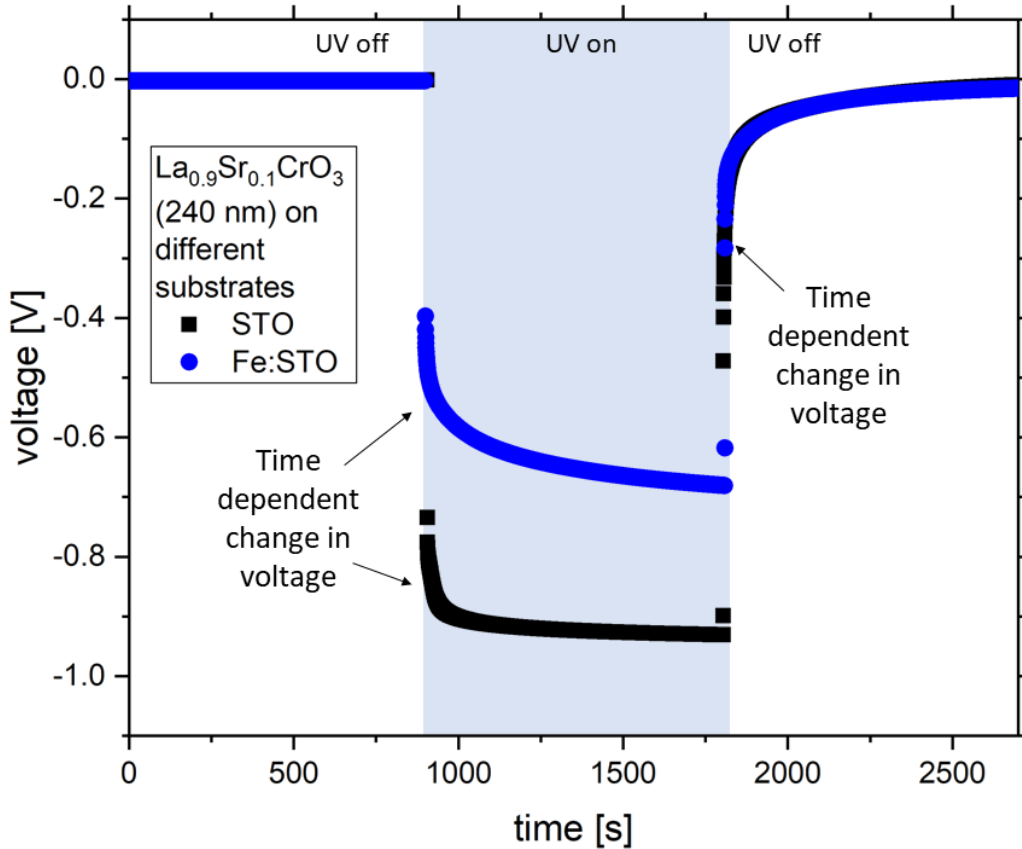


Fig. 41: Time vs. voltage curves for LSCr10/SrTiO₃ and LSCr10/Fe:SrTiO₃ samples at 350 °C in air. At first, the voltage is measured for 15 min without UV light, then for 15 min under UV illumination ($\lambda = 365$ nm), then for 15 min after switching off the UV light. When switching on the UV light, a time dependent change in voltage can be observed for both substrates, but the change occurs at a different speed. When switching off the UV light, a voltage of several hundred mV remains. Here, the time dependency of the decaying voltage appears to be similar for both cases.

These results also strongly suggest that UV absorption within SrTiO₃ is essential for the generation of the photovoltage, i.e. SrTiO₃ acts as the absorber of our high temperature oxide solar cell.

Also, LSF and LSC perovskite-type top layers were tested. These thin films have an intense black color and thus high absorption. Not surprisingly, only low photovoltages were obtained (e.g. 40 mV for LSF of 100 nm thickness). These findings are in line with the results on LSCr, highlighting the importance of a high transmittance in the top layer. However, possibly the different electronic band structure and/or the ionic defect energies in LSC or LSF contribute to the much lower photovoltages as well.

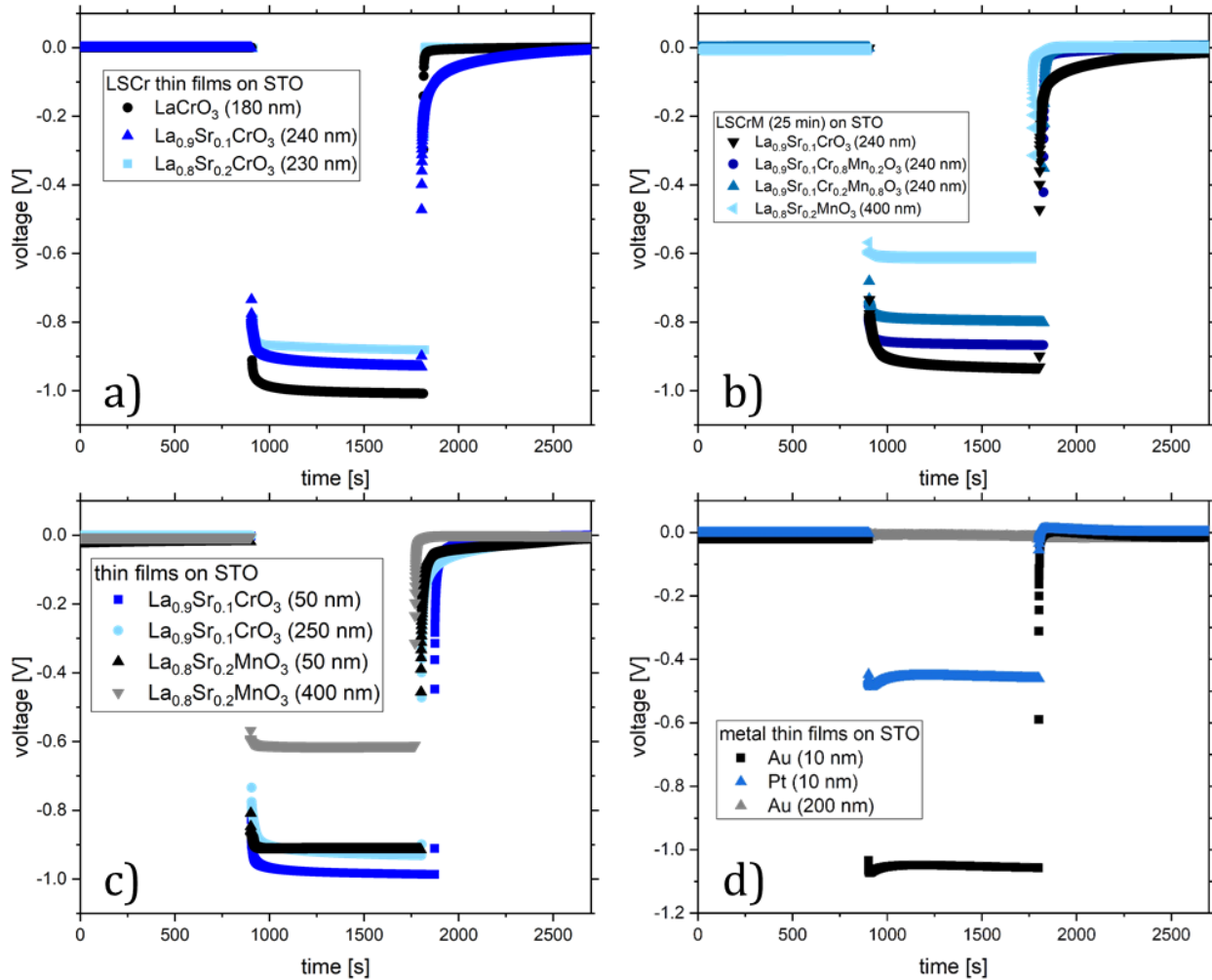


Fig. 42: Voltage-time curves at 350 °C in air for different material combinations before, under and after UV illumination ($\lambda = 365 \text{ nm}$), showing the influence of (a) different Sr dopant concentrations in LSCr, (b) the introduction of Mn to the B site of the LSCr, (c) the thickness of LSCr10 as well as LSM thin films, and (d) metallic thin films.

Very thin metal layers (10 nm Au, 10 nm Pt) with some remaining UV transmittance [285] were also investigated as top layers. The results are plotted in Fig. 42.d. The photovoltages obtained for Pt were only mediocre (400 mV range) but for the very thin Au layer we found 1100 mV at 350 °C and thus the highest value of all layers tested in this study. All these measurements also demonstrate the “robustness” of the PV voltage of SrTiO₃ based high temperature solar cells; it is not a peculiarity of a very special materials combination, but results for many different materials. For the photovoltaic effect upon UV light, the SrTiO₃ single crystal is vital, meaning that the relevant processes are located within the SrTiO₃. The role of the top layer is most likely primarily the introduction of chemical potential differences for electrons (and possibly also for oxygen

vacancies) at the interface and thus the formation of a space charge region in SrTiO₃. This space charge layer in the slightly hole conducting SrTiO₃ acts as barrier for the holes (majority carriers) while attracting photo-generated electrons in SrTiO₃ and swamping them into the top layer. Therefore, many thin films with acceptably low absorption cause photovoltages upon illumination. The space charge region is visible as a very large additional resistance (second semicircle) in impedance spectra and its dependence on UV light is discussed in more detail below. The recombination length of the electrons in our SrTiO₃ single crystals is unknown and hence we do not know from which depth photo-generated electrons can be collected and contribute to the operation of the solar cell. The upper limit is certainly the absorption depth of UV in SrTiO₃.

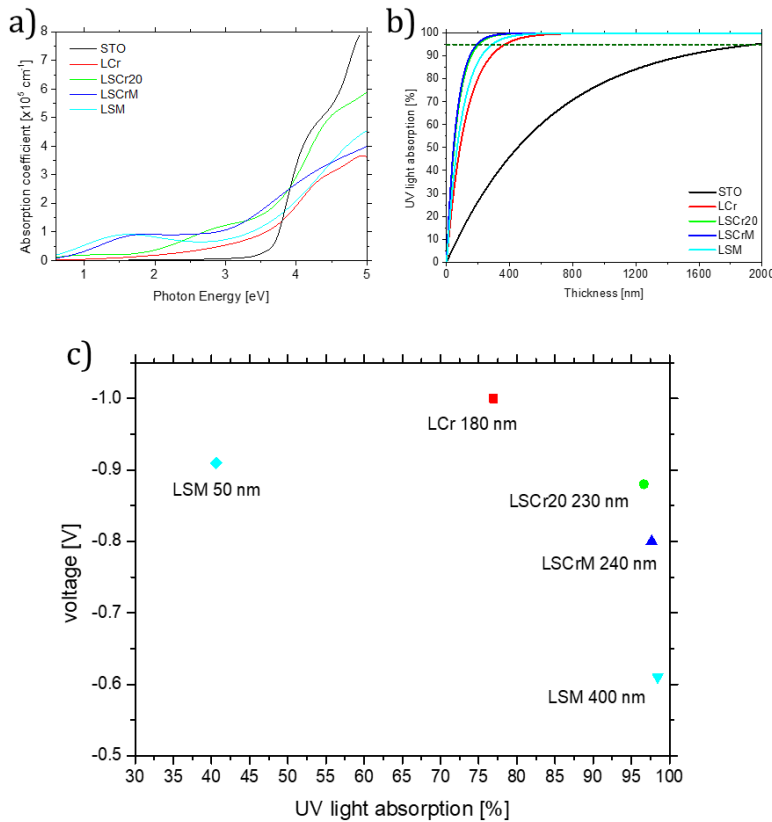


Fig. 43: Absorption spectra for the different materials under consideration (a). Percentage of UV light absorbed (365 nm) as a function of material's thickness. The horizontal dotted line indicates the thickness at which 95% of UV light is absorbed (absorption depth) (b). Measured PV vs percentage of light absorbed for different top layers (c).

This interpretation is also supported by optical SE measurements. The absorption of both oxide thin films (top layers) and SrTiO₃ substrate was investigated. The resulting absorption spectra are shown in Fig. 43.a. From here, considering a 365 nm UV light source (3.4 eV), the percentage of

absorbed light as a function of the material's thickness was calculated (Fig. 43.b). Please note that the obtained spectra are in line with previous reports [283, 286-288]. It should be noticed, however, that slight deviations may arise [114, 289], possibly due to differences in the synthesis method or as a consequence of the technique used for the measurement.

Tab. 13: Absorption measurements. The percentage of UV light absorbed was calculated considering the layers' thickness as retrieved by SEM cross-section data.

Layer	Absorption coefficient at 365 nm [cm^{-1}]	Absorption depth [nm]	Percentage light absorbed [%]
LaCrO ₃ (LCr)	81522	367	76.9
La _{0.8} Sr _{0.2} CrO ₃ (LSCr20)	147603	203	96.6
La _{0.9} Sr _{0.1} Cr _{0.2} Mn _{0.8} O ₃ (LSCrM)	156700	191	97.7
La _{0.8} Sr _{0.2} MnO ₃ (LSM)	104185	288	40.6 (50 nm)
			98.5 (400 nm)
SrTiO ₃ (STO) single crystal	15405	1945	-

The relevant optical properties are summarized in Tab. 13 which also includes the absorption depth of the films, i.e the thickness within which 95 % of the light is absorbed. The relation between absorbed light in such a layer and the photovoltage is shown in Fig. 43.c. For layers with very strong absorption the photovoltage decreases. (The intensities used here are rather high and thus already less than 20 % transmitted light leads to very high photovoltages.) However, a slight difference between Mn and Cr based perovskite top layers seems to remain irrespective of transmittance, since the thin LSM layer with much more transmittance has still a slightly lower OCV than LCr. As far as the SrTiO₃ substrate is concerned, an estimation of 2 μm for the absorption depth was obtained.

6.3.2 Photocurrent under UV

For photovoltaic cells, current voltage curves are frequently reported. However, as will be shown in the following, the current of our SrTiO₃ based PV cells is strongly time dependent and current measurements are most probably accompanied by continuous oxygen stoichiometry changes within the SrTiO₃ single crystals. Accordingly, the cells change continuously during current load and steady state current voltage curves could not be determined. Hence, we focus the following consideration on the short circuit current as the most extreme case of a current flow. This was investigated for an LSCr10/SrTiO₃ cell with 240 nm LSCr10. When switching on the UV light for the very first time, a rather low current in the 2-5 μ A range results (see magnification in Fig. 44a). However, over time this current strongly increases by orders of magnitude. After 15 minutes 0.18 mA are reached but the current is still far from being constant (Fig. 44.a). Long-term measurements in Fig. 44.b show that the current increase becomes slower, but persists on the time scale of many hours. The almost linear long time current increase reaches almost 1 mA after 17 hours. Some samples even showed photocurrents of up to 3.5 mA at 350 °C after several illumination cycles, all for a nominal sample size of 1 cm².

This current increase is not accompanied by a decrease of the OCV, as shown in Fig. 44.c: There, 5 minutes of OCV measurement under UV (reaching 1050 mV) are followed by a short circuit period of 5 minutes with a strong current increase to the several 100 μ A range. Please note that here the sample was already illuminated in a preceding experiment. The initial short circuit current under UV is thus much larger than for the pristine sample, indicating that the sample changes caused by the preceding illumination are still (partly) present. However, despite all these changes, the subsequent OCV measurements show again more than 1 V, indicating that the cell voltage itself is hardly affected by the persisting sample changes upon current. In other words, the cell's power shows a very pronounced enhancement effect during operation. This becomes also visible in continuous P versus voltage V measurements (and the power P versus current I curves) monitored on an LSCr10/SrTiO₃ sample, see Fig. 45. A severe enhancement is found already within several minutes. (Please note that sample changes take place also within a single P(V) curve which takes 10 seconds).

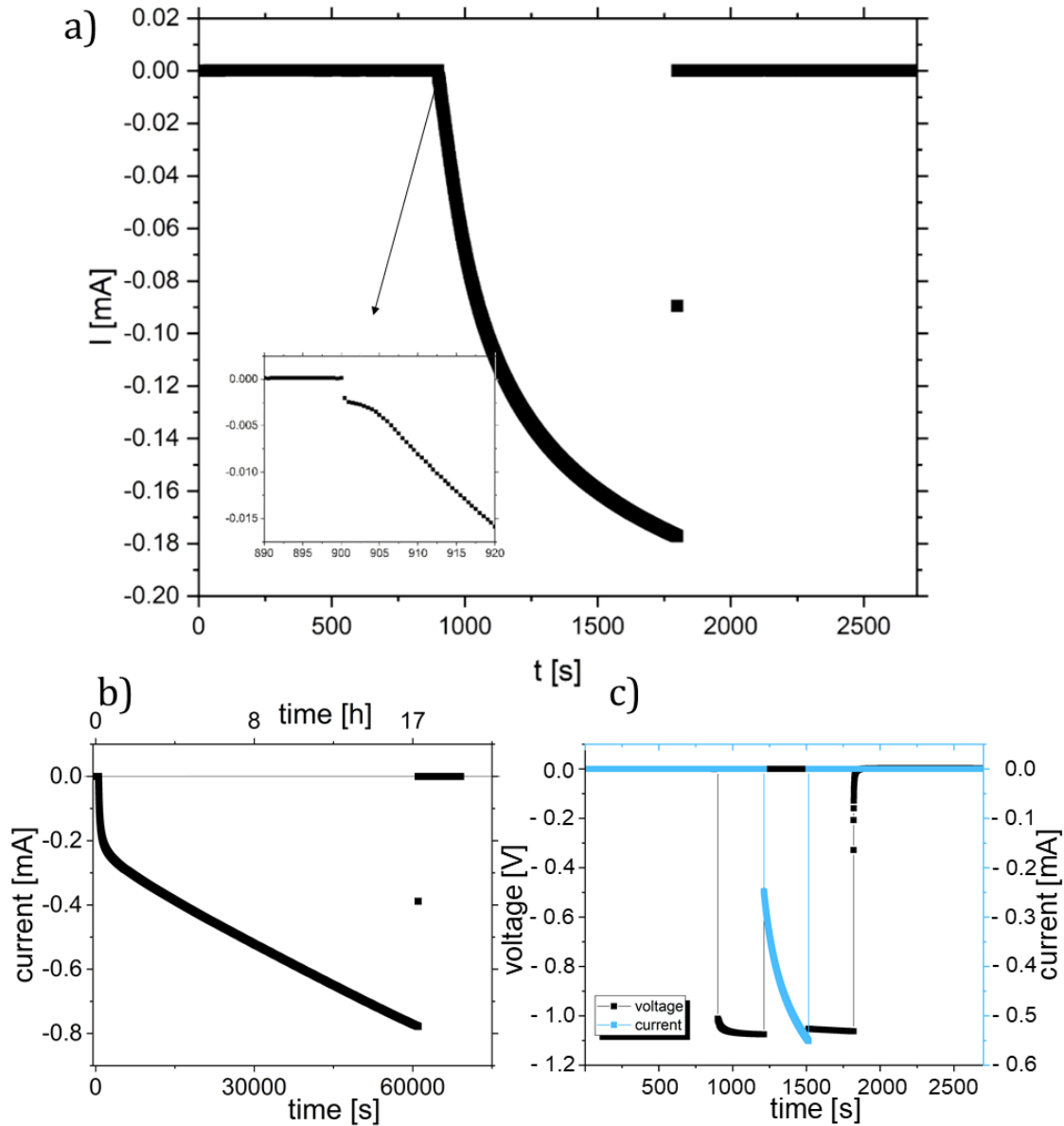


Fig. 44: Current-time measurements for LSCr10 (250 nm thickness) on SrTiO₃ at 350 °C in air (1 point/0.5 s). The measurements show a steady current increase under UV light ($\lambda = 365$ nm) on a short time scale (a) but also a continuous increase even after 17 h under UV light (b). Consecutive voltage, current and voltage measurements indicate only a small effect of the changes under current on the photovoltage (c).

We suppose that the origin of these changes upon current lies within the very nature of the measurement itself. As soon as current flows, there is a voltage drop not only at the external load but also inside the PV cell at the internal resistance. In the specific case of short circuit even the entire photovoltage of more than 1 V is “consumed” in the sample itself. SrTiO₃ is a mixed electronic and ionic conducting material and the ions are strongly blocked at one or both electrodes

used here. Applying a voltage of about 1 V to such a SrTiO_3 sample leads to oxygen stoichiometry polarization, i.e. oxygen vacancy depletion in the SrTiO_3 bulk close to the positive electrode and their accumulation close to the negative one [43, 172, 290]. Often this is associated with a resistance degradation, since also reorganization of electrons and holes takes place for the sake of charge neutrality [291, 292]. Higher conductive regions are formed near to the electrodes and then extend more and more into the bulk. Hence, a steady decrease of the cell resistance results.

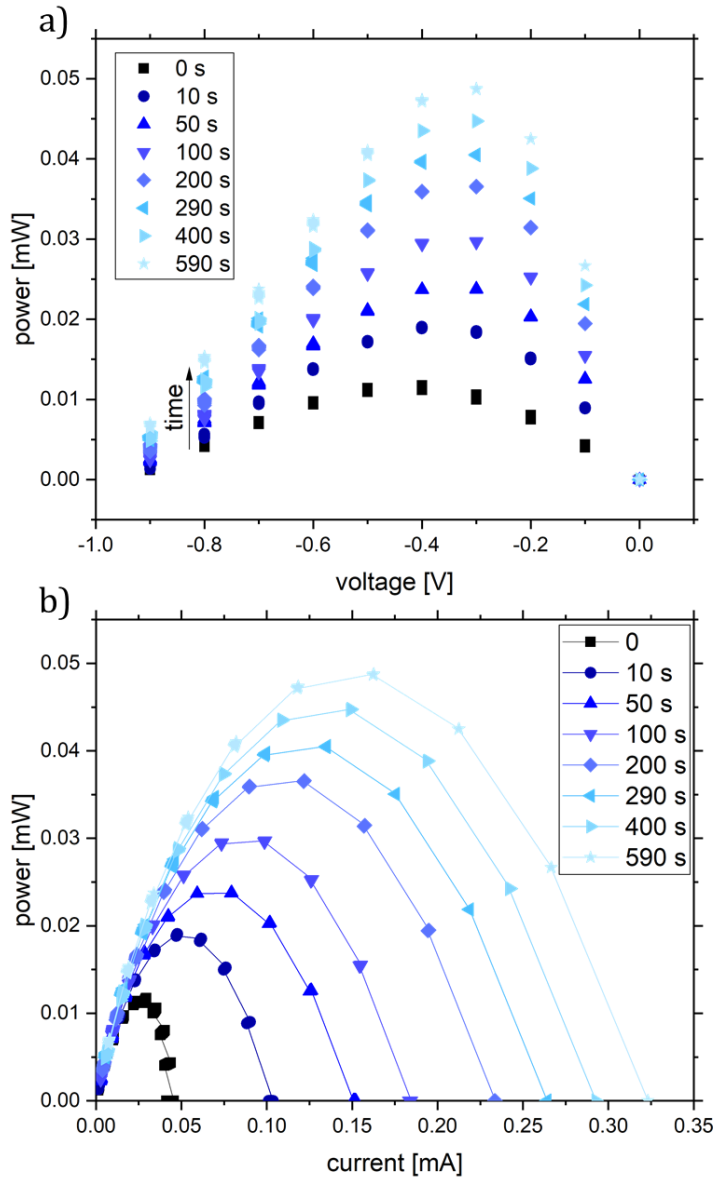


Fig. 45: Power-voltage (a) and power-current (b) curve of a UV illuminated LSCr10/SrTiO₃ cell at 350 °C in air ($\lambda = 365$ nm), highlighting the self-enhancing character of the solar cell. One measurement point requires 1 sec (i.e. 10 sec for one P(V) or P(I) curve); sample size 1 cm².

We expect the same taking place here, though the voltage is not applied by an external source, but is a consequence of the UV illumination. This effect has two implications: Firstly, measuring a well-defined current-voltage curve or a power-voltage curve is not truly possible for these SrTiO₃ based systems, since the cell unavoidably changes during the measurement. Secondly, one can benefit from this self-enhancing effect due to a decrease in SrTiO₃ resistance, leading to a better performance under operation (“self-enhancing solar cell”).

6.3.3 Electrochemical impedance spectroscopy

Electrochemical impedance spectroscopy (EIS) was performed on LSCr10/SrTiO₃ heterojunctions at 350 °C without correction of the open circuit voltage, i.e. under short circuit conditions ($U = 0$ V). Therefore, these measurements give mechanistic insight into the processes found for the current measurements discussed above. The impedance spectrum of the solar cell before illumination is shown in Fig 46.a. The three main features are a high frequency semicircle, a mid frequency arc and a very large low frequency arc. The high frequency semicircle (r.h.s inset in Fig. 8a) reflects the bulk resistance and capacitance of the SrTiO₃ single crystal, with a relative permittivity of 170 calculated from the corresponding capacitance, in accordance with bulk SrTiO₃ at 350°C [110]. The low frequency feature is attributed to the space charge region (SCR) at the SrTiO₃/LSCr10 interface [42] and represents the photoactive part of the cell, which ultimately separates the photo-generated electron-hole pairs in SrTiO₃. Some further details on this space charge impedance can be found in Ref. [42]. Actually, it is nothing but a Schottky barrier found very often between semiconductor/electrode interfaces. In accordance with Ref. [42] the intermediate frequency feature is attributed to the bottom electrode of the PV cell.

The time dependent changes in the impedance spectra under and after UV light illumination are shown in Fig. 46.b-d. The first spectrum measured immediately after switching on UV is completely distorted due to the ongoing changes upon UV and can hardly be analyzed. The second spectrum is started 3 minutes after onset of UV illumination and indicates a strong decrease of the high frequency arc, which is now only partly visible in this measured frequency range. The low frequency part with spiral-type tail indicates that the sample still changes while being measured with frequencies sweeping from high to low values. In the third spectrum (started after 15 minutes) the SrTiO₃ bulk resistance is only visible as an axis intercept and has a value which is two orders

of magnitude smaller than before UV. The remaining low frequency arc might be the remains of the photo-active top space charge layer under UV or the impedance of the bottom electrode/electrolyte contact. (Please note that even without being illuminated itself the bottom layer space charge might change under illumination due to our supposed stoichiometry variation in the SrTiO₃ bulk.) When switching off UV the huge top layer space charge is back already in the very first spectrum (Fig. 46.c), while the high frequency arc of bulk SrTiO₃ only slowly relaxes and increases from spectrum to spectrum. After about 50 minutes the original value is again reached.

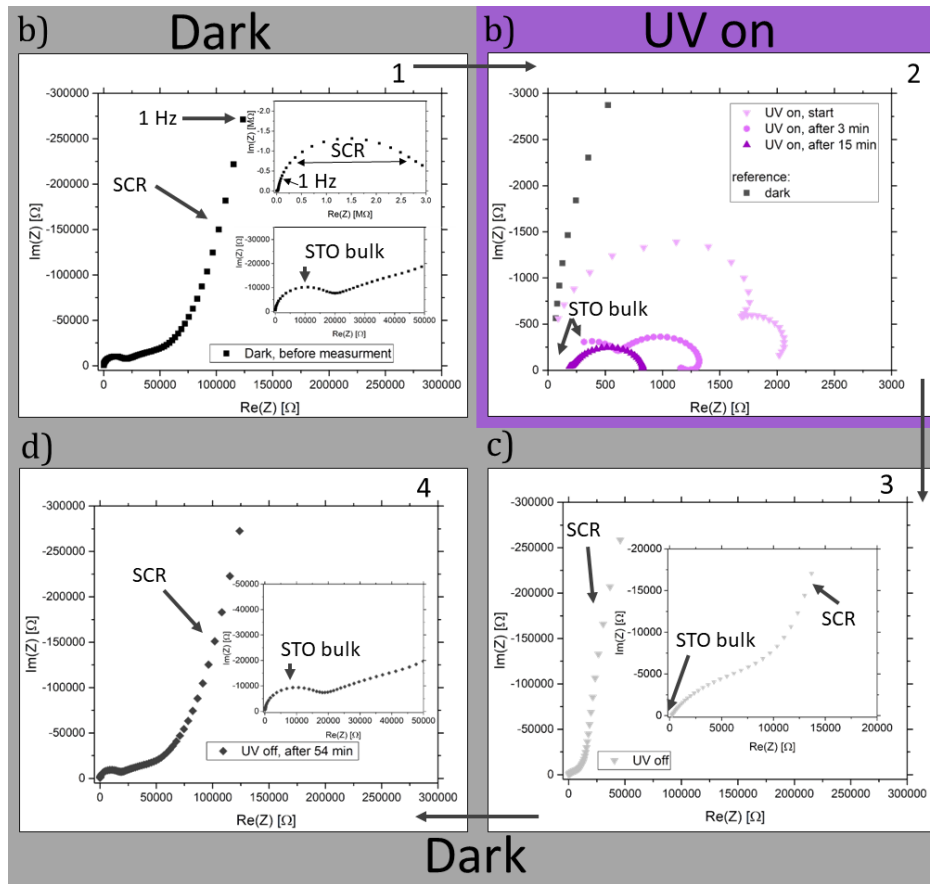


Fig. 46: Impedance spectra of LSCr10/SrTiO₃ samples at 350 °C in air in darkness and under UV light ($\lambda = 365 \text{ nm}$) with: (a) Impedance spectrum of a LSCr10/SrTiO₃ solar cell without UV illumination (“dark”). The three main features are the high, mid and low frequency semicircle. The high frequency semicircle (ω_p approx. 80 kHz) is attributed to the bulk SrTiO₃. The low frequency semicircle (ω_p approx. 0.080 Hz) originates from the space charge region (SCR) at the LSCr/SrTiO₃ interface. The mid frequency feature most likely comes from the bottom electrode. (b) Time dependent evolution of impedance spectra during UV light illumination and (c,d) after UV. The contributions of SrTiO₃ bulk resistance (STO) as well as the resistance of the space charge region (SCR) are identified in the individual impedance spectra. Under UV light, two processes take place: i) The very fast vanishing of the space charge resistance; ii) the continuous drop in SrTiO₃ resistance upon switching on the UV light due to stoichiometry polarization.

From this we conclude that indeed the conductivity and thus also the defect chemical state of the SrTiO₃ bulk changes upon UV under short circuit conditions. As detailed above, this change is most probably nothing but the well-known stoichiometry polarization often found in SrTiO₃ samples upon a voltage, when one or both electrodes are strongly blocking for ionic current, i.e. electrochemical oxygen exchange.

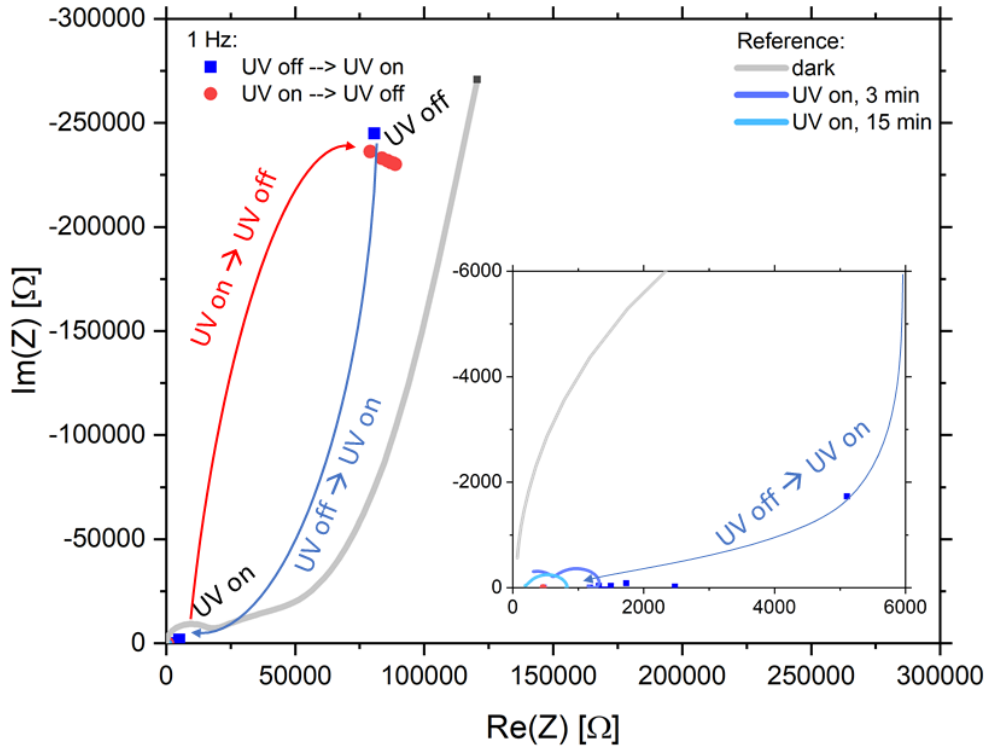


Fig. 47: EIS measurements of a LSCr10/SrTiO₃ cell at 350 °C in air at only 1 Hz for a better time resolution (the grey reference line represents the full spectrum in dark from Fig. 8). The process of switching the UV light ($\lambda = 365$ nm) on leads to lower resistances (i.e. 1 order of magnitude) within the time resolution of 1 second (blue squares). Under UV light, there is a slight, but steady decrease in resistance. Upon switching off the UV light, a very fast increase in resistance (within 1 second) is observed (red circles).

In order to support the consistency of this interpretation, we further looked at the time dependence of the large space charge resistance under and after UV. Since recording an entire impedance spectrum takes several minutes, the time resolution was not sufficiently high to follow this very fast process. Therefore, impedance was measured continuously at 1 Hz (see Fig. 47). This impedance value is in the left half of the space charge arc measured in dark. The location of this frequency within the corresponding arc changes under illumination. However, we also know the

shape of the impedance spectra before, under and after UV light illumination (Fig. 46), which makes analysis straightforward. We see that the impedance at 1 Hz and thus the entire space charge arc changes immediately (i.e. within less than one second) and drastically when illuminating by UV light. This is in line with the immediate changes found in current measurements in Fig. 42. This immediate change under UV light is followed by a steady further decrease in the resistance, which reflects the self-improvement of the cell discussed above. When switching back to dark the huge space charge arc appears again within the first second and the subsequently following slight shift in Fig. 47 might be simply due to the change of the SrTiO₃ bulk itself, which is much slower

6.3.4 Interpretation of the OCV measurements

One characteristic feature of these cells has still to be interpreted: It is the time dependence of the cell voltage under OCV conditions (see Fig. 41). The space charge relaxes within a second when UV light is switched off (see above) and thus zero voltage is expected immediately when stopping illumination. Stoichiometry changes upon current flow (as in the short circuit case) can also not explain these finding since no current flows under OCV. However, we are confident that stoichiometry changes in SrTiO₃ upon UV still play a decisive role as discussed in the following. Our explanations are based on interpretations of UV induced effects in SrTiO₃ single crystals reported in Ref. [13, 40, 41].

In Ref. [40], a strong enhancement of the oxygen incorporation rate into Fe-doped SrTiO₃ was found under UV illumination. Moreover, in Ref. [41], it was shown that substantial conductivity changes result during and after illumination of such SrTiO₃ single crystals. Importantly, these conductivity changes also affect the dark parts of the SrTiO₃ beyond the absorption depth. They are associated with stoichiometry changes due to UV-accelerated oxygen incorporation. Essentially, the hole conductivity of the entire SrTiO₃ sample strongly increases under illumination due to oxygen vacancies being annihilated under UV in the entire bulk. The corresponding time dependence of the conductivity changes upon UV is governed by the chemical diffusion coefficient of oxygen in SrTiO₃. This chemical diffusion is slower for Fe-doped SrTiO₃ compared to undoped SrTiO₃ due to the trapping of hole charge carriers [293]. In other words: the oxygen chemical potential of an illuminated SrTiO₃ samples changes under UV due to oxygen incorporation and when switching off UV, a very high chemical potential (nominal by high oxygen partial pressure) remains in the sample. This can be measured in terms of a positive voltage, particularly when

covering the bottom side of SrTiO₃ with an ion conducting yttria stabilized zirconia (YSZ) layer and thus making SrTiO₃ to a kind of electrode in an electrochemical cell [13]. The measured voltage is nothing but a Nernst-type voltage between the SrTiO₃ (no longer in equilibrium with the gas) and the YSZ covered bottom side. This is sketched in Fig. 48.a, together with the typical voltage curve found in such cells [13] with a mixture of fast photo-effect and slower stoichiometry effects. Most important is the remaining voltage after UV (U_{bat}) which is due to the chemical potential change in SrTiO₃ under UV and only slowly relaxes at ca 350 °C.

Compared to the cell in Ref [13], the top side is continuously covered in our solar cell, e.g. by LSCr, and the ion conducting bottom YSZ layer is missing (see Fig. 48.b). As in the cell with the free SrTiO₃ surface, similar time dependencies are found, but first the voltage further increases upon UV and second the remaining voltage after UV is negative in our case. The following explanation of these phenomena is still hypothetical, but consistent with all data we have so far: The chemical potential of oxygen μ_{O} is given by the difference of the chemical potentials of ionic and electronic species (V_{O} = oxygen vacancies, e = electrons, h = holes):

$$\mu_{\text{O}} = \mu_{\text{O}^{2-}} - 2\mu_e = -\mu_{V_{\text{O}}} + 2\mu_h. \quad (\text{Eq. 16})$$

In contrast to cell type a in Fig. 48 (with free illuminated SrTiO₃ surfaces), UV light does not directly accelerate oxygen incorporation kinetics into SrTiO₃ since the surface of cell b is covered by LSCr. However, in the illuminated part of SrTiO₃ ($\approx 2\text{-}3 \mu\text{m}$ deep as resulting from SE measurements) the UV light causes a split of \square_e into two quasi Fermi levels (one for electrons and one for holes). Therefore, also two quasi chemical potentials of formally neutral oxygen result in accordance with Eq. 16. Owing to a spatially varying absorbance, those quasi chemical potentials show gradients and cause oxygen diffusion within SrTiO₃. Depending on the local concentrations of holes and electrons, the illuminated SrTiO₃ region gets either enriched or depleted of oxygen vacancies. Supposed we pump some oxygen from the illuminated region into the dark part (by chemical diffusion of vacancies and holes), a situation results where the illuminated part has a different defect chemical state and thus also a different (quasi-)Fermi level compared to the initial situation under UV. Not surprisingly the open circuit voltage changes during this oxygen relocation inside SrTiO₃ and this is what supposedly causes the time dependence of the OCV voltage under UV. In Fe-doped SrTiO₃ the change is simply slower since it has a smaller oxygen diffusion coefficient due to its Fe-traps [293]. A simple estimate of a diffusion distance from the measured time of voltage variation (ca. 1000 seconds for Fe- SrTiO₃) and the oxygen diffusion coefficient D in Fe- SrTiO₃ at this temperature ($10^{-8} \text{ cm}^2/\text{s}$ [166, 294]) gives $3 \mu\text{m}$, which is well in line with the

illuminated SrTiO₃ depth according to SE.

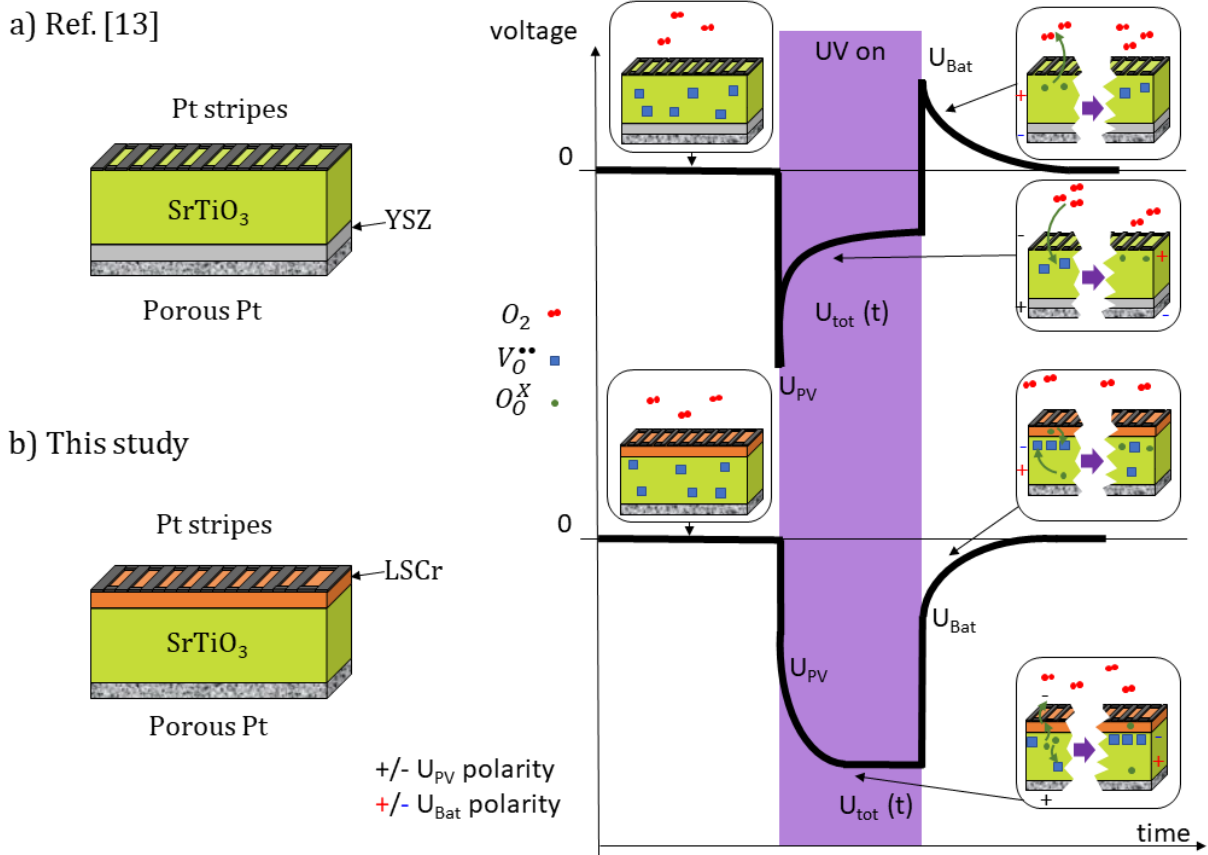


Fig. 48: Schematic representation of a sample with Pt stripes on top of an SrTiO₃ single crystal and a YSZ bottom layer as an electrolyte used in Ref. [13] (a) as well as a sample with a LSCr top layer on an SrTiO₃ single crystal (b). On the right hand side of each sample, the respective voltage-time curve is sketched, highlighting the time dependent processes under UV light. The polarity of the respective voltages, U_{PV} and U_{Bat} , are indicated.

When switching off UV, all PV effects are gone but the formerly illuminated layer is still enriched in oxygen vacancies and has a lower chemical potential of oxygen compared to the rest of the SrTiO₃. This causes a Nernstian cell voltage with an opposite sign compared to the cell in Fig. 48.a (Here the required ion conductor is no longer YSZ, but the SrTiO₃ zone with oxygen vacancies.) The oxygen chemical potential finally relaxes by diffusion inside SrTiO₃ but also by some oxygen incorporation across the top layer and rather quickly decays. Supposed the oxygen incorporation via the top layer is the decisive process during this relaxation, also the same time dependence for Fe:SrTiO₃ and SrTiO₃ can be explained. We are well aware that despite explaining our findings, the given model is not sufficiently backed by independent measurements yet. However, the exact

validation requires many further studies and is beyond the scope of this paper; it is the topic of ongoing and future work.

6.4. Conclusion

Heterojunctions of SrTiO₃ with semi-transparent thin films of different LSCr compositions or Au provide high photovoltages up to more than 1 V at 350 °C. The underlying effect seems to be very robust as both metals and ceramic materials work as a top layer, provided sufficient transparency of the thin film is given. The typically hole depleted space charges of the Schottky contact at the SrTiO₃/top layer interfaces are responsible for the photovoltaic effects. When measuring the current of operating cells, a strong self-enhancing effect due to stoichiometry polarization in the SrTiO₃ single crystal is found. This may increase the current by orders of magnitude while leaving the open circuit photovoltage at its high value. Electrochemical impedance spectroscopy revealed details of the processes under UV light. Two processes under UV light could be identified: Immediately “switching off” the resistance of the space charge region and a continuous drop of the resistance of bulk SrTiO₃ due to stoichiometry polarization. A surprising time dependence of the photovoltage and its slow decay in dark is associated with compositional changes in illuminated SrTiO₃ due to formation of modified oxygen quasi-chemical potentials therein.

Chapter 7: Completing the circle: Application of thin films in SrTiO₃ based solar cells

This chapter is based on the diploma thesis written by Niklas Bodenmüller.

7.1 Introduction

Photovoltaic applications including photovoltaic cells [26, 197, 213, 221, 222, 231] or photo-sensors [179, 180, 185, 295] are reported for (doped) SrTiO₃, mostly operating at room temperature or even below. In oxide materials, at these temperature electronic processes dominate. However, in organohalide perovskite solar cells, even low temperatures suffice for ionic contributions, leading to the rather new and fascinating field of photo-ionics (or opto-ionics) [51]. At higher temperatures, ionic processes also take place in oxides [40, 51]. For SrTiO₃, photo-induced ionic effects are mostly studied for single crystals [13, 41]. In this study, the goal is therefore to evaluate the application thin films in high temperature photovoltaic cells. The advantage of thin films is a potential increase in power due to the lower expected resistance and smaller size, which is relevant for energy micro harvesting applications [19, 296]. However, for thin films, strongly deviating electrochemical behavior has been reported in literature [31, 32] and in Chapters 2 and 3. Therefore, the influence of different defect states and especially the role of cation vacancies on the photovoltage is investigated. Here, polycrystals were also used as a system to investigate the influence of cation nonstoichiometry.

7.2 Experimental

7.2.1 Preparation of pellets

SrTiO₃ pellets were prepared with different Sr/Ti ratios using SrCO₃ (99.995 %, sigma Aldrich, USA) and TiO₂ (99.995 %, Alfa Aesar, USA). The powders were weight in according to the respective stoichiometry of Sr_{0.995}TiO₃, SrTiO₃ and Sr_{1.005}TiO₃. For better mixing, the powders

were milled for 40 min by hand in an agate mortar. Then, the powders were pressed for 10 min using an isostatic press and the obtained pellets were calcined in a corundum crucible at 1150 °C for 3 – 4 h. During heating up, the temperature was held constant at 400 °C for 1 h for outgassing. Again, the pellets were milled and pressed isostatically. The obtained pellets were sintered twice at 1500 °C for 12 h in air. At the bottom, porous Pt paste was brushed on as a counter electrode. As a top electrode, Pt thin films were deposited via DC magnetron sputtering (BAL-TEC MED 020 Coating System; pressure: 2×10^{-2} mbar Ar, 100 mA) using a shadow mask.

7.2.2 Preparation of thin films

Different single crystalline substrates were used in this study, namely undoped SrTiO₃ (STO, 10 x 10 x 0.5 mm³, CrysTec GmbH, Ger), 0.5 % Nb doped SrTiO₃ (Nb:STO, 10 x 10 x 0.5 mm³, CrysTec GmbH, Ger), and 9.5 % Y₂O₃ doped ZrO₂ (YSZ, 10 x 10 x 0.5 mm³, CrysTec GmbH, Ger), all in (100) orientation, and Al₂O₃ (10 x 10 x 0.5 mm³, CrysTec GmbH, Ger) in (0001) orientation.

Metal thin films as well as oxide thin films were fabricated in this study. For preparing the oxide top layer, pulsed laser deposition (PLD) was employed. As a laser source a Kr/F excimer laser Lambda COMPex Pro 201F with a wavelength 248 nm was used with a repetition rate of 5 Hz and a laser fluence of 1.1 J/cm². La_{0.9}Sr_{0.1}CrO₃ (LSCr10) and La_{0.6}Sr_{0.4}CoO₃ (LSC) thin films were deposited at 700 °C and 0.015 mbar or 0.04 mbar, respectively. Nominally undoped and Cr or Fe doped SrTiO₃ (STO, Fe:STO, Cr:STO) thin films were prepared at 0.15 mbar at 650 °C. YBa₂Cu₃O₇ (YBCO) thin films were deposited at 700 °C at 0.15 mbar. Pt thin films were used as current collectors on top of the sample and were deposited using DC magnetron sputtering (BAL-TEC MED 020 Coating System; pressure: 2×10^{-2} mbar Ar, 100 mA). The Pt film was structured via lift-off photolithography. Porous Pt paste was used as a counter electrode. Continuous Pt top layers with 10 nm in thickness were also used as current collectors.

7.2.3 Voltage measurements

Photovoltage measurements were performed in a quartz tube furnace with symmetrical heating or in a micro-contact setup with asymmetrical heating, both described in Ref. [76]. UV light with a wavelength of 365 nm and a power of 2.9 W is used in this study. Voltage measurements were

carried out on a Keithley DMM2000 (Keithley Instruments, USA) at 350 °C in air. After equilibration, the usual measurement program consisted of 15 min in dark, followed by 15 min under UV light irradiation and, finally, again 15 min in darkness.

7.3 Results

7.3.1 Polycrystalline solar cells

Different SrTiO₃ polycrystals were investigated in regard to their photovoltage. A typical sample is sketched in Fig. 49.a. (Note that these geometries do not have a thin oxide film as a top layer, but rather correspond to the sample design in Ref. [13] for single crystals.) The samples differed in their cation stoichiometry (i.e. Sr/Ti ratio), with nominally Sr deficient, stoichiometric, and Sr overstoichiometric SrTiO₃, corresponding to a Sr/Ti ratio of 0.995, 1.000 and 1.005, respectively. The real defect situation in these pellets, however, might differ from the nominal composition due to the Schottky reaction at high temperatures (i.e. during sintering) [34, 44].

The photovoltages obtained for these three different compositions are plotted in Fig. 49.b. For the dark voltage measured before UV illumination, only slight differences are visible. Upon UV illumination, photovoltages in the range of up to 50 mV were measured, with slight deviations in the total photovoltage for the different compositions. However, rather pronounced differences in the time dependent behavior can be seen when switching the UV light off. Here, the photovoltage of the nominally stoichiometric SrTiO₃ sample decays fast to the initial dark voltage. The sample with nominal Sr overstoichiometry (i.e. titanium vacancies) takes significantly longer. For the sample with Sr deficiency, the decay in photovoltage is the slowest in this study and the initial dark voltage is not reached within 15 min after switching the light off. In single crystals, this voltage is attributed to oxygen vacancy related processes in SrTiO₃ [13]. Here, the differences in cation stoichiometry appear to influence the oxygen release and/or oxygen vacancy diffusion. Alternatively, differences due to grain boundaries could play a role.

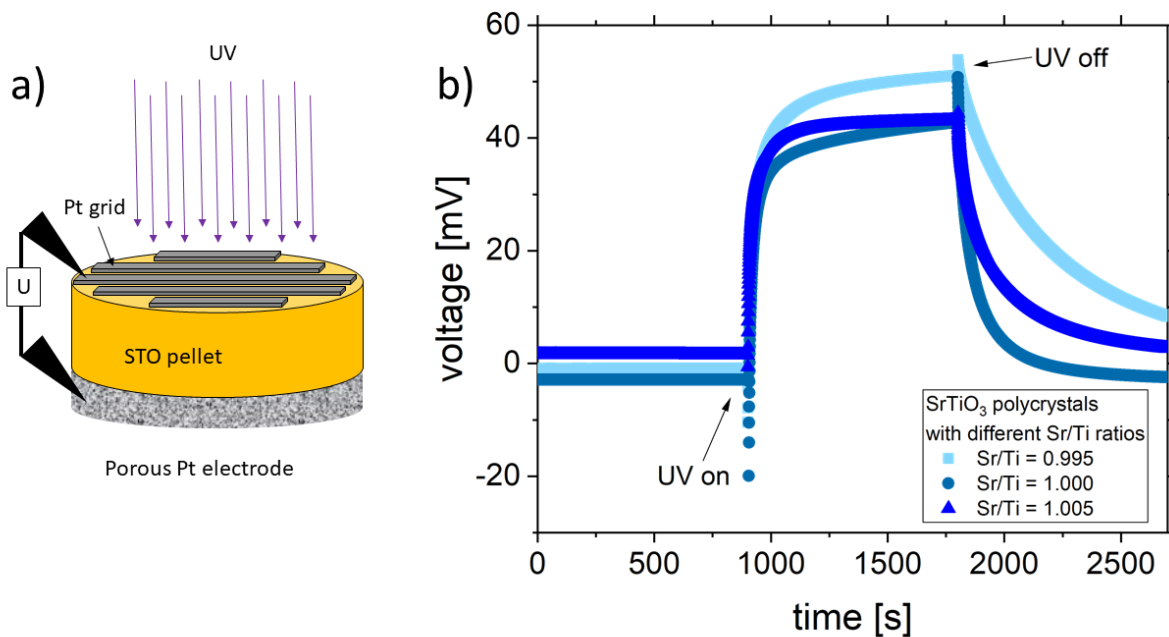


Fig. 49: Photovoltage experiments on polycrystalline SrTiO_3 (STO) samples. A sketch of the sample consisting of a SrTiO_3 polycrystal with a Pt grid on top and a porous Pt counter electrode on bottom is shown in (a). In (b), time dependent voltage measurements for SrTiO_3 pellets with a different nominal Sr/Ti ratio are plotted. The first 900 s are in dark, revealing slight differences in the dark voltage of the samples with different cation stoichiometry. Under UV, a time dependency of the photovoltage is observed, with photovoltages in the range of 40 – 50 mV. Upon switching the UV light off, we see a time dependent decay, with even more pronounced differences for the different samples. Nominally stoichiometric SrTiO_3 decays the fastest, while the Sr deficient sample takes much longer times.

7.3.2 Towards thin film cells: Introduction of additional SrTiO_3 layers in single crystal based solar cells

In this case, nominally undoped or doped SrTiO_3 layers (X:STO where X denotes the dopant) were deposited on top of SrTiO_3 single crystals and, subsequently, $\text{La}_{0.9}\text{Sr}_{0.1}\text{CrO}_3$ top layers were deposited via pulsed laser deposition. A sketch of such a sample is shown in Fig. 50.a. The results of the photovoltages are plotted in Fig. 50.b.

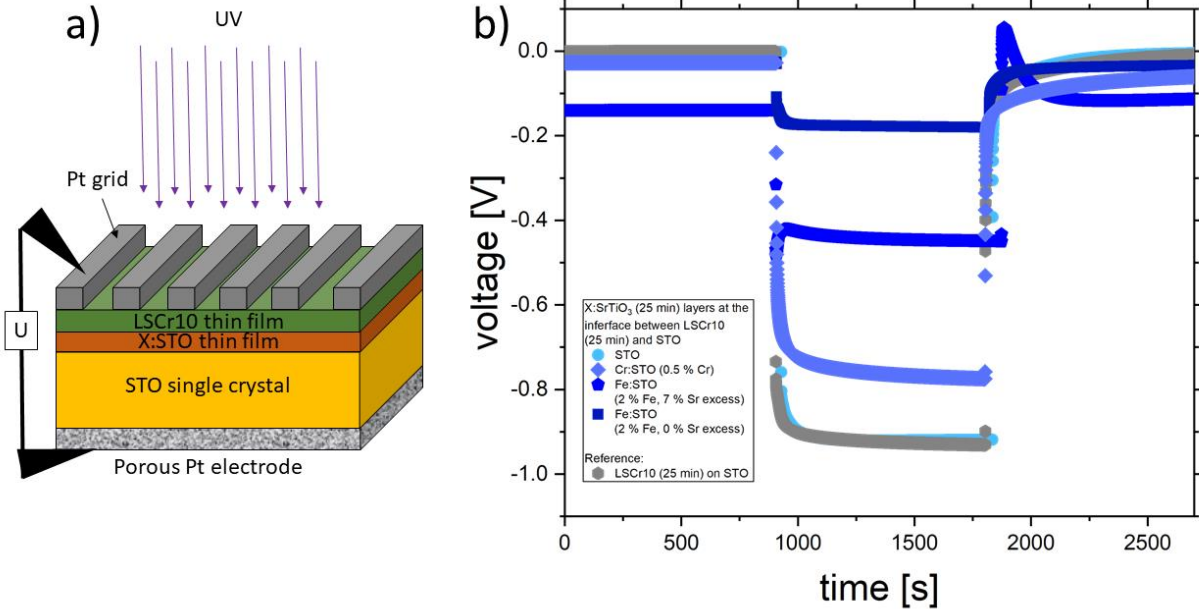


Fig. 50: Photovoltage measurements for samples with interfacial SrTiO_3 thin films. The sample consists of an SrTiO_3 (STO) single crystal with a (doped) SrTiO_3 ($X:\text{STO}$, with X being the dopant element) thin film and an $\text{La}_{0.9}\text{Sr}_{0.1}\text{CrO}_3$ (LSCr10) thin film on top (a). For electrical contact, a Pt grid is used on top and a porous Pt counter electrode on bottom (a). The time dependent measurements reveal a strong influence of the dopant element of the SrTiO_3 thin film on the resulting photovoltage (b). No change in photovoltage is observed for a nominally undoped thin film compared to a sample without an SrTiO_3 thin film (see chapter 6). Cr and Fe doping in the thin film lead to severe changes in the photovoltage, with the most drastic decrease in photovoltage occurring for a $\text{Fe}:\text{SrTiO}_3$ thin film deposited from a stoichiometric target (see chapter 2 and chapter 3).

Here, the influence of additional SrTiO_3 thin films (doped or undoped) are easily visible: Nominally undoped SrTiO_3 thin films do not change the photovoltage compared to the reference consisting just of a SrTiO_3 single crystal and the respective $\text{La}_{0.9}\text{Sr}_{0.1}\text{CrO}_3$ top layer (see chapter 6). In contrast, doped SrTiO_3 thin films between the single crystal and the $\text{La}_{0.9}\text{Sr}_{0.1}\text{CrO}_3$ top layer lead to a significant change in photovoltage. In the case of Cr doped SrTiO_3 thin films with a nominal Cr concentration of 5 %, a decrease in photovoltage by 150 mV is observed. For Fe doping, an even more pronounced decrease in photovoltage is obtained. Here, two different Fe doped thin films were used: The Fe doped thin film deposited from a stoichiometric target with 2 % Fe yields about -200 mV, which corresponds to a decrease in photovoltage by 750 mV compared to the reference. When using a thin film deposited from a 2 % Fe doped target with 7 % Sr excess (see chapter 2), a photovoltage of approx. -450 mV is obtained, corresponding to a decrease by 500 mV

compared to the reference. In both cases, a severe decrease in photovoltage is observed, but the thin film with ideal stoichiometry (see chapter 2) yields more than double the photovoltage of the Sr deficient thin films, thus revealing the drastic influence of cation stoichiometry on the photovoltage. In this regard, the nearly unaffected photovoltage obtained with the undoped SrTiO₃ thin film (which also has Sr deficiency, see chapter 3) is rather surprising. However, this effect is addressed in section 7.4.

7.3.3 Thin film based solar cells

Since nominally undoped SrTiO₃ thin films worked for solar cells with interfacial thin films, solar cells based on SrTiO₃ thin films were prepared. Three different geometries were investigated and all are shown in Fig. 51.d-f. The photovoltage for the Nb:SrTiO₃ based solar cell (see Fig. 51.d) is plotted in Fig. 51.a. Here, a photovoltage of about 160 mV is found. Note that the sign of the photovoltage is positive here. In chapter 6, only negative photovoltages were obtained for the La_{0.9}Sr_{0.1}CrO₃/SrTiO₃ heterojunction. This suggests that the photovoltage measured in Fig. 51.a does not originate from the La_{0.9}Sr_{0.1}CrO₃/SrTiO₃ heterojunction, but rather from the SrTiO₃/Nb:SrTiO₃ p-n junction. For the yttria stabilized zirconia (YSZ) based sample in Fig. 51.e, a photovoltage of -120 mV was measured (see Fig. 51.b). Thus, photovoltages are much lower than for the SrTiO₃ single crystal based solar cells. Furthermore, a surprisingly high dark voltage was found upon switching the UV light off. In Fig. 51.c, the results for the Al₂O₃ based sample (see Fig. 51.f) is shown. With this sample geometry, next to no effect was found.

All these thin film based solar cells have an unexpectedly low photovoltage in common. Different possible problems of these thin film based solar cells are identified:

- Pinholes: Pinholes, i.e. small areas uncovered by the respective oxide layer, might lead to a short circuit when contacted with Pt (e.g. Pt current collector).
- Thin film related issues: As established in previous chapters, the defect chemistry of thin films differs significantly from single crystals. Differences in the Fermi level influence the photovoltage. Moreover, their often strongly increased defect concentrations may enhance the recombination rate.

- Substrate effects: The high photovoltage for the undoped SrTiO₃ thin film on top of a SrTiO₃ single crystal in section 7.3.2 might not be a result of the thin film, but rather of the underlying SrTiO₃ substrate.

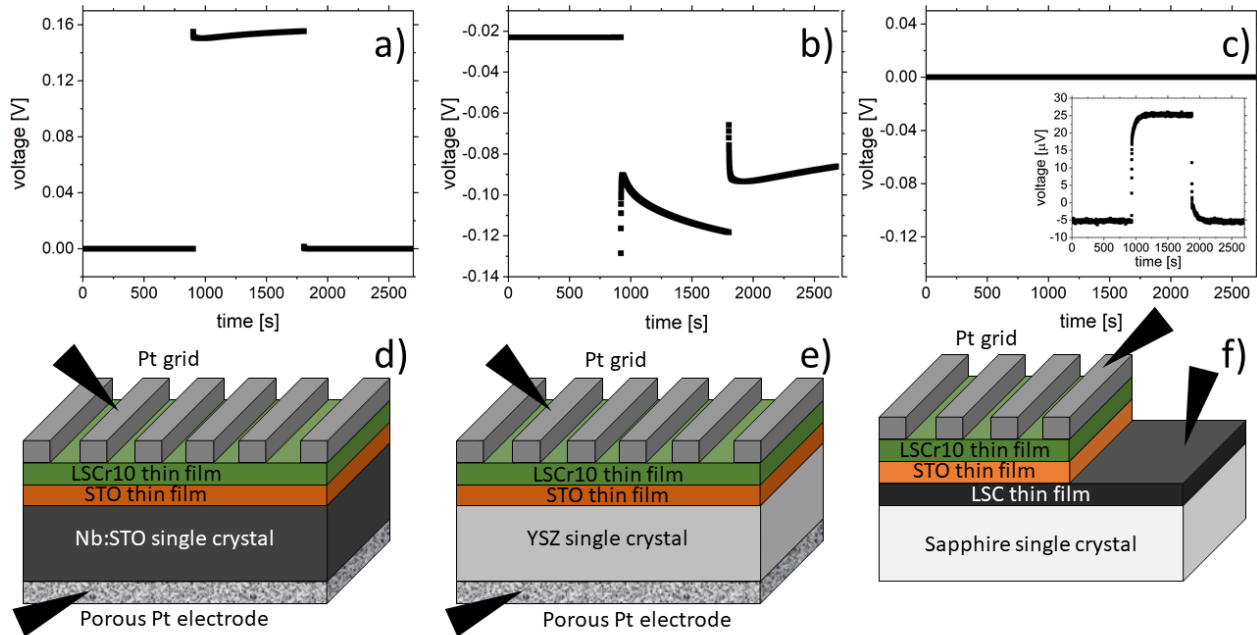


Fig. 51. Photovoltages on thin film cells. In (a), (b), and (c), the voltage vs. time curves are shown for the respective sample geometries in (d), (e), and (f). For the measurement in (a) for sample (d), a photovoltage in the range of 160 mV with a positive sign is obtained, while for $\text{La}_{0.9}\text{Sr}_{0.1}\text{CrO}_3/\text{SrTiO}_3$ heterojunctions only photo voltages with a negative sign were obtained so far in this study. Thus, the origin of the photovoltage could be the $\text{SrTiO}_3/\text{Nb}:\text{SrTiO}_3$ p-n junction. The photovoltages measured in (b), corresponding to (e), are in the range of -120 mV, showing a negative sign as expected. However, severe time depend changes occur after switching the UV light off. In the voltage-time curve in (c) for the sample geometry in (f), next to no photovoltage is obtained.

7.3.4 Microelectrode measurements

Since the first attempts of thin film based SrTiO₃ solar cells did not result in the expected photovoltages, another approach was carried out. Four samples were fabricated which should help distinguishing between the individual issues. Using microelectrodes, pinholes are expected to be less problematic due to the smaller size. In addition, the substrate variation, using nominally undoped SrTiO₃ and Nb:SrTiO₃. In the case of nominally undoped SrTiO₃, a contribution of the

substrate to the measured photovoltage is possible. When switching to Nb:SrTiO₃, a different heterojunction is formed, which could influence the photovoltage in a different way. Pinholes (if present in the thin films) are not expected to change the result for undoped SrTiO₃ substrates, but are expected to drastically influence the results for Nb doped SrTiO₃ single crystals. Due to the need for micro-contact measurements, the measurement setup was changed from the tube furnace to an asymmetrically heated micro-contact setup described in Ref. [76].

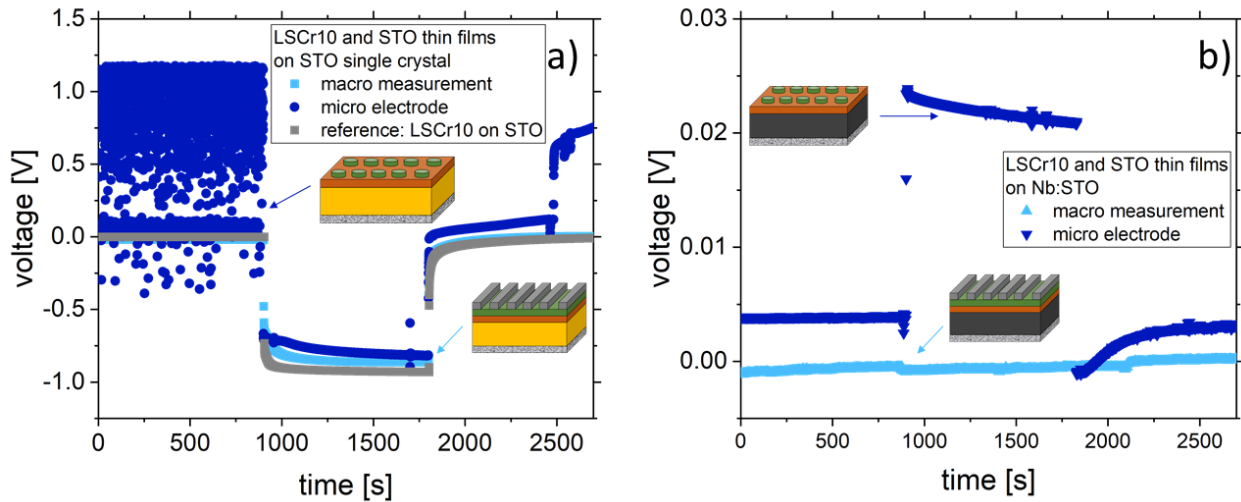


Fig. 52: Application of microelectrodes for photovoltage measurements. In (a), photovoltages obtained for SrTiO₃ single crystals in two different geometries are compared: The sample with microelectrodes shows good agreement with the “macro” geometry (which is the standard geometry used so far) under UV light irradiation. Only in dark, the measurement with microelectrodes is strongly influenced by noise. In (b), a Nb:STO single crystal is used as a substrate and the macro geometry is compared to microelectrode measurements. Here, next to no photovoltage is obtained for the macro geometry. In contrast, a photovoltage of 20 mV (note the positive sign) is observed when using microelectrodes.

The results for the La_{0.9}Sr_{0.1}CrO₃/SrTiO₃ interface on top of a SrTiO₃ single crystal are shown in Fig. 52.a. In dark, the measurement using microelectrodes is heavily dominated by noise. Upon switching the UV light on, the noise vanishes and a photovoltage of -820 mV (further increasing up to -860 mV) is measured, which is in line with the results for the macro sample. The higher noise is attributed to the increased resistance. Therefore, microelectrodes can be a suitable tool for photovoltage measurements in high temperature photovoltaic cells, with their results being well transferable to macro geometries. For the Nb:SrTiO₃ based macro sample in Fig. 52.b, only a photovoltage in the range of -0.5 mV is found, which is significantly lower than the photovoltages found in SrTiO₃ based samples. Note that it is also significantly lower than the photovoltage for a

similar sample measured in the tube furnace (see Fig. 51.a), highlighting the possible influence of pinholes in this sample. When switching to the microelectrodes, a higher photovoltage of about 20 mV is found (cf. Fig. 52.b), accompanied with a change in the sign of the voltage. While the photovoltage is still lower than in Fig. 51.a, these measurements are in line in regard to the change in the sign of the photovoltage observed for this system. For microelectrode measurements, we do not expect pinholes to be a problem as this setup was also used for all conductivity measurements on SrTiO₃ thin films, yielding proper results, see chapter 2 and chapter 3. However, for the photovoltage measurements, still a significant change in open circuit photovoltage between the thin films deposited on the two different substrates is observed. Since pinholes are ruled out here, we can pin down the problem to either thin film or the substrate or an interplay of both factors. From these measurements we conclude that the photovoltages are strongly affected by the bottom interface and it seems that the underlying SrTiO₃ substrate plays a crucial role for the high photovoltages found in the respective sample geometries.

7.3.5 A new hope: Using an ohmic contact

As shown previously, photovoltages originating in SrTiO₃ single crystals are much larger than their counterpart in thin film cells and SrTiO₃ thin films on SrTiO₃ single crystals seem to behave different than the single crystal. In order to further analyze this effect, the top layer was adjusted accordingly. YBa₂Cu₃O₇ (YBCO) is reported in literature as an ohmic contact for SrTiO₃ [297]. Hence, photovoltaic cells consisting of SrTiO₃/YBa₂Cu₃O₇ or SrTiO₃/SrTiO₃/YBa₂Cu₃O₇ interfaces were prepared. A sketch of these samples is shown in Fig. 53.a and 53.c, respectively. The photovoltage measured for the sample shown in Fig 53.a is plotted in Fig. 53.b. Here, only a small photovoltage of about -100 mV is observed. In contrast, the photovoltage measured for the sample plotted in Fig. 53.c is in the range of -450 mV (see Fig. 53.d). In this case, the micro-contact measurement was used, but – as established in section 3.4 – the differences between the different setups are rather small voltages, tending to be even lower in the micro-contact setup than in the tube furnace. Here, a drastic increase in photovoltage by nearly a factor of five is observed for the addition of the SrTiO₃ thin film between the single crystal and the YBa₂Cu₃O₇. While we cannot be completely sure as to where the photovoltage originates (at this point both YBa₂Cu₃O₇/SrTiO₃ thin film and SrTiO₃ thin film/SrTiO₃ single crystal interfaces might be the origin of the

photovoltage), we can surely conclude that there is a significant difference between the SrTiO_3 thin film and substrate in regard to photovoltage generation. The difference between the two sample geometries is addressed in section 7.4.

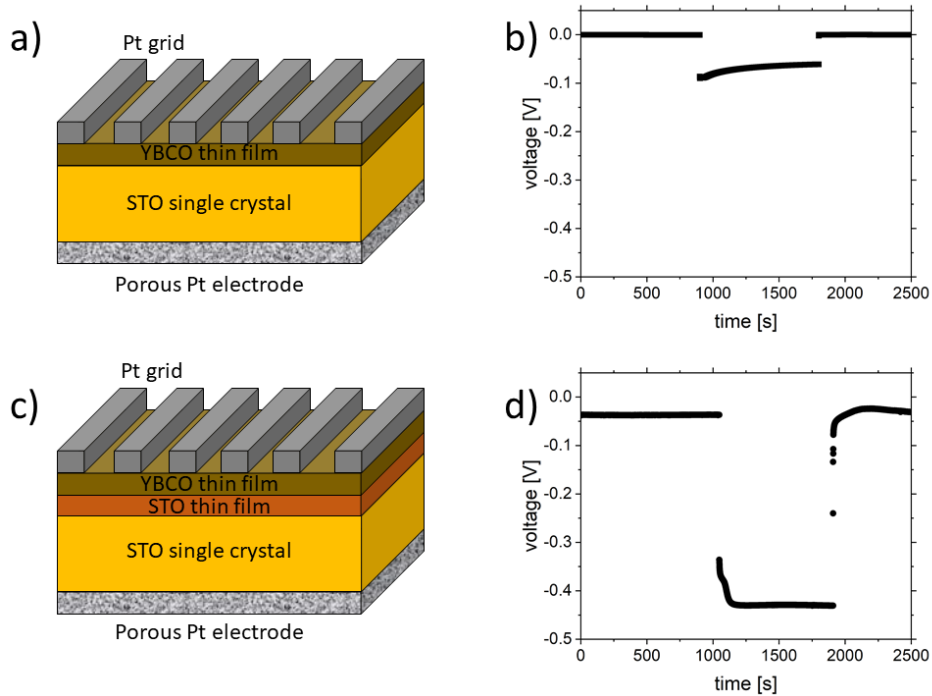


Fig. 53: Photovoltage measurements using $\text{YBa}_2\text{Cu}_3\text{O}_7$ (YBCO) thin films. When using $\text{YBa}_2\text{Cu}_3\text{O}_7$ as a thin film on top of an SrTiO_3 single crystal (a), a rather low photovoltage in the range of -100 mV results. In contrast, when using an SrTiO_3 thin film between the $\text{YBa}_2\text{Cu}_3\text{O}_7$ thin film and the single crystal (c), a drastic increase in photovoltage is observed, yielding -450 mV (d). While the origin of the photovoltage (i.e. either $\text{YBa}_2\text{Cu}_3\text{O}_7/\text{SrTiO}_3$ thin film or SrTiO_3 thin film/ SrTiO_3 substrate) is unclear, we can conclude a deviation in the behavior of SrTiO_3 thin film and single crystal in terms of photovoltage generation.

7.4 Discussion

In this study, a different behavior between thin film cells and single crystal based cells is observed. Here, two systems are addressed, namely $\text{La}_{0.9}\text{Sr}_{0.1}\text{CrO}_3/\text{SrTiO}_3$ and the $\text{YBa}_2\text{Cu}_3\text{O}_7/\text{SrTiO}_3$ based heterojunctions.

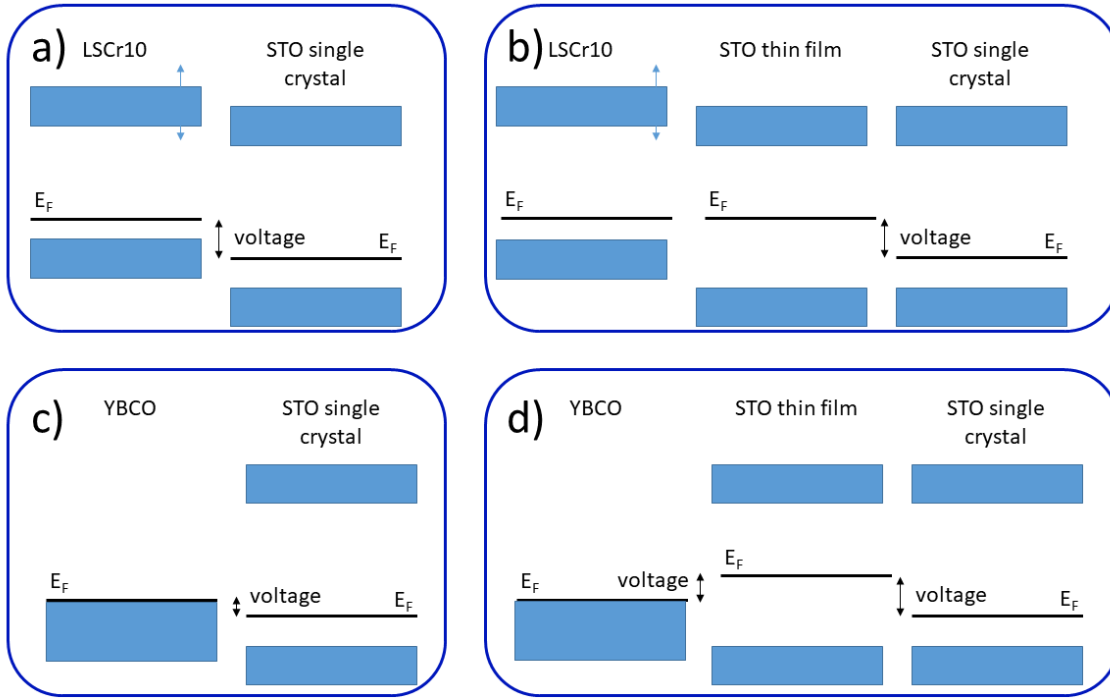


Fig. 54: Sketched band structure of different SrTiO_3 based heterojunctions, highlighting the difference between SrTiO_3 single crystals and thin films. The $\text{La}_{0.9}\text{Sr}_{0.1}\text{CrO}_3/\text{SrTiO}_3$ heterojunction based on single crystalline SrTiO_3 exhibits a difference in Fermi level, which under UV results in a photovoltage (a). Note that the Fermi level for the nominally undoped SrTiO_3 single crystal is essentially slightly acceptor doped. For the SrTiO_3 thin film, mid-gap Fermi level pinning occurs due to Sr vacancies (see chapter 3), leading to a shift in Fermi level compared to SrTiO_3 single crystal (b). A mid-gap Fermi level for the SrTiO_3 thin film lowers the difference in Fermi level between the $\text{La}_{0.9}\text{Sr}_{0.1}\text{CrO}_3$ thin film and the SrTiO_3 thin film, thus lowering the photovoltage obtained from only thin film based cells (e.g. in Fig. 3). The band offset between the SrTiO_3 thin film and single crystal might explain the high photovoltage observed in Fig 2.b. The opposite case is shown for a $\text{YBa}_2\text{Cu}_3\text{O}_7$ thin film on top of a SrTiO_3 single crystal (c), which is known to be an ohmic contact. Consequently, only a very small photovoltage is obtained. With the addition of a SrTiO_3 thin film between the $\text{YBa}_2\text{Cu}_3\text{O}_7$ thin film and the SrTiO_3 single crystal, rather pronounced differences in the Fermi level are present (d). Indeed, an increase in photovoltage is observed for such a sample (see Fig. 5). Taking the sign of the voltage into account, the SrTiO_3 thin film/ SrTiO_3 single crystal is possibly the dominating interface, highlighting the vast difference in the defect state of thin film and bulk SrTiO_3 .

In the first case, a high photovoltage is found for $\text{La}_{0.9}\text{Sr}_{0.1}\text{CrO}_3$ thin film on a SrTiO_3 single crystal (see Fig. 50.b, Fig. 52.a and chapter 6). In the band structure, $\text{La}_{0.9}\text{Sr}_{0.1}\text{CrO}_3$ is p-type due to Sr doping and the SrTiO_3 single crystal is also slightly p-type due to titanium vacancies (see Fig. 54.a). There is a Fermi level offset between the $\text{La}_{0.9}\text{Sr}_{0.1}\text{CrO}_3$ and the SrTiO_3 single crystal, causing the high photovoltage under UV light. As discussed in chapter 3, Sr vacancies present in SrTiO_3 thin films lead to a mid-gap Fermi level pinning. When adding such a thin film, the Fermi

level of the thin film is higher than the Fermi level of the single crystal, coming closer to the respective Fermi level of $\text{La}_{0.9}\text{Sr}_{0.1}\text{CrO}_3$ (see Fig. 54.b). Not surprisingly, no change in photovoltage is observed for the addition of such a thin film to the previous system. However, the origin of the photovoltage shifts from the $\text{La}_{0.9}\text{Sr}_{0.1}\text{CrO}_3/\text{SrTiO}_3$ (thin film) interface to the SrTiO_3 (thin film)/ SrTiO_3 (single crystal) junction. With this in mind, it appears now much less surprising that thin film based cells utilizing the $\text{La}_{0.9}\text{Sr}_{0.1}\text{CrO}_3/\text{SrTiO}_3$ (thin film) interface yield overall very low photovoltages, see Fig. 51. The other system is the $\text{YBa}_2\text{Cu}_3\text{O}_7/\text{SrTiO}_3$ heterojunction. When using a $\text{YBa}_2\text{Cu}_3\text{O}_7$ thin film on top of a SrTiO_3 single crystal, only small photovoltages result, e.g. in Fig. 53.b, indicating rather well-matched Fermi levels (see Fig. 54.c). In the case in Fig. 53.c-d, the Fermi level of the additional SrTiO_3 thin film has a Fermi level well above both other materials (cf. Fig. 54.d). With this pronounced difference in Fermi levels in Fig. 54.d, a higher photovoltage would result for both junctions, but with opposite signs. Taking into account that the absorption of the single crystal is much higher than the absorption of the thin film, the $\text{SrTiO}_3/\text{SrTiO}_3$ junction is likely to be the dominating factor. Not surprisingly, an increase in photovoltage is observed in Fig. 53.d. Note that the photovoltages resulting for the cases in Fig. 54.a-d all have a negative sign. Considering the difference in Fermi level, this fits with the SrTiO_3 (thin film)/ SrTiO_3 (single crystal) junction as the origin of the photovoltage in Fig. 54.d. Here, we expect an even higher photovoltage for the $\text{SrTiO}_3/\text{SrTiO}_3$ interface, but a fraction of the photovoltage is “consumed” by the $\text{YBa}_2\text{Cu}_3\text{O}_7/\text{SrTiO}_3$ interface. Hence, we can identify Sr vacancy induced mid-gap states in the thin films as a possible reason for the vastly deviating photovoltaic behavior of thin films and single crystals, thus completing the circle started in chapters 2 and 3.

7.5 Conclusions

Photovoltage measurements were carried out on different samples, using polycrystalline and single crystalline substrates as well as thin film cells. For the polycrystals, a change in the time dependent behavior upon switching the UV light off was observed. Here, cation vacancies and defect interactions might influence this behavior. For thin film cells, a significant deviation from single crystal based solar cells was found. It is shown that material combinations that work well for SrTiO_3 single crystals can not be directly transferred to thin film applications, and vice versa. A phenomenological explanation of the observed trends highlights the role of Sr vacancies for the

photovoltages in thin film based heterojunctions. The Fermi levels of SrTiO₃ single crystals and thin films vastly differ, with Sr vacancies leading to mid-gap Fermi level pinning in the case of thin films and titanium vacancies leading to acceptor states in single crystals. This finding is highly relevant for the optimization of SrTiO₃ thin film solar cells.

Chapter 8: Summary

In this work, point defects in SrTiO₃ thin films were investigated by different chemical and physical characterization methods with emphasis on the role cation and oxygen vacancies for different applications. More specific, as Sr vacancies proved to be the main source of the deviation between thin films and bulk samples, special attention was drawn to these cation defects. The results are discussed for thin film optimization and photovoltage separately. First, the main points concerning the defect chemistry in thin films are summarized:

- Slightly Fe doped SrTiO₃ thin films deposited from stoichiometric targets (using different laser fluences) exhibit ultra-low conductivity, down to the electronic intrinsic point, i.e. the lowest possible electronic charge carrier concentration ($c_e = c_h$). These thin films are found to exhibit severe Sr deficiency.
- Sr vacancies are easily introduced in SrTiO₃ during the deposition process, often vastly exceeding equilibrium vacancy concentrations.
- By adding Sr excess to the PLD target, stoichiometric thin films are obtained, yielding bulk-like conductivity values. Thus, using Sr overstoichiometric targets is a facile experimental route to achieve optimized stoichiometry. Here, conductivity measurements prove to be more sensitive towards thin film stoichiometry than lab-scale RSM measurements and, thus, should be considered as a quality assessment tool for thin film optimization.
- This ultra-low pseudo-intrinsic conductivity is not a peculiarity of a certain thin film composition, but can be found for a vast range of Fe doping concentration as well as for other acceptor dopants (Al, Ni) and even nominally undoped SrTiO₃ thin films. Thus, it is a general property of SrTiO₃ thin films deposited via pulsed laser deposition.
- We identified Sr vacancies as the common feature responsible for the massive decrease in conductivity. In addition to Sr vacancies, the Sr deficiency can induce other defects, especially antisite defects. In this study, a change in site occupation of Fe from the B-site (acting as an acceptor) towards the A-site (acting as a donor) was found. Similar changes in site occupation are also reported in literature, most notably the lattice site change of Ti.
- From these defects found in SrTiO₃ thin films, we deduced a model featuring acceptor states (e.g. Fe doping, Sr vacancies, impurities, ...), mid gap states (Sr vacancies) and donor states

(antisite defects). This three-level system explains the robust Fermi-level pinning observed for many films.

- Sr compensation in SrTiO₃ thin films removes not only the mid-gap states attributed to the Sr vacancies, but also the need for nonstoichiometry accommodation and, thus, the need for antisite defects, i.e. the donor states.
- Sr deficient SrTiO₃ polycrystals behave differently since in this case the Sr deficiency is given by the Schottky disorder and is, thus, an equilibrium concentration (corresponding to the equilibrium at 1500 °C). Hence, there is no need for antisite defect formation, which removes the donor states from the sample. In this case, even a slight increase in conductivity is found for higher amounts of Sr deficiency.

For photovoltages, single crystal based systems were investigated first, and the study was then extended to thin film based cells as well. The most important results are listed below:

- The La_{0.9}Sr_{0.1}CrO₃/SrTiO₃ heterojunction yields high photovoltages of about 1 V.
- The high temperature photovoltage effect is quite robust in SrTiO₃ based systems, yielding high photovoltages also for other interfaces such as LaCrO₃/SrTiO₃, La_{0.8}Sr_{0.2}MnO₃/SrTiO₃, and even Au/SrTiO₃.
- A time dependent change in photovoltage under light is attributed to the change in photovoltage due to the change in oxygen stoichiometry at the interface. After switching the UV light off, a battery-type voltage remains, which comes from the change in oxygen content in the sample under UV.
- In short-circuit conditions, a self-enhancing effect is observed for single crystal based photovoltaic cells, leading to higher current or power output under illumination. This effect is attributed to stoichiometry polarization, leading to a decrease in SrTiO₃ resistance. Mechanistic information obtained via impedance spectroscopy also shows the decrease in SrTiO₃ resistance under light as well as a collapse of the space charge resistance as soon as the UV light is switched on.
- Thin films used as interfacial layers between the SrTiO₃ substrate and the La_{0.9}Sr_{0.1}CrO₃ top electrode also influence the overall photovoltage. Doped thin films deposited from stoichiometric targets lead to a more or less pronounced decrease in photovoltage. Using

an undoped SrTiO_3 thin film at the interface, however, does not affect the photovoltage compared to the single crystal based $\text{SrTiO}_3/\text{La}_{0.9}\text{Sr}_{0.1}\text{CrO}_3$ heterojunction.

- When using such an undoped SrTiO_3 thin film for a thin film based cell, severe differences become visible. Interfaces yielding high photovoltages for single crystal based cells show next to no photovoltage response when using a SrTiO_3 thin film, and vice versa. The different behavior might be caused by the different Fermi level in the films due to their drastically different defect chemistry.

Chapter 9: References

1. Parmesan, C. and G. Yohe, *A globally coherent fingerprint of climate change impacts across natural systems*. Nature, 2003. **421**(6918): p. 37-42.
2. Walther, G.-R., E. Post, P. Convey, A. Menzel, C. Parmesan, T.J.C. Beebee, J.-M. Fromentin, O. Hoegh-Guldberg, and F. Bairlein, *Ecological responses to recent climate change*. Nature, 2002. **416**(6879): p. 389-395.
3. Thomas, C.D., A. Cameron, R.E. Green, M. Bakkenes, L.J. Beaumont, Y.C. Collingham, B.F.N. Erasmus, M.F. de Siqueira, A. Grainger, L. Hannah, L. Hughes, B. Huntley, A.S. van Jaarsveld, G.F. Midgley, L. Miles, M.A. Ortega-Huerta, A. Townsend Peterson, O.L. Phillips, and S.E. Williams, *Extinction risk from climate change*. Nature, 2004. **427**(6970): p. 145-148.
4. Moss, R.H., J.A. Edmonds, K.A. Hibbard, M.R. Manning, S.K. Rose, D.P. van Vuuren, T.R. Carter, S. Emori, M. Kainuma, T. Kram, G.A. Meehl, J.F.B. Mitchell, N. Nakicenovic, K. Riahi, S.J. Smith, R.J. Stouffer, A.M. Thomson, J.P. Weyant, and T.J. Wilbanks, *The next generation of scenarios for climate change research and assessment*. Nature, 2010. **463**(7282): p. 747-756.
5. Nikolaidis, P. and A. Poullikkas, *A comparative overview of hydrogen production processes*. Renewable and Sustainable Energy Reviews, 2017. **67**: p. 597-611.
6. Kumar Sahu, B., *A study on global solar PV energy developments and policies with special focus on the top ten solar PV power producing countries*. Renewable and Sustainable Energy Reviews, 2015. **43**: p. 621-634.
7. Jäger-Waldau, A., *Photovoltaics and renewable energies in Europe*. Renewable and Sustainable Energy Reviews, 2007. **11**(7): p. 1414-1437.
8. Omer, A.M., *Green energies and the environment*. Renewable and Sustainable Energy Reviews, 2008. **12**(7): p. 1789-1821.
9. Jacobson, A.J., *Materials for Solid Oxide Fuel Cells*. Chemistry of Materials, 2010. **22**(3): p. 660-674.
10. Haile, S.M., *Fuel cell materials and components ☆☆☆The Golden Jubilee Issue—Selected topics in Materials Science and Engineering: Past, Present and Future, edited by S. Suresh*. Acta Materialia, 2003. **51**(19): p. 5981-6000.
11. Ursua, A., L.M. Gandia, and P. Sanchis, *Hydrogen Production From Water Electrolysis: Current Status and Future Trends*. Proceedings of the IEEE, 2012. **100**(2): p. 410-426.
12. Ni, M., M.K.H. Leung, and D.Y.C. Leung, *Technological development of hydrogen production by solid oxide electrolyzer cell (SOEC)*. International Journal of Hydrogen Energy, 2008. **33**(9): p. 2337-2354.
13. Walch, G., B. Rotter, G.C. Brunauer, E. Esmaeili, A.K. Opitz, M. Kubicek, J. Summhammer, K. Ponweiser, and J. Fleig, *A solid oxide photoelectrochemical cell with UV light-driven oxygen storage in mixed conducting electrodes*. Journal of Materials Chemistry A, 2017. **5**(4): p. 1637-1649.
14. Strukov, D.B., G.S. Snider, D.R. Stewart, and R.S. Williams, *The missing memristor found*. Nature, 2008. **453**(7191): p. 80-83.

15. Yang, J.J., D.B. Strukov, and D.R. Stewart, *Memristive devices for computing*. Nature Nanotechnology, 2013. **8**(1): p. 13-24.
16. Jeong, D.S., R. Thomas, R.S. Katiyar, J.F. Scott, H. Kohlstedt, A. Petraru, and C.S. Hwang, *Emerging memories: resistive switching mechanisms and current status*. Reports on Progress in Physics, 2012. **75**(7): p. 076502.
17. Atzori, L., A. Iera, and G. Morabito, *The Internet of Things: A survey*. Computer Networks, 2010. **54**(15): p. 2787-2805.
18. Gubbi, J., R. Buyya, S. Marusic, and M. Palaniswami, *Internet of Things (IoT): A vision, architectural elements, and future directions*. Future Generation Computer Systems, 2013. **29**(7): p. 1645-1660.
19. Tarancón, A., *Powering the IoT revolution with heat*. Nature Electronics, 2019. **2**(7): p. 270-271.
20. Funck, C., C. Bäumer, S. Wiefels, T. Hennen, R. Waser, S. Hoffmann-Eifert, R. Dittmann, and S. Menzel, *Comprehensive model for the electronic transport in Pt/SrTiO₃ analog memristive devices*. Physical Review B, 2020. **102**(3): p. 035307.
21. Sediva, E., W.J. Bowman, J.C. Gonzalez-Rosillo, and J.L.M. Rupp, *Investigation of the Eightwise Switching Mechanism and Its Suppression in SrTiO₃ Modulated by Humidity and Interchanged Top and Bottom Platinum and LaNiO₃ Electrode Contacts*. Advanced Electronic Materials, 2019. **5**(9): p. 1800566.
22. Kubicek, M., R. Schmitt, F. Messerschmitt, and J.L.M. Rupp, *Uncovering Two Competing Switching Mechanisms for Epitaxial and Ultrathin Strontium Titanate-Based Resistive Switching Bits*. ACS Nano, 2015. **9**(11): p. 10737-10748.
23. Muenstermann, R., T. Menke, R. Dittmann, and R. Waser, *Coexistence of filamentary and homogeneous resistive switching in Fe-doped SrTiO₃ thin-film memristive devices*. Advanced Materials, 2010. **22**(43): p. 4819-4822.
24. Kato, H. and A. Kudo, *Visible-Light-Response and Photocatalytic Activities of TiO₂ and SrTiO₃ Photocatalysts Codoped with Antimony and Chromium*. The Journal of Physical Chemistry B, 2002. **106**(19): p. 5029-5034.
25. Tan, H., Z. Zhao, W.-b. Zhu, E.N. Coker, B. Li, M. Zheng, W. Yu, H. Fan, and Z. Sun, *Oxygen Vacancy Enhanced Photocatalytic Activity of Pervoskite SrTiO₃*. ACS Applied Materials & Interfaces, 2014. **6**(21): p. 19184-19190.
26. Wang, J.-Y., W. Zhai, K.-X. Jin, and C.-L. Chen, *The Rectifying Property and Photovoltaic Effect in the La_{0.8}Ag_{0.2}MnO₃/SrTiO₃-Nb Heterojunction*. Chinese Physics Letters, 2013. **30**(6): p. 067301.
27. Zhao, K., Y. Huang, Q. Zhou, K.-J. Jin, H. Lu, M. He, B. Cheng, Y. Zhou, Z. Chen, and G. Yang, *Ultraviolet photovoltage characteristics of SrTiO₃-Si heterojunction*. Applied Physics Letters, 2005. **86**(22): p. 221917.
28. Zhao, S.G., J.F. Cheng, T. Zhang, Y. Xie, X.L. Yan, W. Liu, J.Y. Wang, and K.X. Jin, *Photovoltaic effect in heterojunction composed of charge-ordering Pr_{0.75}Na_{0.25}MnO₃ and Nb-SrTiO₃*. Physica B: Condensed Matter, 2014. **454**: p. 42-44.
29. Denk, I., W. Münch, and J. Maier, *Partial Conductivities in SrTiO₃: Bulk Polarization Experiments, Oxygen Concentration Cell Measurements, and Defect-Chemical Modeling*. Journal of the American Ceramic Society, 1995. **78**(12): p. 3265-3272.

30. Moos, R. and K.H. Hardtl, *Defect Chemistry of Donor-Doped and Undoped Strontium Titanate Ceramics between 1000° and 1400°C*. Journal of the American Ceramic Society, 1997. **80**(10): p. 2549-2562.
31. Gries, U.N., M. Kessel, F.V.E. Hensling, R. Dittmann, M. Martin, and R.A. De Souza, *Behavior of cation vacancies in single-crystal and in thin-film SrTiO₃: The importance of strontium vacancies and their defect associates*. Physical Review Materials, 2020. **4**(12): p. 123404.
32. Kubicek, M., S. Taibl, E. Navickas, H. Hutter, G. Fafilek, and J. Fleig, *Resistive states in strontium titanate thin films: Bias effects and mechanisms at high and low temperature*. Journal of Electroceramics, 2017. **39**(1): p. 197-209.
33. Souza, R.A.D., J. Fleig, R. Merkle, and J. Maier, *SrTiO₃: A Model Electroceramic*. Zeitschrift für Metallkunde, 2003. **94**(3): p. 218-225.
34. Akhtar, M.J., Z.-U.-N. Akhtar, R.A. Jackson, and C.R.A. Catlow, *Computer Simulation Studies of Strontium Titanate*. Journal of the American Ceramic Society, 1995. **78**(2): p. 421-428.
35. Adepalli, K.K., J. Yang, J. Maier, H.L. Tuller, and B. Yildiz, *Tunable Oxygen Diffusion and Electronic Conduction in SrTiO₃ by Dislocation-Induced Space Charge Fields*. Advanced Functional Materials, 2017. **27**(22).
36. Metlenko, V., A.H.H. Ramadan, F. Gunkel, H. Du, H. Schraknepper, S. Hoffmann-Eifert, R. Dittmann, R. Waser, and R.A. De Souza, *Do dislocations act as atomic autobahns for oxygen in the perovskite oxide SrTiO₃?* Nanoscale, 2014. **6**(21): p. 12864-12876.
37. Abrantes, J.C.C., J.A. Labrincha, and J.R. Frade, *Applicability of the brick layer model to describe the grain boundary properties of strontium titanate ceramics*. Journal of the European Ceramic Society, 2000. **20**(10): p. 1603-1609.
38. Guo, X., J. Fleig, and J. Maier, *Determination of electronic and ionic partial conductivities of a grain boundary: method and application to acceptor-doped SrTiO₃*. Solid State Ionics, 2002. **154-155**: p. 563-569.
39. Vollmann, M., R. Hagenbeck, and R. Waser, *Grain-Boundary Defect Chemistry of Acceptor-Doped Titanates: Inversion Layer and Low-Field Conduction*. Journal of the American Ceramic Society, 1997. **80**(9): p. 2301-2314.
40. Merkle, R., R. Souza, and J. Maier, *Optically Tuning the Rate of Stoichiometry Changes: Surface-Controlled Oxygen Incorporation into Oxides under UV Irradiation*. Angewandte Chemie (International ed. in English), 2001. **40**: p. 2126-2129.
41. Viernstein, A., M. Kubicek, M. Morgenbesser, G. Walch, G.C. Brunauer, and J. Fleig, *High-Temperature Photochromism of Fe-Doped SrTiO₃ Caused by UV-Induced Bulk Stoichiometry Changes*. Advanced Functional Materials, 2019. **29**(23): p. 1900196.
42. Brunauer, G.C., B. Rotter, G. Walch, E. Esmaeili, A.K. Opitz, K. Ponweiser, J. Summhammer, and J. Fleig, *UV-Light-Driven Oxygen Pumping in a High-Temperature Solid Oxide Photoelectrochemical Cell*. Advanced Functional Materials, 2016. **26**(1): p. 120-128.
43. Waser, R., T. Baiatu, and K.-H. Härdtl, *dc Electrical Degradation of Perovskite-Type Titanates: I, Ceramics*. Journal of the American Ceramic Society, 1990. **73**(6): p. 1645-1653.
44. Kuganathan, N., F. Baiutti, A. Tarancón, J. Fleig, and A. Chroneos, *Defect energetics in the SrTiO₃-LaCrO₃ system*. Solid State Ionics, 2021. **361**: p. 115570.

45. Lei, Q.Y., G.Z. Liu, and X.X. Xi, *Structural Characterization of Homoepitaxial SrTiO₃ Films Grown by Pulsed Laser Deposition*. Integrated Ferroelectrics, 2013. **141**: p. 128-133.
46. Markovich, M., J. Roqueta, J. Santiso, E. Lakin, E. Zolotoyabko, and A. Rothschild, *Epitaxial growth of Nb-doped SrTiO₃ films by pulsed laser deposition*. Applied Surface Science, 2012. **258**(23): p. 9496-9500.
47. Groenen, R., J. Smit, K. Orsel, A. Vailionis, B. Bastiaens, M. Huijben, K. Boller, G. Rijnders, and G. Koster, *Research Update: Stoichiometry controlled oxide thin film growth by pulsed laser deposition*. APL Mater., 2015. **3**: p. 70701-70701.
48. Keeble, D.J., S. Wicklein, L. Jin, C.L. Jia, W. Egger, and R. Dittmann, *Nonstoichiometry accommodation in SrTiO₃ thin films studied by positron annihilation and electron microscopy*. Physical Review B, 2013. **87**(19): p. 195409.
49. McGuire, S., D.J. Keeble, R.E. Mason, P.G. Coleman, Y. Koutsonas, and T.J. Jackson, *Variable energy positron beam analysis of vacancy defects in laser ablated SrTiO₃ thin films on SrTiO₃*. Journal of Applied Physics, 2006. **100**(4): p. 044109.
50. Mackie, R.A., S. Singh, J. Laverock, S.B. Dugdale, and D.J. Keeble, *Vacancy defect positron lifetimes in strontium titanate*. Physical Review B, 2009. **79**(1): p. 014102.
51. Senocrate, A., E. Kotomin, and J. Maier, *On the Way to Optoionics*. Helvetica Chimica Acta, 2020. **103**(7): p. e2000073.
52. Fleig, J. and M. Kubicek, *Light may harm or help*. Nature Materials, 2018. **17**(5): p. 389-391.
53. Kim, G.Y., A. Senocrate, T.-Y. Yang, G. Gregori, M. Grätzel, and J. Maier, *Large tunable photoeffect on ion conduction in halide perovskites and implications for photodecomposition*. Nature Materials, 2018. **17**(5): p. 445-449.
54. Lenser, C., A. Koehl, I. Slipukhina, H. Du, M. Patt, V. Feyer, C.M. Schneider, M. Lezaic, R. Waser, and R. Dittmann, *Formation and Movement of Cationic Defects During Forming and Resistive Switching in SrTiO₃ Thin Film Devices*. Advanced Functional Materials, 2015. **25**(40): p. 6360-6368.
55. Raab, N., C. Bäumer, and R. Dittmann, *Impact of the cation-stoichiometry on the resistive switching and data retention of SrTiO₃ thin films*. AIP Advances, 2015. **5**(4).
56. Zhang, H., L. Yan, and H.U. Habermeier, *Unusual ultraviolet photoconductivity in single crystalline SrTiO₃*. Journal of Physics Condensed Matter, 2013. **25**(3).
57. Chambers, S.A., *Understanding the mechanism of conductivity at the LaAlO₃/SrTiO₃(001) interface*. Surface Science, 2011. **605**(13): p. 1133-1140.
58. Ohtomo, A. and H.Y. Hwang, *A high-mobility electron gas at the LaAlO₃/SrTiO₃ heterointerface*. Nature, 2004. **427**(6973): p. 423-426.
59. Keeble, D.J., S. Wicklein, R. Dittmann, L. Ravelli, R.A. Mackie, and W. Egger, *Identification of A- and B-Site Cation Vacancy Defects in Perovskite Oxide Thin Films*. Physical Review Letters, 2010. **105**: p. 226102-226102.
60. Wicklein, S., A. Sambri, S. Amoruso, X. Wang, R. Bruzzese, A. Koehl, and R. Dittmann, *Pulsed laser ablation of complex oxides: The role of congruent ablation and preferential scattering for the film stoichiometry*. Applied Physics Letters, 2012. **101**(13).
61. Fukushima, K. and S. Shibagaki, *Nb doped SrTiO₃ thin films deposited by pulsed laser ablation*. Thin Solid Films, 1998. **315**(1-2): p. 238-243.

62. Fukushima, K. and S. Shibagaki, *Niobium doping effect on resistivity of epitaxially grown Nb-SrTiO₃ thin films by laser ablation method*. Journal of Electroceramics, 1999. **4**(SUPPL. 1): p. 81-90.
63. Taibl, S., G. Fafilek, and J. Fleig, *Impedance spectra of Fe-doped SrTiO₃ thin films upon bias voltage: inductive loops as a trace of ion motion*. Nanoscale, 2016. **8**(29): p. 13954-13966.
64. Ohnishi, T., K. Shibuya, T. Yamamoto, and M. Lippmaa, *Defects and transport in complex oxide thin films*. Journal of Applied Physics, 2008. **103**(10).
65. Droubay, T.C., L. Qiao, T.C. Kaspar, M.H. Engelhard, V. Shutthanandan, and S.A. Chambers, *Nonstoichiometric material transfer in the pulsed laser deposition of LaAlO₃*. Applied Physics Letters, 2010. **97**(12): p. 124105-124105.
66. Schoofs, F., T. Fix, A.S. Kalabukhov, D. Winkler, Y. Boikov, I. Serenkov, V. Sakharov, T. Claeson, J.L. MacManus-Driscoll, and M.G. Blamire, *Optimized transport properties of LaAlO₃/SrTiO₃ heterointerfaces by variation of pulsed laser fluence*. Journal of Physics Condensed Matter, 2011. **23**(30).
67. Ohnishi, T., M. Lippmaa, T. Yamamoto, S. Meguro, and H. Koinuma, *Improved stoichiometry and misfit control in perovskite thin film formation at a critical fluence by pulsed laser deposition*. Applied Physics Letters, 2005. **87**(24): p. 1-3.
68. Orsel, K., R. Groenen, B. Bastiaens, G. Koster, G. Rijnders, and K.-J. Boller, *Influence of the oxidation state of SrTiO₃ plasmas for stoichiometric growth of pulsed laser deposition films identified by laser induced fluorescence*. APL Materials, 2015. **3**(10): p. 106103.
69. Liu, G.Z., Q.Y. Lei, and X.X. Xi, *Stoichiometry of SrTiO₃ films grown by pulsed laser deposition*. Applied Physics Letters, 2012. **100**(20): p. 202902.
70. LeBeau, J.M., R. Engel-Herbert, B. Jalan, J. Cagnon, P. Moetakef, S. Stemmer, and G.B. Stephenson, *Stoichiometry optimization of homoepitaxial oxide thin films using x-ray diffraction*. Applied Physics Letters, 2009. **95**: p. 142903-142905.
71. McCoy, M.A., R.W. Grimes, and W.E. Lee, *Phase stability and interfacial structures in the SrO-SrTiO₃ system*. Philosophical Magazine A, 1997. **75**(3): p. 833-846.
72. Wagner, A., M. Butterling, M.O. Liedke, K. Potzger, and R. Krause-Rehberg, *Positron annihilation lifetime and Doppler broadening spectroscopy at the ELBE facility*. AIP Conference Proceedings, 2018. **1970**(1): p. 040003.
73. Olsen, J.V., P. Kirkegaard, N.J. Pedersen, and M. Eldrup, *PALSfit: A new program for the evaluation of positron lifetime spectra*. physica status solidi c, 2007. **4**(10): p. 4004-4006.
74. Tuomisto, F. and I. Makkonen, *Defect identification in semiconductors with positron annihilation: Experiment and theory*. Reviews of Modern Physics, 2013. **85**(4): p. 1583-1631.
75. Krause-Rehberg, R. and H.S. Leipner, *Positron annihilation in semiconductors: defect studies*. Springer Series in Solid-State Sciences. 1999: Springer.
76. Huber, T.M., A.K. Opitz, M. Kubicek, H. Hutter, and J. Fleig, *Temperature gradients in microelectrode measurements: Relevance and solutions for studies of SOFC electrode materials*. Solid State Ionics, 2014. **268**: p. 82-93.
77. Siebenhofer, M., T. Huber, W. Artner, J. Fleig, and M. Kubicek, *Substrate stoichiometry changes during pulsed laser deposition: a case study on SrTiO₃*. Acta Materialia, 2021. **203**: p. 116461.

78. Slouka, C., G. Holzlechner, L. Andrejs, E. Navickas, H. Hutter, and J. Fleig, *Oxygen Ion Conduction in Bulk and Grain Boundaries of Nominally Donor-Doped Lead Zirconate Titanate (PZT): A Combined Impedance and Tracer Diffusion Study*. Journal of the American Ceramic Society, 2015. **98**(10): p. 3259-3269.
79. Jamnik, J. and J. Maier, *Treatment of the Impedance of Mixed Conductors Equivalent Circuit Model and Explicit Approximate Solutions*. Journal of The Electrochemical Society, 1999. **146**(11): p. 4183-4188.
80. Jamnik, J. and J. Maier, *Generalised equivalent circuits for mass and charge transport: chemical capacitance and its implications*. Physical Chemistry Chemical Physics, 2001. **3**(9): p. 1668-1678.
81. Jamnik, J., J. Maier, and S. Pejovnik, *A powerful electrical network model for the impedance of mixed conductors*. Electrochimica Acta, 1999. **44**(24): p. 4139-4145.
82. Shilo, D., E. Lakin, and E. Zolotoyabko, *Measurement of subtle strain modifications in heterostructures by using X-ray mapping in reciprocal space*. Journal of Applied Crystallography, 2001. **34**(6): p. 715-721.
83. Suzuki, T., Y. Nishi, and M. Fujimoto, *Defect structure in homoepitaxial non-stoichiometric strontium titanate thin films*. Philosophical Magazine A, 2000. **80**: p. 621-637.
84. Tarsa, E.J., E.A. Hachfeld, F.T. Quinlan, J.S. Speck, and M. Eddy, *Growth-related stress and surface morphology in homoepitaxial SrTiO₃ films*. Applied Physics Letters, 1996. **68**(4): p. 490-492.
85. Xu, C., S. Wicklein, A. Sambri, S. Amoruso, M. Moors, and R. Dittmann, *Impact of the interplay between nonstoichiometry and kinetic energy of the plume species on the growth mode of SrTiO₃ thin films*. Journal of Physics D: Applied Physics, 2014. **47**(3).
86. Brooks, C.M., L.F. Kourkoutis, T. Heeg, J. Schubert, D.A. Muller, and D.G. Schlom, *Growth of homoepitaxial SrTiO₃ thin films by molecular-beam epitaxy*. Applied Physics Letters, 2009. **94**: p. 162905-162905.
87. Freedman, D.A., D. Roundy, and T.A. Arias, *Elastic effects of vacancies in strontium titanate: Short- and long-range strain fields, elastic dipole tensors, and chemical strain*. Physical Review B, 2009. **80**(6): p. 064108.
88. Schou, J., *Physical aspects of the pulsed laser deposition technique: The stoichiometric transfer of material from target to film*. Applied Surface Science, 2009. **255**: p. 5191-5198.
89. Willmott, P.R. and J.R. Huber, *Pulsed laser vaporization and deposition*. Reviews of Modern Physics, 2000. **72**(1): p. 315-328.
90. Dam, B., J.H. Rector, J. Johansson, J. Huijbregtse, and D.G.D. Groot, *Mechanism of incongruent ablation of SrTiO₃*. Journal of Applied Physics, 1998. **83**(6): p. 3386-3389.
91. Keeble, D.J., R.A. Mackie, W. Egger, B. Löwe, P. Pikart, C. Hugenschmidt, and T.J. Jackson, *Identification of vacancy defects in a thin film perovskite oxide*. Physical Review B, 2010. **81**(6): p. 064102.
92. Amoruso, S., A. Sambri, and X. Wang, *Propagation dynamics of a LaMnO₃ laser ablation plume in an oxygen atmosphere*. Journal of Applied Physics, 2006. **100**(1): p. 013302.
93. Christen, H.M. and G. Eres, *Recent advances in pulsed-laser deposition of complex oxides*. Journal of physics: Condensed Matter, 2008. **20**: p. 264005-264005.

94. Hu, H., F. Shao, J. Chen, M. Döbeli, Q. Song, Q. Zhang, D. Zhao, J. Miao, X. Xu, and Y. Jiang, *Incongruent pulsed laser deposition strategy for thin film growth of $\text{Ca}_3\text{Co}_4\text{O}_9$ thermoelectric compound*. *Ceramics International*, 2019. **45**(10): p. 13138-13143.
95. Kan, D. and Y. Shimakawa, *Controlled cation stoichiometry in pulsed laser deposition-grown BaTiO_3 epitaxial thin films with laser fluence*. *Applied Physics Letters*, 2011. **99**(8): p. 81907-81907.
96. Kobayashi, S., Y. Tokuda, T. Ohnishi, T. Mizoguchi, N. Shibata, Y. Sato, Y. Ikuhara, and T. Yamamoto, *Cation off-stoichiometric $\text{SrMnO}_{3-\delta}$ thin film grown by pulsed laser deposition*. *Journal of Materials Science*, 2011. **46**(12): p. 4354-4360.
97. Konomi, I., T. Motohiro, M. Horii, and M. Kawasumi, *Angular distribution of elemental composition of films deposited by laser ablation of a SrZrO_3 target*. *Journal of Vacuum Science & Technology A*, 2008. **26**(6): p. 1455-1461.
98. Ojeda-G-P, A., C.W. Schneider, M. Döbeli, T. Lippert, and A. Wokaun, *Angular distribution of species in pulsed laser deposition of $\text{La}_x\text{Ca}_{1-x}\text{MnO}_3$* . *Applied Surface Science*, 2015. **336**: p. 150-156.
99. Ojeda-G-P, A., C.W. Schneider, M. Döbeli, T. Lippert, and A. Wokaun, *The importance of pressure and mass ratios when depositing multi-element oxide thin films by pulsed laser deposition*. *Applied Surface Science*, 2016. **389**: p. 126-134.
100. Schraknepper, H., C. Bäumer, F. Gunkel, R. Dittmann, and R.A. De Souza, *Pulsed laser deposition of SrRuO_3 thin-films: The role of the pulse repetition rate*. *APL Materials*, 2016. **4**(12).
101. Tyunina, M. and S. Leppävuori, *Effects of laser fluence, size, and shape of the laser focal spot in pulsed laser deposition using a multielemental target*. *Journal of Applied Physics*, 2000. **87**(11): p. 8132-8142.
102. Yu, C., A.S. Sokolov, P. Kulik, and V.G. Harris, *Stoichiometry, phase, and texture evolution in PLD-Grown hexagonal barium ferrite films as a function of laser process parameters*. *Journal of Alloys and Compounds*, 2020. **814**: p. 152301.
103. Fuchs, D., M. Adam, P. Schweiss, S. Gerhold, S. Schuppler, R. Schneider, and B. Obst, *Structural properties of slightly off-stoichiometric homoepitaxial $\text{SrTi}_x\text{O}_{3-\text{delta}}$ thin films*. *Journal of Applied Physics*, 2000. **88**(4): p. 1844-1850.
104. Karjalainen, A., V. Prozheeva, I. Makkonen, C. Gugushev, T. Markurt, M. Bickermann, and F. Tuomisto, *Ti_{Sr} antisite: An abundant point defect in SrTiO_3* . *Journal of Applied Physics*, 2020. **127**(24): p. 245702.
105. Choi, M., F. Oba, and I. Tanaka, *Role of Ti Antisitelike Defects in SrTiO_3* . *Physical Review Letters*, 2009. **103**(18): p. 185502.
106. Liu, B., V.R. Cooper, H. Xu, H. Xiao, Y. Zhang, and W.J. Weber, *Composition dependent intrinsic defect structures in SrTiO_3* . *Physical Chemistry Chemical Physics*, 2014. **16**(29): p. 15590-15596.
107. Osawa, N., R. Takahashi, and M. Lippmaa, *Hole trap state analysis in SrTiO_3* . *Applied Physics Letters*, 2017. **110**(26).
108. Hensling, F.V.E., C. Baeumer, M.-A. Rose, F. Gunkel, and R. Dittmann, *SrTiO_3 termination control: a method to tailor the oxygen exchange kinetics*. *Materials Research Letters*, 2020. **8**(1): p. 31-40.
109. Breckenfeld, E., R. Wilson, J. Karthik, A.R. Damodaran, D.G. Cahill, and L.W. Martin, *Effect of Growth Induced (Non)Stoichiometry on the Structure, Dielectric Response, and*

- Thermal Conductivity of SrTiO₃ Thin Films*. Chemistry of Materials, 2012. **24**(2): p. 331-337.
110. De Souza, R.A., J. Fleig, J. Maier, O. Kienzle, Z. Zhang, W. Sigle, and M. Rühle, *Electrical and Structural Characterization of a Low-Angle Tilt Grain Boundary in Iron-Doped Strontium Titanate*. Journal of the American Ceramic Society, 2003. **86**(6): p. 922-928.
 111. Maier, R.A., A.C. Johnston-Peck, and M.P. Donohue, *(Magic Dopant) Amphoteric Behavior of a Redox-Active Transition Metal Ion in a Perovskite Lattice: New Insights on the Lattice Site Occupation of Manganese in SrTiO₃*. Advanced Functional Materials, 2016. **26**(45): p. 8325-8333.
 112. Kubicek, M., A. Limbeck, T. Frmling, H. Hutter, and J. Fleig, *Relationship between cation segregation and the electrochemical oxygen reduction kinetics of La_{0.6}Sr_{0.4}CoO_{3-δ} thin film electrodes*. Journal of the Electrochemical Society, 2011. **158**(6): p. B727-B734.
 113. Ohly, C., S. Hoffmann-Eifert, X. Guo, J. Schubert, and R. Waser, *Electrical Conductivity of Epitaxial SrTiO₃ Thin Films as a Function of Oxygen Partial Pressure and Temperature*. Journal of the American Ceramic Society, 2006. **89**(9): p. 2845-2852.
 114. Rothschild, A., W. Menesklou, H.L. Tuller, and E. Ivers-Tiffée, *Electronic Structure, Defect Chemistry, and Transport Properties of SrTi_{1-x}Fe_xO_{3-y} Solid Solutions*. Chemistry of Materials, 2006. **18**(16): p. 3651-3659.
 115. Wang, J., T. Fang, S. Yan, Z. Li, T. Yu, and Z. Zou, *Highly efficient visible light photocatalytic activity of Cr–La codoped SrTiO₃ with surface alkalinization: An insight from DFT calculation*. Computational Materials Science, 2013. **79**: p. 87-94.
 116. Tonda, S., S. Kumar, O. Anjaneyulu, and V. Shanker, *Synthesis of Cr and La-codoped SrTiO₃ nanoparticles for enhanced photocatalytic performance under sunlight irradiation*. Physical Chemistry Chemical Physics, 2014. **16**(43): p. 23819-23828.
 117. Wang, D., J. Ye, T. Kako, and T. Kimura, *Photophysical and Photocatalytic Properties of SrTiO₃ Doped with Cr Cations on Different Sites*. The Journal of Physical Chemistry B, 2006. **110**(32): p. 15824-15830.
 118. Shi, J., J. Ye, L. Ma, S. Ouyang, D. Jing, and L. Guo, *Site-Selected Doping of Upconversion Luminescent Er³⁺ into SrTiO₃ for Visible-Light-Driven Photocatalytic H₂ or O₂ Evolution*. Chemistry – A European Journal, 2012. **18**(24): p. 7543-7551.
 119. Okhay, O., A. Wu, P.M. Vilarinho, and A. Tkach, *Low temperature dielectric characterization of Mg-doped SrTiO₃ thin films prepared by sol-gel*. Applied Physics Letters, 2010. **96**(15): p. 152906.
 120. Shenoy, U.S., H. Bantawal, and D.K. Bhat, *Band Engineering of SrTiO₃: Effect of Synthetic Technique and Site Occupancy of Doped Rhodium*. The Journal of Physical Chemistry C, 2018. **122**(48): p. 27567-27574.
 121. Shenoy, U.S. and D.K. Bhat, *Electronic structure engineering of SrTiO₃ via rhodium doping: A DFT study*. Journal of Physics and Chemistry of Solids, 2021. **148**: p. 109708.
 122. Lu, H., D. Lee, K. Klyukin, L. Tao, B. Wang, H. Lee, J. Lee, T.R. Paudel, L.-Q. Chen, E.Y. Tsymbal, V. Alexandrov, C.-B. Eom, and A. Gruverman, *Tunneling Hot Spots in Ferroelectric SrTiO₃*. Nano Letters, 2018. **18**(1): p. 491-497.
 123. Walsh, A., C.R.A. Catlow, A.G.H. Smith, A.A. Sokol, and S.M. Woodley, *Strontium migration assisted by oxygen vacancies in SrTiO₃ from classical and quantum mechanical simulations*. Physical Review B, 2011. **83**(22): p. 220301.

124. Parras, J.P., A.R. Genreith-Schriever, H. Zhang, M.T. Elm, T. Norby, and R.A. De Souza, *Is ReO_3 a mixed ionic–electronic conductor? A DFT study of defect formation and migration in a $B^VI O_3$ perovskite-type oxide*. *Physical Chemistry Chemical Physics*, 2018. **20**(12): p. 8008-8015.
125. Li, Y., S.N. Phattalung, S. Limpijumnong, J. Kim, and J. Yu, *Formation of oxygen vacancies and charge carriers induced in the n-type interface of a $LaAlO_3$ overlayer on $SrTiO_3$ (001)*. *Physical Review B*, 2011. **84**(24): p. 245307.
126. Kalabukhov, A., R. Gunnarsson, J. Börjesson, E. Olsson, T. Claeson, and D. Winkler, *Effect of oxygen vacancies in the $SrTiO_3$ substrate on the electrical properties of the $LaAlO_3/SrTiO_3$ interface*. *Physical Review B*, 2007. **75**(12): p. 121404.
127. Oliveira, F.S., A.C. Favero, S.T. Renosto, M.S.d. Luz, and C.A.M.d. Santos, *Kinetics of Vacancy Doping in $SrTiO_3$ Studied by in situ Electrical Resistivity*. *Materials Research*, 2018. **21**.
128. Azough, F., S.S. Jackson, D. Ekren, R. Freer, M. Molinari, S.R. Yeandel, P.M. Panchmatia, S.C. Parker, D.H. Maldonado, D.M. Kepaptsoglou, and Q.M. Ramasse, *Concurrent La and A-Site Vacancy Doping Modulates the Thermoelectric Response of $SrTiO_3$: Experimental and Computational Evidence*. *ACS Applied Materials & Interfaces*, 2017. **9**(48): p. 41988-42000.
129. Ohnishi, T., K. Shibuya, T. Yamamoto, and M. Lippmaa, *Defects and transport in complex oxide thin films*. *Journal of Applied Physics*, 2008. **103**(10): p. 103703.
130. Ohnishi, T., T. Yamamoto, S. Meguro, H. Koinuma, and M. Lippmaa, *Pulsed laser ablation and deposition of complex oxides*. *Journal of Physics: Conference Series*, 2007. **59**: p. 514-519.
131. Tokuda, Y., S. Kobayashi, T. Ohnishi, T. Mizoguchi, N. Shibata, Y. Ikuhara, and T. Yamamoto, *Strontium vacancy clustering in Ti-excess $SrTiO_3$ thin film*. *Applied Physics Letters*, 2011. **99**(3): p. 033110.
132. XueJiang, MinglongWei, C.H. Chan, YingyueWang, RuilianLai, JianboWang, JiyanDai, and XiaoyanQiu, *Effect of deposition temperature on ultra-low voltage resistive switching behavior of Fe-doped $SrTiO_3$ films*. *Applied Physics Letters*, 2020. **116**(10): p. 102101.
133. Kwon, D.-H., S. Lee, C.S. Kang, Y.S. Choi, S.J. Kang, H.L. Cho, W. Sohn, J. Jo, S.-Y. Lee, K.H. Oh, T.W. Noh, R.A. De Souza, M. Martin, and M. Kim, *Unraveling the Origin and Mechanism of Nanofilament Formation in Polycrystalline $SrTiO_3$ Resistive Switching Memories*. *Advanced Materials*, 2019. **31**(28): p. 1901322.
134. Szot, K., R. Dittmann, W. Speier, and R. Waser, *Nanoscale resistive switching in $SrTiO_3$ thin films*. *physica status solidi (RRL) – Rapid Research Letters*, 2007. **1**(2): p. R86-R88.
135. Hensling, F.V.E., D.J. Keeble, J. Zhu, S. Brose, C. Xu, F. Gunkel, S. Danylyuk, S.S. Nonnenmann, W. Egger, and R. Dittmann, *UV radiation enhanced oxygen vacancy formation caused by the PLD plasma plume*. *Scientific Reports*, 2018. **8**(1): p. 8846.
136. Ohly, C., S. Hoffmann-Eifert, K. Szot, and R. Waser, *Electrical conductivity and segregation effects of doped $SrTiO_3$ thin films*. *Journal of the European Ceramic Society*, 2001. **21**(10): p. 1673-1676.
137. Chi, Y.-T., M. Youssef, L. Sun, K.J. Van Vliet, and B. Yildiz, *Accessible switching of electronic defect type in $SrTiO_3$ via biaxial strain*. *Physical Review Materials*, 2018. **2**(5): p. 055801.

138. Iglesias, L., A. Sarantopoulos, C. Magén, and F. Rivadulla, *Oxygen vacancies in strained SrTiO₃ thin films: Formation enthalpy and manipulation*. Physical Review B, 2017. **95**(16): p. 165138.
139. Vailionis, A., H. Boschker, W. Siemons, E.P. Houwman, D.H.A. Blank, G. Rijnders, and G. Koster, *Misfit strain accommodation in epitaxial ABO₃ perovskites: Lattice rotations and lattice modulations*. Physical Review B, 2011. **83**(6): p. 064101.
140. Koehl, A., D. Kajewski, J. Kubacki, C. Lenser, R. Dittmann, P. Meuffels, K. Szot, R. Waser, and J. Szade, *Detection of Fe²⁺ valence states in Fe doped SrTiO₃ epitaxial thin films grown by pulsed laser deposition*. Physical Chemistry Chemical Physics, 2013. **15**(21): p. 8311-8317.
141. Reinle-Schmitt, M.L., C. Cancellieri, A. Cavallaro, G.F. Harrington, S.J. Leake, E. Pomjakushina, J.A. Kilner, and P.R. Willmott, *Chemistry and structure of homoepitaxial SrTiO₃ films and their influence on oxide-heterostructure interfaces*. Nanoscale, 2014. **6**(5): p. 2598-2602.
142. Morgenbesser, M., S. Taibl, M. Kubicek, A. Schmid, A. Viernstein, C. Herzig, F. Baiutti, J. de Dios Sirvent, M.O. Liedke, M. Butterling, A. Wagner, W. Artner, A. Limbeck, A. Tarancon, and J. Fleig, *Cation non-stoichiometry in Fe: SrTiO₃ thin films and its effect on the electrical conductivity*. in preparation.
143. Doolittle, L.R., *A semiautomatic algorithm for rutherford backscattering analysis*. Nuclear Instruments and Methods in Physics Research Section B: Beam Interactions with Materials and Atoms, 1986. **15**(1): p. 227-231.
144. Kottler, C., M. Döbeli, F. Glaus, and M. Suter, *A spectrometer for low energy heavy ion ERDA*. Nuclear Instruments and Methods in Physics Research Section B: Beam Interactions with Materials and Atoms, 2006. **248**(1): p. 155-162.
145. Hayakawa, S., Y. Makiyama, T. Esumi, S. Qiao, A. Morikawa, S. Tohno, H. Namatame, and T. Hirokawa, *Simultaneous Detection of X-Ray Fluorescence and Conversion Electrons for Depth Selective XAFS Analysis*. AIP Conference Proceedings, 2007. **882**(1): p. 869-871.
146. Ruosi, A., C. Raisch, A. Verna, R. Werner, B.A. Davidson, J. Fujii, R. Kleiner, and D. Koelle, *Electron sampling depth and saturation effects in perovskite films investigated by soft x-ray absorption spectroscopy*. Physical Review B, 2014. **90**(12): p. 125120.
147. Ravel, B. and M. Newville, *ATHENA, ARTEMIS, HEPHAESTUS: data analysis for X-ray absorption spectroscopy using IFEFFIT*. J Synchrotron Radiat, 2005. **12**(Pt 4): p. 537-41.
148. Stavitski, E. and F.M. de Groot, *The CTM4XAS program for EELS and XAS spectral shape analysis of transition metal L edges*. Micron, 2010. **41**(7): p. 687-94.
149. Rodewald, S., J. Fleig, and J. Maier, *The Distribution of Grain Boundary Resistivities in SrTiO₃ Polycrystals: A Comparison Between Spatially Resolved and Macroscopic Measurements*. Journal of The European Ceramic Society - J EUR CERAM SOC, 2001. **21**: p. 1749-1752.
150. Maier, R.A., E. Cockayne, M. Donohue, G. Cibir, and I. Levin, *Substitutional Mechanisms and Structural Relaxations for Manganese in SrTiO₃: Bridging the Concentration Gap for Point-Defect Metrology*. Chemistry of Materials, 2020. **32**(11): p. 4651-4662.
151. de Groot, F.M.F., J. Faber, J.J.M. Michiels, M.T. Czyżyk, M. Abbate, and J.C. Fuggle, *Oxygen 1s X-ray absorption of tetravalent titanium oxides: A comparison with single-particle calculations*. Physical Review B, 1993. **48**(4): p. 2074-2080.

152. Zhao, Q. and X.-L. Cheng, *Study on the Ti K, L_{2,3}, and M Edges of SrTiO₃ and PbTiO₃*. The Journal of Physical Chemistry A, 2020. **124**(2): p. 322-327.
153. Kubacki, J., D. Kajewski, A. Koehl, M. Wojtyniak, R. Dittmann, and J. Szade, *X-ray absorption and resonant photoemission studies of Mn doped SrTiO₃ epitaxial films*. Radiation Physics and Chemistry, 2013. **93**: p. 123-128.
154. Schlappa, J., C.F. Chang, Z. Hu, E. Schierle, H. Ott, E. Weschke, G. Kaindl, M. Huijben, G. Rijnders, D.H.A. Blank, L.H. Tjeng, and C. Schüßler-Langeheine, *Resonant soft x-ray scattering from stepped surfaces of SrTiO₃*. Journal of Physics: Condensed Matter, 2011. **24**(3): p. 035501.
155. Zucca, R., *Electrical compensation in semi-insulating GaAs*. Journal of Applied Physics, 1977. **48**(5): p. 1987-1994.
156. Laguta, V.V., I.V. Kondakova, I.P. Bykov, M.D. Glinchuk, A. Tkach, P.M. Vilarinho, and L. Jastrabik, *Electron spin resonance investigation of Mn²⁺ ions and their dynamics in Mn-doped SrTiO₃*. Physical Review B, 2007. **76**(5): p. 054104.
157. Valant, M., T. Kolodiaznyy, I. Arčon, F. Aguesse, A.-K. Axelsson, and N.M. Alford, *The Origin of Magnetism in Mn-Doped SrTiO₃*. Advanced Functional Materials, 2012. **22**(10): p. 2114-2122.
158. Tkach, A., P.M. Vilarinho, D. Nuzhnyy, and J. Petzelt, *Sr- and Ti-site substitution, lattice dynamics, and octahedral tilt transition relationship in SrTiO₃:Mn ceramics*. Acta Materialia, 2010. **58**(2): p. 577-582.
159. Lu, D., Y. Zheng, and L. Yuan, *Electron Paramagnetic Resonance Study on Oxygen Vacancies and Site Occupations in Mg-Doped BaTiO₃ Ceramics*. Materials, 2019. **12**(9): p. 1525.
160. Serna-Gallén, P., H. Beltrán-Mir, E. Cordoncillo, A.R. West, R. Balda, and J. Fernández, *Site-selective symmetries of Eu³⁺-doped BaTiO₃ ceramics: a structural elucidation by optical spectroscopy*. Journal of Materials Chemistry C, 2019. **7**(44): p. 13976-13985.
161. Lu, D.-Y., T. Ogata, H. Unuma, X.-C. Li, N.-N. Li, and X.-Y. Sun, *Self-compensation characteristics of Eu ions in BaTiO₃*. Solid State Ionics, 2011. **201**(1): p. 6-10.
162. Kim, J.H., S.H. Yoon, and Y.H. Han, *Effects of Y₂O₃ addition on electrical conductivity and dielectric properties of Ba-excess BaTiO₃*. Journal of the European Ceramic Society, 2007. **27**(2): p. 1113-1116.
163. Maier, R.A., K.F. Garrity, A. Ozarowski, M.P. Donohue, G. Cibir, and I. Levin, *Effects of octahedral tilting on the site of substitution of manganese in CaTiO₃*. Acta Materialia, 2021. **207**: p. 116688.
164. Groszewicz, P.B., L. Koch, S. Steiner, A. Ayrikyan, K.G. Webber, T. Frömling, K. Albe, and G. Buntkowsky, *The fate of aluminium in (Na,Bi)TiO₃-based ionic conductors*. Journal of Materials Chemistry A, 2020. **8**(35): p. 18188-18197.
165. Klyukin, K. and V. Alexandrov, *Effect of intrinsic point defects on ferroelectric polarization behavior of SrTiO₃*. Physical Review B, 2017. **95**(3): p. 035301.
166. De Souza, R.A., *Oxygen Diffusion in SrTiO₃ and Related Perovskite Oxides*. Advanced Functional Materials, 2015. **25**(40): p. 6326-6342.
167. Tang, A.S., J. Pellicciari, Q. Song, Q. Song, S. Ning, J.W. Freeland, R. Comin, and C.A. Ross, *XMCD study of magnetism and valence state in iron-substituted strontium titanate*. Physical Review Materials, 2019. **3**(5): p. 054408.

168. Merkle, R. and J. Maier, *Defect association in acceptor-doped SrTiO₃: case study for Fe²⁺Ti⁴⁺O and Mn²⁺Ti⁴⁺O*. Physical Chemistry Chemical Physics, 2003. **5**(11): p. 2297-2303.
169. Saiful Islam, M., *Ionic transport in ABO₃ perovskite oxides: a computer modelling tour*. Journal of Materials Chemistry, 2000. **10**(4): p. 1027-1038.
170. Szafraniak, B., Ł. Fuśnik, J. Xu, F. Gao, A. Brudnik, and A. Rydosz, *Semiconducting Metal Oxides: SrTiO₃, BaTiO₃ and BaSrTiO₃ in Gas-Sensing Applications: A Review*. Coatings, 2021. **11**(2): p. 185.
171. Trabelsi, H., M. Bejar, E. Dhahri, M.A. Valente, and M.P.F. Graça, *Oxygen-vacancy-related giant permittivity and ethanol sensing response in SrTiO_{3-δ} ceramics*. Physica E: Low-dimensional Systems and Nanostructures, 2019. **108**: p. 317-325.
172. Rodewald, S., N. Sakai, K. Yamaji, H. Yokokawa, J. Fleig, and J. Maier, *The Effect of the Oxygen Exchange at Electrodes on the High-Voltage Electrocoloration of Fe-Doped SrTiO₃ Single Crystals: A Combined SIMS and Microelectrode Impedance Study*. Journal of Electroceramics, 2001. **7**(2): p. 95-105.
173. Bodenmüller, N., *Cation nonstoichiometry in SrTiO₃ based solid oxide solar cells*, in *Institute of Chemical Technologies and Analytics*. 2020, TU Wien.
174. Amaral, L., A. Tkach, P.M. Vilarinho, and A.M.R. Senos, *New Insights into the Effect of Nonstoichiometry on the Electric Response of Strontium Titanate Ceramics*. The Journal of Physical Chemistry C, 2019. **123**(1): p. 710-718.
175. Rodewald, S., J. Fleig, and J. Maier, *Microcontact Impedance Spectroscopy at Single Grain Boundaries in Fe-Doped SrTiO₃ Polycrystals*. Journal of the American Ceramic Society, 2001. **84**(3): p. 521-530.
176. Kubicek, M., G.M. Rupp, S. Huber, A. Penn, A.K. Opitz, J. Bernardi, M. Stöger-Pollach, H. Hutter, and J. Fleig, *Cation diffusion in La_{0.6}Sr_{0.4}CoO_{3-δ} below 800 °C and its relevance for Sr segregation*. Physical Chemistry Chemical Physics, 2014. **16**(6): p. 2715-2726.
177. Assavachin, S., B.A. Nail, R. V. Goncalves, J.R. Mulcahy, S.E. Lloyd, and F.E. Osterloh, *Ferroelectric surface photovoltage enhancement in chromium-doped SrTiO₃ nanocrystal photocatalysts for hydrogen evolution*. Materials Advances, 2020. **1**(5): p. 1382-1389.
178. Horikiri, F., T. Ichikawa, L.Q. Han, A. Kaimai, K. Yashiro, H. Matsumoto, T. Kawada, and J. Mizusaki, *Nb-Doped SrTiO₃-Based High-Temperature Schottky Solar Cells*. Japanese Journal of Applied Physics, 2005. **44**(11): p. 8023-8026.
179. Xing, J., K. Zhao, H.B. Lu, X. Wang, G.Z. Liu, K.J. Jin, M. He, C.C. Wang, and G.Z. Yang, *Visible-blind, ultraviolet-sensitive photodetector based on SrTiO₃ single crystal*. Optics Letters, 2007. **32**(17): p. 2526-2528.
180. Xing, J., C. Zhao, E.-J. Guo, and F. Yang, *High-Performance Ultraviolet Photodetector Based on Polycrystalline SrTiO₃ Thin Film*. IEEE Sensors Journal - IEEE SENS J, 2012. **12**: p. 2561-2564.
181. Zhao, K., K.-j. Jin, Y. Huang, S. Zhao, H. Lu, M. He, Z. Chen, Y. Zhou, and G. Yang, *Ultraviolet fast-response photoelectric effect in tilted orientation SrTiO₃ single crystals*. Applied Physics Letters, 2006. **89**(17): p. 173507.
182. Zhou, N., K. Zhao, H. Liu, Z. Lu, H. Zhao, L. Tian, W. Liu, and S. Zhao, *Ultrafast photovoltaic effects in miscut Nb-doped SrTiO₃ single crystals*. Journal of Applied Physics, 2009. **105**(8): p. 083110.

183. Shablaev, S.I. and A.I. Grachev, *Investigation of the photoelectric component of the light-induced resistance-drop mechanism in SrTiO₃ crystals*. Physics of the Solid State, 2015. **57**(8): p. 1500-1504.
184. Ge, C., K.-j. Jin, Q.-h. Zhang, J.-y. Du, L. Gu, H.-z. Guo, J.-t. Yang, J.-x. Gu, M. He, J. Xing, C. Wang, H.-b. Lu, and G.-z. Yang, *Toward Switchable Photovoltaic Effect via Tailoring Mobile Oxygen Vacancies in Perovskite Oxide Films*. ACS Applied Materials & Interfaces, 2016. **8**(50): p. 34590-34597.
185. Wang, L., K.-j. Jin, J. Xing, C. Ge, H.-b. Lu, W.-j. Zhou, and G.-z. Yang, *High-sensitivity SrTiO₃ photodetectors with paralleled multiple interdigital electrode cells*. Applied Optics, 2013. **52**(15): p. 3473-3476.
186. Zhou, W.-j., K.-j. Jin, H.-z. Guo, C. Ge, M. He, and H.-b. Lu, *Electrode effect on high-detectivity ultraviolet photodetectors based on perovskite oxides*. Journal of Applied Physics, 2013. **114**(22): p. 224503.
187. Jin, K., Y. Zhang, B. Luo, J. Wang, C. Chen, and T. Wu, *Self-powered ultraviolet photovoltaic effects based on metal/SrTiO₃ Schottky junctions*. EPL (Europhysics Letters), 2013. **103**: p. 57007.
188. Yang, Y. and Y. Cheng, *Factors Affecting the Performance and Applicability of SrTiO₃ Photoelectrodes for Photoinduced Cathodic Protection*. Journal of The Electrochemical Society, 2017. **164**: p. C1067-C1075.
189. Suzuki, Y., Y. Okamoto, and N. Ishii, *Dye-sensitized solar cells using double-oxide electrodes: A brief review*. Journal of Physics: Conference Series, 2015. **596**.
190. Yamaura, J., Y. Muraoka, T. Yamauchi, T. Muramatsu, and Z. Hiroi, *Ultraviolet light selective photodiode based on an organic-inorganic heterostructure*. Applied Physics Letters, 2003. **83**(11): p. 2097-2099.
191. Yamaura, J.-I., Y. Muraoka, T. Muramatsu, T. Yamauchi, and Z. Hiroi, *Photocarrier injection to organic compounds*. Synthetic Metals, 2005. **152**(1): p. 385-388.
192. Zhou, Y., J. Zhu, X. Liu, and Z. Wu, *Photovoltaic effect of ferroelectric Pb(Zr_{0.52}Ti_{0.48})O₃ deposited on SrTiO₃ buffered n-GaAs by laser molecular beam epitaxy*. Functional Materials Letters, 2017. **10**(04): p. 1750036.
193. Liang, H., L. Cheng, X. Zhai, N. Pan, H. Guo, J. Zhao, H. Zhang, L. Li, X. Zhang, X. Wang, C. Zeng, Z. Zhang, and J.G. Hou, *Giant photovoltaic effects driven by residual polar field within unit-cell-scale LaAlO₃ films on SrTiO₃*. Sci Rep, 2013. **3**: p. 1975.
194. Luo, X., S. Xue, and J. Zhang, *Applications of Ferroelectric Materials in the Field of Photovoltaics*. General Chemistry, 2020. **6**: p. 190032-190032.
195. Beyreuther, E., A. Thiessen, J. Becherer, S. Grafström, K. Dörr, and L.M. Eng, *Probing electronic defect states in manganite/SrTiO₃ heterostructures by surface photovoltage spectroscopy*. Materials Science and Engineering: B, 2011. **176**(5): p. 446-452.
196. Beyreuther, E., S. Grafström, C. Thiele, K. Dörr, and L.M. Eng, *Surface Photovoltage Spectroscopy for the Investigation of Perovskite Oxide Interfaces*. MRS Proceedings, 2011. **902**: p. 0902-T07-05.
197. Wen, J., H. Guo, J. Xing, H. Lü, K.-J. Jin, M. He, and G. Yang, *High-sensitivity photovoltage based on the interfacial photoelectric effect in the SrTiO_{3-δ}/Si heterojunction*. Science China Physics, Mechanics and Astronomy, 2010. **53**(11): p. 2080-2083.

198. Wu, Z. and J. Gao, *Photocarrier injection and photo-resistance in SrTiO₃/GaAs p-n junctions*. EPL (Europhysics Letters), 2012. **100**: p. 57003.
199. Jin, K., Y. Li, Z. Wang, H. Peng, W. Lin, A. Kyaw, Y. Jin, K.-J. Jin, X. Sun, C. Soci, and T. Wu, *Tunable photovoltaic effect and solar cell performance of self-doped perovskite SrTiO₃*. AIP Advances, 2012. **2**.
200. Zheng, Y.T., Z.L. Zhang, and Y.L. Mao, *Photovoltaic response enhancement of SrTiO₃/TiO₂ composite*. Journal of Alloys and Compounds, 2013. **554**: p. 204-207.
201. Cho, S., J.-W. Jang, W. Zhang, A. Suwardi, H. Wang, D. Wang, and J.L. MacManus-Driscoll, *Single-Crystalline Thin Films for Studying Intrinsic Properties of BiFeO₃-SrTiO₃ Solid Solution Photoelectrodes in Solar Energy Conversion*. Chemistry of Materials, 2015. **27**(19): p. 6635-6641.
202. Nakashima, S., T. Uchida, D. Nakayama, H. Fujisawa, M. Kobune, and M. Shimizu, *Bulk photovoltaic effect in a BiFeO₃ thin film on a SrTiO₃ substrate*. Japanese Journal of Applied Physics, 2014. **53**: p. 09PA16.
203. Zhang, Z., G. Liu, and Y. Mao, *Improved separation efficiency of photogenerated carriers for Fe₂O₃/SrTiO₃ heterojunction semiconductor*. International Journal of Hydrogen Energy, 2013. **38**(22): p. 9349-9354.
204. Zhang, J., C. Tang, and J.H. Bang, *CdS/TiO₂-SrTiO₃ heterostructure nanotube arrays for improved solar energy conversion efficiency*. Electrochemistry Communications, 2010. **12**(8): p. 1124-1128.
205. Han, R., M.A. Melo, Z. Zhao, Z. Wu, and F.E. Osterloh, *Light Intensity Dependence of Photochemical Charge Separation in the BiVO₄/Ru-SrTiO₃:Rh Direct Contact Tandem Photocatalyst for Overall Water Splitting*. The Journal of Physical Chemistry C, 2020. **124**(18): p. 9724-9733.
206. Dho, J., *Electrode size dependent I-V characteristics and photovoltaic effect in the oxide p-n junctions Pr_{0.7}Ca_{0.3}MnO₃/Nb:SrTiO₃ and La_{0.7}Ca_{0.3}MnO₃/Nb:SrTiO₃*. Solid State Communications, 2010. **150**(45): p. 2243-2247.
207. Luo, C., K.X. Jin, C.L. Chen, and T. Wu, *Suppression of photovoltaic effect by magnetic field in Pr_{0.65}(Ca_{0.75}Sr_{0.25})_{0.35}MnO₃/Nb:SrTiO₃ heterostructure*. Applied Physics Letters, 2013. **103**(21): p. 212401.
208. Sheng, Z.G., B.C. Zhao, W.H. Song, Y.P. Sun, J.R. Sun, and B.G. Shen, *Change in photovoltage due to an external magnetic field in a manganite-based heterojunction*. Applied Physics Letters, 2005. **87**(24): p. 242501.
209. Wang, C., K.-j. Jin, R.-q. Zhao, H.-b. Lu, H.-z. Guo, C. Ge, M. He, C. Wang, and G.-z. Yang, *Ultimate photovoltage in perovskite oxide heterostructures with critical film thickness*. Applied Physics Letters, 2011. **98**(18): p. 181101.
210. Muramatsu, T., Y. Muraoka, and Z. Hiroi, *Photocarrier injection and the I-V characteristics of La_{0.8}Sr_{0.2}MnO₃/SrTiO₃:Nb heterojunctions*. Solid State Communications, 2004. **132**(5): p. 351-354.
211. Wang, C., Z.F. Li, X.M. Chen, J.M. Liu, Z.M. Liu, H.Y. Cui, Y. Yang, and W. Lu, *Study of carrier behavior in La_{0.9}Ba_{0.1}MnO_{3-δ}/SrTiO₃:Nb p-n heterojunction*. Thin Solid Films, 2008. **516**(12): p. 4282-4287.
212. Wu, Z.P., L. Wang, and J. Gao, *Rectifying characteristics, magnetic tunability, and photovoltaic response in La_{0.8}Hf_{0.2}MnO₃/0.7 wt% Nb-SrTiO₃ heteroepitaxial junctions*. Journal of Applied Physics, 2012. **111**(7): p. 07D723.

213. Qi, Y., H. Ni, M. Zheng, J. Zeng, Y. Jiang, and J. Gao, *Photoresponse in $La_{0.9}Hf_{0.1}MnO_3/0.05\text{wt}\%Nb\text{-doped SrTiO}_3$ heteroepitaxial junctions*. AIP Advances, 2018. **8**(5): p. 055806.
214. Sun, J.R., B.G. Shen, Z.G. Sheng, and Y.P. Sun, *Temperature-dependent photovoltaic effects in the manganite-based heterojunction*. Applied Physics Letters, 2004. **85**(16): p. 3375-3377.
215. Sun, J.R., C.M. Xiong, B.G. Shen, P.Y. Wang, and Y.X. Weng, *Manganite-based heterojunction and its photovoltaic effects*. Applied Physics Letters, 2004. **84**(14): p. 2611-2613.
216. Sun, J.R., C.H. Lai, and H.K. Wong, *Photovoltaic effect in $La_{0.7}Ce_{0.3}MnO_3\text{-}/SrTiO_3\text{-}Nb$ heterojunction and its oxygen content dependence*. Applied Physics Letters, 2004. **85**(1): p. 37-39.
217. Qian, T., T.F. Zhou, and X.G. Li, *Study on the stability of charge-ordered state and rectifying properties of heteroepitaxial structure for manganites*. Journal of Electroceramics, 2008. **21**(1): p. 85-90.
218. Qiu, J., H.-B. Lu, K.-J. Jin, M. He, and J. Xing, *Manganite-layer thickness-dependent photovoltaic effect of $La_{0.9}Sr_{0.1}MnO_3/SrNb_{0.01}Ti_{0.99}O_3$ p-n heterojunction*. Physica B: Condensed Matter, 2007. **400**(1): p. 66-69.
219. Zhou, W.-j., K.-j. Jin, H.-z. Guo, X. He, M. He, X.-l. Xu, H.-b. Lu, and G.-z. Yang, *Significant enhancement of photovoltage in artificially designed perovskite oxide structures*. Applied Physics Letters, 2015. **106**(13): p. 131109.
220. Wang, J., D. Cao, Y. Zhou, X. Wang, Z. Jiao, and J. Gao, *Series resistance effects in $La_{0.5}Ca_{0.5}MnO_3/SrTiO_3:Nb(0\ 0\ 1)$ heterojunctions*. Journal of Physics D: Applied Physics, 2015. **48**: p. 385104.
221. Wang, J.Y., W. Zhai, B.C. Luo, K.X. Jin, and C.L. Chen, *Time response of photovoltage in $La_{0.9}Li_{0.1}MnO_3/SrTiO_3\text{-}Nb$ heterojunction under ultraviolet light*. Solid State Communications, 2014. **187**: p. 10-12.
222. Wang, J., B. Luo, S. Wang, Q. Shao, J. Zhao, and Z. Guo, *Rectifying and ultraviolet photovoltage characteristics of $La_{0.9}Na_{0.1}MnO_3/SrTiO_3\text{-}Nb$ heterostructures*. Applied Physics Letters, 2017. **111**(13): p. 132101.
223. Wang, J., J. Bai, H. Xing, S. Wang, M. Wang, K. Jin, and C. Chen, *Temperature-dependent photovoltage response in $La_{0.9}Li_{0.1}MnO_3/SrTiO_3\text{-}Nb$ heterojunction induced by a low intensity pulse laser*. Solid State Communications, 2017. **251**: p. 35-38.
224. Jin, K.X., Y.X. Zhai, H. Li, Y.F. Tian, B.C. Luo, and T. Wu, *Favorable ultraviolet photoelectric effects in $TbMnO_3/Nb\text{-}SrTiO_3$ heterostructures*. Solid State Communications, 2014. **199**: p. 39-42.
225. Sun, J.R., S.Y. Zhang, B.G. Shen, and H.K. Wong, *Rectifying and photovoltaic properties of the heterojunction composed of $CaMnO_3$ and Nb-doped $SrTiO_3$* . Applied Physics Letters, 2005. **86**(5): p. 053503.
226. Wang, K., W. Gao, H.W. Zheng, F.Z. Li, M.S. Zhu, G. Yang, G.T. Yue, Y.K. Liu, and R.K. Zheng, *Heteroepitaxial growth of Cu_2O films on Nb- $SrTiO_3$ substrates and their photovoltaic properties*. Ceramics International, 2017. **43**(18): p. 16232-16237.
227. Shang, D.S., J.R. Sun, L. Shi, Z.H. Wang, and B.G. Shen, *Resistance dependence of photovoltaic effect in $Au/SrTiO_3:Nb(0.5\ \text{wt}\%)$ Schottky junctions*. Applied Physics Letters, 2008. **93**(17): p. 172119.

228. Yang, F., H. Zhang, Z.Y. Liu, Y.R. Jiang, M.Y. Han, and F.G. Chang, *Photovoltaic effect of $YBa_2Cu_3O_{7-\delta}/SrTiO_3:Nb$ heterojunction annealed in different oxygen partial pressure*. Materials Letters, 2014. **130**: p. 51-53.
229. Muraoka, Y., T. Muramatsu, J. Yamaura, and Z. Hiroi, *Photogenerated hole carrier injection to $YBa_2Cu_3O_{7-x}$ in an oxide heterostructure*. Applied Physics Letters, 2004. **85**(14): p. 2950-2952.
230. Asakura, D., J.W. Quilty, K. Takubo, S. Hirata, T. Mizokawa, Y. Muraoka, and Z. Hiroi, *Photoemission Study of $YBa_2Cu_3O_x$ Thin Films under Light Illumination*. Physical Review Letters, 2004. **93**(24): p. 247006.
231. Hao, F.X., C. Zhang, X. Liu, Y.W. Yin, Y.Z. Sun, and X.G. Li, *Photovoltaic effect in $YBa_2Cu_3O_{7-\delta}/Nb$ -doped $SrTiO_3$ heterojunctions*. Applied Physics Letters, 2016. **109**(13): p. 131104.
232. Zhao, S., A. Gu, X. Yan, L. Hao, Y. Xie, T. Zhang, and K. Jin, *Transport and photoresponse properties in $Pr_{0.5}Ca_{0.5}CoO_3/Nb-SrTiO_3$ heterostructure*. EPL (Europhysics Letters), 2015. **108**: p. 67007.
233. Wang, X., Q. Zhou, H. Li, C. Hu, L. Zhang, Y. Zhang, Y. Zhang, Y. Sui, and B. Song, *Self-powered ultraviolet vertical and lateral photovoltaic effect with fast-relaxation time in $NdNiO_3/Nb:SrTiO_3$ heterojunctions*. Applied Physics Letters, 2018. **112**(12): p. 122103.
234. Li, H., K.X. Jin, S.H. Yang, J. Wang, M. He, B.C. Luo, J.Y. Wang, C.L. Chen, and T. Wu, *Ultraviolet photovoltaic effect in $BiFeO_3/Nb-SrTiO_3$ heterostructure*. Journal of Applied Physics, 2012. **112**(8): p. 083506.
235. Wang, L., S. Dash, L. Chang, L. You, Y. Feng, X. He, K.-j. Jin, Y. Zhou, H.G. Ong, P. Ren, S. Wang, L. Chen, and J. Wang, *Oxygen Vacancy Induced Room-Temperature Metal–Insulator Transition in Nickelate Films and Its Potential Application in Photovoltaics*. ACS Applied Materials & Interfaces, 2016. **8**(15): p. 9769-9776.
236. Wang, S., H. Li, K. Zhao, S. Zhao, M. Chen, J. Chen, J. Wang, and G. Fu, *Rectifying and photovoltage characteristics of $Bi_2Sr_2Co_2O_{10}/Nb$ -doped $SrTiO_3$ heterojunction*. Applied Physics A, 2011. **105**(2): p. 407-410.
237. Zhu, Y., Y. Liu, J. Wang, L. Zhao, K. Zhan, and Y. Chen, *Temperature modulating rectifier behavior and photovoltaic response of $VO_x/Nb:SrTiO_3$ heterojunctions*. Journal of Physics D: Applied Physics, 2020. **53**.
238. Lu, Z.-q., H. Ni, K. Zhao, W.-x. Leng, Y.-C. Kong, and H.-K. Wong, *Fast photovoltaic effects tuned by vicinal interface microstructure in manganite-based all-perovskite-oxide heterojunctions*. Applied Optics, 2011. **50**(31): p. G23-G26.
239. Jin, K.-j., H.-b. Lu, K. Zhao, C. Ge, M. He, and G.-z. Yang, *Novel Multifunctional Properties Induced by Interface Effects in Perovskite Oxide Heterostructures*. Advanced Materials, 2009. **21**(45): p. 4636-4640.
240. Ni, H., S.L. Da, K. Zhao, Y.-C. Kong, H.K. Wong, and S.Q. Zhao, *Temperature-dependent transport and transient photovoltaic properties of $La_{2/3}Ca_{1/3}MnO_3/Nb:SrTiO_3$ heteroepitaxial p-n junction*. Journal of Applied Physics, 2012. **112**(2): p. 023101.
241. Blakers, A.W., A. Wang, A.M. Milne, J. Zhao, and M.A. Green, *22.8% efficient silicon solar cell*. Applied Physics Letters, 1989. **55**(13): p. 1363-1365.
242. Boix, P.P., S. Agarwala, T.M. Koh, N. Mathews, and S.G. Mhaisalkar, *Perovskite Solar Cells: Beyond Methylammonium Lead Iodide*. The Journal of Physical Chemistry Letters, 2015. **6**(5): p. 898-907.

243. Carlson, D.E. and C.R. Wronski, *Amorphous silicon solar cell*. Applied Physics Letters, 1976. **28**(11): p. 671-673.
244. Green, M.A., *The path to 25% silicon solar cell efficiency: History of silicon cell evolution*. Progress in Photovoltaics: Research and Applications, 2009. **17**(3): p. 183-189.
245. Green, M.A., E.D. Dunlop, J. Hohl-Ebinger, M. Yoshita, N. Kopidakis, and A.W.Y. Ho-Baillie, *Solar cell efficiency tables (Version 55)*. Progress in Photovoltaics: Research and Applications, 2020. **28**(1): p. 3-15.
246. Noel, N.K., S.D. Stranks, A. Abate, C. Wehrenfennig, S. Guarnera, A.-A. Haghighirad, A. Sadhanala, G.E. Eperon, S.K. Pathak, M.B. Johnston, A. Petrozza, L.M. Herz, and H.J. Snaith, *Lead-free organic–inorganic tin halide perovskites for photovoltaic applications*. Energy & Environmental Science, 2014. **7**(9): p. 3061-3068.
247. Strümpel, C., M. McCann, G. Beaucarne, V. Arkhipov, A. Slaoui, V. Švrček, C. del Cañizo, and I. Tobias, *Modifying the solar spectrum to enhance silicon solar cell efficiency—An overview of available materials*. Solar Energy Materials and Solar Cells, 2007. **91**(4): p. 238-249.
248. Wang, R., M. Mujahid, Y. Duan, Z.-K. Wang, J. Xue, and Y. Yang, *A Review of Perovskites Solar Cell Stability*. Advanced Functional Materials, 2019. **29**(47): p. 1808843.
249. Rühle, S., A.Y. Anderson, H.-N. Barad, B. Kupfer, Y. Bouhadana, E. Rosh-Hodesh, and A. Zaban, *All-Oxide Photovoltaics*. The Journal of Physical Chemistry Letters, 2012. **3**(24): p. 3755-3764.
250. Dittrich, T., V. Duzhko, F. Koch, V. Kytin, and J. Rappich, *Trap-limited photovoltage in ultrathin metal oxide layers*. Physical Review B, 2002. **65**(15): p. 155319.
251. Herion, J., E.A. Niekisch, and G. Scharl, *Investigation of metal oxide/cuprous oxide heterojunction solar cells*. Solar Energy Materials, 1980. **4**(1): p. 101-112.
252. Iwanowski, R.J. and D. Trivich, *Enhancement of the photovoltaic conversion efficiency in Cu/Cu₂O schottky barrier solar cells by H⁺ ion irradiation*. physica status solidi (a), 1986. **95**(2): p. 735-741.
253. Rakhshani, A.E., *Preparation, characteristics and photovoltaic properties of cuprous oxide—a review*. Solid-State Electronics, 1986. **29**(1): p. 7-17.
254. Rai, B.P., *Cu₂O solar cells: A review*. Solar Cells, 1988. **25**(3): p. 265-272.
255. Katayama, J., K. Ito, M. Matsuoka, and J. Tamaki, *Performance of Cu₂O/ZnO Solar Cell Prepared By Two-Step Electrodeposition*. Journal of Applied Electrochemistry, 2004. **34**(7): p. 687-692.
256. Minami, T., Y. Nishi, T. Miyata, and J.-i. Nomoto, *High-Efficiency Oxide Solar Cells with ZnO/Cu₂O Heterojunction Fabricated on Thermally Oxidized Cu₂O Sheets*. Applied Physics Express, 2011. **4**(6): p. 062301.
257. Nishi, Y., T. Miyata, and T. Minami, *Effect of inserting a thin buffer layer on the efficiency in n-ZnO/p-Cu₂O heterojunction solar cells*. Journal of Vacuum Science & Technology A, 2012. **30**(4): p. 04D103.
258. Li, D., C.-J. Chien, S. Deora, P.-C. Chang, E. Moulin, and J.G. Lu, *Prototype of a scalable core–shell Cu₂O/TiO₂ solar cell*. Chemical Physics Letters, 2011. **501**(4): p. 446-450.
259. Musselman, K.P., A. Wisnet, D.C. Iza, H.C. Hesse, C. Scheu, J.L. MacManus-Driscoll, and L. Schmidt-Mende, *Strong Efficiency Improvements in Ultra-low-Cost Inorganic Nanowire Solar Cells*. Advanced Materials, 2010. **22**(35): p. E254-E258.

260. Musselman, K.P., A. Marin, A. Wisnet, C. Scheu, J.L. MacManus-Driscoll, and L. Schmidt-Mende, *A Novel Buffering Technique for Aqueous Processing of Zinc Oxide Nanostructures and Interfaces, and Corresponding Improvement of Electrodeposited ZnO-Cu₂O Photovoltaics*. *Advanced Functional Materials*, 2011. **21**(3): p. 573-582.
261. Musselman, K.P., A. Marin, L. Schmidt-Mende, and J.L. MacManus-Driscoll, *Incompatible Length Scales in Nanostructured Cu₂O Solar Cells*. *Advanced Functional Materials*, 2012. **22**(10): p. 2202-2208.
262. Cui, J. and U.J. Gibson, *A Simple Two-Step Electrodeposition of Cu₂O/ZnO Nanopillar Solar Cells*. *The Journal of Physical Chemistry C*, 2010. **114**(14): p. 6408-6412.
263. Yang, S.Y., L.W. Martin, S.J. Byrnes, T.E. Conry, S.R. Basu, D. Paran, L. Reichertz, J. Ihlefeld, C. Adamo, A. Melville, Y.-H. Chu, C.-H. Yang, J.L. Musfeldt, D.G. Schlom, J.W.A. III, and R. Ramesh, *Photovoltaic effects in BiFeO₃*. *Applied Physics Letters*, 2009. **95**(6): p. 062909.
264. Rani, R.A., A.S. Zoolfakar, A.S. Ismail, S.S.A. Karim, M.H. Mamat, and M. Rusop, *High sensitivity ultra-violet photosensor based on nanostructured Nb₂O₅*. *AIP Conference Proceedings*, 2019. **2151**(1): p. 020031.
265. Fang, X., L. Hu, K. Huo, B. Gao, L. Zhao, M. Liao, P.K. Chu, Y. Bando, and D. Golberg, *New Ultraviolet Photodetector Based on Individual Nb₂O₅ Nanobelts*. *Advanced Functional Materials*, 2011. **21**(20): p. 3907-3915.
266. Ozel, K., A. Atilgan, N.E. Koksall, and A. Yildiz, *A route towards enhanced UV photo-response characteristics of SnO₂/p-Si based heterostructures by hydrothermally grown nanorods*. *Journal of Alloys and Compounds*, 2020. **849**: p. 156628.
267. Chen, Y., C. Zhu, M. Cao, and T. Wang, *Photoresponse of SnO₂ nanobelts grown in situ on interdigital electrodes*. *Nanotechnology*, 2007. **18**(28): p. 285502.
268. Takubo, N., Y. Muraoka, and Z. Hiroi, *Conductivity Switching by Ultraviolet Light in Tin Dioxide Thin Films*. *Applied Physics Express*, 2009. **2**: p. 045501.
269. Takubo, N., Y. Muraoka, and Z. Hiroi, *Effect of UV light irradiation in SnO₂ thin film*. *Journal of Physics: Conference Series*, 2009. **148**: p. 012025.
270. Huang, M.-H., J.-Y. Xia, Y.-M. Xi, and C.-X. Ding, *Study on photochromism in SrTiO₃:Fe ceramic powder*. *Journal of the European Ceramic Society*, 1997. **17**(14): p. 1761-1765.
271. Rossella, F., P. Galinetto, G. Samoggia, V. Trepakov, and L. Jastrabik, *Photoconductivity and the structural phase transition in SrTiO₃*. *Solid State Communications*, 2007. **141**(2): p. 95-98.
272. Mehra, S., S. Bishnoi, L. Goswami, G. Gupta, A.K. Srivastava, and S. Narain Sharma, *Detailed chemical mechanism of the phase transition in nano-SrTiO₃ perovskite with visible luminescence*. *Inorganic Chemistry Communications*, 2020. **120**: p. 108125.
273. Zhang, S., D. Guo, M. Wang, M.S. Javed, and C. Hu, *Magnetism in SrTiO₃ before and after UV irradiation*. *Applied Surface Science*, 2015. **335**: p. 115-120.
274. Katsu, H., H. Tanaka, and T. Kawai, *Anomalous Photoconductivity in SrTiO₃*. *Japanese Journal of Applied Physics*, 2000. **39**(Part 1, No. 5A): p. 2657-2658.
275. Liu, H., K. Zhao, N. Zhou, H. Lu, M. He, Y. Huang, K.-J. Jin, Y. Zhou, G. Yang, S. Zhao, A. Wang, and W. Leng, *Photovoltaic effect in micrometer-thick perovskite-type oxide multilayers on Si substrates*. *Applied Physics Letters*, 2008. **93**(17): p. 171911.

276. Yue, Z.J., K. Zhao, S.Q. Zhao, Z.Q. Lu, X.M. Li, H. Ni, and A.J. Wang, *Thickness-dependent photovoltaic effects in miscut Nb-doped SrTiO₃ single crystals*. Journal of Physics D: Applied Physics, 2009. **43**(1): p. 015104.
277. Ojeda-G-P, A., M. Döbeli, and T. Lippert, *Influence of Plume Properties on Thin Film Composition in Pulsed Laser Deposition*. Advanced Materials Interfaces, 2018. **5**(18): p. 1701062.
278. Tebano, A., E. Fabbri, D. Pergolesi, G. Balestrino, and E. Traversa, *Room-Temperature Giant Persistent Photoconductivity in SrTiO₃/LaAlO₃ Heterostructures*. ACS Nano, 2012. **6**(2): p. 1278-1283.
279. Gurwitz, R., R. Cohen, and I. Shalish, *Interaction of light with the ZnO surface: Photon induced oxygen "breathing," oxygen vacancies, persistent photoconductivity, and persistent photovoltage*. Journal of Applied Physics, 2014. **115**(3): p. 033701.
280. Ho, Y.-C., M.N.F. Hoque, E. Stoneham, J. Warzywoda, T. Dallas, and Z. Fan, *Reduction of Oxygen Vacancy Related Traps in TiO₂ and the Impacts on Hybrid Perovskite Solar Cells*. The Journal of Physical Chemistry C, 2017. **121**(43): p. 23939-23946.
281. Scafetta, M.D., Y.J. Xie, M. Torres, J.E. Spanier, and S.J. May, *Optical absorption in epitaxial La_{1-x}Sr_xFeO₃ thin films*. Applied Physics Letters, 2013. **102**(8): p. 081904.
282. Mildner, S., J. Hoffmann, P.E. Blöchl, S. Techert, and C. Jooss, *Temperature- and doping-dependent optical absorption in the small-polaron system Pr_{1-x}Ca_xMnO₃*. Physical Review B, 2015. **92**(3): p. 035145.
283. Nomerovannaya, L.V., A.A. Makhnev, and A.Y. Rumyantsev, *Evolution of the optical properties of single-crystal La_{1-x}Sr_xMnO₃*. Physics of the Solid State, 1999. **41**(8): p. 1322-1326.
284. Raffaele, R., H.U. Anderson, D.M. Sparlin, and P.E. Parris, *Transport anomalies in the high-temperature hopping conductivity and thermopower of Sr-doped La(Cr,Mn)O₃*. Physical Review B, 1991. **43**(10): p. 7991-7999.
285. Khan, M.S.R. and A. Reza, *Optical and electrical properties of optimized thin gold films as top layer of MIS solar cells*. Applied Physics A, 1992. **54**(2): p. 204-207.
286. Sushko, P.V., L. Qiao, M. Bowden, T. Varga, G.J. Exarhos, F.K. Urban, D. Barton, and S.A. Chambers, *Multiband Optical Absorption Controlled by Lattice Strain in Thin-Film LaCrO₃*. Physical Review Letters, 2013. **110**(7): p. 077401.
287. Zhang, K.H.L., Y. Du, A. Papadogianni, O. Bierwagen, S. Sallis, L.F.J. Piper, M.E. Bowden, V. Shutthanandan, P.V. Sushko, and S.A. Chambers, *Perovskite Sr-Doped LaCrO₃ as a New p-Type Transparent Conducting Oxide*. Advanced Materials, 2015. **27**(35): p. 5191-5195.
288. Frye, A., R.H. French, and D.A. Bonnell, *Optical Properties and Electronic Structure of Oxidized and Reduced Single-Crystal Strontium Titanate*. Zeitschrift für Metallkunde, 2003. **94**(3): p. 226-232.
289. Capizzi, M. and A. Fropa, *Optical Gap of Strontium Titanate (Deviation from Urbach Tail Behavior)*. Physical Review Letters, 1970. **25**(18): p. 1298-1302.
290. Rodewald, S., J. Fleig, and J. Maier, *Resistance Degradation of Iron-Doped Strontium Titanate Investigated by Spatially Resolved Conductivity Measurements*. Journal of the American Ceramic Society, 2000. **83**(8): p. 1969-1976.
291. Rodewald, S., J. Fleig, and J. Maier, *Measurement of conductivity profiles in acceptor-doped strontium titanate*. Journal of the European Ceramic Society, 1999. **19**(6): p. 797-801.

292. Baiatu, T., R. Waser, and K.-H. Härdtl, *dc Electrical Degradation of Perovskite-Type Titanates: III, A Model of the Mechanism*. Journal of the American Ceramic Society, 1990. **73**(6): p. 1663-1673.
293. Maier, J., *Mass Transport in the Presence of Internal Defect Reactions—Concept of Conservative Ensembles: III, Trapping Effect of Dopants on Chemical Diffusion*. Journal of the American Ceramic Society, 1993. **76**(5): p. 1223-1227.
294. De Souza, R.A., V. Metlenko, D. Park, and T.E. Weirich, *Behavior of oxygen vacancies in single-crystal SrTiO₃: Equilibrium distribution and diffusion kinetics*. Physical Review B, 2012. **85**(17): p. 174109.
295. Lu, X., P. Jiang, and X. Bao, *Phonon-enhanced photothermoelectric effect in SrTiO₃ ultra-broadband photodetector*. Nature communications, 2019. **10**(1): p. 138-138.
296. Tarancón, A. and N. Pryds, *Functional Oxide Thin Films for Advanced Energy and Information Technology*. Advanced Materials Interfaces, 2019. **6**(15): p. 1900990.
297. Noll, F., W. Münch, I. Denk, and J. Maier, *SrTiO₃ as a prototype of a mixed conductor conductivities, oxygen diffusion and boundary effects*. Solid State Ionics, 1996. **86-88**(PART 2): p. 711-717.